Spectroscopic Studies of the Model Traction Fluid Bis(Cyclohexyl) Succinate and Related Molecules

By

Rorie Dempster B.Sc. (Hons)

(Hatfield College)

A Thesis submitted for the degree of
Doctor of Philosophy

University of Durham
Chemistry Department
September
1994

To Kirsteen and my Parents

Declaration

The work described in this thesis was carried out in the University of Durham between October 1991 and September 1994. This work has not been submitted, either completely or in any part, for a degree in this or any other University and is the original work of the author except where acknowledged by reference.

Acknowledgements

I am very grateful for the help of my supervisor Professor Jack Yarwood. His encouragement and assistance has been invaluable.

I would also like to thank Shell Research for the funding for this project. Special thanks goes to Dr. C. G. Shelton for his help with interpretation and the structuring of my thesis and to Laurence Scales for producing the state of the art three dimensional pressure and film thickness profiles for the EHD contact.

There are many other people that have provided me with help and encouragement throughout my three years of study that require mentioning.

Dr. J.P.S. Badyal acted as my supervisor for my final year when Jack had moved to Sheffield and Drs. C.W and V. Anderson and family provided me with great hospitality during my stays in Sheffield. My thanks goes to them.

We then move on to my friends without whom my three years of study would not have been as much fun. I would like to thank the people in Jack's research group (past and present) Simon, Jon, Nigel , Reena and Bryan, my housemates in Sutton Street Don, Pete and Rob, Terry Harrison for assisting with instrumentation and computing problems, and all the people who helped keep me sane in the computer room Tim, Simon, Rachel, Helen, Mark, Leela and Penny.

Finally, I would like to thank Kirsteen and my parents for always being there, and I dedicate this thesis to them.

Abstract

Fourier transform infra-red spectroscopy/microscopy and Raman scattering/microscopy have been used to try and relate the microscopic behaviour (i.e. the molecular properties) with the macroscopic behaviour (i.e. the viscosity) of the model traction fluid Bis(cyclohexyl) Succinate. Other structurally related compounds have also been studied to assist with interpretation.

Variable temperature studies produced few conclusive changes, with the balance between density and temperature effects giving rise to few spectroscopically visible changes. Some correlation between the viscosity of the molecules studied and the changes observed was seen. The appearance of two distinct carbonyl stretching bands which change in intensity with temperature indicates an intramolecular conformational change.

There is considerable broadening of all the vibrational bands of the molecules studied as the pressure is increased indicating an increase in the vibrational relaxation rate. Repulsive interactions are also seen to dominate as the pressure is increased. Analysis using the Kubo model has shown that the carbonyl stretching band is more likely to be formed in the slow modulation regime.

Unusual behaviour is exhibited in some spectra obtained from the dynamic pressure studies including unusual band shapes and negative going bands. The combination of high pressure, shear rate, and temperature in the centre of the elastohydrodynamic contact only allows the bis(cyclohexyl) succinate molecules to assume a single conformation. As these conditions lessen, the molecules become less constrained and different behaviour is observed. Three dimensional pressure and film thickness profiles have been used to explain the changes seen in terms of a combination of pressure and film thickness changes.

Solution studies show there are strong attractive dipole-dipole interactions, probably localised at the carbonyl group, between the bis(cyclohexyl) succinate molecules.

Using the Eyring fluid model and viscosity data, the molecular behaviour has been related to the viscosity of the molecules.

TABLE OF CONTENTS

CHAPTER 1

Introduction

1.0 Introduction

In this thesis, the relationship between microscopic (molecular) properties, probed using vibrational spectroscopic methods, and macroscopic properties e.g. viscosity, of a specific type of model lubricant have been studied. The overall objective of this research is to gain fundamental knowledge from which superior lubricants may be designed.

The lubrication of machinery in which contacting surfaces move relative to one another is essential for the efficient operation of any such motion. The primary function of a lubricant is to separate two adjacent moving surfaces, thereby reducing friction and increasing the mechanical efficiency and decreasing the wear of the surfaces. The secondary functions are to dissipate any heat which is evolved by the moving surfaces and to carry away any wear particles or impurities preventing further wear to the surfaces. Lubrication is achieved by the formation of a film between mutually opposed surfaces of the machine. The film bears the load and the shear generated by the surfaces and reduces the friction to a minimum. The lubricant must possess a long lifetime i.e. it must not rapidly degrade under the operating conditions, and it must not corrode any part of machinery with which it comes into contact with. The suitability of a lubricant depends on the viscosity and the response of the viscosity to the conditions encountered during the lubrication process i.e. high pressure, high local temperature and variable shear rate.

Traction fluids are a special type of lubricant. Modern traction drives transfer mechanical shaft power from a source to a load efficiently by means of metal rollers running on a film of traction fluid against similar rollers. A traction drive depends on the rate of shearing of a very thin fluid film to transmit variable torques from the input members to the output members. Traction fluids are selected because they have a very high pressure viscosity index. (i.e. as the pressure increases, the viscosity of the fluid also increases). The local pressure on the fluid trapped in the contact area is momentarily increased to several thousand atmospheres. (N.B. 1 atmosphere = 1 bar = $1*10^5$Pa)

Therefore, the local fluid viscosity must increase enough so that the film supports a substantial normal force without permitting the metal parts to come in contact with one another. The properties desirable for traction fluids are the same as those for lubricants mentioned above. In addition, the traction fluid must resist deterioration and maintain its viscosity during shearing. Traction drives do not operate successfully where the traction fluid viscosity is so high due to low temperature that the fluid can not be pumped, or so thin due to high temperature that no adequate fluid film can be maintained.

The performance of a traction fluid must ultimately depend on the molecular properties of the fluid. Flexibility, size, and shape of a traction fluid molecule and interactions with the surrounding molecules determines the bulk fluid properties[1]. Various techniques which allow the probing of molecular properties have been used to discover how phenomena such as rotations, translations, interactions, and properties such as size and shape control bulk fluid responses as a function of pressure, temperature, and shear rate. The techniques fall into two main categories:

1) Spectroscopic techniques[2]

2) Molecular modelling[3,4]

Analysis using these methods allows the detailed probing of molecular dynamics and interactions in the fluid. If this is coupled with measurements of bulk fluid properties, attempts can be made qualitatively to relate the molecular composition to the physical properties of the fluid. Therefore, parts of the molecule can be altered accordingly to enable better traction fluids to be designed with physical properties closer to the ideal.

1.1 Lubrication

It was the work of Osborne Reynolds[5] (1842-1912) on the behaviour of shafts or journals rotating in bearings that began the modern day studies of lubrication. Today, there is a large amount of published work related to tribology.

There are several mechanisms by which lubrication can occur. These include hydrodynamic, elastohydrodynamic, boundary, and extreme pressure lubrication. Each of these rely on the properties of the lubricant and the surfaces to different extents.

1.1.1 Hydrodynamic Lubrication

The word hydrodynamic conveys two ideas: a liquid (hydro) and relative motion (dynamic).

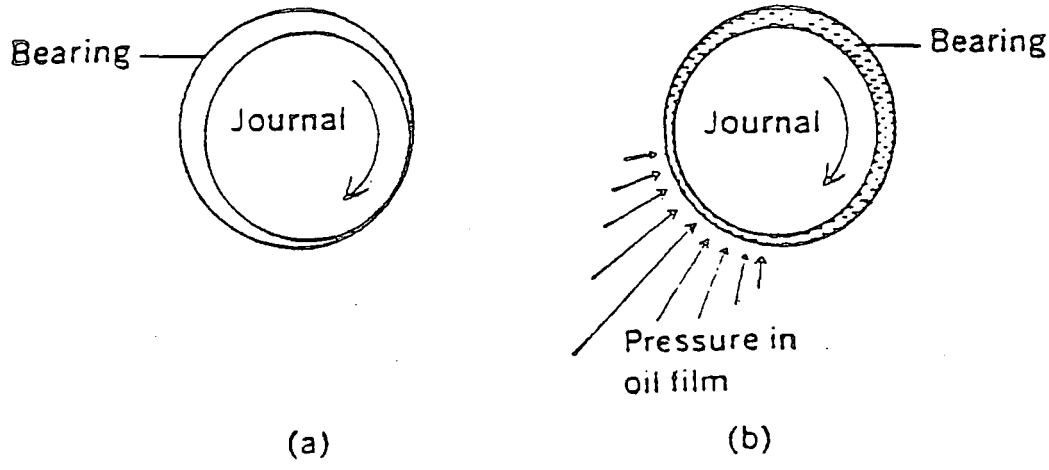

Figure 1.1. Example of hydrodynamic lubrication in a journal bearing. Journal or shaft rotating clockwise in a bearing. (a) Unlubricated, the shaft climbs up to the right. (b) In the presence of a suitable lubricant, the shaft moves to the left and drags a wedge of oil with it. Under ideal hydrodynamic conditions, the oil pressure can support the load and all the friction arises from the viscous resistance of the oil. Adapted from reference 6

Consider figure 1.1. If a shaft or journal rotates in a clockwise direction in a dry bearing it crawls up the right hand side of the bearing as shown in figure 1.1a. If a lubricant is added, the system runs properly, and the shaft is displaced to the opposite side of the bearing (figure 1.1b) and drags a converging wedge of fluid between it and

the bearing surface. Therefore, there is an increase in velocity of flow as the fluid passes through the narrowing constriction between the moving surfaces. Reynolds showed[5] that because the liquid is viscous, this produces a build up of liquid pressure in the fluid wedge which, under favourable conditions, is sufficient to keep the surfaces completely apart.

From the pioneering work by Reynolds, it was apparent that there are two features that are essential in hydrodynamic lubrication[6]. These are that the liquid must be viscous, and the geometry of the surfaces must be such that when one surface moves over another, a convergent wedge of liquid is formed (figure 1.1).

In hydrodynamic lubrication, all of the friction arises from shearing of the lubricant film. It is therefore determined by the viscosity of the oil. (The less viscous the oil, the lower the friction). But, if the viscosity of the oil is too small, the distance of nearest approach becomes such that it is smaller than the surface irregularities. The film may then be penetrated, and consequently there is an increase in friction and wear. The distance of nearest approach gets smaller as the load on the bearing increases. This also occurs when the shear rate decreases, or when the viscosity of the oil is low. The heating of the oil in the contact due to friction causes a decrease in the viscosity, and this can also lead to film penetration. This problem can be solved by increasing the amount of oil available for the contact or by adding viscosity index improvers (usually high molecular weight polymers) to the oil in small amounts (1-5%).

Providing the surfaces are smooth, and the shaft and bearing are aligned properly, the friction in hydrodynamic lubrication is very low. The main problems associated with hydrodynamic lubrication are associated with starting or stopping since the film thickness of the oil is theoretically zero when the speed is zero.

1.1.2 Elastohydrodynamic Lubrication

Elastohydrodynamic (EHD) lubrication occurs when the surfaces do not conform well to one another and the load is concentrated into a small contact area. The operating pressures at the point of contact can reach up to hundreds of times (40kbar = 4GPa) that in hydrodynamic lubrication. The relatively low hydrodynamic pressures generated in the

converging region are unlikely to be able to separate the surfaces in the high pressure region of the contact (Hertzian zone). EHD lubrication works because under the extreme pressure of the contact zone, the fluid becomes extremely thin ($\cong 10^{-6}$m) and the viscosity is increased by several orders of magnitude[6].

As the fluid flows into the converging surfaces of the inlet region a reduction in velocity occurs creating hydrodynamic pressure. At the leading edge of the Hertzian region this hydrodynamic pressure is sufficient to separate the two surfaces. Once this is achieved, the fluid can not escape from the Hertzian region, since the viscosity is too great and the film too thin for escape of the fluid in the short time in which the surfaces pass through the contact. The fluid entering the contact becomes trapped between the surfaces, and at the high pressures in the Hertzian region, behaves like a solid separating layer. It is this layer that prevents the surfaces coming into contact. The friction resulting from the extreme pressure in EHD lubrication is much greater (100 times) than in hydrodynamic lubrication but it is still considerably less than if unlubricated. This type of lubrication is known as elastohydrodynamic because in the Hertzian region the extreme pressures developed in the fluid cause the surfaces to deform elastically. Consequently, EHD lubrication is dependent on the properties of both the fluid and the surface material. The Hertzian region is named after H. Hertz who in 1881, analysed the contact between elastic bodies under conditions where the region of contact is very much smaller than the radius of curvature.[7]

A schematic profile of the contact zone and the corresponding fluid pressure profile in EHD lubrication are shown in figures 1.2 and 1.3 respectively. It should be noted that figure 1.2 was drawn using a convention that is frequently employed to graphically illustrate an EHD contact. In reality, the film thickness is very much thinner than it is long, therefore the vertical dimensions are usually expanded about 1000 times more than the horizontal dimensions. The presence of a pressure spike at the outlet of the contact is a result of secondary elastic deformation of the contact which forms a 'lip' in order to constrict the outflow of fluid from the contact zone and maintain the continuity of flow across the system.

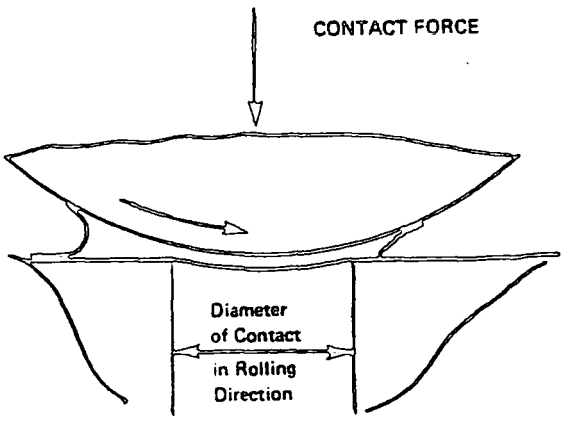

Figure 1.2. Diagram of real contact zone with lubricant. Adapted from reference 9

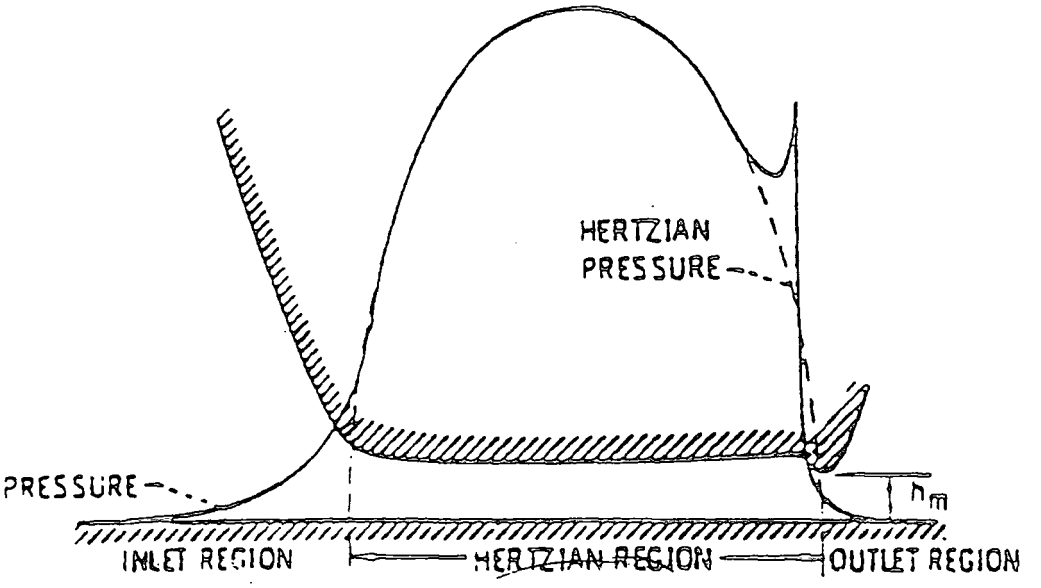

Figure 1.3. Elastohydrodynamic pressure profile. Adapted from reference 10

The success of EHD lubrication depends heavily on film thickness. In turn, this depends primarily[8] on the mean relative velocity of the contacting surfaces, the lubricant viscosity, and the pressure viscosity coefficient. An increase in any of these parameters will cause an increase in film thickness. Generally, the pressure/viscosity relationship dominates. The effect of pressure on the viscosity is counteracted to some extent by the decrease in viscosity due to local heating which is a result of friction inherent in all EHD contacts. As with hydrodynamic lubrication, high temperatures can cause a breakdown in effective EHD lubrication. Additives (usually polymers) can be incorporated into the lubricants to help to solve this problem.

The knowledge of what controls fluid viscosity and the pressure and temperature dependence at a molecular level is of great importance in the understanding of better EHD lubricants. Molecular properties can be probed which help to determine viscosity temperature and viscosity pressure relationships for a range of fluids. Therefore, molecular structures that minimise the viscosity/temperature coefficient and at the same time optimise the viscosity/pressure behaviour can be developed and tested. The work in this thesis is part of that strategy. The study is mainly concerned with conditions appropriate to EHD lubrication.

1.1.3 Boundary Lubrication

If pressures are too high, running speeds too low or surface roughness too great, penetration of the lubricant film will occur. Therefore, contact will take place between the asperities, friction will rise and more importantly, wear will take place. If the conditions are too severe, lubricant breakdown occurs and the system finally seizes so badly that it can no longer operate successfully.

The viability of the system is greatly enhanced if a small quantity (less than 1%) of surface active organic compound is added to the fluid which has a negligible effect on the viscosity of the lubricant. This additive functions because it forms a surface film which is strongly attached to the metal surfaces. Generally the surface film is one or two molecules thick which can prevent metal to metal contact. This type of lubrication is known as boundary lubrication. It has been found that the best boundary lubricant

additives are long chain molecules with active (polar) end groups e.g. alcohols, amines, carboxylic acids. When the material, dissolved in the lubricant, meets the metal (or other solid surface) the active group is adsorbed onto the solid and gradually builds up the surface layer. The film becomes strongly attached to the surface and the attraction between the chains themselves makes it very difficult to penetrate the film. If two surfaces covered with such films come into contact they tend to slide over their outermost faces and friction is reduced. Some penetration occurs, but not as much if only the fluid were used.

The best boundary lubricants cease to be effective above 200-250°C. As the temperature is increased, the strength of the surface attachment is weakened and the rate of transfer/pickup of surfactant is increased. This gives a marked increase in friction and surface damage occurs.

1.1.4 Extreme Pressure Lubrication

If machines are to operate under severe conditions, extreme pressure (EP) lubricants are used. The name EP lubrication is a slight misnomer since it is not the pressure, but the temperature reached between the sliding surfaces that controls the EP lubrication process.

The EP additive is present in the fluid in only a small amount (less than 1%). The most common additives used for this purpose contain phosphorus, chlorine, or sulphur. They function by reacting with the metal surface, the molecules becoming chemisorbed, to form a surface film which prevents metal to metal contact. The EP additives usually only react at high temperatures, so are usually incorporated with boundary lubricants in the fluid. This ideally means that when the boundary lubricants cease to be effective, the EP lubricants will begin to work, ensuring protection even under high temperature conditions.

The behaviour is shown schematically in figure 1.4. Curve I is for paraffin oil (base oil) and shows that the friction is initially high and increases as the temperature becomes raised. Curve II is for a fatty acid dissolved in the base oil (boundary lubrication), it becomes physisorbed on the surface to provide good lubrication from

room temperature up to the temperature at which desorption becomes dominant. Curve III is for a typical EP additive dissolved in the base oil. This reacts very slowly at temperatures below Tr so that in this range the lubrication is poor, while above Tr, the protective film is formed and effective lubrication is provided up to a very high temperature. Curve IV is obtained when both a boundary lubricant additive (e.g. an amine, alcohol or carboxylic acid) and an EP additive are present in the base oil. Good lubrication is provided below Tr by the fatty acid, and above Tr by the EP additive. At higher temperatures, a deterioration in lubricating properties will occur for curves III and IV.

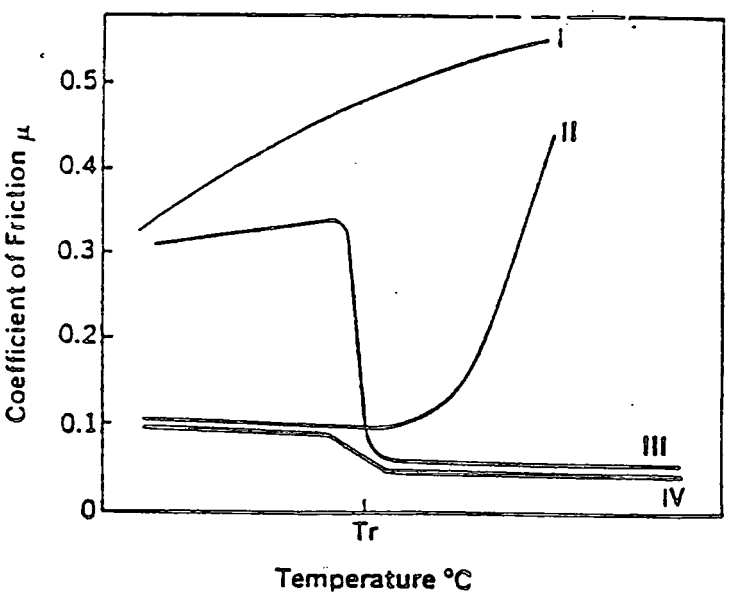

Figure 1.4. Schematic graph showing the frictional behaviour of metal surfaces in the presence of various types of lubricant. Adapted from reference 6.

1.2 Viscosity

Viscosity is the property of a fluid, whether liquid or gas, which characterises flow behaviour. Flow itself is a continuous deformation process occurring under the action of an externally applied force.

The concept of viscosity, or in this case, momentum transport, embraces the idea of the internal friction between the molecules of the fluid i.e. whenever any part of a fluid is caused to move, neighbouring parts tend to be carried along too, these processes being ultimately molecular in origin. This resistance to development of velocity differences within a fluid is the essential feature of viscosity.

The characteristic of viscosity is very important e.g. viscosity determines which forces are to be overcome when fluids are used in pipes, bearings etc. and controls the flow of liquid in such processes as spraying and injection moulding. It also determines whether the flow will be streamlined or turbulent, whether fluids mix and their heat transfer characteristics. Viscosity is a valuable tool for the physical chemist as the viscosity coefficient is profoundly influenced by the size, shape and arrangement of the molecules.

A more exact definition of viscosity can be developed by introducing the terms 'shearing stress' and 'rate of shear'. Consider the flow of liquid between two parallel plates, each of area A m^2, and h m apart, when a force of N Newtons is applied to the upper plate causing it to move with velocity v ms^{-1}, relative to the lower one. (figure 1.5).

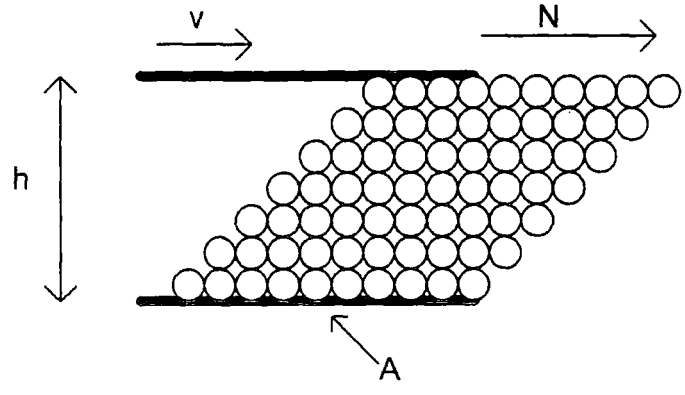

Figure 1.5. Viscous flow between two parallel surfaces. Adapted from reference 11

$$F = \text{Shearing Stress} = \frac{\text{Force}}{\text{Area}} = \frac{N}{A} \qquad 1.1$$

$$D = \text{Mean rate of shear} = \frac{\text{Velocity Difference}}{\text{Distance Between Plates}} = \frac{v}{h} \qquad 1.2$$

The rate of shear and velocity gradient are not synonymous where lines of shear are curved. Flow properties of all materials are defined by the relationship between shearing stress and rate of shear.

There are 2 main types of material :-

1. Newtonian Fluids
2. Non-Newtonian Fluids

1.2.1 Newtonian Fluids

In Newtonian fluids, shearing stress is directly proportional to the mean rate of shear.

$$F = \eta D \qquad 1.3$$

η is the viscosity coefficient, dynamic viscosity, or simply the 'viscosity' of the liquid and its dimensions' are Pa.s or poise, in honour of Poiseuille, the pioneer of viscosity. (The viscosity of H_2O at an ambient temperature is 0.01 poise or 1 centipoise.)

The measure of Fluidity is $\frac{1}{\eta}$, the reciprocal of viscosity.

Some viscometers give a direct measure of the ratio of η to the density ρ. This ratio of $\frac{\eta}{\rho}$ is known as the 'kinematic viscosity' ratio, the units of which are Stokes or m^2s^{-1}

In general water, simple organic liquids, dilute suspensions and emulsions and gases are Newtonian in character.

1.2.2 Non-Newtonian Fluids

There are many materials of great industrial importance, particularly those in the form of more concentrated suspensions and emulsions, that are Non-Newtonian. These 'anomalous liquids' are of two degrees of complexity :-

a) Those fluids for which the relationship between shearing stress and rate of shear can be uniquely defined by a curve or by a straight line which does not pass through the origin.

b) Those fluids for which a single (F, D) curve is insufficient to characterise their flow behaviour completely. Such materials, if subjected , for example, to a constant rate of shear, may exhibit gradually increasing or decreasing shearing stress i.e. their fluid characteristics are time dependent. Thixotropic materials are of this type : they gradually thicken when allowed to rest and become progressively thinner when sheared. This process is completely reversible without change in temperature. This phenomenon is very important as thixotropy has been reported in a variety of materials from paints, oils and clays to honey, ice cream and chocolate.

A family of materials of importance in the field of synthetic polymers is described as 'visco-elastic' because they combine some of the properties of a viscous liquid with some of the properties of an elastic solid. Such materials require specialised techniques to elucidate the relationship between stress, rate of shear and magnitude of shear.

1.2.3 Viscous Flow

Viscous flow has four key features :-

1) The viscosity resistance increases with the rate of deformation.

2) The molecules do not return to their original position when the applied force is removed. The flow involves a non-reversible change and the friction involved in producing the viscous flow manifests as heat in the liquid - this is why the oil in a bearing warms up after the bearing has been running for some time.

3) The viscosity of a liquid decreases with increasing temperature. This is because the increased thermal energy enables molecules to escape more easily from

their neighbours i.e. less external force is required to increase the flow. For example, with a lubricating oil, each rise in temperature of 10°C decreases the viscosity by a factor of about 2. Similarly, if the temperature is reduced by the same amount, the viscosity is increased by a factor of 2. This is why it is hard to start an engine on a cold morning - the oil is too viscous. As it warms up, the viscosity is reduced and the engine runs more easily.

4) Viscosity increases as pressure increases. i.e. the atoms or molecules are squeezed closer together, making it harder for them to escape their neighbours. At modest pressures, such as those in the bearings of a car engine, the effect is not too great, but there are situations where the effect can be enormous e.g. the contact pressures between the gear cog-wheels of a car compared with the aforementioned bearings. Under these conditions, the viscosity of the oil may be increased a thousand fold. This is fortunate as it implies that the greater the pressure applied to the lubricant, the greater its viscosity and the higher its resistance to extremes. In practice, many pieces of machinery function successfully because of this natural property of most lubricants to increase their viscosity when they are subjected to high pressures.

1.3 Viscosity Models

There are various models that have been developed to try and understand how the viscosity varies with temperature, pressure, and flow rate. Some of the more important ones are described below.

1.3.1 Viscosity-Temperature

Since the publication of Reynolds'[5] work on olive oil, a considerable number of viscosity temperature laws have been proposed for lubricating oils.

Reynolds demonstrated that viscosity can be described in terms shown below.

$$\eta = Re^{-\alpha T} \qquad 1.4$$

where R and α are constants.

However, this equation is only valid over a limited temperature range and the variation of the viscosity must also be small[5].

Of the many[12] temperature laws proposed, Vogel's equation has been shown to describe the variation of viscosity with temperature most accurately.

$$\eta = ke^{b/(T+\theta)} \qquad 1.5$$

k, b and θ are constants and each has a definite physical significance :-

k, with units of viscosity, is related to fluid viscosity.

b, the unit of temperature, expresses the inherent viscosity-temperature variation of the fluid.

θ expresses the temperature at which the oil would have infinite viscosity if it did not freeze to a solid i.e. when $T = -\theta$, the term $e^{b/(T+\theta)}$ becomes infinite.

Thus the Vogel equation is a complex one, because the 3 constants have to be found. In practice, this means that the viscosity of the fluid has to be known for 3 different sets of conditions.

None of the viscosity-temperature equations have proven to be satisfactory over an extended range of temperatures and over all types of fluid. However, the viscosity-temperature variation can be defined by the fluids viscosity index (V.I.). The greater this index, the less dependent the liquid's viscosity on temperature.

The V.I. is calculated by measuring fluid viscosity at 2 standard temperatures, 100°F and 200°F. A ratio is calculated relating measured viscosities to the viscosities of 2 oils with standard viscosity indices. The greater the ambient viscosity of the fluid, the greater that fluid's temperature-viscosity dependence. This implies that in choosing a lubricant with a high ambient viscosity to aid the mechanism of EHD lubrication, one must accept a greater temperature induced viscosity decrease.

The ideal would therefore be a fluid with a high ambient viscosity and the viscosity-temperature variation of a lower viscosity fluid. Because of this, additives known as viscosity index improvers are often added to base lubricants in order to increase the viscosity index. These additives normally belong to the polymeric-aliphatic

or polymeric-aromatic groups and are applied in concentrations of up to 10%. Their effectiveness lies in that they boost the ambient fluid viscosity while having little adverse effect on its viscosity-temperature dependence. There are, however, disadvantages. At high shear rates, polymer alignment can occur, which implies that viscosity decreases. This is known as reversible shear thinning. Furthermore, under extreme conditions polymer chain cleavage may result, which is known as irreversible shear thinning. Chemical degradation can also occur.

1.3.2 Viscosity-Pressure

In 1893 Barus[13] proposed the following equation for the isothermal viscosity-pressure dependence of liquids :-

$$\ln \frac{\eta}{\eta_0} = \alpha p \qquad 1.6$$

where η is the viscosity of the liquid at a pressure p, η_0 is the viscosity at atmospheric pressure, and α is the pressure-viscosity coefficient which is characteristic of the fluid. The greater the value of α the greater the dependence of viscosity on pressure. α is dependent on the temperature of the fluid.

Unfortunately, the Barus equation is only valid to a reasonable approximation at low pressures and over a moderate pressure range. At higher pressures, a linear relationship is no longer observed (figure 1.5).

This non-linear behaviour can lead to considerable errors in theoretical EHD calculations in which the pressure viscosity performance must be estimated e.g. when predicting fatigue life dependent upon friction in bearings. Consequently, there have been many subsequent attempts to find more satisfactory pressure viscosity relationships[14,15]. These correlations are more successful at higher pressures, however they are always more complex than the Barus relationship as they include constant terms which are varied depending on the class of lubricant being considered.

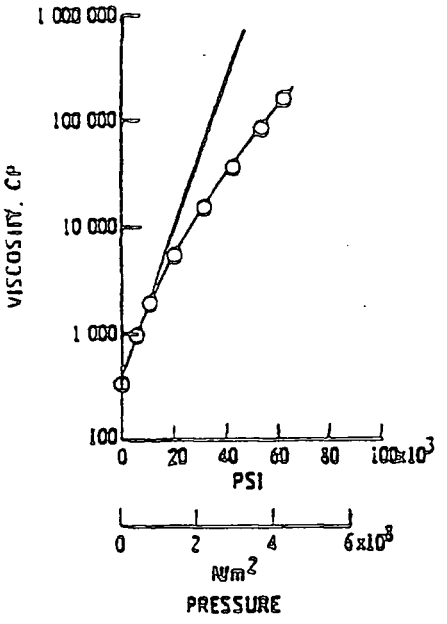

Figure 1.5. Schematic graph showing the non-linear dependence of viscosity and pressure. Adapted from reference 10

1.3.3 Viscosity and Flow Rate

Many theories of liquid viscosity have been proposed from a molecular viewpoint[16], one of the most successful is Eyring's theory for viscous flow. The flow of liquid is a rate process, which implies that the theory of absolute reaction rates could be applied to the problem of viscosity. This was proposed by Eyring and co-workers[17]. In this theory, the movement of a molecule from one equilibrium position to the next is regarded as equivalent to the passage of the system over a potential energy barrier. This movement requires the expenditure of energy as work is done in "pushing back" the other molecules, and this energy is dependent on viscosity.

For a small shearing force, the viscosity can be expressed in terms of $\Delta G^{\#}$ the Gibbs Free Energy of activation for viscous flow, the molar volume V, Avogadro's number N, the gas constant R, Planck's constant h, the molecular weight M, and the temperature T

$$\eta\frac{V}{N}h = \nu\frac{M}{N}h = \exp\left(\frac{\Delta G^{\#}}{RT}\right) \quad 1.7$$

where η is the viscosity and ν the kinematic viscosity.

It follows from simple transition state theory that:

$$\Delta V^{\#} = RT\left(\frac{\partial \ln \nu}{\partial p}\right)_T \qquad 1.8$$

$$\Delta H^{\#} = R\left(\frac{\partial \ln \nu}{\partial T^{-1}}\right)_p \qquad 1.9$$

$$\Delta S^{\#} = R \ln\left(\frac{Nh}{M\nu}\right) + \frac{\Delta H^{\#}}{T} \qquad 1.10$$

$\Delta V^{\#}$ and $\Delta H^{\#}$ are convenient measures of the pressure and temperature dependence of kinematic viscosity, and $\Delta V^{\#}$ alone can be regarded as a kind of pressure-viscosity coefficient.[16,18].

This model has been known for many years. On rearranging equation 1.7 and replacing $\Delta G^{\#}$ by $\Delta H^{\#}$-$T\Delta S^{\#}$, we get,

$$\eta = \left[\left(\frac{hN}{V}\right)\exp\left(\frac{-\Delta S^{\#}}{R}\right)\right]\exp\left(\frac{\Delta H^{\#}}{RT}\right) \qquad 1.11$$

Since the molar volume does not vary greatly with temperature, and $\Delta S\#$ being taken as a constant[16] equation 1.11 becomes

$$\eta = B\exp\left(\frac{E_{vis}}{RT}\right) \qquad 1.12$$

E_{vis} is the activation energy per mole for viscous flow. This relationship had been suggested in the 19th century by both Arrhenius[19] and by Reynolds[5].

This model works well for many liquids and has been used widely to describe the behaviour of lower molecular weight molecules[20,21] and more recently, the behaviour of lubricants[16,18].

1.4 Traction

In under a century, petroleum powered automobiles have become the most dominant element in world society. They have created the auto and oil industries as major global employers and have become the world's primary source of transportation. However, they have also become one of the world's greatest sources of air pollution. Since the turn of the century, the internal combustion engine has been the preferred source of propulsion over steam and electricity. This is despite of its basic and persistent limitation: its lack of power at low engine speeds. The opposite of this provides both steam and electricity with their major advantage i.e. they develop maximum torque at stall when they are needed to accelerate the automobile from a standstill.

The internal combustion engine does have many factors in its favour. It is a low cost, portable power source which can be started immediately (electric power sources also have this ability). It can also provide a high power to weight ratio and has a long range without the need for refuelling. High speeds are also attainable.

Today due to advanced technology, hardened steel rolling surfaces used instead of gears produce durable, continuously variable traction drives. These have automotive control, high performance because of their use of a synthetic traction fluid and a competitive cost. These modern traction drives are used extensively in machinery in industry, not in automobiles as was the initial aim. However, the advantage of a continuously variable gearbox in a combustion engine is that it allows the combustion engine to be run at constant speeds where it is most efficient and powerful.

Modern traction drives transfer mechanical shaft power from a source to a load efficiently by means of metal rollers running on a film of traction fluid against mating metal rollers. These rollers can be cones, cylinders, discs, rings, spheres, or toroids. The metal is generally hardened steel or chromium plating on some other metal and the fluid could be oil, silicone or a synthetic hydrocarbon. Three elements must be present[9] if the drive of which they are part is to be called a traction drive:

1) Input metal rollers.

2) Traction fluid

3) Output metal rollers

This definition avoids the usual meaning of the word "traction" (to pull). It also implies that a car wheel on the road is not a traction drive. The wheel is rubber, the road surface is not a roller, and the contact area is not deliberately lubricated.

A traction drive depends on the low-rate shearing of very thin films to transmit substantial forces from its input members to its output members. The fluids used are selected because of their very high viscosity pressure index. When the local pressure on the fluid trapped in the contact area is momentarily increased to several thousand atmospheres, the local fluid viscosity increases enough so that the film supports a substantial normal force without permitting the metal parts to come into contact with each other. Only a low relative shearing rate is necessary to develop the tangential drive forces required.

Surface irregularities may be large relative to the film thickness, but the compression of the metal in the contacting surfaces is often hundreds of times greater than the film thickness. Consequently, the irregularities in the surface have little effect in the transfer of the traction forces from one rolling element to the other. This transfer is due largely to the shear developed in the fluid film, and is directly proportional to the rate the film is sheared and the film properties. Since the transfer of traction forces is due to shear motion, there will be no transfer if there is no shear motion.

All traction drives have small shear motions in the direction of rolling that cause a creep of the contact. This is the useful shear motion (there are others which are less useful e.g. skew, in which the forces are not aligned with the direction of motion, and rotational) which is necessary to transfer the traction force in the driving direction.

Traction forces are generated in traction drives as a function of load on the contact. The ratio of force to load is affected by the fluid properties. All the losses in a contact are converted to heat which is conducted away by the metal and some of the fluid, but temperatures in the contact can reach destructive levels in the fluid if shear becomes excessive. If the drive geometry is such that the rotational and skew components of the shear are large, the only way to hold the losses within a safe range is to limit the load and the traction forces.

Insufficient contact force for the needed traction will increase the required creep rate and may cause uncontrolled contact creep, or gross slip. Most drives can be damaged by excessive creep and need adequate constant force. Ideally, the contact force should increase directly with the required traction force and be imposed on the contact before the traction force increases.

The elements in a traction drive may be chosen to make the drive ratio

$$r = \frac{\textbf{input speed, rpm}}{\textbf{output speed, rpm}} \qquad 1.12$$

a variable under the control of the operator. This variable ratio has provided a powerful impetus for the development of automotive applications. The search for improved continuously variable transmissions has led to increasingly better materials and lubricants and to increasingly competent designs. As yet, none have proved practical for commercial automotive transmissions, but active development work is in process in many laboratories.

It is hoped, through projects related to the one outlined in this thesis, that an improved understanding of how the behaviour of the fluid in an EHD contact is dependent on its molecular structure will enable the development of improved lubricants for use within a traction drive, which has been proved to be more efficient than the commercial transmissions used today.

1.5 Use of Spectroscopic Techniques to Study the Molecular Dynamics, Interactions, and Conformations of Non-Rigid Molecules.

Spectroscopic techniques are used routinely to probe molecular interactions and their behaviour under high temperature and pressure, so that the understanding of how these properties effect the macroscopic properties of the fluid can be furthered. This is achieved through the analysis of vibrational frequencies, band intensities, and band shapes or the associated correlation function as a function of concentration, temperature and pressure.

Due to the more accessible theoretical approach to interpreting the data, such investigations have usually been centred around reasonably small rigid molecules[22-25]. This is particularly apparent in most models for molecular reorientational motion in dense fluids[22.23.25-27] where a rigid molecular framework is assumed.

For more flexible systems, the interpretation of results is more complicated due to the increase in internal motions. Increased flexibility makes a significant difference to molecular motions and interactions, which in turn alters the values of physical parameters. i.e. diffusion coefficients[28]. Therefore, flexibility must be taken into account when attempting the interpretation of vibrational band shapes and correlation functions of longer chain molecules[29]. Methods of analysis and interpretation of vibrational spectra of flexible molecules are limited, as those developed are designed to deal with simple rigid molecules. Consequently, such fluids need to be studied using various techniques, and by employing the knowledge gained from simpler systems, useful information about the intermolecular potentials and molecular dynamics can be obtained.

This section is a brief discussion of some of the work of this nature already carried out. It will be concerned with the work carried out on alkanes, cyclohexyl systems and finally will outline some of the work carried out on lubricant systems.

1.5.1 Alkanes

The conformational populations and dynamics of normal alkanes and their derivatives have been studied extensively. Providing the molecule is relatively short, the number of trans/gauche conformers may be small enough for vibrational spectroscopy to be able to distinguish them. The calculation of normal co-ordinates and vibrational frequencies of the conformers can also be used in analysing the observed spectrum[30].

By monitoring the spectral intensities[31], it has been shown that increasing the temperature favours an increased gauche contribution to the molecular structure[32] as does increasing the pressure[31,33]. This is due to molecular volume effects. Wong[34,35] reported that in long alkyl chains (e.g. n-hexadecane) the pressure induced trans/gauche transformation does not occur below 10kbar (1GPa) because it is prevented by lateral compression which causes a full extension of the alkyl chains, resulting in a reduction in the total volume.

Wong[33-35] also reported that the vibrational bands of alkanes also broaden upon increasing the pressure. The amount of broadening depends on the mode being studied, but it is usually a consequence of the pressure-induced conformational disorder. This broadening is in common with observations made by Jonas[36-38] on a number of simpler systems.

The Raman spectral width behaviour of deuterated alkanes as a function of chain length with temperature was studied by Wunder et al[39]. They concluded the temperature dependence of the antisymmetric CH_2 stretching mode, for low molecular weight alkanes, can be explained in terms of end over end rotation of the molecule. However for this mode, with chain lengths longer than propane, hindered internal motions contribute to the band widths. The broadening occurs through the coupling of the anti symmetric CH_2 stretching mode to backbone torsional motions which hinder the oscillation of the CH_2 groups. As the chain length increases, overall rotation becomes hindered, until eventually it is too slow to contribute to the observed band width. Broadening is then solely a consequence of internal motions, and the band width is seen to become independent of chain length.

1.5.2 Cyclohexyl Systems

Cyclohexane compounds are the most important of all cycloalkanes because of their wide occurrence in nature. The most stable form of cyclohexane and its mono and poly substituted derivatives is the chair form[40]. These compounds exist in a dynamic equilibrium between two conformers of the chair form inter converting rapidly. Spectroscopic measurements indicate that the energy barrier to chair-chair inter conversion is about 45kJ/mol[41]. The reasons for the relative stability of the chair form are briefly outlined below.

Due to the rotation of the C-C bonds, the ring can flex into different structures. (Figure 1.7)

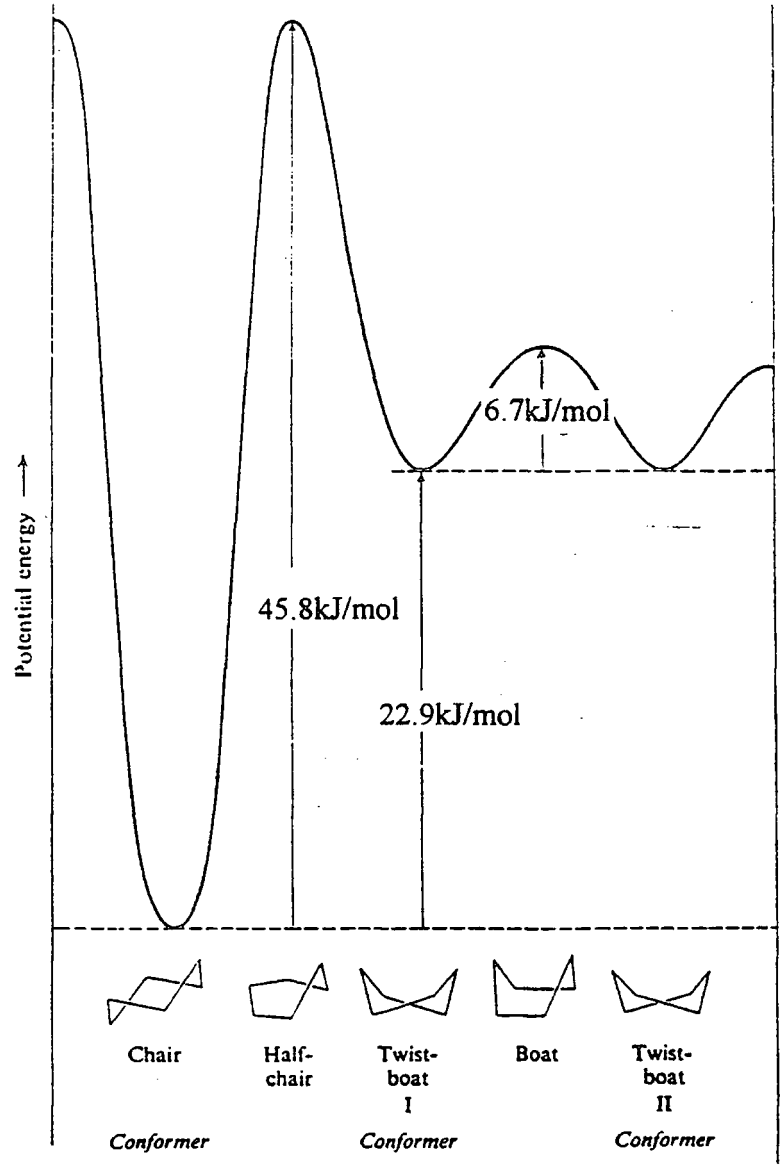

Figure 1.7. The conformations of cyclohexane and their relative stabilities. Adapted from reference 42

As can be seen, two of the structures, the chair and the twist boat forms lie at potential minima and consequently these are known as conformers. The potential energy differences are contributed to the three different types of intramolecular repulsive interaction.

1. Angle strain

i.e. if the C-C-C bond angles are significantly different from the free tetrahedral value 109°28', considerable strain is placed on the bonds and the structure becomes unstable.

2. Torsional strain

The strain due to the eclipsing of neighbouring bonds.

3. Steric strain

The strain due to the repulsive interaction of atoms approaching each other too closely.

Spectroscopic measurements[41] indicate that boat cyclohexane is approximately 29kJ/mol (7.1kcal) less stable than chair cyclohexane, although this value is reduced to about 23kJ/mol (5.5kcal) by twisting slightly, thereby relieving some of the torsional strain. (Figure 1.7) Even the twist boat conformation is still far more strained than the chair conformation, and molecules adopt this geometry only rarely and under special circumstances.

There are two distinct types of C-H bonds in the chair form of cyclohexane. Those oriented perpendicularly to the plane of the ring are called axial bonds, while those in the same plane as the ring are equatorial bonds. The significance of these two types of bond becomes apparent when substitution of the ring occurs. (Figure 1.8) Any substituent experiences less repulsion in the equatorial position than in the axial position.

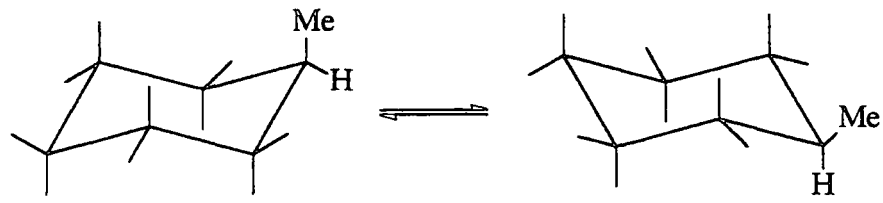

Axial Equatorial

Figure 1.8

The axial methyl group and the two axial hydrogens on the same side of the ring experience repulsion from one another, while the equatorial methyl group points away from the ring and consequently no repulsion occurs. The axial form of methylcyclohexane was predicted to be ~7.2 kJ/mol less stable than the equatorial form[40], and this was verified by low temperature NMR studies[43].

The stabilities of disubstituted cyclohexyl systems follow the same principles as above, but are more complicated due to the cis and trans forms.

1.5.3 Effects of Temperature and Pressure on Conformational Equilibria of Substituted Cyclohexanes

The infra red spectrum of cyclohexane-d_{12} has been obtained as a function of pressure by Gilson and Haines[44,45]. They used previous vibrational studies of variable temperature[46] and variable pressure[47] changes of C-H bonds of adamantane-d_{15} to aid in their studies of the phase changes in cyclohexane-d_{12}. Two phase transitions were found at 5.3 and 7.4kbar (0.53 and 0.74GPa). The C-H stretching region in the highest pressure phase was very similar to that observed at low temperature indicating that these were identical. The phase transition with temperature has also been studied by vibrational spectroscopy[48,49] including an infra red study of single crystals under pressure[49], although in the latter case, the pressure at which the spectra were recorded was not reported.

In cases where two conformers are energetically different (all mono substituted and certain disubstituted compounds) it should be possible to distinguish between them spectroscopically. Effects of temperature and pressure variation upon relative populations can then be monitored. By using the work conducted on cyclohexane derivatives, which are related to larger synthetic lubricants, it may assist in the characterisation of changes occurring in the real lubricant systems.

A considerable amount of data (infra red and Raman) has been reported concerning mono and di substituted cyclohexanes. These compounds have axial and equatorial conformers that give rise to spectra that are sufficiently distinct, due to the dipolar carbon-halogen bonds, to allow complete assignment to specific vibrational

modes of each conformer. For example, the symmetric C-Cl stretches of axial and equatorial conformers of chlorocyclohexane occur at 685cm^{-1} and 753cm^{-1} respectively[50], allowing the effects of pressure and temperature to be easily monitored.

The bulk of this work was concerned with relating spectral data to conformational changes occurring under conditions of high pressure and low temperature. These extreme conditions were studied because the resultant crystalline phases formed from mixtures of the conformers in the liquid state are often composed of only a single conformer. This implies that the complete spectra of both conformers can be obtained by selectively varying the temperature and pressure to give the desired solid phase. (e.g. trans-1,2-bromochlorocyclohexane crystallises in the diequatorial phase at low temperature and in the diaxial form at high pressure.[51,52] Most of this work has been reviewed by Klaboe[53], so will not be discussed further here.

The effect of pressure on the conformational equilibria of chlorocyclohexane, dichlorocyclohexane and dibromocyclohexane in CS_2 solution using infra red spectroscopy has been studied by Christian and co-workers[54]. It was found that increased pressure induced an increase in the concentration of axial conformers as these occupy a smaller molecular volume than the corresponding equatorial conformers.

Alkyl cyclohexanes prove far more difficult to study as the assignment of vibrational bands to specific vibrations of different conformers is complicated because the normal modes contain a mixture of stretching, bending, and torsional vibrations[55]. They also contain certain components due to both axial and equatorial conformations[56].

Zhizhin and Sterin[56] used infra red spectroscopy to study the temperature induced changes in the conformational equilibrium of methyl cyclohexane and found that increased temperature increased the axial conformer concentration. They also studied 1-methyl-4-ethyl cyclohexane[57] and used absorbance changes to deduce that increased temperature increases the concentrations of the higher energy conformations of the molecule.

The temperature and pressure dependence of the infra red spectra of methylcyclohexane and the dimethyl cyclohexanes have been reported.[58,59] Most of the work has been conducted in the solid phase, but high pressure liquid spectra of

methylcyclohexane and cis-1,3-dimethylcyclohexane appeared to indicate the presence of axial and diaxial conformers respectively. This pressure induced increase in axial conformer concentration is contradicted by Gardiner et al[60] who studied the Raman spectra of methylcyclohexane as a function of temperature and pressure, but only in the liquid phase. The observed spectral variations were attributed to both molecular dynamic changes and an increase in the concentration of the equatorial conformer as both temperature and pressure were varied.

1.5.4 Molecular Studies of Lubricants and Traction Fluids

In recent years the determination of structure/property relationships using spectroscopic techniques and viscometers has been used extensively in order to assist in the design of improved functional fluids. (See section 1.6).

Gillies et al have used ^{13}C-NMR spin-lattice relaxation and the Nuclear Overhauser Effect to interpret the molecular motions of dicyclohexyl compounds[61-63] (traction fluids) as well as hydrocarbon chains[64,65] (low traction lubricants). Their main studies centred around 2,4-dicyclohexyl-2-methylpentane[61] (DCMP) which is a commercially used traction fluid and they used 2,4-dicyclohexylpentane, 1,3-dicyclohexylpropane, and 1,2-dicyclohexylethane to assist them with the interpretations[62,63] (Figure 1.9)

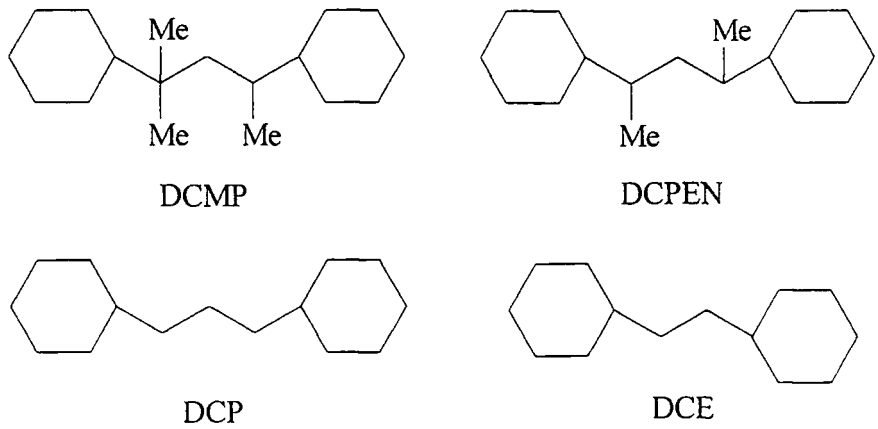

Figure 1.9.

All four structures are described as having a semi-rigid backbone structure. Decreasing the branching and increasing the length of the alkyl chain between the cyclohexyl rings allows more flexibility. The methyl groups in DCMP and DCPEN show unhindered motion with both Me* being very similar. As can be expected, the Me* in DCMP is less hindered than the other chain Me groups.[61]

There have also been studies of lubricants using infra red and Raman spectroscopies.[66-68] By varying one or more of pressure, temperature and solvent attempts have been made to relate the molecular properties to bulk fluid properties.

Methods have also been developed for probing directly into concentrated contacts. The main techniques developed are based upon electromagnetic radiation. The only limitation this has is that one of the two surfaces of the contact must be made of a material transparent in the frequency range of the radiation used i.e. glass, sapphire or diamond.

Optical interferometry employs visible light and has been widely used to map elastohydrodynamic film thicknesses in contacts[63]. It has also been applied to the study of antiwear additive film formation in contacts.[70]

Infra red emission radiometry enables the temperature profiles of the lubricant in a concentrated contact[71,72] to be determined. Such information can also be processed to yield lubricant shear stresses in contacts.[73-75]

Lauer et al have conducted some work on using infra red emission spectroscopy[76,77] and later, transmission infra red dichroic spectroscopy was carried out with a hydrodynamic contact to study molecular alignment[78] showing evidence of shear alignment of polymer additives.

Gardiner et al have used Raman emission spectroscopy with an elastohydrodynamic point contact[79-81] to study the pressure generated therein. Some Raman vibrational frequencies are pressure sensitive and the frequency shift of these vibrations can therefore be used to measure the pressure within an EHD contact[80]. Pressure profiles have been obtained for both static entrapments[79,82] and rolling EHD contacts.[81] The high resolution of Gardiner's system (3-5μm) gives detailed information and the pressure spike is clearly observed.[81] A big advantage of Raman over infra red is

that glass discs, as opposed to sapphire or diamond can be used as the transparent medium. The main disadvantages are that very thick oil films are required (>1μm) which means that studies are limited to full film EHD rather than mixed or boundary lubrication and the choice of lubricants is limited to pure synthetic basestocks since mineral oils and aromatics give problems of fluorescence which can obscure the weak Raman signal. The high energy of the exciting laser radiation may lead to local heating within the contact which in turn will lead to breakdown of the lubricant film.[81]

A complementary technique, infra red micro-reflection absorption spectroscopy was developed by Cann and Spikes.[83] Detailed infra red reflection absorption spectra can be obtained from within and around an operating EHD contact. Consequently, it is possible to study the behaviour of lubricant molecules in such contacts.

This approach has many applications and has recently been used to study greases[84.85] and changes in composition and loss of bulk grease structure have been observed. The main limitation of this technique is that it is not a true surface sensitive technique and the spatial resolution is poor. However, results have demonstrated that this technique can be used to observe both physical and chemical effects within concentrated lubricated contacts under realistic conditions of pressure and strain rate.[83]

This thesis describes work using infra red micro-reflection absorption spectroscopy in the hope to further the fundamental knowledge associated with lubricant behaviour under traction.

1.6 Molecular Design of Traction Fluids

In the last ten years, there has been a great surge of interest, particularly in Japan[86-91] in the development of better and cheaper traction fluids. The great majority of this effort has been directed towards novel cycloalkyl hydrocarbons which are structurally similar to the original patented products[91] based on 2,4-dicyclohexyl-2-methylpentane.

Various theories have been proposed for the molecular features which may be associated with high fluid traction coefficients. This has included consideration of molecular alignment and cog-like interlocking under EHD conditions[92]. The principal requirement for a high traction coefficient is a high degree of molecular rigidity, also seen as a high flow activation volume[18] (or pressure-viscosity coefficient). In general, the molecular rigidity can be shown to be qualitatively associated with the presence of cycloalkyl groups and a high degree of alkyl chain branching.[92-94]

Alternative fluid classes were also designed[95] to possess the necessary molecular attributes that may generate high tractional performance. A brief outline of the design procedure is outlined below.

Traditionally, ester-based lubricants, e.g. aviation turbine lubricants, are associated with high viscosity indices, low pressure-viscosity coefficients and low traction coefficients, and the technology was well known. This "type casting" of esters to such properties relates to the high degree of intramolecular flexibility present for the particular structures used as lubricants i.e. straight chain or mildly branched aliphatic di-, tri-, and tetra esters. By (1) the selection of rigidity inducing substituents and (2) the enhancement of the rigidity by making adjacent combinations of these functional groupings, a family of novel ester-based traction fluids was designed.[95]

This process evolved from studies on cyclohexyl cyclohexane carboxylate[95] (figure 1.10).

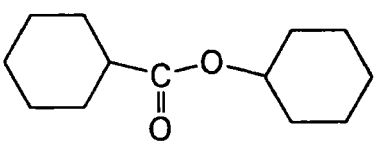

Cyclohexyl Cyclohexane Carboxylate

Figure 1.10

It was found that the cyclohexyl group directly attached to the ester carbonyl carbon is significantly less constrained in its rotational motion than the grouping attached to the "ether" oxygen.[95]

To achieve a higher viscosity for the proposed traction fluids, diesters were designed. Analogous to cyclohexyl cyclohexane carboxylate, the diol diesters (cyclohexyl groups attached to the carbonyl carbon) displayed significantly poorer traction coefficients than the comparable diacid diesters with the ether oxygen attachment.[95]

It was also found that increasing the chain length of the diacid played an important part in the compounds traction capabilities. On increasing the chain length beyond the C-4 acid i.e. succinic acid HOOC-CH_2-CH_2-COOH, there is a steady decrease in the traction coefficient, which can be associated with the greater flexibility of the intervening CH_2 units. It was also found that going from the C-3 acid to the C-4 acid did not produce any significant change in traction coefficient.

To optimise the diester structures to achieve the maximum rigidity, short chain alkyl substituents were also added. Substitution on the 2, 3, or 4 positions of the cyclohexyl group has minimal effect on the intramolecular rigidity, so the best place for substitution was on the diacid. It was found that highly branched compounds had high traction coefficients.[96]

From these studies, Bis(cyclohexyl) Succinate, BCS. (figure 1.11) was earmarked as a potential model traction fluid.

To be able to use the spectroscopic techniques of infra red and Raman to probe the molecular dynamics and interactions of a fluid, and then to use this information to relate the molecular properties to the macroscopic properties of the fluid e.g. viscosity, the fluid must consist of non-rigid molecules. BCS also relates closely to commercial traction fluids while remaining simple enough to allow the study of its molecular dynamics.

The molecule contains cyclohexyl rings, two ester groups and a short hydrocarbon chain. It should therefore, be possible to probe the whole molecule with information being available about the interactions at various parts of the molecule.

BCS is, therefore, a suitable molecule to use in the study of the effect that molecular dynamics have on macroscopic properties as a function of temperature, pressure and solution.

The work in this thesis is an attempt to probe the microscopic properties of the traction fluid BCS. Various bands along the whole length of the molecule have been studied as a function of one or more of temperature, pressure and solution.

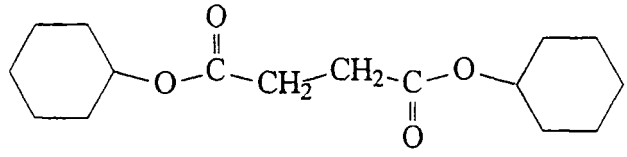

Bis(cyclohexyl) Succinate
"BCS"

Figure 1.11. The structure of Bis(cyclohexyl) Succinate.

References

1. A. Bondi, Chapter 1 of "Rheology Theory and Applications", 4th Ed. F. R. Eirich, Academic Press, New York (1967)
2. J. Yarwood, A. Whitley, D.G. Gardiner and M.P. Dare-Edwards, in Proc IV NATO Conf (1988) - "Reactive and Flexible Molecules in Liquids", NATO ASI Series C: Mathmatical and Physical Sciences - Vol 291, ed. Th. Dorfmuller, Kluwer Academic Publishers. (1989)
3. J.H.R. Clarke and D. Brown, J. Chem. Phys., 86(3), 1542-7 (1987)
4. D.M. Heyes, J. Non-Newtonian. Fl. Mech., 27, 47-85 (1988)
5. O. Reynolds, Phil. Trans., 177, 157. (1886)
6. F.P. Bowden and D. Tabor, "Friction: An Introduction to Tribology", Science Study Series No. 41 Heinemann Educational Books Ltd, London (1974)
7. H.R. Hertz, J. Reine Angew. Math. (Crelle's j.), 92, 156-171, (1881)
8. D. Dowson and G.R. Higginson, "Elasto-Hydrodynamic Lubrication", SI Edition, Permagon Press (1977)
9. F.W. Heilich III and E.E. Schube, "Traction Drives: Selection and Application", Dekker, New York (1983)
10. L.D. Wedeven, Lubr. Eng., 31, 291-296 (1990)
11. A. Dinsdale and F. Moore, "Viscosity and its Measurement", Chapman and Hall Ltd.,London (1962)
12. R.F. Crouch and A. Cameron, J. Inst. Pet., 47, 307 (1961)
13. P. Barus, Am. J. Sci., 45, 87-96 (1893)
14. C.J.A. Roelands, J.C. Vlutger and H.I. Waterman, J. Basic. Eng., 11, 601 (1963)
15. L.B. Sargent ,A.S.L.E. Trans., 26, 1 (1981)
16. T. Kyotani, Y. Tamai and Y. Horita, A.S.L.E. Trans., 26, 538-44, (1983)
17. S. Glasstone, K.J. Laidler, H. Eyring, "The Theory of Rate Processes", McGraw-Hill Book Co., New York (1941)
18. T. Kyotani, H. Yoshitake, T. Ito and T. Tamai, A.S.L.E. Trans., 29, 102-6, (1986)
19. S. Arrhenius, Z. Physik. Chem., 4, 226, (1889)
20. S.G. Brush, Chem. Rev., 62, 513, (1962)
21. M. Mooney, Trans. Soc. Rheol., 1, 63, (1957)

22. J. Yarwood, Ann. Rep. Roy. Soc. Chem., C, 79, 157 (1982)

23. W.G. Rothschild, "Dynamics of Molecular Liquids", John Wiley and Sons (1984)

24. J. Yarwood, NATO ASI Ser. C., 135 (Mol. Liquids), p. 357-82, Reidel (1984)

25. D. Steele, Stud. Phys. Theor. Chem., 20 (Vib. Intensities Infrared Raman Spectrosc.), 398 (1982)

26. W.A. Steele, NATO ASI Ser. C., 135 (Mol. Liquids), p. 357-84, Reidel (1984)

27. W.A. Steele and R.M. Lynden-Bell, J. Phys. Chem., 88, 6514 (1984)

28. N.A. Walker, D.M. Lamb, S.T. Adamy, J. Jonas and M.P. Dare-Edwards, J. Phs. Chem., 92, 3675, (1988)

29. J. Yarwood, A. Whitley, D.G. Gardiner and M.P. Dare-Edwards, in "Reactive and Flexible Molecules in Liquids", ed. Th. Dorfmuller, Kluwer Academic Publishers. pp61-62, (1989)

30. R.G. Snyder, J. Chem. Phys., 47, 1316 (1967)

31. D.J. Gardiner, M.P. Dare-Edwards and N.A. Walker, Nature, 316, 614 (1985)

32. J. Devaure and J. Lascombe, Nouv. J. Chim., 3, 579 (1979)

33. P.T.T. Wong, H.H. Mantsch and R.G. Snyder, J. Chem. Phys., 79, 2369 (1983)

34. P.T.T. Wong, in "Current perspective in High Pressure Biology", Ed. R.E. Marquis, Pub. Academic, London (1987)

35. P.T.T. Wong and H.H. Mantsch, J. Chem. Phys., 83, 3268 (1985)

36. J. Schroeder, V.H. Schiemann, P.T. Sharko and J. Jonas, J. Chem. Phys., 66, 3215 (1977)

37. K. Tanabe and J. Jonas, Chem. Phys., 38, 131 (1979)

38. K. Tanabe and J. Jonas, J. Chem. Phys., 67, 4222 (1977)

39. S.L. Wunder, M.I. Bell and G. Zerbi, J. Chem. Phys.,85, 3827 (1986)

40. E.L. Elliel, "Conformational Analysis", Interscience Publishers, New York (1965)

41. J. McMurry, "Organic Chemistry", 2nd Ed, Brooks/Cole Publishing Company, California, (1988)

42. R.T. Morrison and R.N. Boyd, "Organic Chemistry", 3rd ed., Allyn and Bacon Inc., (1978)

43. H. Booth and J.R. Everett, J.C.S. Perkin II, ??, 255, (1980)

44. J. Haines and D.F.R. Gilson, J. Phys. Chem., 93, 7920, (1989)

45. J. Haines and D.F.R. Gilson, J. Phys. Chem., 94, 4712, (1989)

46. R.M. Corn, V.L. Shannon, R.G. Snyder and H.L. Strauss, J. Chem. Phys, 81, 5231, (1984)

47. D. Salmon, V.L. Shannon and H.L. Strauss, J. Chem. Phys, 90, 773, (1989)

48. A.C.R LeRoy, Hebd. Seances Acad. Sci. Paris, 261B, 4022, (1965)

49. C.W. Brown, R.J. Obremski, E.R. Lippincott, J. Chem. Phys., 52, 2253, (1970)

50. T. Woldbaek, Acta. Chem. Scand., 36, 641, (1982)

51. P. Klaboe, Acta. Chem. Scand., 25, 695, (1971)

52. H.T. Hornvelt and P. Klaboe, Acta. Chem. Scand., 25, ??, (1971)

53. P. Klaboe, Z. Chem. Leipzig, 21, 381, (1981)

54. S.D. Christian, J.G. Grundes and P. Klaboe, J. Am. Chem. Soc., 97, 3864, (1975)

55. R.G. Snyder and J.H. Schachtsneider, Spectrochim. Acta., 21, 169, (1965)

56. G.N. Zhirzin and K.E. Sterin, Zh. Prikl. Spektrosk., 5, 377, (1966)

57. G.N. Zhirzin and K.E. Sterin, "Vibrational Spectra and Structure", ed Durig, 9, 195, (198?)

58. J.L.Lauer and M.E. Peterkin, Appl. Spectrosc., 28, 41, (1974)

59. J.L.Lauer and M.E. Peterkin, Devo. Appl. Spectrosc., 28, 59, (1974)

60. D.J. Gardiner, G.S. Bassi and G.D. Galvin, Appl. Spectrosc., 38, 313, (1984)

61. D.G. Gillies, S.L. Matthews and L.H. Sutcliffe, Mag. Res., 28, 171, (1990)

62. D.G. Gillies, S.L. Matthews and L.H. Sutcliffe, Mag. Res., 29, 777, (1991)

63. D.G. Gillies, S.L. Matthews and L.H. Sutcliffe, J. Mol. Liq., 54, 205, (1992)

64. L.M. Bull, D.G. Gillies, S.L. Matthews L.H. Sutcliffe and A.J. Williams, Mag. Res., 29, 273, (1991)

65. D.G. Gillies, S.L. Matthews and L.H. Sutcliffe, Mag. Res., 29, 1221, (1991)

66. A. Whitley, PhD Thesis, Durham University (1990)

67. N.A. Walker, PhD Thesis Newcastle-Upon-Tyne Polytechnic, (1986)

68. G.S. Bassi, PhD Thesis Newcastle-Upon-Tyne Polytechnic, (1983)

69. H.A. Spikes and C.J. Hammond, A.S.L.E. Trans., 24, 542, (1981)

70. I.N. Lacey, G.H. Kelsall, H.A. Spikes and P.B. Macpherson, A.S.L.E. Trans., 29, 299, (1986)

71. U.K. Ausherman, J.H.S Nagara, D.M. Sanborn and W.O. Winer, Trans. A.S.M.E., Jour. Lubr. Tech., 98, 236, (1976)

72. J.L.Lauer and V.W. King, A.S.L.E. Trans. 24, 331, (1981)

73. P.M. Cann and H.A. Spikes, Proc. 14th Leeds-Lyon Symp. on Trib. Interface Dynamics. (1987)

74. P.M. Cann and H.A. Spikes, S.T.L.E Trans. 32, 414, (1989)

75. H.S. Chang and H.A. Spikes, Synth. Lubr. 9, 91, (1992)

76. J.L.Lauer and V.W. King, Trans. A.S.M.E. Jour. Lubr. Tech., 103, 65, (1981)

77. J.L.Lauer and M.E. Peterkin, A.S.L.E. Trans., 21, 250, (1978)

78. J.L.Lauer, A.S.M.E. Jour. Lubr. Tech., 101, 67, (1979)

79. D.J. Gardiner, E. Baird, A.C. Gorvin, W.E. Marshall and M.P. Dare-Edwards, Wear, 91, 111, (1983)

80. D.J. Gardiner, M. Bowden, J. Daymond, A.C. Gorvin, and M.P. Dare-Edwards, Jour. Appl. Spect., 38, , 282, (1984)

81. E.M. Baird, PhD Thesis Newcastle-Upon-Tyne Polytechnic, (1988)

82. J.L. Mansot and J.M. Martin, Proc. 12th Lees-Lyon Symp. on Tribology, 237, (1985)

83. P.M. Cann and H.A. Spikes, Tribol. Trans., 3, 248, (1991)

84. P.M. Cann, B.P. Williamson, R.C. Coy and H.A. Spikes, J. Phys. D:Appl. Phys., 25, A124, (1992)

85. P.M. Cann and H.A. Spikes, Lubr. Eng., 48, 335, (1992)

86. Idemitsu Kosan Co. Ltd.,a) Japanese Patent No. 60/35095 (1985), b) US Patent No. 60/86197 (1985)

87. Nippon Petrochemicals Co. Ltd., Japanese Patent No. 60/86197 (1985)

88. Nippon Steel Chemical Co. Ltd.,/ Mitsubishi Co. Ltd., Japanese Patent No. 61/81492 (1986)

89. Nippon Oil Co. Ltd., a)Japanese Patent No. 61/162595 (1986) b) European Patent No. 207776

90. Toa Nenryo Kogyo K.K., Japanese Patent Nos. a) 61/188495 (1986) b) 62/153395 (1987) c) 62/153393 (1987)

91. Monsanto, UK Patent No. 1357406 (1971)

92. K.H. Hentschel, J. Synth. Lubr. 2, 143, (1985)

93. M. Muraki, Trib. Int. 20, 347, (1987)

94. T. Kyotani, Y. Yamada, T. Tezuka, H. Yamamoto and Y. Tamai, Sekiyu Gakkaishi, 30, 353, (1987)

95. M.P. Dare-Edwards, Synth. Lubr., 8, 197, (1991)

96. R. Dhein, K.H. Hentschel, H. Winter and H. Vojalek, Erdoc and Koule- Erdgas-Petrochemie, Verein, 35, 518, (1982)

CHAPTER 2

Vibrational Spectroscopy

2.0 Introduction

In order to relate bulk fluid physical properties to the molecular structure using vibrational spectroscopy it is necessary to be able to extract information about molecular dynamics in fluids. A wide range of concentrations, temperatures, and pressures is needed. Therefore it is important to understand how infra-red and Raman spectral bands arise from molecular vibrations of condensed systems, how intermolecular potentials are modulated by molecular motions, and how interactions with the intermolecular potential affect the frequency and relaxation processes of a vibration.

Using this knowledge and the observed spectral changes, it may be possible to postulate which molecular motions control a particular physical property. Then a link between micro- and macroscopic fluid properties may be obtained. This could lead to a better understanding of how molecular structure can be modified so as to improve the desired macroscopic behaviour.

2.1 Vibrational Spectroscopy

2.1.1 Infra-red Absorption

When a molecule is irradiated with an infra-red beam, the oscillating electromagnetic field of the beam and the molecule interact. For a molecule to be able to interact with the electromagnetic field and absorb or emit a photon of frequency ν it must posses a transient dipole oscillating at that frequency. If this condition is met, there is a possibility of the vibrational mode, of energy

$$E = h\nu \qquad (2.1)$$

absorbing or emitting a photon (fig 2.1).

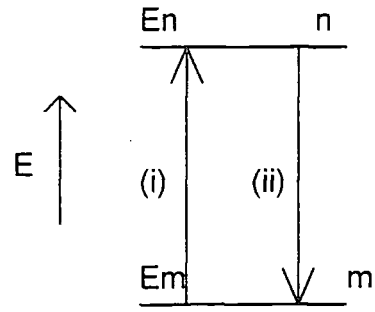

Figure 2.1. Schematic diagram of a molecule absorbing or emitting a photon.

(i) $m + hc\bar{\nu} \rightarrow m^*$ (absorption)

(ii) $m^* + hc\bar{\nu} \rightarrow m + 2hc\bar{\nu}$ (emission)

Both the above expressions arise through interactions of the molecule, m (with m* being the excited state), with the electromagnetic radiation.

The transition dipole is expressed in terms of the transition dipole moment R_ν which for a transition between lower and upper vibrational states v' and v'' described by the wave functions $\psi_{v''}$ and $\psi_{v'}$ is defined as

$$R^{v'v''} = \int \psi^*_{v'} \hat{\mu} \psi_{v''} dQ \qquad (2.2)$$

where $\hat{\mu}$ is the total dipole operator, $Q = r - r_e$ the displacement of the inter nuclear distance from equilibrium, and R = the transition dipole moment. For a homonuclear diatomic molecule $\hat{\mu} = 0$, R = 0 and all the vibrational transitions are forbidden. For a heteronuclear diatomic molecule $\hat{\mu}$ is non-zero and varies with Q. This variation can be expressed as a Taylor Series expansion.

$$\hat{\mu} = (\bar{\mu})_e + (\partial\mu/\partial Q_i)_e Q_i + 1/2!\left(\partial^2\mu/\partial Q_i^2\right)_e Q_i^2 + \ldots\ldots \qquad (2.3)$$

where e refers to the equilibrium configuration.

For a harmonic oscillator, $\hat{\mu}$ can be taken to be

$$\hat{\mu} = (\bar{\mu})_e + (\partial\mu/\partial Q)_e Q \qquad (2.4)$$

Therefore, this gives

$$R^{v'v''} = (\bar{\mu})_e \int \psi^*_{v'} \psi_{v''} \partial Q + (\partial\mu/\partial Q)_e \int \psi^*_{v'} Q \psi_{v''} \partial Q + \ldots \qquad (2.5)$$

Since $\psi_{v'}$ and $\psi_{v''}$ are eigenfunctions of the same Hamiltonian, they are orthogonal which means that when $v' \neq v''$,

$$\int \psi^*_{v'} \psi_{v''} \partial Q = 0 \qquad (2.6)$$

and therefore the transient dipole becomes

$$R^{v'v''} = (\partial\mu/\partial Q)_e \int \psi^*_{v'} Q \psi_{v''} \partial Q + \ldots \qquad (2.7)$$

The intensity of a particular absorption band is proportional to the square of the transition dipole moment $\left(I \propto |R_v|^2\right)$. Therefore only if a transition gives rise to a non-

zero transition dipole moment will it contribute any intensity to the spectra. The first term in equation 2.7 is non-zero only if $\Delta v=\pm 1$. Since $\Delta v=v''-v'$ the selection rule is effectively $\Delta v=\pm 1$ for the harmonic oscillator approximation. It can be seen from equation 2.7 that the molecule need not have a permanent dipole moment. The rule for absorption requires only a change in the dipole, possibly from zero. Some vibrations do not affect the molecular dipole moment and so they neither absorb nor emit radiation. Such vibrations are said to be inactive.

When a normal mode is raised by two or more vibrational energy levels (e.g. v=0 $\rightarrow$v=2), absorbing radiation at a frequency of almost, but never, exactly twice the fundamental frequency (i.e. v=0$\rightarrow$v=1) an overtone band arises (figures 2.2a and 2.2b). It is a consequence of anharmonicity of vibrations which requires that the higher terms than $(\partial\mu/\partial Q)_e$ in equation 2.3 have to be included in the expression for the total dipole moment operator (2.4). This results in non-zero terms in equation 2.7 for values of $\Delta v=$ ± 1, ± 2, ± 3, etc. and the overtone transitions then become allowed. There is also the possibility of combination bands. This occurs when two normal vibrational modes are excited to a higher vibrational level together absorbing a photon equal to the sum of the energies of the transitions (figure 2.2c). Overtone and combination bands usually have less than ten percent of the intensity of the fundamental modes due to the reduced probability of their occurrence. Fundamental, overtone and combination transitions are illustrated in figure 2.2.

The intensity of the absorption bands depends on the difference between the population of the initial and the excited state as well as $(\partial\mu/\partial Q)^2$. The greater the population of the initial state, the greater the probability of a transition occurring and the more intense the absorption band will be. The Boltzmann distribution law gives

$$N_f/N_i = (g_f/g_i)\exp(-\Delta E/k_bT) \qquad (2.8)$$

where g_i and g_f are the degeneracies of the initial and final states respectively. If ΔE is much larger than k_bT (k_bT = 208 cm^{-1} at 300K) then the ratio N_f/N_i is much less than

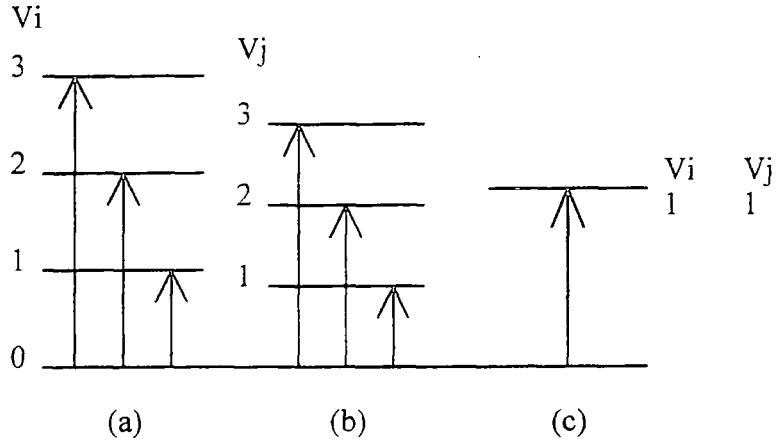

Figure 2.2 Overtone and combination bands involving vibrations ν_i and ν_j. a), b)Fundamental and overtone, and (c) combination transitions, showing the result of V_i and V_j being excited simultaneously giving a resultant equal to the sum of $V_{i0} \rightarrow V_{i1}$ and $V_{j0} \rightarrow V_{j1}$.

2.1.2 Raman Scattering

The Raman effect can be described as the inelastic scattering of light by matter. When a photon of light, too low in energy to excite an electronic transition, interacts with a molecule it can be scattered in one of three ways. It can be elastically scattered and thus retain its incident energy or it can be inelastically scattered by either giving up energy to, or by removing energy from, the molecule.

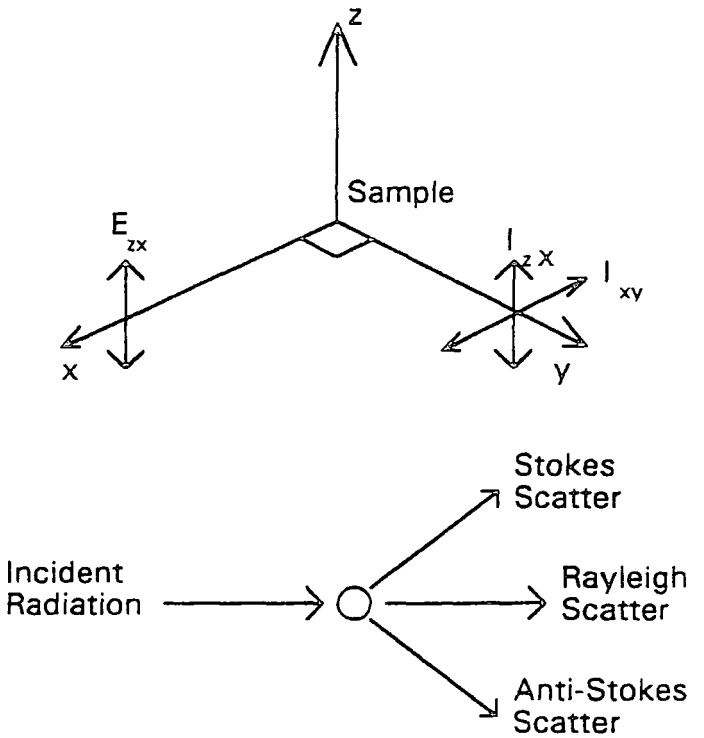

figure 2.3

Figure 2.3 shows a schematic representation of the process. Polarised laser light, E_{zx}, is passed through a sample and scattering, usually 90° scattering, is observed. The out coming radiation can be collected in any plane, but usually in the same plane as the incident radiation (I_{VV}, or in this case I_{zx}), or in a plane perpendicular to the incident light (I_{VH}, or in this case I_{xy}). Three processes can occur :

1) $\nu_{incident} + \omega_{vib/rot}$ (< 1%)

i.e. $\nu=1 \rightarrow$ excited state $\rightarrow \nu=0$

2) $\nu_{incident}$ (> 99%)

i.e. $\nu=0 \rightarrow$ excited state $\rightarrow \nu=0$

3) $\nu_{incident} - \omega_{vib/rot}$ (< 1%)

i.e. $\nu=0 \rightarrow$ excited state $\rightarrow \nu=1$

Processes 1 and 3 are Raman scattering processes and process 2 is a Rayleigh scattering process. For 1, $E = h(\nu_o + \nu_v)$ and this is known as Anti-Stokes scattering. For 2, $E = h(\nu_o - \nu_v)$ and this is known as Stokes scattering. These processes can be represented diagramatically as figure 2.4.

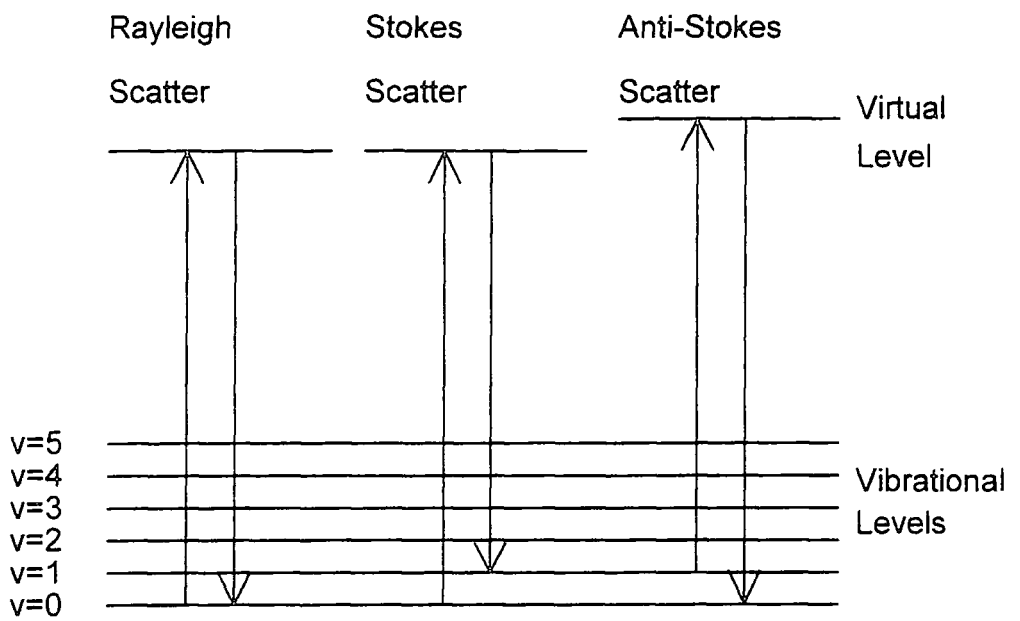

figure 2.4 Rayleigh, Stokes and anti-Stokes scattering

According to a Boltzmann Distribution, equation 2.8, the relative populations of the v=0 and v=1 levels, at room temperature, are such that the Stokes intensity is always much greater than that of the Anti-Stokes intensity.

If a molecule is placed in an electric field, then the electron cloud will be distorted inducing a dipole in the molecule regardless of whether there is a permanent molecular dipole moment or not. The magnitude of this induced dipole moment (μ) depends on the strength of the electric field and the molecular polarisability tensor, α.

$$\mu = \alpha E + (\beta E^2 + \chi E^3 + ...etc) \qquad (2.9)$$

usually only the first term is considered.

This polarisability tensor has components α_{ij} which can be expressed in the form:

$$\begin{bmatrix}\mu_x\\ \mu_y\\ \mu_z\end{bmatrix}=\begin{bmatrix}\alpha_{xx} & \alpha_{xy} & \alpha_{xz}\\ \alpha_{yx} & \alpha_{yy} & \alpha_{yz}\\ \alpha_{zx} & \alpha_{zy} & \alpha_{zz}\end{bmatrix}\begin{bmatrix}E_x\\ E_y\\ E_z\end{bmatrix} \qquad (2.10)$$

This implies:

$$\mu_X = \alpha_{XX}E_X + \alpha_{XY}E_Y + \alpha_{XZ}E_Z \qquad (2.11)$$

μ_y and μ_z follow similarly

α_{ii} is the principle component of the polarisability i.e. isotropic part and α_{ij} is the anisotropic part. The isotropic parts of the polarisability tensor for a chemical bond are represented below:

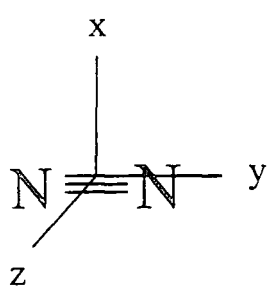

Figure 2.5. The isotropic parts of the polarisability tensor for a chemical bond.

α_{yy} lies along the N-N axis, with α_{xx} and α_{zz} along the other two axes.

$$\alpha_{yy} > \alpha_{xx} = \alpha_{zz}$$

Therefore, as it is easier to distort the electron cloud along the bond and as polarisability is, in reality, the ability to distort electrons, α_{yy} will be greatest.

i.e. the greater the polarisability $\Rightarrow$ the more distortion of electrons

If the electric field which induces the dipole, oscillates at a frequency ν_0, then the dipole will also oscillate at that frequency, scattering light of that frequency. (2.12)

$$E_{inc} = E_o\cos(2\pi\nu_o t) \qquad (2.12)$$

This field will cause the induced dipole to oscillate according to equation 2.13

$$\mu_{induced} = \alpha E_{inc} = \alpha E_0 \cos(2\pi\nu_0 t) \quad (2.13)$$

The oscillating dipole can now radiate electromagnetic radiation of frequency ν_0. This is the process known as Rayleigh scattering. If the polarisability of the molecule changes during a normal vibration, then the vibration can interact with the oscillating dipole. For a harmonic oscillator, the normal co-ordinate Q (i.e. the displacement of the internuclear distance from equilibrium) of a vibration is a function of time and oscillates according to equation 2.14

$$Q = Q_0 \cos(2\pi\nu_i t) \quad (2.14)$$

Where ν_i is the frequency of the ith vibration.

The value for small vibrational amplitudes, arising from the polarisability of the molecule changing during the vibration, can be expressed as a Taylor Series. (2.15)

$$\alpha = \alpha_e + (\partial\alpha/\partial Q)_e Q + (\partial\alpha/\partial Q)^2 (Q^2/2!) \text{etc.} \quad (2.15.)$$

Therefore, for a harmonic oscillator

$$\alpha = \alpha_e + (\partial\alpha/\partial Q) Q_0 (2\pi\nu_i t) \quad (2.16)$$

This then leads to

$$\mu' = \alpha_e E_0 \cos(2\pi\nu_0 t) + (\partial\alpha/\partial Q)_e \left[Q_0 E_0 (\cos(2\pi\nu_i t))(\cos(2\pi\nu_0 t)) \right] \quad (2.17)$$

Therefore:

$$\mu' = \alpha_e E_0 \cos(2\pi\nu_0 t) + 1/2(\partial\alpha/\partial Q)_e \, Q_0 E_0 [\cos 2\pi(\nu_0 - \nu_i)t + \cos 2\pi(\nu_0 + \nu_i)t]$$

(2.18)

The first part of equation 2.18 is the Rayleigh Scattering term. The second part of the equation describes Raman Scattering with $(\nu_0-\nu_i)$ due to Stokes scattering and $(\nu_0+\nu_i)$ due to Anti-Stokes scattering. However, using this classical approach, relative intensities can not be predicted.

From equation 2.18, it can be seen that Raman scattering will not occur unless the derivative $(\partial\alpha/\partial Q)$ is non-zero. i.e. in order for Raman scattering to occur from a vibration, the vibration must give rise to a change in the polarisability of the molecule.

The quantum treatment of Raman scattering considers a molecule colliding with the incident photon and being raised from the v=0 level to an unstable level much higher than v=1. The molecule instantaneously returns to the v=0 level emitting a photon of the same energy as the incident photon. This process is Rayleigh scattering.

Raman scattering occurs when a small proportion of the excited molecules do not return to their original state, but to one that is at a higher or lower vibrational energy level. Consequently, the scattered photon is of a different energy to the exciting photon. Stokes scattering arises from transitions from v=0 to v=1, emitting a photon of energy $E = h(\nu_0 - \nu_v)$. Anti-Stokes scattering arises from transitions from v=1 to v=0, absorbing a photon.

Combination bands are also present in Raman spectra. The overtone and combination bands are at a much lower intensity than the fundamental bands.

2.2 Study Of Molecular Dynamics Using Vibrational Spectroscopy

Since their original use for identifying compounds by providing a characteristic "fingerprint", infra-red and Raman spectroscopy have come a long way. These techniques are now used extensively to study dynamic processes in liquids by studying band shapes and frequency shifts, and calculating correlation functions. The progress in these techniques has come about due to significant developments in experimental techniques. Fourier transform infra-red has become routine providing better resolution than dual beam instruments, and very sensitive detectors have been developed. For Raman spectroscopy, better photomultiplier tubes are available, recent advances have led to CCD chips being used as detectors (see chapter 3), and improved resolution can be gained using improved laser sources. To aid with these developments, computers allow rapid data sampling, storage, and processing.

2.2.1 Peak Frequencies And Band Shapes

Peak frequencies depend on force constants, atomic masses, bond distances, bond angles, and electric charges. i.e. bond length/strength and the geometry. All these are modified by molecular interactions with the surrounding potential e.g. electron clouds, solvent molecules etc. Band profiles and widths depend on dynamic properties e.g. atomic and molecular motions.

If the previous theory for infra-red and Raman is considered, then for each vibrational mode, an infinitely narrow delta function would be found corresponding to transitions of the type $E = h\nu$ found at the corresponding frequency ν. This is not the case. Bands of various widths and shapes are seen due to molecular motions and interactions. (figure 2.6)

The vibrational band shape is dependent on the "lifetime" of a molecule in an excited vibrational state. When an oscillator is instantaneously excited to a higher vibrational level, it only has a finite time in this level before oscillator medium interactions return it to the ground state. The life time of the excited state gives the band width increment $\Delta\omega$ (estimated by the energy time uncertainty principle[1] $\tau\Delta E \approx h$

or $\tau\Delta\omega = 1$). Therefore the radiation induced transitions between ground and upper levels show a frequency distribution. The band shape is also dependent on the spread of the vibrational transition frequencies of a particular vibrational mode. An explanation of both these processes is given in section 2.4.

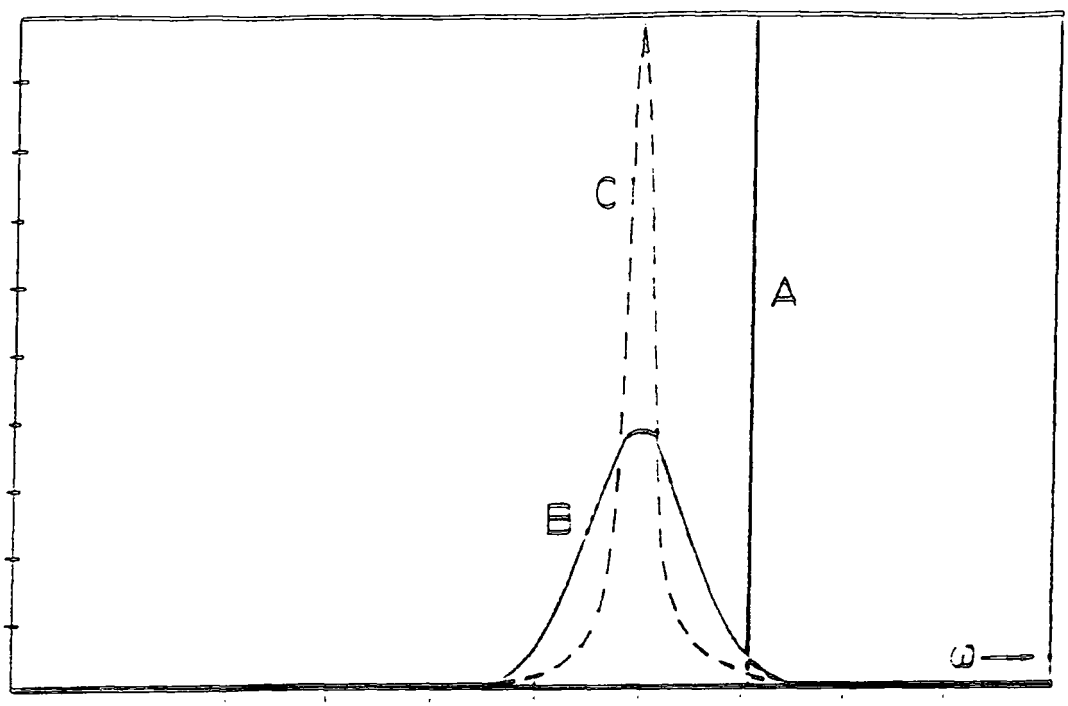

Figure 2.6. The effect of environment on the broadening of a given vibrational mode. A) dilute gas. B) liquid with slow molecular motions (little motional narrowing, for example at low temperature). C) liquid with more rapid molecular motions and significant motional narrowing. Reproduced by permission from reference 7.

2.2.2 Chemical Potential - Frequency Shifts and Intermolecular Interactions

At an infinite separation, the intermolecular energy, U, between two atoms, A and B, is zero, and the total energy is given by equation 2.19

$$E_T^c = E_A + E_B \qquad (2.19)$$

When the molecules are brought to a distance r_{AB}, this energy is modified. (2.20)

$$E_T(r) = E_A + E_B + U_{AB}(r) \qquad (2.20)$$

Therefore:

$$U_{AB}(r) = E_T^{\infty} - E_T(r) \qquad (2.21)$$

Equation 2.22 expresses the work done in bringing molecules A and B to an intermolecular distance r_{AB}.

$$U_{AB}(r) = \int_r^{\infty} F(r)dr \qquad (2.22)$$

r = equilibrium distance.

Therefore, the intermolecular force can be written as equation 2.23.

$$F(r) = -\left(dU(r)/dr\right) \qquad (2.23)$$

F(r) is positive for repulsive forces, and negative for attractive forces.

The general form of the total (overall) interaction energy can be represented in the form shown below. This is known as the Lennard - Jones potential. (2.24 and figure 2.7)

$$U(r) = b/r^{12} - a \cdot r^{6} \qquad (2.24)$$

the second term being made up of several contributions.

The simple model potential is usually written in the empirical form (2.25)

$$U(r) = 4\varepsilon\left\{(\sigma/r)^{12} - (\sigma/r)^{6}\right\} \qquad (2.25)$$

$\sigma = (2)^{-1\,6} r_{min}$ and is a measure of intermolecular separation for the minimum energy (equilibrium) and ε is a measure of the potential energy well depth.

This model is only strictly valid for spherical non-polar molecules or atoms and is highly successful for such cases. e.g. CH_4, H_2.

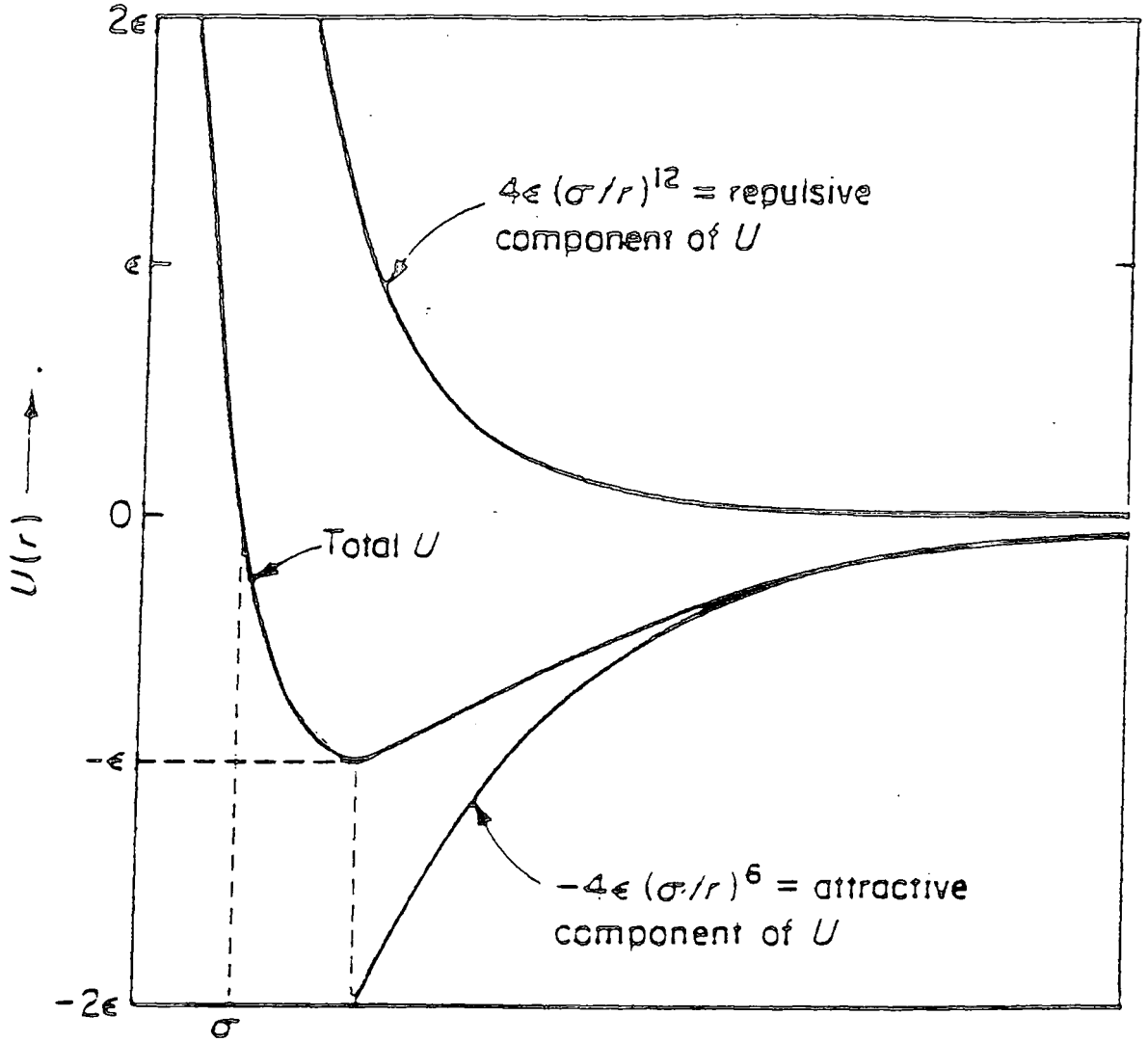

Figure 2.7. Lennard Jones potential

When molecules are placed in solution, the intermolecular forces change. This change in the forces is felt by the bonds in the molecule and causes a change in the frequency of the vibrational modes. The major types of interaction are dipole-dipole, dispersive, inductive, and repulsive. The first three of these are long range forces which are slowly varying, whilst repulsive forces are short range forces which are rapidly varying.

Drickamer and co-workers have studied the influence of different types of intermolecular interactions on vibrational frequencies[1,2]. They found that repulsive

forces give a blue frequency shift and attractive forces a red frequency shift. This has since been further supported by molecular dynamics simulations[3].

2.3 Band Shapes and Correlation Functions

Relaxation mechanisms and molecular motions can be analysed using Raman and/or infra-red spectroscopy by direct analysis of the band shape or by obtaining the correlation function of the band by Fourier transformation. Which method used depends on which shows the effects most clearly, which can be interpreted most easily, and the quality and the reliability of the correlation function obtained.

2.3.1 Correlation Functions.

The Fourier transform (2.26)

$$F(p) = \int \partial q . \exp(ipq) . f(q) \qquad (2.26)$$

decomposes a function of an independent variable p with an integral sum over a continuous range of an associated variable q. Substituting p with ω and q with t, the experimental spectral profile $I(\omega)$ can be transformed into the time domain by (2.27)

$$F(t) = \int \partial \omega . I(\omega) . \exp(-i\omega t) \qquad (2.27)$$

where $\omega = 2\pi\bar{\nu}c$ ($\bar{\nu}$ cm^{-1})

The time range for vibrational spectroscopy is 0.1psec to 100psec. Therefore, it is ideal for the study of rapid motions and interactions in fluids.

Infra-red and Raman band shapes are conveniently considered to be Fourier transformations of certain time autocorrelation functions ϕ_t.

Measurement of polarisation characteristics of Raman scattered light, allows for the separation of isotropic $I_{iso}(\omega)$ and anisotropic $I_{aniso}(\omega)$ parts of the scattered light.

From equation (2.9), the induced dipole P_i can be represented as shown in equations 2.28.

$$\begin{aligned} P_x &= E_x\alpha_{xx} + E_y\alpha_{xy} + E_z\alpha_{xz} \\ P_y &= E_x\alpha_{yx} + E_y\alpha_{yy} + E_z\alpha_{yz} \\ P_z &= E_x\alpha_{zx} + E_y\alpha_{zy} + E_z\alpha_{zz} \end{aligned} \qquad (2.28)$$

The matrix (2.9), known as the Raman tensor, will, if a vibration is Raman active, have at least one of the components changed.

As described earlier (2.18) the intensity of Raman lines depends on the polarisability tensor $\alpha' = (\partial\alpha/\partial Q)$ with each component of the polarisability tensor contributing to α'. The observed scattering will be an average over all orientations of the molecules.

Two quantities are invariant under rotation[6]:

1) The mean value of the isotropic part of the derivative polarisability α'. (2.29)

2) The anisotropy $\gamma(\alpha)$ which is a measure of the deviation of the polarisability from a spherical shape.(2.30)

$$\alpha' = \frac{1}{3}(\alpha'_{xx} + \alpha'_{yy} + \alpha'_{zz}) \qquad (2.29)$$

$$\gamma(\alpha) = \frac{1}{2}\left[(\alpha'_{xx} - \alpha'_{yy})^2 + (\alpha'_{yy} - \alpha'_{zz})^2 + (\alpha'_{zz} - \alpha'_{xx})^2 + 6(\alpha'_{xy} + \alpha'_{yz} + \alpha'_{zx})^2\right] \qquad (2.30)$$

When the incident radiation plane is polarised, by averaging over all the orientations of the molecule, the mean value of squares of all the derivative tensor elements can be expressed as in equations 2.31.

$$\alpha'_{ii}{}^2 = \alpha'_{xx}{}^2 = \alpha'_{yy}{}^2 = \alpha'_{zz}{}^2 = \frac{1}{45}(45\alpha'^2 + 4\gamma'^2)$$

$$\alpha'_{ij}{}^2 = \alpha'_{xy}{}^2 = \alpha'_{xz}{}^2 = \alpha'_{zy}{}^2 = \frac{1}{15}\gamma'^2 \qquad (2.31)$$

The observation of Raman light is normally made at ninety degrees to the direction of propagation of the beam (figure 2.3). I_{zx} and I_{xy} represent scattering originating from dipoles orientated in the same direction and at ninety degrees to the electric vector of the exciting beam E_{zx} respectively. As I is proportional to $E^2.(\partial\alpha/\partial Q)_e^2$, the following expressions can be obtained (2.32 and 2.33).

$$I_{zx} = k.E_{zx}{}^2 \alpha'_{zz}{}^2 = \frac{K}{45}\left(45\alpha'^2 + 4\gamma'^2\right) \qquad (2.32)$$

$$I_{xy} = k.E_{zx}{}^2 \alpha'_{xz}{}^2 = \frac{K}{15}\gamma'^2 \qquad (2.33)$$

where k and K are constants.

From this, the expression for the depolarisation ratio is.

$$\rho = \frac{\left[(K/15)\gamma'^2\right]}{\left[(K/45)\left(45\alpha'^2 + 4\gamma'^2\right)\right]} \qquad (2.34)$$

Therefore on simplification:

$$\rho = \frac{\left(3\gamma'^2\right)}{\left(45\alpha'^2 + 4\gamma'^2\right)} \qquad (2.35)$$

Measurement of $I_{zx} = I_{VV}$ and $I_{xy} = I_{VH}$ allows the separation of α'^2 and $4\gamma'^2$ (2.36 to equation 2.40).

$$I_{VV} = K.\alpha'^2 + K\left(\frac{4}{45}\right)\gamma'^2 \qquad (2.36)$$

$$I_{VH} = \left(\frac{K}{15}\right)\gamma'^2 \qquad (2.37)$$

Therefore,

$$I_{VV} = K\alpha'^2 + \frac{4}{3}I_{VH} \quad (2.38)$$

Finally, this leads to

$$I_{iso} = I_{VV} - \frac{4}{3}I_{VH} \qquad (2.39)$$

$$I_{aniso} = I_{VH} \qquad (2.40)$$

The infra-red band profile measurement $I_{ir}(\omega)$ is more straight forward.

The components of the time autocorrelation function, ϕ_t are modulated by different relaxation processes. The isotropic part of the Raman spectra gives information about vibrational relaxation, whilst the anisotropic part and the infra-red spectra contain contributions from both the vibrational relaxation and the reorientational relaxation.

For an infra-red band with normalised intensity $I_{ir}(\omega)$[2,7]

$$\phi_v(t)\phi_{IR}(t) = \langle Q_i(0)Q_i(t)\rangle\langle P_1[\bar{\mu}_i(0).\bar{\mu}_i(t)]\rangle = \int I_{ir}(\omega)\exp(i\omega t)\partial\omega \qquad (2.41)$$

$\langle Q_i(0)Q_i(t)\rangle$ is the vibrational relaxation function,

$P_1 = \cos\theta_i(t)$ where $\theta_i(t)$ is the angle of the transition dipole of the ith molecule at time t.

$\left\langle P_1\left[\vec{\mu}_i(0).\vec{\mu}_i(t)\right]\right\rangle$ is the first Legendre polynomial pure rotational (or reorientational) correlation function where μ is the unit vector along the direction of the transition moment corresponding to the normal co-ordinate Q_i of the ith molecule.

The infra-red reorientational correlation function describes the reorientation of the vector lying in the direction of the permanent dipole moment.

Things are more complicated in Raman spectra due to the polarisability components and derivatives which have tensorial properties.

For normalised intensities, it can be shown[2] that:

$$\phi_v(t) = \langle Q_i(0)Q_i(t)\rangle = \int I_{iso}(\omega)\exp(i\omega t)\partial\omega \qquad (2.42)$$

$$\phi_v(t)\phi_{2R}(t) = \langle Q_i(0)Q_i(t)\rangle\left\langle P_2\left[\vec{\mu}_i(0).\vec{\mu}_i(t)\right]\right\rangle = \int I_{aniso}(\omega)\exp(i\omega t)\partial\omega \qquad (2.43)$$

Therefore, the vibrational relaxation function can be measured directly from I_{iso}.
The second order Legendre polynomial $P_2 = \frac{1}{2}\left(3\cos^2\theta_i(t) - 1\right)$ arises from the Raman experiment measuring the reorientation of the tensor[2].
$\langle Q_i(0)Q_i(t)\rangle$ is the vibrational relaxation function and includes all the non-reorientational contributions to the decay of the total correlation function.

The instrument resolution function is characterised by a function whose Fourier transformation, in the time domain, is $\phi_s(t)$. Therefore the autocorrelation function becomes: (2.44 to 2.49)

$$\phi_{ir}(t) = \phi_v^{ir}(t)\phi_{1R}(t)\phi_s(t) \qquad (2.44)$$

$$\phi_{iso}(t) = \phi_v^{iso}(t)\phi_s(t) \qquad (2.45)$$

$$\phi_{aniso}(t) = \phi_v^{aniso}(t)\phi_{2R}(t)\phi_s(t) \qquad (2.46)$$

This implies:

$$\phi_v^{iso}(t) = \frac{\phi_{iso}(t)}{\phi_s(t)} \qquad (2.47)$$

$$\phi_{1R}(t) = \frac{\phi_{ir}(t)}{\phi_{iso}(t)} \qquad (2.48)$$

$$\phi_{2R}(t) = \frac{\phi_{aniso}(t)}{\phi_{iso}(t)} \qquad (2.49)$$

Thus, for determination of $\phi_v^{iso}(t)$, a correction for the finite slit width must be made. It is assumed that the slit profile is a pure Gaussian function whose width is equivalent to the slit.

The separation of the three correlation functions is only feasible if $\phi_v^{iso}(t) \neq \phi_v^{ir}(t) \neq \phi_v^{aniso}(t)$ and equations 2.48 and 2.49 only hold if the vibrational and reorientational relaxation processes are statistically independent[2]. For statistical independence it is necessary for the two processes to occur on different time scales.

From previous studies[8], it has been shown that for molecules similar in size to BCS, that reorientational relaxation occurs much slower than vibrational relaxation. It may thus be possible to assume that the band width arises entirely from vibrational relaxation. This is useful if the calculation and separation of two correlation functions is not possible e.g. weak and noisy $I_{VH}(\omega)$ component.

BCS has some advantages over smaller molecules, including that the vibrational and reorientational motions can be considered separately (see figure 4.6 showing I_{VV} and I_{VH} bandwidths) due to molecular size and fluid density. BCS has many spectral bands enabling the motions and interactions of the whole molecule and parts of the molecule to be investigated.

However, this also has disadvantages. It is difficult to model the motion of complicated molecules and there are difficulties in obtaining the correlation functions of molecules with many vibrational modes due to their overlapping.

2.3.2 Problems Involved in Obtaining Correlation Functions

There are a number of experimental problems to overcome before the digitised band intensity is correct.

In Raman spectroscopy, the incoming laser beam must be fully polarised. This can be done by passing the laser light through a polariser placed in front of the sample. Highly polarised bands might also cause a problem because of leakage from the $I_{VV}(\omega)$ spectrum into that of $I_{VH}(\omega)$. Therefore, the measured $I_{VH}^{obs}(\omega)$ may be different to the true value. (2.50)

$$I_{VH}^{obs}(\omega) = I_{VH}^{t}(\omega) + C I_{VV}(\omega) \qquad (2.50)$$

Bartoli and Litovitz[9] found values of $C \approx 0.2\%$ for typical polarised bands. This problem can be overcome by using measurements on $459cm^{-1}$ band in CCl_4 which has a well known[10] depolarisation ratio to calculate $I_{VH}^{t}(\omega)$ from $I_{VH}^{obs}(\omega)$.

The most serious difficulties arise with achieving an accurate baseline and a good signal to noise ratio, especially in the wings of the band. If the signal to noise ratio is poor for weak bands, the resulting correlation functions are very noisy with imprecise correlation time determination[11]. With longer experimental times (photon counting or multi-channel detection (Raman)) or fast scanning (Fourier transform infra-red)) these problems can usually be overcome.

The baseline determination is a more serious problem due to the difficulty in obtaining a meaningful background, especially for the pure liquid.

Computational procedures have been devised to help overcome difficulties with optical problems e.g. interference fringes.

Also, as well as the problem with sampling the data, a number of factors limiting the accuracy of the determined correlation function also occur. The band centre must be

found accurately[12]. To achieve this data is collected at smaller frequency intervals, but longer experiment; times are required. Combination bands, overtones, and the presence of another vibrational mode of similar frequency make it difficult to determine the band centre. Combination bands and overtones are sometimes eliminated by isotopic substitution, also in some cases by calculation[13], but frequency shifts and the fractional intensity of the various species present are needed and it has to be assumed that the relaxation processes effect each isotopic band in the same way.

For two different bands close together there is no reliable solution to the band centre problem, particularly for large molecules such as BCS. Overlapping bands also restrict the maximum frequency range over which the band can be measured. If it is only possible to measure the spectrum between certain limits ω_i and ω_f, this restricts the time resolution which may be achieved[14] (2.51).

$$\Delta t = \frac{\pi}{\left[2\pi c(\nu_0 - \nu_i)\right]} = \frac{16 \times 10^{-12}}{(\nu_0 - \nu_i)} \qquad (2.51)$$

ν_0 and ν_i in cm^{-1}.

This limitation can be quite serious. If $(\nu_0-\nu_i)=100cm^{-1}$ then the corresponding time resolution is 0.2psec. Therefore, it is difficult to properly define the short time part of the correlation function C(t) if the time resolution and relaxation time is short i.e. a broad band. To describe the short term part of C(t), $(\nu_0-\nu_i)=10 \times$ full width of the band at half maximum height should be aimed for. For BCS there are likely to be difficulties in obtaining accurate correlation functions due to the limits imposed on the analysis due to the presence of many vibrational modes contributing to the spectra. In this case, it may not be possible to measure the correlation functions due to the closeness of the other bands. Inaccuracies in the measurement of the wings of the band means that the correlation functions are not accurately determined for the short time part of molecular dynamics.[2]

The requirement of sampling at an interval $\Delta\omega$ leads[14] to a periodic C(t) function with period

$$\tau = \frac{2\pi}{\Delta\omega} \qquad (2.52)$$

Therefore, the calculated correlation function is only reliable up to a time[2] $\pi/\Delta\omega$. $\Delta\omega$ is usually controlled by the instrumental slit width ∂s such that $\Delta\omega \leq \partial s$. Therefore, the range is given by

$$t = \frac{\pi}{(2\pi c \partial s)} \approx \frac{16 \times 10^{-12}}{\partial s} \text{sec} \qquad (2.53)$$

∂s is the slit width in cm^{-1}.

If $\partial s = 1 cm^{-1}$ the correlation function is valid out to 16psec. Except for narrow bands (long correlation times) obtained with poor resolution this is not normally a limiting factor.

In some infra-red bands errors can arise in the computed correlation function if the band profile is seriously distorted by the rapid variation in refractive index $RI(\omega)$ through the band, but this effect can be corrected if $RI(\omega)$ and the absorption coefficient can be measured separately[2].

2.3.3 Correlation Times

If it is possible, to separate the various correlation functions, it is often convenient to characterise the function by obtaining the corresponding correlation time τ_x when:

$$\langle \tau_x \rangle = \int_0^t \phi_x(t) \partial t \qquad (2.54)$$

∂t is the expected time limit which is controlled by the spectral resolution.

If $\phi_X(t)$ function can be written as $\phi_X(t) = \exp(-t/\tau_X)$, then the integrated value $<\tau_X>$ is equivalent to the "decay" time τ_X^e measured directly from $\phi_X(t)$ vs.t curve (i.e. the time required for $\phi_X(t)$ to fall from 1 to 1/e).(See figure 2.8)

If, due to experimental uncertainties, it is not possible to calculate $\phi_X(t)$ accurately then, assuming $\phi_X(t) = \exp(-t/\tau_X)$ holds, τ_X can be calculated from

$$\tau_x \cong \left(\pi c \Delta\nu_{1/2}\right)^{-1} \qquad (2.55)$$

where $\Delta\nu_{1/2}$ is the apparent full-width at half maximum height in cm^{-1}.

If $\phi_X(t)$ can be obtained but integration is not possible, τ_X can be calculated from the slope of a plot of $\ln\phi_X(t)$ against t at longer times when $\phi_X(t)$ becomes exponential regardless of the details of the relaxation process.

On estimating correlation functions from bandwidths, there is a loss of information as the time development of the correlation function is no longer observed, only an average is observed. However, possessing the correlation time for the vibrational or reorientational relaxation of a mode can still help with the understanding of molecular dynamics and interactions, through models and theoretical calculations of relaxation processes from which an estimate for the correlation time can be obtained.

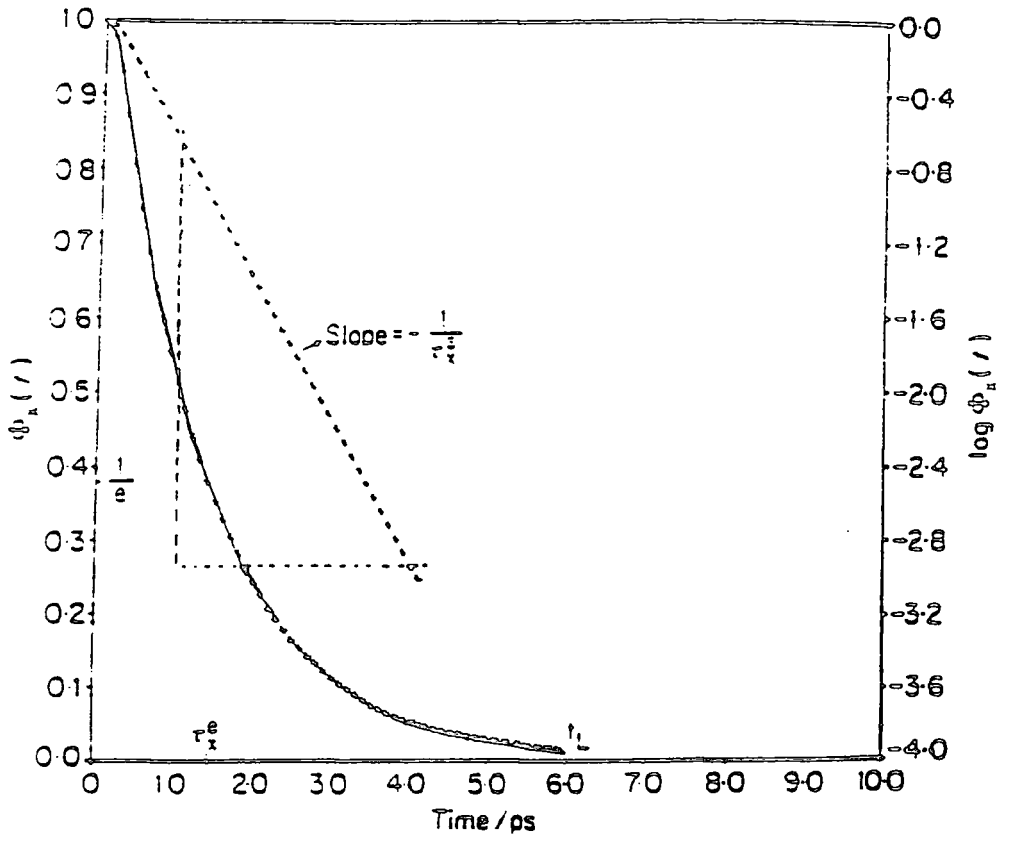

Figure 2.8. Correlation function for pure Lorentzian band of half width (FWHM)= 7cm^{-1}, showing the various correlation times that can be produced. Reproduced by permission from reference 7

2.4 Relaxation Processes

In a liquid, there are usually many different relaxation processes contributing to the overall relaxation of a particular vibrational mode. The processes that occur are determined by the molecular motions and interactions that occur in the fluid.

A rapid relaxation rate has a corresponding correlation function that decays rapidly and consequently, a small correlation time. In the frequency domain, this is seen as a relatively broad band. If the relaxation rate is slow, the opposite is seen.

By comparing the shape of the vibrational bands and/or the correlation functions for a system, as a function of concentration, temperature, and pressure, it may be possible to evaluate the predominant relaxation processes and gain an insight into the molecular motions and interactions in a liquid.

2.4.1 Vibrational Relaxation

Vibrational relaxation is essentially a measure of the efficiency with which molecules interact with one another. For a given vibrational mode of a molecule, there are a number of processes which contribute to the vibrational relaxation of that mode and consequently to the band shape and the decay of $\phi_v(t)$. These may include one or more of the following[15].

a)Vibrational Energy Relaxation/Transfer

In this process, the energy of the excited system is transferred into translations, rotations or other vibrations close in frequency. The population difference is reduced by the dissipation of energy into the surrounding lattice molecules.

b)Intramolecular Vibrational Relaxation

The vibrational energy moves from the originally excited mode to a different mode in the same molecule.

c)Resonance Vibrational Energy Transfer

The energy loss of an upper oscillator is the subsequent energy gain to the same oscillator level on an adjacent molecule. Relatively strong interactions between molecules in a liquid sometimes cause part of the excitation energy to shift to another molecule by resonant transfer. During this transfer, neighbouring molecules are performing vibrational motions simultaneously. The vibrational energy in this situation is different from the single molecule vibrational energy. As the transfer process starts during the excitation process, the excitation energy will be influenced by this intermolecular vibrational coupling. The disordered liquid results in different pairs of molecules being coupled with different coupling strengths and, because of this, the resonance effect causes a distribution of the excitation energies. This results in band broadening called "inhomogeneous broadening".

d)Vibrational Dephasing

In this process, band broadening effects are occurring because of a loss of phase coherence of the excited vibrations in a particular mode[15,16]. There are two ways of this occurring. One is through inhomogeneous broadening, and the other is through homogeneous broadening.

In a disordered condensed phase, the sharp transition frequency ω_0 of a two oscillator system is "smeared" out into a continuous, non-reversible distribution of vibrational transition frequencies. All the molecules possess a slightly different vibrational frequency, which leads to the gradual decay of the sum function due to destructive interference (figure 2.9). This leads to inhomogeneous broadening. The band broadening occurs due to the spread of the inhomogeneities in the oscillator frequencies which the electromagnetic field of the beam effectively samples. The interactions which cause inhomogeneous broadening fluctuate rapidly due to fast transitional and rotational motions. This causes a partial averaging of all the possible energy levels because spectroscopy has a limited time resolution and therefore can not show the instantaneous situation. Motional narrowing weakens the frequency dispersion and a slower decay of the vibrational relaxation function occurs.

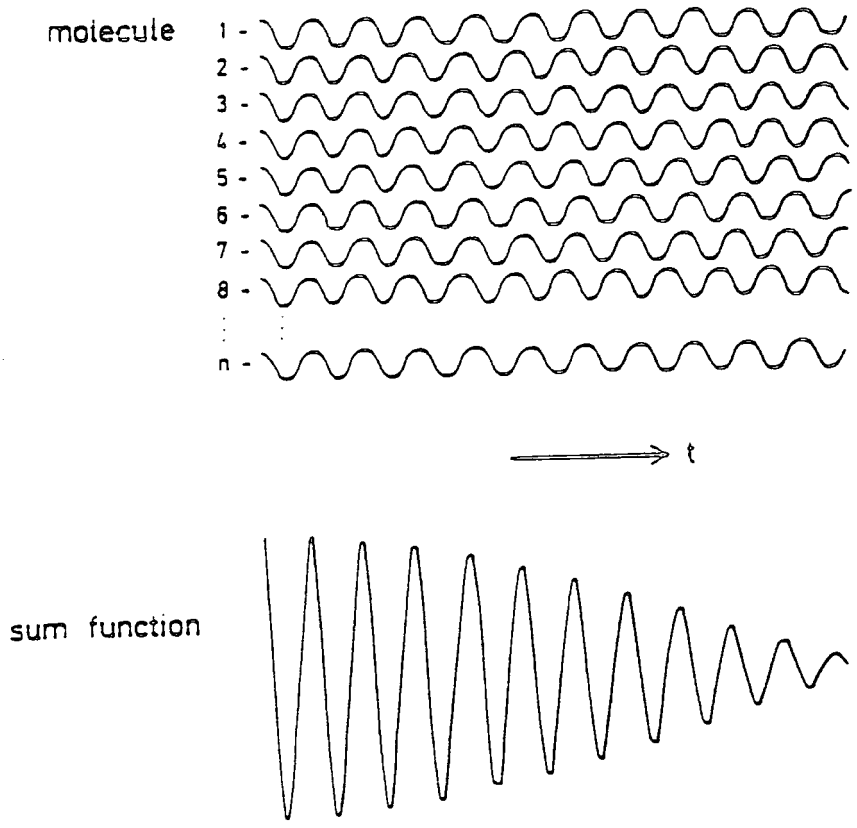

Figure 2.9. Inhomogeneous broadening. Reproduced by permission from reference 2

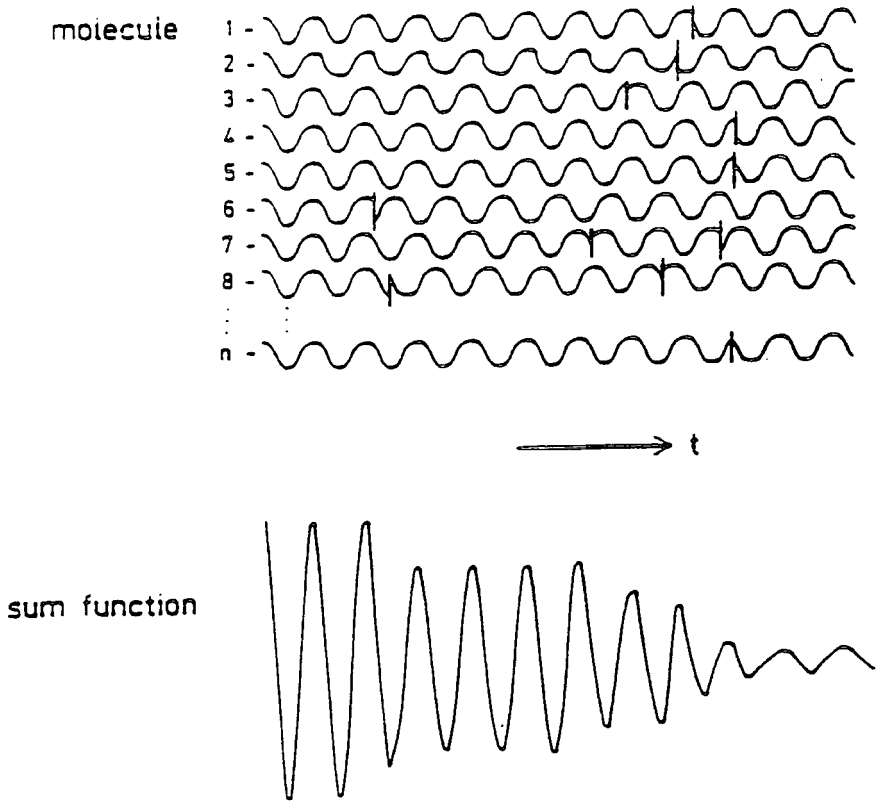

Figure 2.10. Homogeneous broadening. Reproduced by permission from reference 2

The second type of vibrational dephasing is homogeneous broadening. This model assumes that intermolecular interactions only act during very short time collisions which then cause phase shifts.(figure 2.10)

The first two effects a) and b) are essentially vibrational depopulation effects or energy relaxation processes. c) and d) are phase relaxation processes and are broadening effects with resonance vibrational energy transfer being an inhomogeneous effect caused by the loss of oscillator phase arising from the coupling of oscillators involved in the energy transfer.

Assuming statistical independence of the two types of processes then, (2.56)

$$\phi_v(t) = \phi_E(t)\phi_{pp}(t) \qquad (2.56)$$

where E implies energy relaxation and pp phase relaxation.

It is generally found that broadening by phase relaxation processes are the dominant contributions to bandwidths in liquids. Energy relaxation processes are usually much slower because vibrational energy is in most cases much higher than rotational or translational energies and therefore, dissipation of energy is only possible by complicated processes.

Inhomogeneous broadening processes depend on the spread of different vibrational frequencies of the active molecule. Therefore, the rate of vibrational relaxation is a result of the extent of the frequency distribution caused by the surrounding intermolecular potential. Therefore, in principal the measurement of vibrational relaxation functions allow the study of such potentials. The major difficulty is that loss of phase coherence may occur through many different types of interaction e.g. dipole-dipole, dipole-quadrapole etc. or due to repulsive potentials. Fortunately, these different types of interaction may sometimes be distinguished experimentally[7] and sometimes it can be shown that one type is predominant for a particular vibrational mode. In favourable cases, variation of concentration, temperature and pressure will enable the nature and behaviour of the interaction to be studied in detail. To achieve this, it is necessary for a detailed description of the mechanism of vibrational relaxation.

There is also a need for the use of fully descriptive models[7] for each type of interaction. This enables the understanding of when and why a particular process will predominate and how this should manifest itself in correlation functions.

2.4.2 Reorientational Relaxation

The decay of the correlation function is known as reorientational relaxation. The reorientational correlation function $\left\langle P_l\left[\vec{\mu}_i(0).\vec{\mu}_i(t)\right]\right\rangle$ can often be obtained from the Raman I_{VH}-I_{VV} experiment. It can also be obtained from the purely rotational far infra-red[17] and depolarised Rayleigh[18] spectra. The processes which give rise to the reorientational band width increment and lead to a decay of the associated reorientational correlation function are similar to the dephasing processes. The rotational transition energies are small compared to the vibrational excitation energies encountered in mid infra-red and Raman.

An ensemble average over a Boltzmann distribution is observed. This ensemble average of rotational energies leads to a loss of initial coherence of the reorientational correlation function and therefore the rotational energies are smeared out. It is the nature and rate of collisions and reorientation which control the rotational energies and therefore the observed relaxation. Consequently, the observation of reorientational correlation functions allow an insight into the rate of collisions and reorientational motions. The reorientational motion for larger molecules becomes slower due to size and steric hindrances. It also becomes more difficult to describe using theoretical models. Vibrational relaxation plays a more important role in determining the band shapes for larger molecules. For large molecules in mid infra-red and Raman, it is unlikely that reorientational correlation functions, which arise as a consequence of overall molecular rotation , can be extracted adequately.

If intramolecular reorientation is significant, it may contribute an observable increment to the band width and reorientational correlation functions for such motions could be obtained. Intramolecular motion is extremely difficult to model for large, flexible molecules. Spectroscopic studies can help to give an idea of the flexibility of molecules and which interactions are important in controlling this. Flexibility must, in

some way, control the macroscopic properties of a fluid. Therefore any information obtained could be linked to these properties.

References

1. A. Messiah. "Quantum Mechanics I". John Wiley and Sons, New York (1957)
2. R. Arndt and G. Doge, "Infra red and Raman Studies on Molecular Dynamics in Liquids", Chapter 6 of "Spectroscopy and Dynamics of Molecular Liquids", Ed. D. Steele and J. Yarwood, Elsevier (1991)
3. A.M. Benson, Jr. and H.G. Drickamer, J. Chem. Phys., 27, 1164 (1957)
4. R.R. Wiederkehr and H.G. Drickamer, J. Chem. Phys., 28, 311 (1958)
5. D. Levesque, J.J. Weiss and D. Oxtoby, J. Chem. Phys., 68, 5528 (1978); ibid., 72, 2744 (1980)
6. D.J. Gardiner and P.R. Graves. "Practical Raman Spectroscopy". Springer-Verlag Berlin Hindleberg (1989)
7. J. Yarwood and R. Arndt, "Study of Intermolecular Interactions in the Liquid Phase", Chapter 4 of "Molecular Association", Vol. 2, ed. R. Foster, Academic Press (1979)
8. D.G. Gillies, S.L. Matthews and L.H. Sutcliffe, Mag. Res., 29, 1221, (1991)
9. F.J. Bartoli and T.A. Litovitz, J. Chem. Phys., 56, 404 (1972)
10. W.F. Murphy, M.V. Evans and P. Bender, J. Chem. Phys., 47, 1836 (1967)
11. G. Doge, R. Arndt and J. Yarwood, Chem. Phys., 47, 387 (1977)
12. J. Vincent-Geisse, J. Soussen-Jacob, C. Breoillard, J.C. Briquet and T. Nguyen-tan, Mol. Phys. ,34, 145 (1977)
13. P. Van Konynenberg and W.A. Steele, J. Chem. Phys., 56, 4776 (1972)
14. B. Keller and F. Kneubuhl, Helv. Physica. Acta., 45, 1127 (1972)
15. W.G. Rothschild, "Dynamics of Molecular Liquids", John Wiley and Sons (1984)
16. S. Bratos and E. Marechal, Phys. Rev., 4, 1078 (1971)
17. J.S. Rowlinson and M. Evans, "Annual Reports, A, 1975", The Chemical Society, London (1975)
18. B.J. Berne and R. Pecora, Ann. Rev. Phys. Chem.,26, 233 (1974)

CHAPTER 3

Experimental

3.1 Raman Spectroscopy

Initial Raman measurements were obtained using a Cary Model 82 Spectrometer linked to a Glen-Spectra IBM-SCADAS (Spectrometer Control and Data Acquisition System). Excitation was provided by the green 514.5nm laser line of a Cambridge Lasers CL-4 argon ion laser.

In this instrument, light passes through a monochromator where it is dispersed by a premonochromator set only to allow the 514.5nm line to pass through. It is then focused into a 90° scattering compartment and onto the sample. Scattered light from the sample passes through a polariser, if polarisation analysis is required, and then through a light scrambler to remove any polarisation properties from the scattered light. Light is then directed onto the entrance slit of the monochromator. Light detection is provided by cooled photomultipliers linked to the photon counting electronics of the computer system.

A resolution of $3cm^{-1}$ was used for all measurements.

The more recent measurements were obtained using a Renishaw Ramascope.

Carrying out conventional Raman spectroscopy is very time consuming and can be a major undertaking. This has led to it being confined to specialist research laboratories, with the emphasis of use being largely on fundamental science. Conventional Raman imaging is far more difficult and there is no straightforward way of obtaining Raman images from a conventional Raman spectrometer.

With this in mind D. Batchelder[1] adapted an idea for a Raman Microscope/Microprobe. He decided to combine fairly recent technological developments and apply them to Raman Spectroscopy/Imaging in order to optimise the instrument. These developments were:

1. Cooled C.C.D. (Charge Coupled Device) Camera.

This provided a very sensitive electronic 'photographic plate' of high efficiency and very low noise. See appendix for more information.

2. Optical multilayer thin film interference filters

These are manufactured to a very high specification and enable the centre wavelength of their pass band to be tuned by tilting them with respect to the incoming beam. The filters have a high throughput in their pass band whilst retaining high rejection of wavelengths outside this band.

3. Development of Personal Computers

These provided a means of controlling the filters and processing and displaying the image from the C.C.D. camera.

The use of a conventional optical microscope provided a convenient means of enabling the operation of the system as both a Raman Microprobe (Raman spectrometer with high spatial resolution) and Raman Microscope (Raman imaging system with high spatial resolution).

The fundamental function of a Raman system is to deliver suitable exciting laser light to a sample, collect the resulting Rayleigh and Raman scattered light, filter this to remove the unwanted Rayleigh light, and detect and analyse the remaining Raman light.

A fully specified Ramascope has three possible modes of operation which are described below. Schematic diagrams of each of these operational modes and a diagram of the Ramascope are shown in figures 3.1 to 3.4. These will be referred to in the following descriptions.

3.1.1 Raman Microprobe Mode

Light from a very small part of the sample is collected and used to produce a Raman spectrum.

Excitation is provided by a relatively low power laser (25mW). Component (1) is the 'Plasma line rejection filter'. This spectrally filters the output from the laser to provide a more 'monochromatic' excitation beam. It is in fact a thin interference band pass filter which blocks all emissions from the laser except the main lasing line. These unwanted emissions arise mainly as the result of non-lasing transitions in the laser plasma.

The spatial filter (2) improves the quality of the laser's beam profile (i.e. its spatial distribution of intensity). This consists of a microscope objective focusing the beam through a pinhole with a second objective following this which is mounted on a computer controlled translation stage which allows its focus to be adjusted. In the microprobe mode the objective is positioned so that it is focused on the pinhole in order to produce a collimated spatially clean beam.

The beam produced by the spatial filter assembly is deflected by mirrors (3) and (4) onto a Holographic Notch Filter (HNF) (5).[2] This has the property of reflecting light of only the laser wavelength whilst transmitting all other wavelengths. Thus, the laser beam is deflected into the microscope and down onto the sample (7) via mirror (6) which may be moved from the beam path to enable ordinary use of the microscope.

The incident beam is then focused to a tiny spot on the sample by the microscope objective, with the resulting Rayleigh and Raman light from the spot being collected and passed back into the microscope via the same objective. This light, still travelling as a collimated beam, passes via mirror (6) to the HNF which reflects light of the laser wavelength (Rayleigh scattered light) harmlessly back into the lower half of the instrument. The Raman light has wavelengths shifted from that of the laser and so is transmitted by the filter and allowed to continue through the system.

A number of optional components may now be included: a second HNF (8) to further reduce the Rayleigh intensity, a polariser (9) to enable the analysis of the polarisation of the Raman light and a half-wave plate (10) to rotate the polarisation of the Raman light and improve the throughput of, primarily, the imaging filters.

The remainder of the instrument is in many ways similar to a conventional grating spectrograph. A lens (11a) focuses the beam of Raman light through an adjustable entrance slit (12a). This controls the resolution of the system and blocks unwanted stray light from reaching the detector.

A lens (13a) recollimates the beam before it is deflected by a reflecting prism (14a) onto a diffraction grating (15a). This is mounted on a computer controlled rotary stage to enable control of the beam's angle of incidence, and therefore the central

wavelength of the measured spectrum. The grating prism deflects the dispersed light through lens (17) which images the spectrum across the surface of the C.C.D. chip.

By displaying a graph of intensity against vertical position on the C.C.D., and attaching the appropriate scales, a conventional intensity versus wavenumber spectrum can be produced.

3.1.2. Raman Imaging Mode (Raman Microscope Mode)

This provides a photograph like image of the sample taken using only light from a selected Raman peak.

The laser delivery optics 1-10 as described previously are common to the imaging mode. However, in this mode the second objective in the spatial; filter (2) is moved by the computer so that the laser line is no longer focused on the pinhole (i.e. it is defocused). Consequently, the beam is no longer collimated and so, in turn, is no longer focused to a tiny spot on the sample by the microscope. Instead, an area of the sample is illuminated with laser light which provides the necessary conditions for image formation. The imaging light that passes back up into the system is not collimated, contrasting with the situation in the microprobe mode.

After the Rayleigh scattered light has been removed by the HNF, the beam is deflected down into the middle portion of the spectrometer by a computer controlled moveable mirror (11b), which is automatically moved into the beam path when the imaging mode is selected by the user. A further deflection by mirror (12b) occurs and the imaging beam is incident on the thin film interference filters (13b). These filters have a narrow pass band and are used to isolate the light from a chosen Raman band that is characteristic of the material of interest. The filters are tuned to a particular Raman frequency by adjusting their angle of incidence with respect to the incoming beam. To enable this, the filters are mounted on a computer controlled rotary stage. A number of filters are needed to cover the required range of possible Raman frequencies and these are arranged in a computer controlled wheel, with the appropriate filter being automatically placed in the beam path for the user selected Raman frequency.

The imaging beam, now made up solely of light from the selected Raman peak, proceeds via mirror (15b) and movable mirror (16b), which operates as per moveable mirror (11b), to the C.C.D. imaging lens (17). This focuses onto the C.C.D. to produce a photograph like image representing the two-dimensional distribution of the material characterised by the selected Raman peak.

3.1.3. High Resolution Mode

This mode enables a high resolution spectrum to be taken over a limited spectral range using only a tiny portion of the sample.

The laser delivery optics have the same arrangement as in the microprobe mode, producing a beam focused to a spot on the sample.

The Rayleigh and Raman scattered light are passed up the microscope and into the spectrometer where they are separated by the HNF. The movable mirror (11b) is placed in the beam path and the beam is deflected onto mirror (12b). The filter wheel is moved to allow the beam to proceed to a Fabry Perot Interferometer (FP) (14b) which is moved into the beam path automatically when this mode is entered.

The FP has a very narrow pass band whose central frequency can be controlled by varying the voltage applied to the device.

The output from the FP passes via mirrors (15b) and (16b) to the C.C.D. focusing lens (17). This focuses the light onto the C.C.D. to produce a small spot only a few pixels across, and these are binned together to effectively provide a single element photo detector. The wavelength passed is moved through the desired range by applying a series of stepped voltages to the FP. A single C.C.D. exposure is made for each applied voltage and an intensity verses voltage graph is plotted which, when equipped with the appropriate scales is the familiar intensity verses wavenumber Raman spectra.

All the Raman measurements were conducted in the Raman Microprobe mode with a slitwidth of 12μm (resolution of 2-3cm^{-1}), with the liquids or solutions contained in optically flat cuvettes. The laser spot was focused into the bulk liquid and 180° back

scattering was used. The heptane used was of 99+% spectrophotometric grade purity obtained from the 'Aldrich Chemical Company Limited'. Solutions were made up by volume to the required mole fraction.

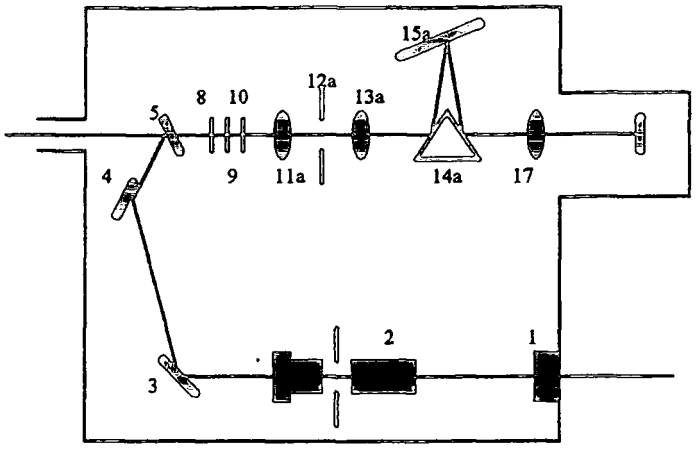

Figure 3.1. Schematic diagram of the Microprobe Mode

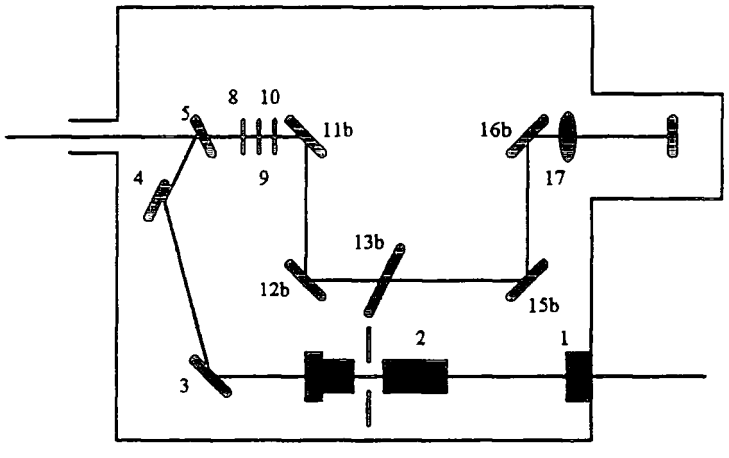

Figure 3.2. Schematic diagram of the Imaging Mode

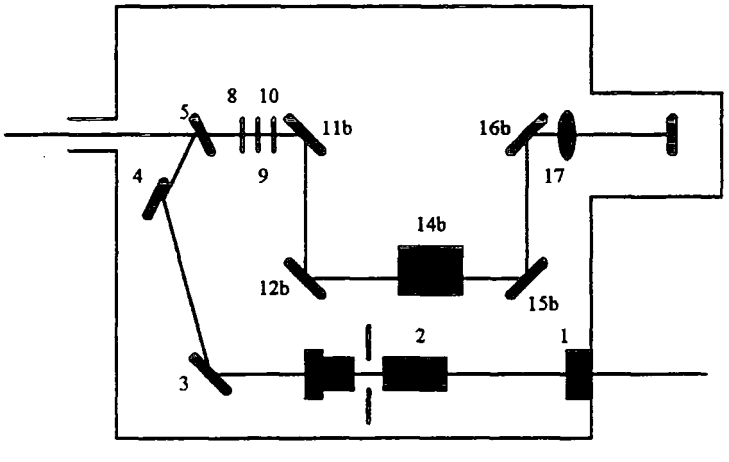

Figure 3.3. Schematic diagram of the High Resolution Mode

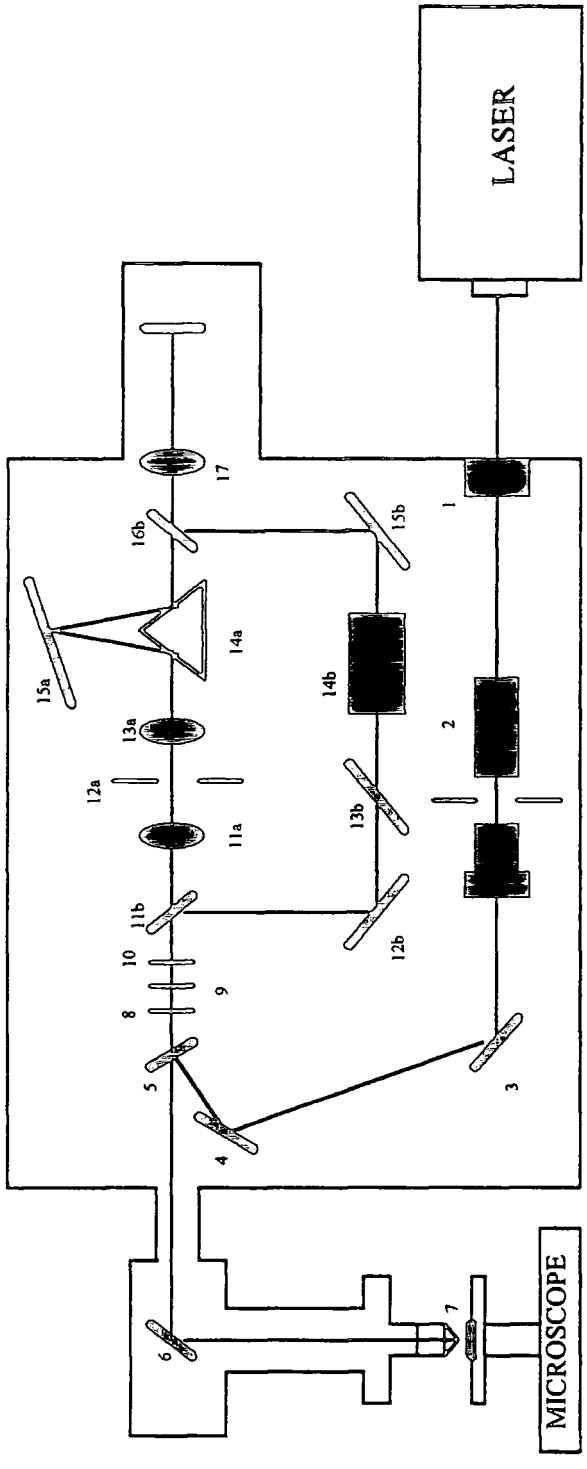

(1) Plasma Line Rejection Filter
(2) Spatial Filter
(3) Mirror
(4) Mirror
(5) Holographic Notch Filter
(6) Mirror
(7) Sample
(8) Second HNF
(9) Polariser
(10) Waveplate
(11a) Lens
(11b) Moveable Mirror
(12a) Adjustable Slit
(12b) Mirror
(13a) Lens
(13b) T.F.F. Wheel
(14a) Reflecting Prism
(14b) Fabry Perot Interferometer
(15a) Diffraction Grating
(15b) Mirror
(16b) Moveable Mirror
(17) C.C.D. Focussing Lens

Figure 3.4. Schematic diagram of the Renishaw imaging Raman spectrometer.

3.2 Infra Red Spectroscopy

The mid infra-red 600cm^{-1}-3500cm^{-1} work was carried out using both dispersive and Fourier transform instruments.

The early work was conducted on a Perkin Elmer 580B instrument. This is a double beam instrument i.e. the background and the sample spectra are recorded simultaneously and ratioed in the instrument. A ceramic tube heated to 1200°C is used as the source of continuous radiation. Broadband infra red radiation from the source is divided into reference and sample beams. The sample absorbs radiation from the beam, whilst the reference beam passes through unaffected. Both beams are then combined and pass through a monochromator and are then focused onto a thermocouple detector. The alternating signal from the detector is amplified and then demodulated to give separate sample and reference beam signals. These are then ratioed to give the corresponding transmittance value of the sample. Spectra may also be recorded in absorbance or single beam.

The later work was carried out using a Mattson Instruments Sirius Fourier Transform Infra-red Spectrometer and a Mattson Instruments Polaris Fourier Transform Infra-red Spectrometer, with the high pressure work conducted on the Sirius and the temperature work conducted on the Polaris. The optics of both these instruments are very similar. Figure 3.5 illustrates the setup of the Sirius. The Fourier Transform instruments are single beam instruments and therefore interferograms are recorded for sample and background separately and a ratio is performed in the frequency domain to obtain the absorption spectra. Both instruments have a water cooled globar source, germanium coated potassium bromide beam splitters, and liquid nitrogen cooled Mercury Cadmium Telluride (MCT) detectors. A resolution of 4cm^{-1} was used in obtaining the data.

The work conducted at Thornton Research Centre was carried out using a Spectra Tech IR Plan Model 2 Microscope which was interfaced to a Perkin Elmer 1760FT spectrometer. The spectrometer was again a single beam Fourier transform machine with a MCT detector. The IR Plan microscope is a conventional research grade visible light instrument and a high performance infra red sampling accessory for use with

FT-IR spectrometers. It uses either the FT-IR's detector, or can be equipped with an optional dedicated MCT detector. It is equipped with a Reflachromat objective, which is a two mirror, reflecting Cassegrainian design. The reflecting optics produce no chromatic aberrations which make it ideal for use in the infra red region. It is capable of sampling in transmittance or reflectance.

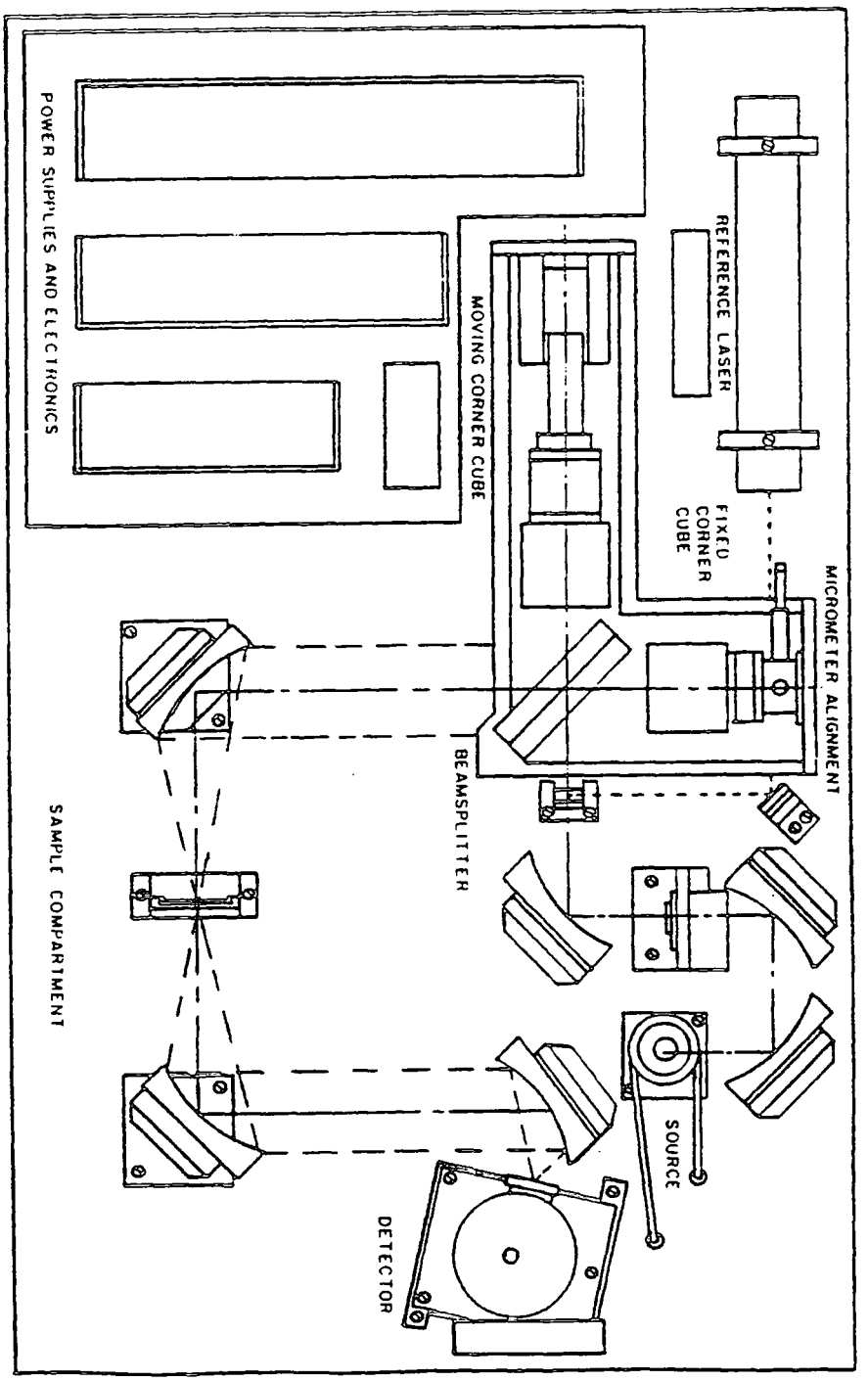

Figure 3.5. The Mattson Sirius 100 FT-IR Instrument.

3.2.1. Solution Studies

Solution studies were carried out using an 8μm path length between potassium bromide plates and a resolution of 2.3cm^{-1}. All solvents used were of 99+% spectrophotometric grade obtained from Aldrich. The solutions were made up by volume to the required mole fraction. Spectra were obtained by ratioing single beam spectra of solution and solvent. If needed, water vapour subtraction was conducted.

3.2.2. Temperature Studies

Spectra of all the liquids were obtained at room temperature and 323-423K in increments of 10K using a Beckman-RIIC variable temperature unit VLT-2, which incorporates a Eurotherm TEM-IC Automatic Temperature Controller with a range from 83K to 523K. Spectra were also obtained for BCS at 276-285K. The temperature is controlled by simply setting the correct temperature on the dial and the internal heating coil is controlled by a thermostat. The cell was mounted in a cell block holder. Heating to maintain the required temperature was provided by two electrical coils mounted on the sides of the cell block. A copper-constantan thermocouple was mounted in a hole in the cell block and this was connected to the temperature control unit. A second thermocouple was mounted in a hole in the liquid cell top plate to measure the actual temperature of the cell unit.(Figure 3.6)

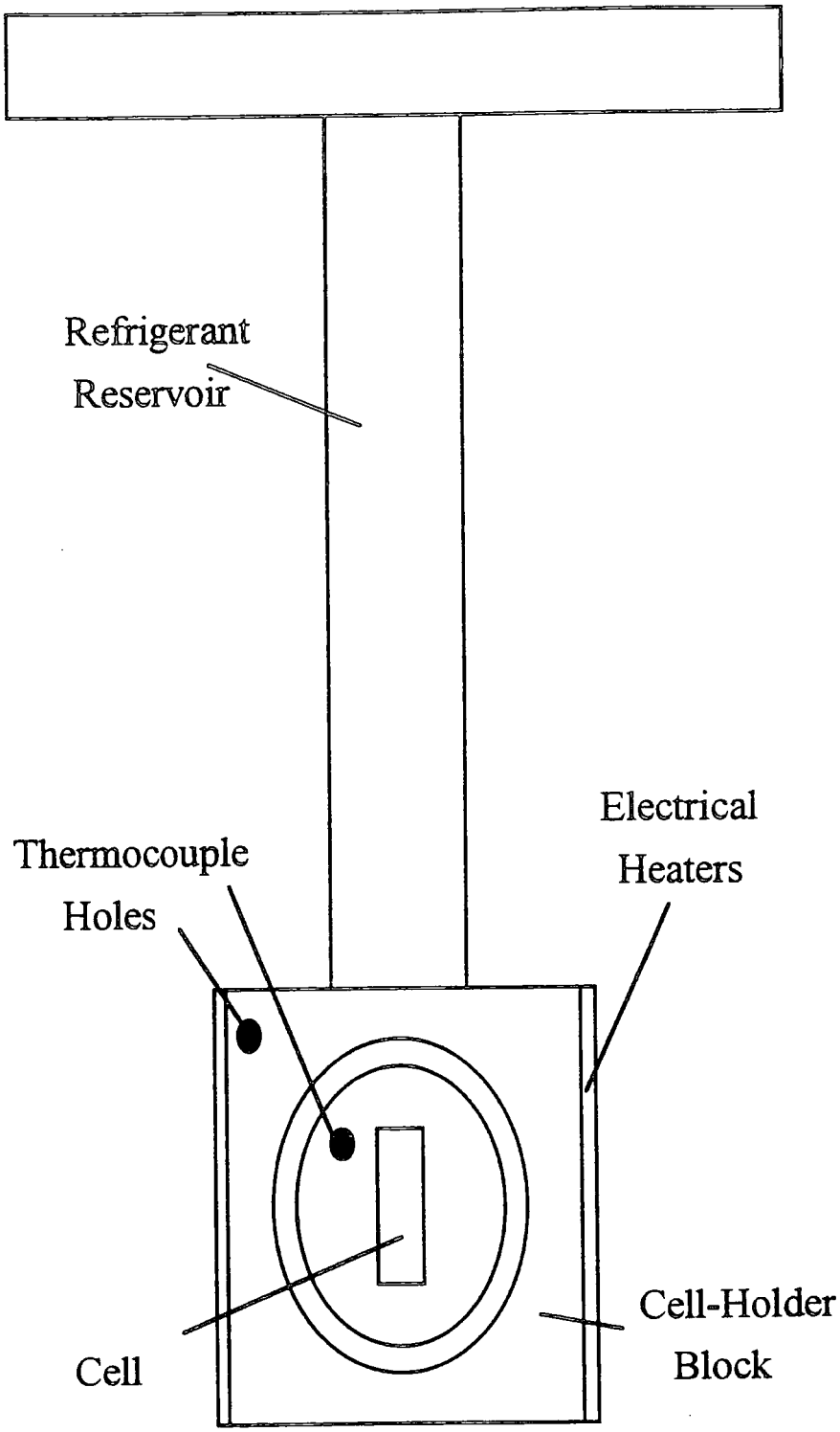

Figure 3.6. Variable temperature cell mounting block

3.2.3. Static High Pressure Studies

High pressure mid infra-red spectra were obtained using a diamond anvil cell (DAC)[3], designed and manufactured by Dr. D. Adams of "Diacell Products"[4]. In this cell (figure 3.7), high pressure is applied to a sample by forcing two flat faced diamond anvils (of type IIA diamonds) together along a common axis. One diamond is mounted on a plate of hardened tool steel set into the base of a cylinder. The other opposing diamond is mounted, in a similar way, on a piston, also of hardened tool steel, which fits tightly into the cylinder. If the cell is being used with liquids, a gasket is required to hold the liquid in place. For this work, gaskets of 0.08mm were used. For Raman spectroscopy, it is more usual to use a gasket of 0.2mm. The sample is held in a tiny hole, of approximately 0.5mm diameter, in the gasket, between the two diamond faces. A cradle system holds the DAC and facilitates high pressure generation by the lever action of a hydraulically operated piston. The "Hydrapak" pump, manufactured by "Tangye Limited", was employed to generate the pressure for the system. A 50:50 mixture of brake fluid oil and castor oil was found to operate as the best pressure transmitting fluid in the pump.

Pressure determination in the DAC was achieved using two different methods. The first, a primary standard, used the pressure related shift of the strong fluorescence emission lines, R1 and R2, of ruby found at 14400 and 14430cm^{-1} respectively[5-7] (Figure3.8). In ruby purely electronic transitions are responsible for the R-lines. The transitions take place between the ^2E and $^4A_2$ crystal field split states of the Cr^{3+} ion. The ^2E state is split into two states $\overline{E}$ and $2\overline{A}$ and it is this splitting which is responsible for the two peaks. These lines show a linear frequency shift of 0.77 and 0.86cm^{-1}/kbar respectively, to at least 50kbar[5-7].

The DAC was set up under a microscope by placing the gasket over the face of the cylinder diamond and then, using a syringe needle, a drop of the required liquid can then be placed onto the diamond face. A small amount of powdered ruby can then be introduced to the gasket hole. It must be insured that the ruby fills no more than 20% of the gasket hole otherwise, as pressure is applied, this may cause a non-hydrostatic

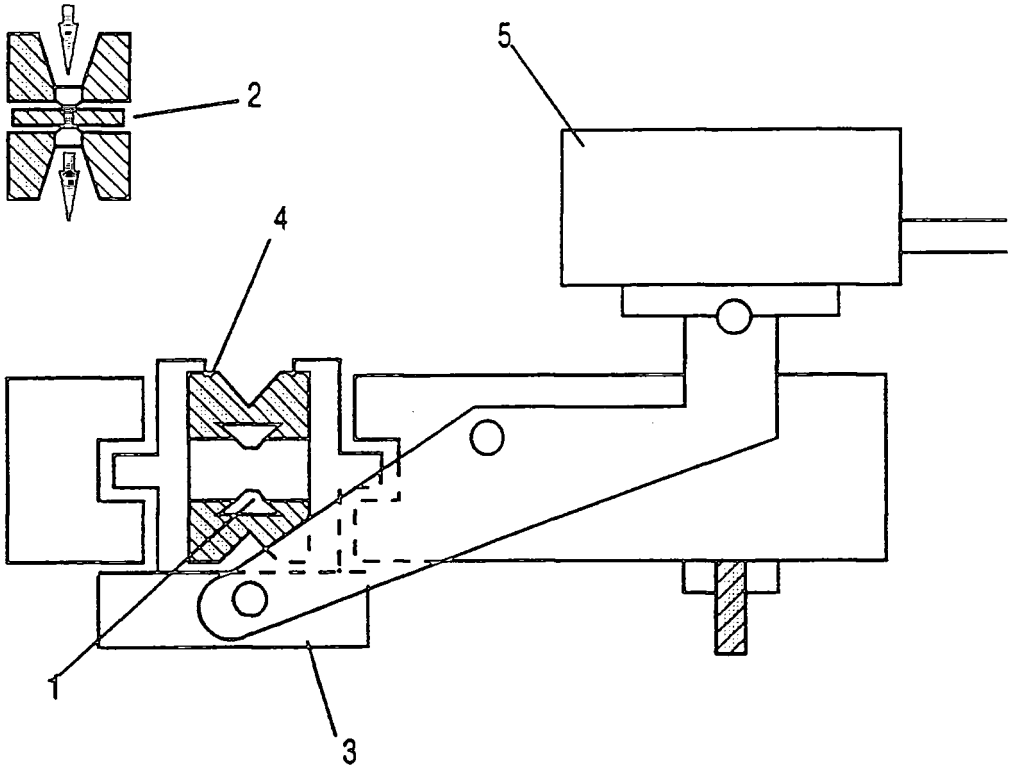

Figure 3.7. The Diamond Anvil Cell and pressurising system: (1) diamond anvil, (2) DAC with gasket, (3) pressure transmitting plate, (4) pistons, (5) piston attached to the pump.

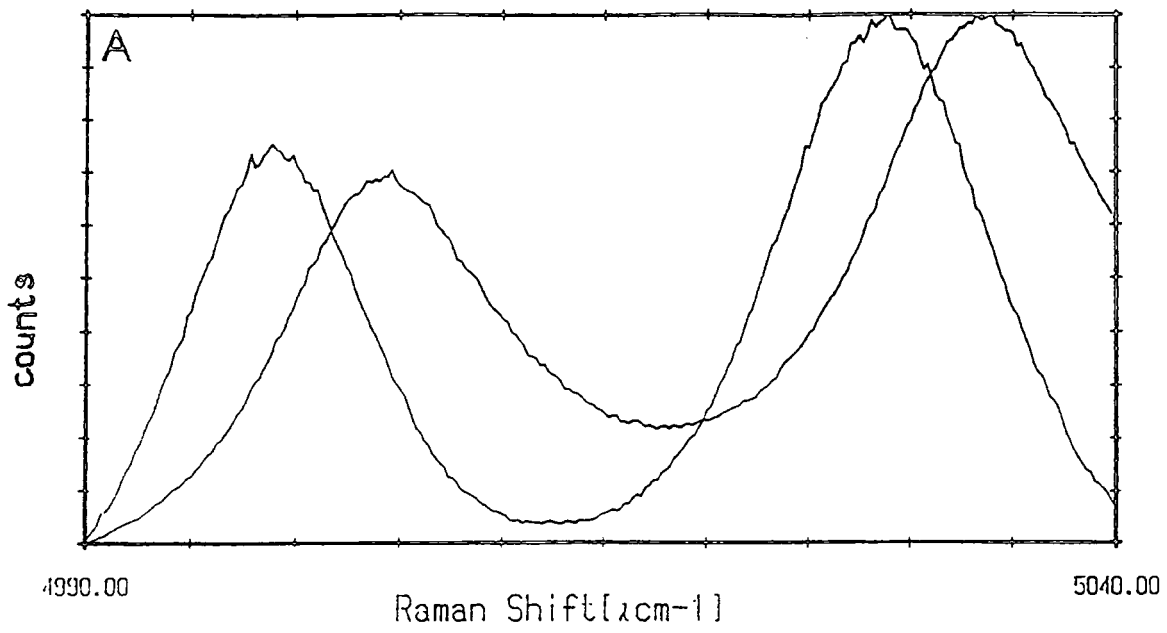

Figure 3.8. Typical ruby fluorescence spectra.

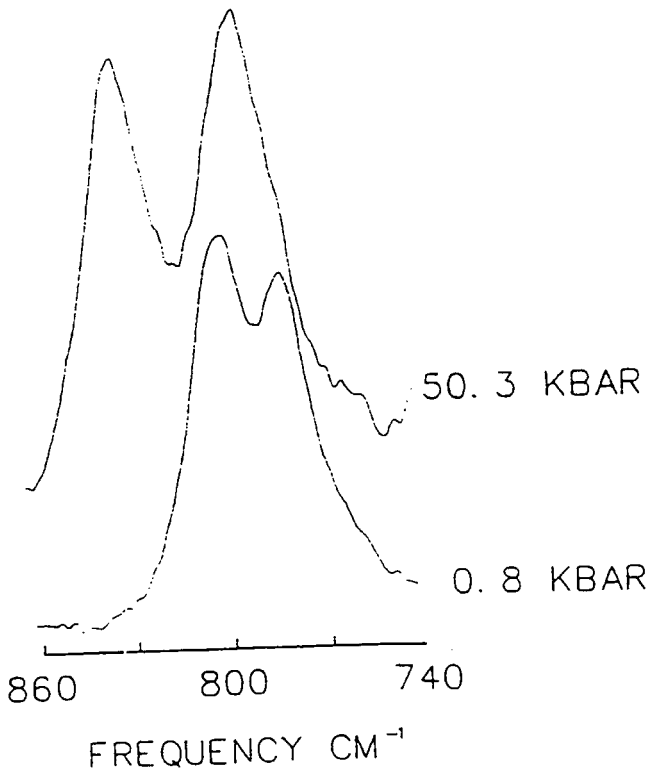

Figure 3.9. Infra red spectrum of crystalline quartz.

environment. Non-hydrostatic pressure in the liquid sample may arise due to a number of reasons. Some of the major ones being:

1. A poorly drilled gasket hole.

2. The hole is offset from true alignment with the diamond faces.

3. There is too much ruby present, or the pieces of ruby are too big.

4. The majority of the liquid has been squeezed out from the gasket hole.

However, non-hydrostatic pressure can be readily observed as the ruby lines tend to broaden considerably and do not retain their 29cm^{-1} spacing[6,7].

The second method of pressure calibration, a secondary standard, used the pressure shift of the infra red bands of crystalline quartz.[8-19] This method has several advantages over using the shift of the ruby lines[5-7] and the use of the pressure shift of the antisymmetric stretching bands of sodium nitrite and sodium nitrate[20]. These are listed below:

1. The pressure is deduced directly from an infra red experiment.

2. Crystalline quartz has a relatively simple infra red spectrum with sharp bands restricted to the frequency range below 1100cm^{-1}. (figure 3.9)

3 These infra red bands are strong enough to be observed when a small amount of crystalline quartz powder is mixed with a pressure transmitting medium.

4. Crystalline quartz is practically insoluble in water, unlike sodium nitrite and sodium nitrate, enabling the study of aqueous systems.

5. At room temperature no structural phase transition in crystalline quartz has been observed in the pressure range up to 100kbar[21].

Among the infra red bands of crystalline quartz, the frequency of the 801cm^{-1} band is particularly sensitive to pressure, and the shift is comparable with that of ruby[6]. Infra-red spectra through the DAC were obtained by ratioing single beam spectra of the relevant liquid in the DAC against single beam spectra of deuterated hexadecane in the DAC. This was necessary to minimise the effects of fringes in the interferrogram produced by a small percentage of radiation being reflected by the diamond faces.

The pressure determination using ruby was carried out on the Cary82 instrument. Using three flat mirrors, a 0° scattering configuration is employed with the laser being brought through the back of the DAC.

Using crystalline quartz, the calibration can be conducted on the infra red instrument using the same configuration as for the normal experiments.

3.2.4. Dynamic High Pressure Studies

Dynamic high pressure spectra were obtained using a sliding elastohydrodynamic (EHD) contact (Figure 3.10) which was placed under the Spectra Tech Microscope. A steel ball of diameter 2.54cm was mounted as shown and can be rotated using a motor. A diamond disc was mounted in a steel/aluminium plate and placed over the ball. This plate can be loaded with weights. The EHD device was placed on an XYZ micropositioning table under the microscope. The size of the area selecting aperture was varied so that spectra could be recorded from regions specifically within the inlet or exit zone of the contact enabling a picture of infra-red behaviour of a lubricant across a loaded contact to be built up as a function of load and rolling speed. There was also a facility for a polariser to be inserted in the beam path allowing dichroic ratios to be measured, from which molecular orientations may be inferred.

Due to the problems encountered with the vibrations of the motor, the eccentricities of the ball and the thickness of the fluid film sampled, the S/N ratio was not good and consequently a resolution of $8cm^{-1}$ was used in obtaining the data.

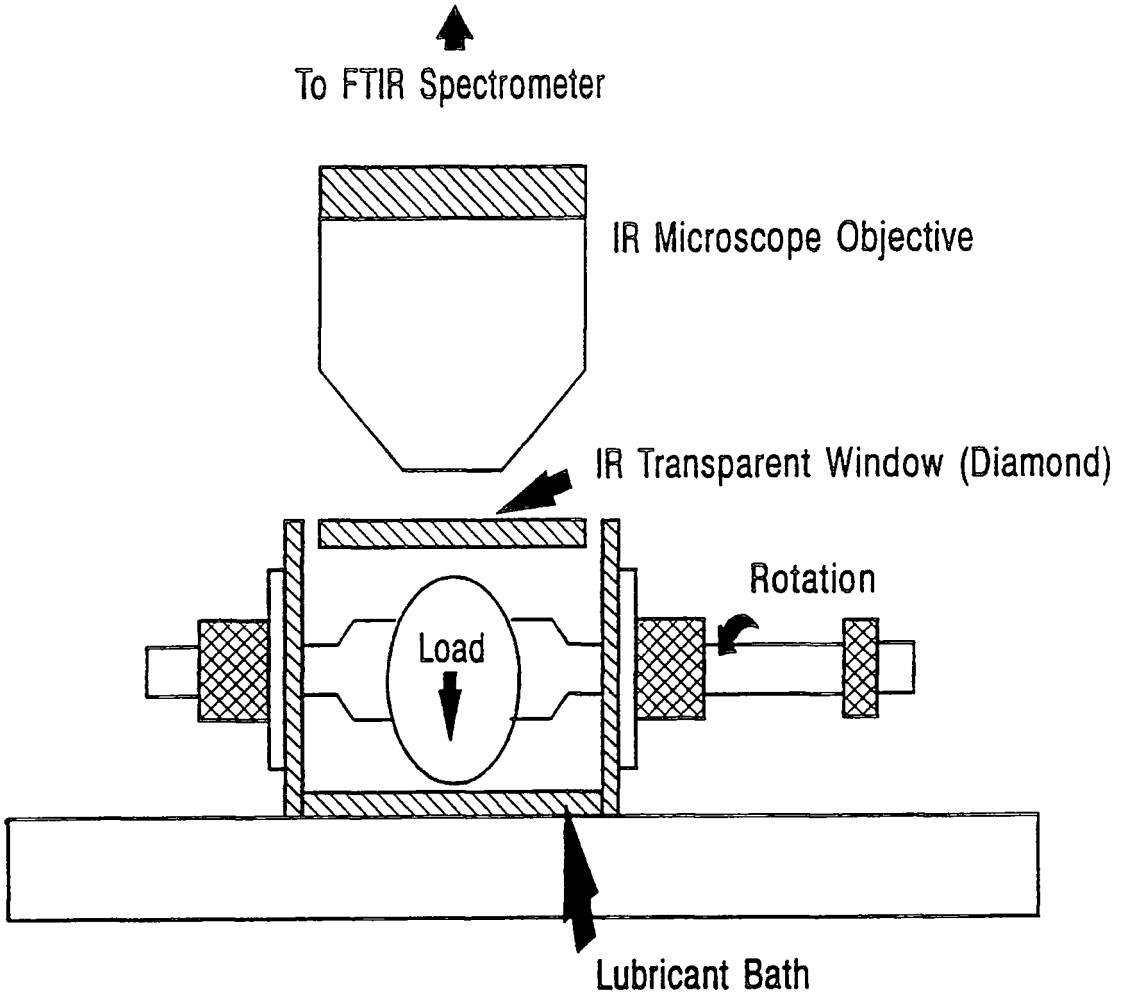

Figure 3.10 Schematic illustration of the "in lubro" rig for the in-situ examination of lubricants in an EHD contact.

References

1. D. Batchelder, Meas. Sci. Technol., 3, 561-563, (1992).
2. S.M. Mason, N. Conroy, M.N. Dixon and K.P.J. Williams, Spectrochimica Acta, 49A, 633, (1993).
3. D.M. Adams, S.J. Payne and K. Martin, Appl. Spectroscopy., 27, 377, (1973)
4. Dr. D.M. Adams, Diacell Products, 54, Ash Tree Road, Oadby, Leicester. LE2 5TD, England.
5. R.A. Forman, G.J. Piermarini, J.D. Barnett and S. Block, Science., 176, 284 (1972)
6. G.J. Piermarini, S. Block, J.D. Barnett and R.A. Forman, J. Appl. Phys., 46, 2774 (1975)
7. D.M. Adams, R. Appleby and S.K. Sharma, J. Phys E., 9, 1140 (1976)
8. P.T.T. Wong, D.J. Moffat and F.L. Baudais, Appl. Spectrosc., 39, 733 (1985)
9. P.T.T. Wong, Vibrational Spectra and Structure, 16, 357 (1987)
10. P.T.T. Wong, in "High Pressure Chemistry and Biochemistry, R. van Eldik and J. Jonas, Eds., 381-400, D. Reidel, Amsterdam, (1987)
11. P.T.T. Wong, D.J. Siminovitch and H.H. Mantsch, Biochim. Biophys. Acta, 947, 139 (1988)
12. M. Auger, H.C. Jarrell, I.C.P. Smith, D.J. Siminovitch, H.H. Mantsch and P.T.T. Wong, Biochemistry, 27, 6086 (1988)
13. P.T.T. Wong, T.E. Chagwedera and H.H. Mantsch, J. Chem. Phys., 87, 4487 (1987)
14. P.T.T. Wong and H.H. Mantsch, Chem. Phys. Lipids., 46, 213 (1988)
15. P.T.T. Wong and H.H. Mantsch, Biophys. J. ,54, 781 (1988)
16. D.J. Siminovitch, P.T.T. Wong and H.H. Mantsch, Chem. Phys. Lipids, 46, 79 (1988)
17. M. Auger, H.C. Jarrell, I.C.P. Smith, P.T.T. Wong, D.J. Siminovitch and H.H. Mantsch, Biochemistry, 26, 8513 (1987)
18. P.T.T. Wong and H.H. Mantsch, J. Colloid and Interf. Sci., 129, 258 (1989)
19. P.T.T. Wong and C. Huang, Biochemistry, 28, 1259 (1989)
20. D.D. Klug and E. Whalley, Rev. Sci. Instrum., 54, 1205 (1983)
21. C.W.F.T. Pirtorius, Progress Solid State Chem., 11, 77 (1976)

CHAPTER 4

Introduction to Results

The following four chapters summarise all the results obtained for the work in this thesis.

The Raman data were obtained on the Ramascope using a slit width of $3cm^{-1}$ and exposure times varying between 180 and 360 seconds depending on the relevant signal to noise ratio. The isotropic spectra were computed from the polarised and depolarised spectra using the relationship $I_{iso} = I_{VV} - \frac{4}{3} I_{VH}$ (see chapter 2), and the I_{VH} spectra were taken to be the anisotropic part of the spectrum.

For the mid infra red spectra, water vapour subtraction was performed where necessary. All peak frequencies and bandwidths (Full Width at Half Maximum Height, FWHM) were measured by hand on plotted out spectra. All the major bands had relative intensities calculated where possible, or relative absorbances, i.e. peak heights, calculated when band overlap prevented intensity measurements. Only the calculations exhibiting some change are mentioned in the text. When correlation times are quoted, the slit function has not been removed.

Errors were estimated against spectral resolution, signal to noise ratio and reproducibility. For all the relative intensity measurements, an error of approximately 6% was apparent whilst for the relative absorbance measurements, this rose to 7%. Other errors are quoted in the relevant text.

As mentioned previously, this work was devised primarily with the intention of deducing how molecular interactions and dynamics effect the bulk fluid properties of bis(cyclohexyl) succinate, BCS (figure 1.8). To assist with the interpretation, other related molecules were also studied (figure 4.1).

Figures 4.2-17 display the Raman isotropic and anisotropic, and the mid infra red spectra of all the molecules shown in figure 4.1. The position of the major bands for each molecule are listed in tables 4.1-6, along with assignments from the literature[1-3].In all cases the units for the Raman shift are wavenumbers.

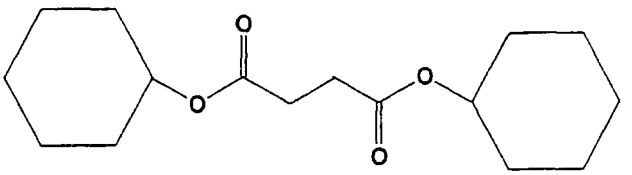

Bis(cyclohexyl) Succinate, BCS

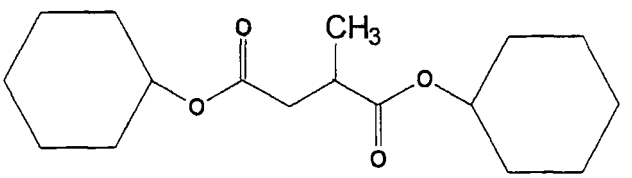

Bis(cyclohexyl)-2-Methyl Succinate, BC2MS

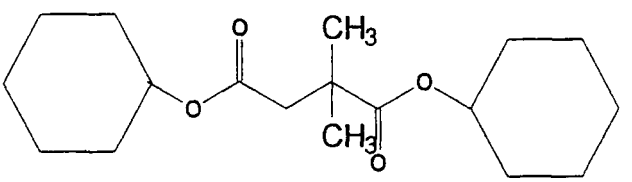

Bis(cyclohexyl)-2,2-Dimethyl Succinate, BC22DMS

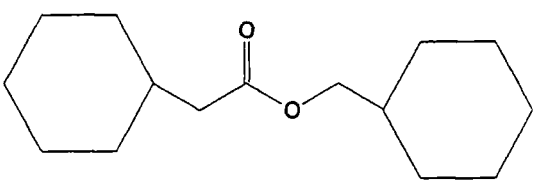

Cyclohexyl Methyl Cyclohexyl Acetate, CMCA

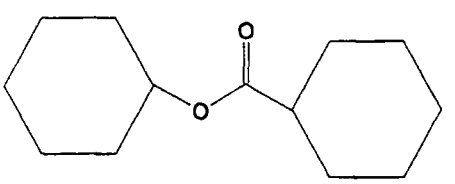

Cyclohexyl Cyclohexane Carboxylate, CCC

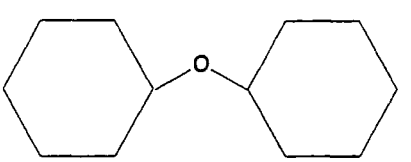

Biscyclohexyl Ether, BCE

Figure 4.1. BCS and related molecules.

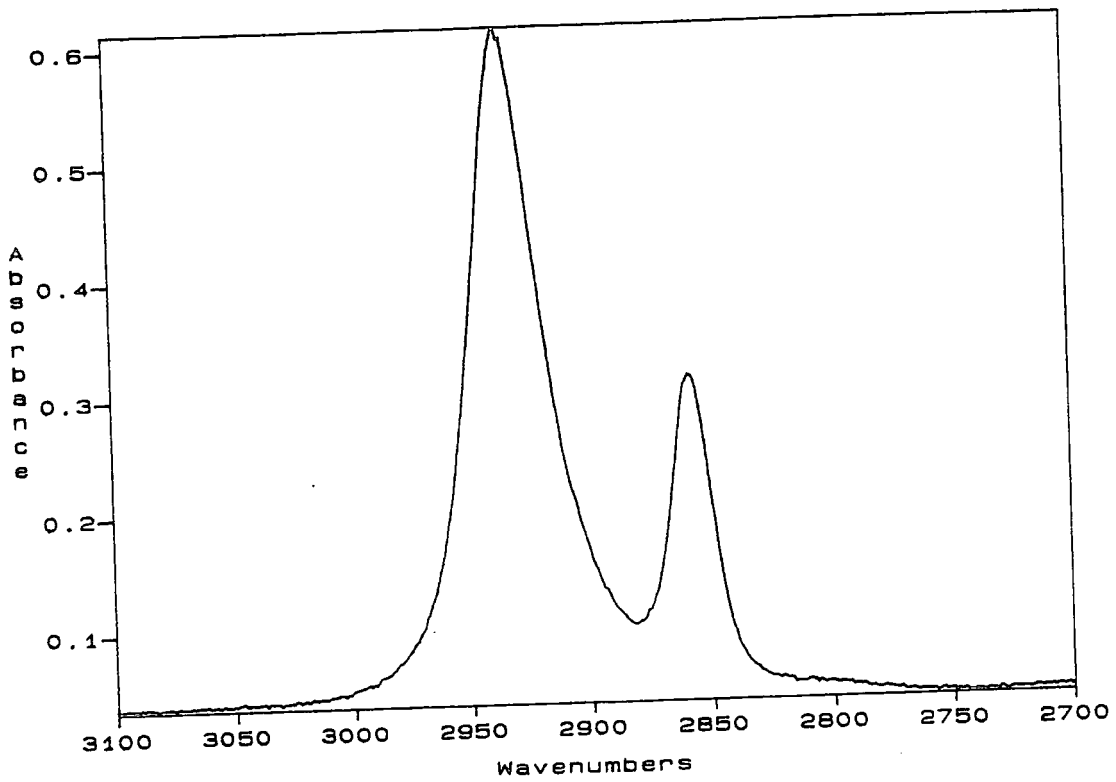

Figure 4.2. 3100-2800cm^{-1} region of the infra red spectrum of bis(cyclohexyl) succinate, BCS.

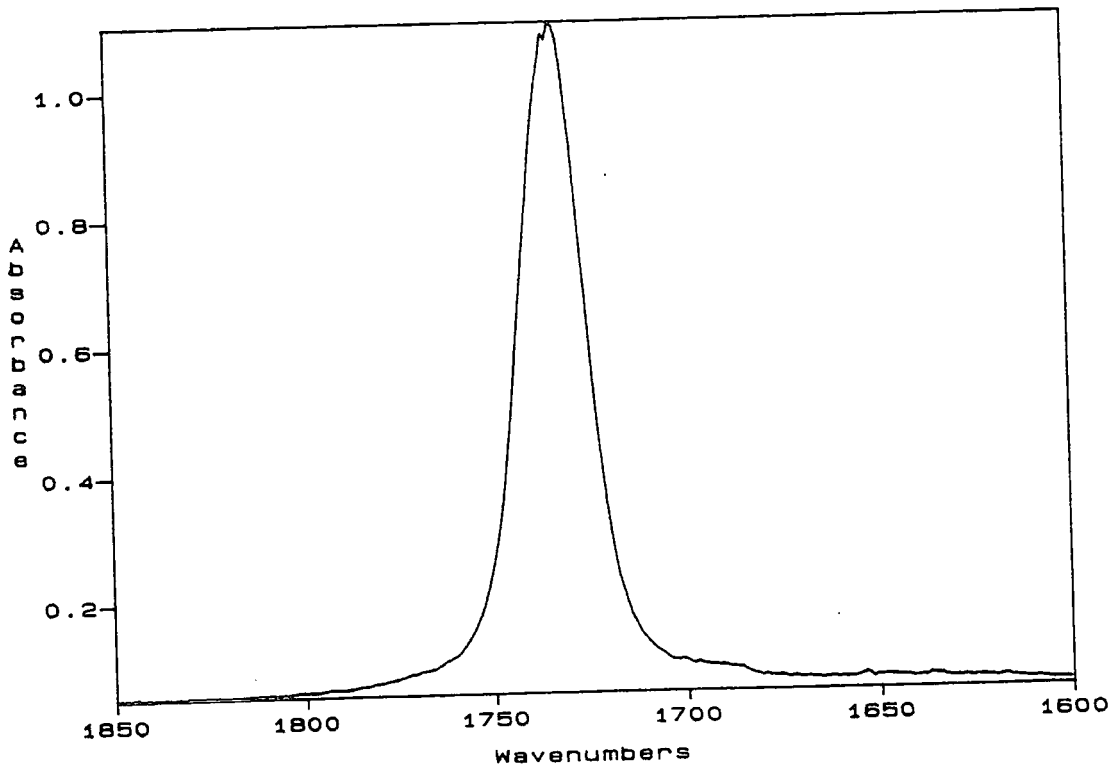

Figure 4.3. 1850-1600cm^{-1} region of the infra red spectrum of bis(cyclohexyl) succinate, BCS.

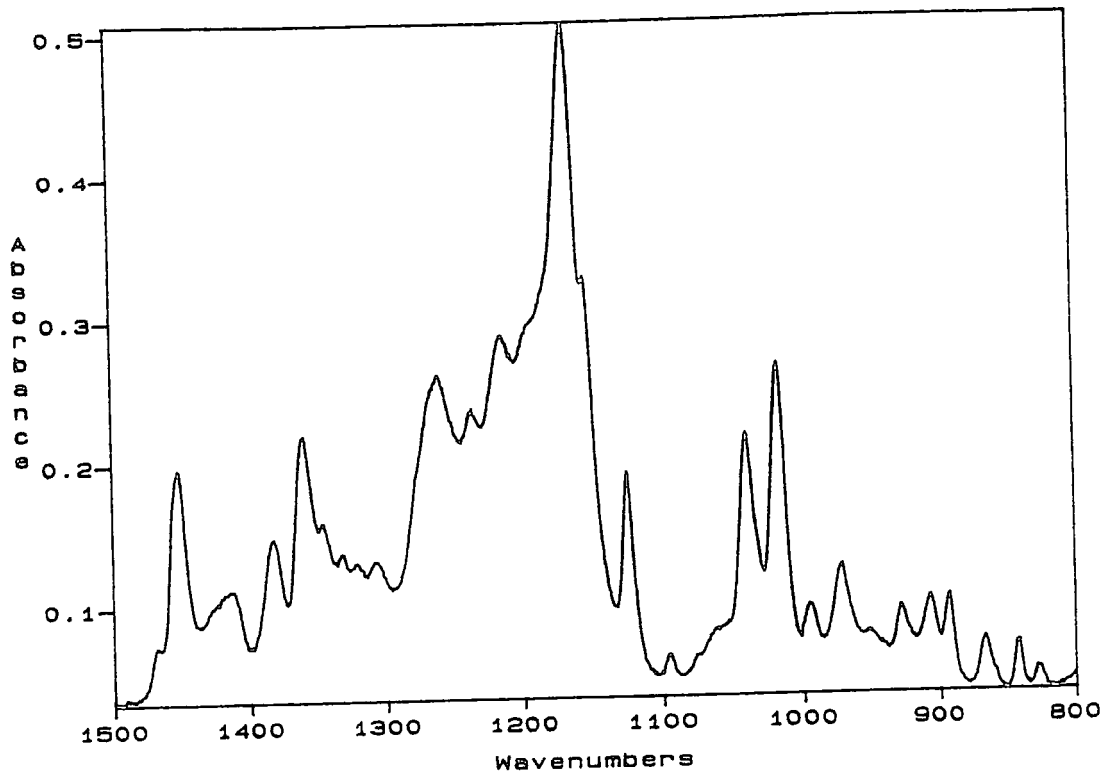

Figure 4.4. 1600-800cm^{-1} region of the infra red spectrum of bis(cyclohexyl) succinate, BCS.

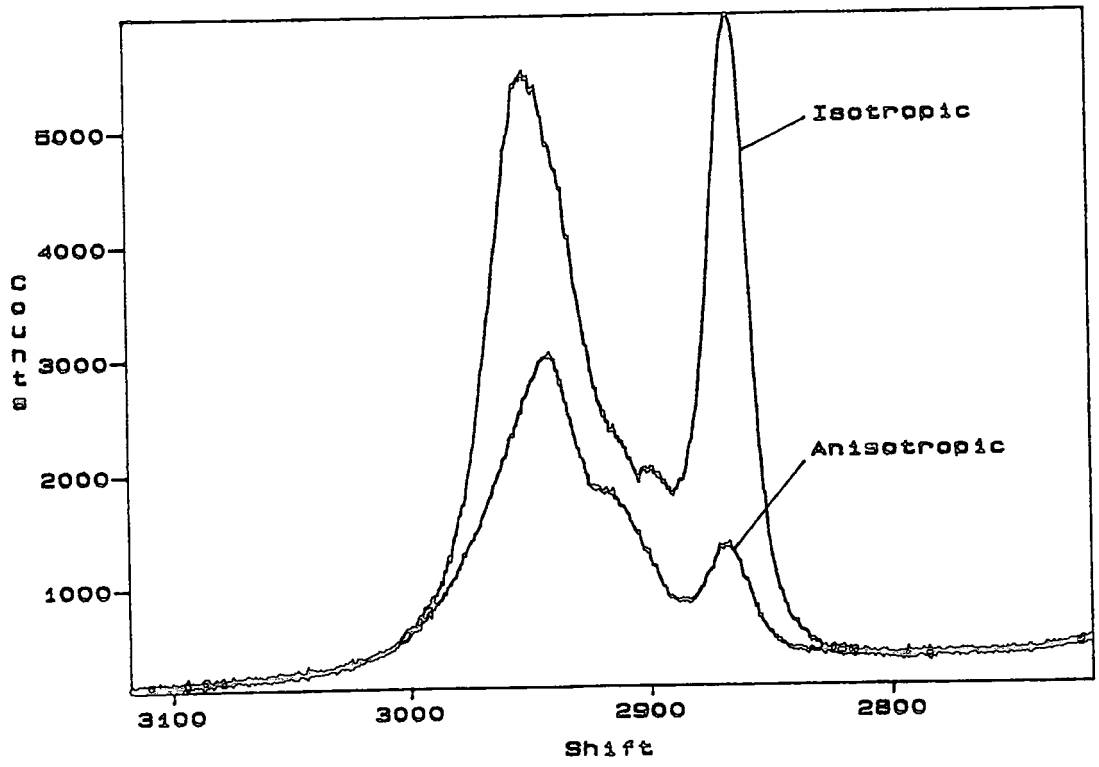

Figure 4.5. 3100-2700cm-1 region of the isotropic and anisotropic Raman spectra of bis(cyclohexyl) succinate, BCS.

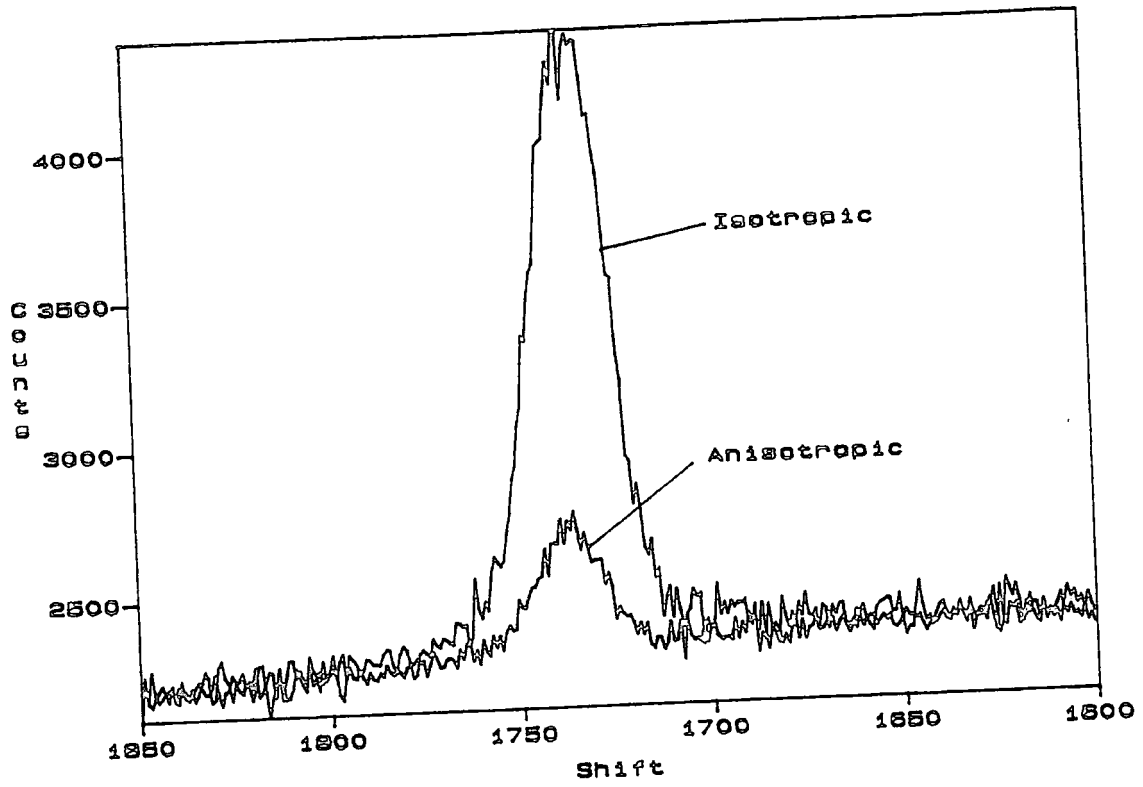

Figure 4.6. 1850-1600cm-1 region of the isotropic and anisotropic Raman spectra of bis(cyclohexyl) succinate, BCS.

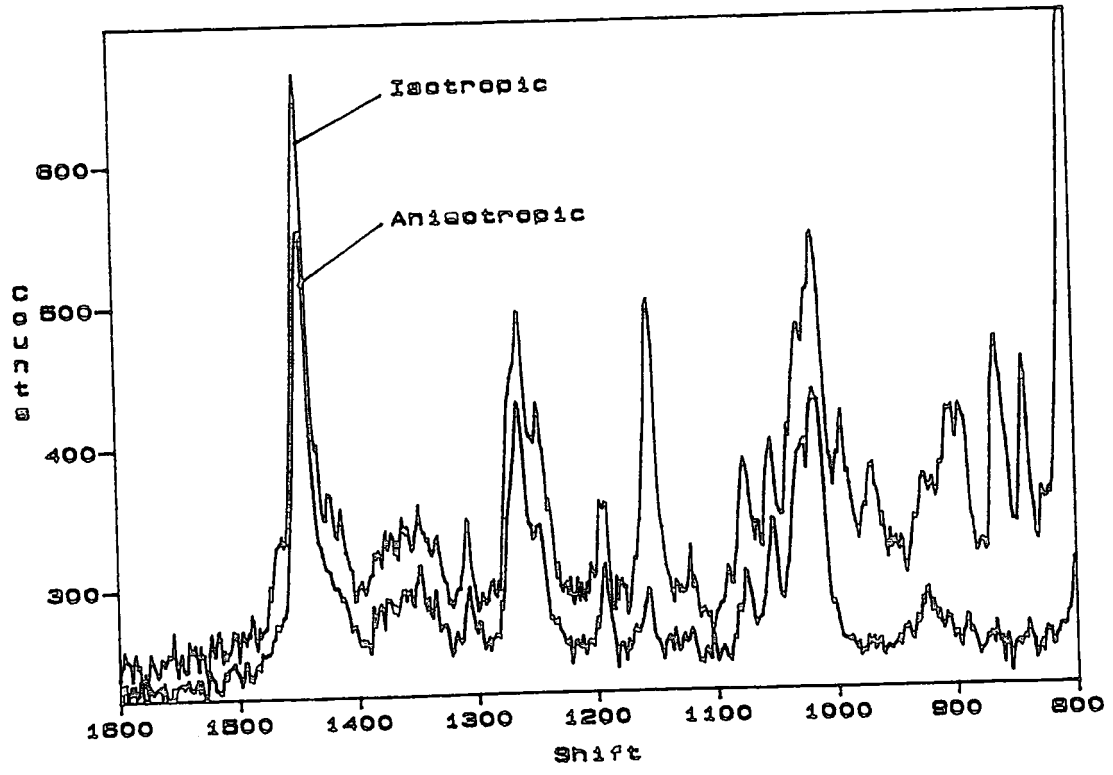

Figure 4.7. 1600-800cm-1 region of the isotropic and anisotropic Raman spectra of bis(cyclohexyl) succinate, BCS.

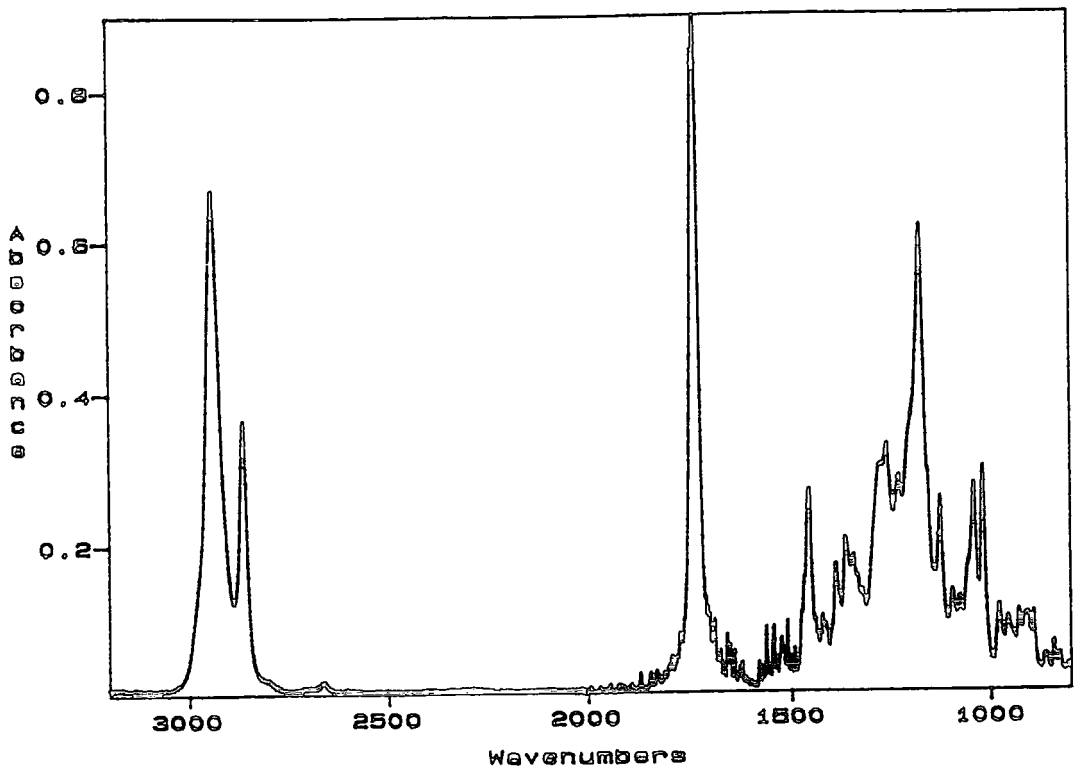

Figure 4.8. Infra red spectrum of bis(cyclohexyl)-2-methyl succinate, BC2MS

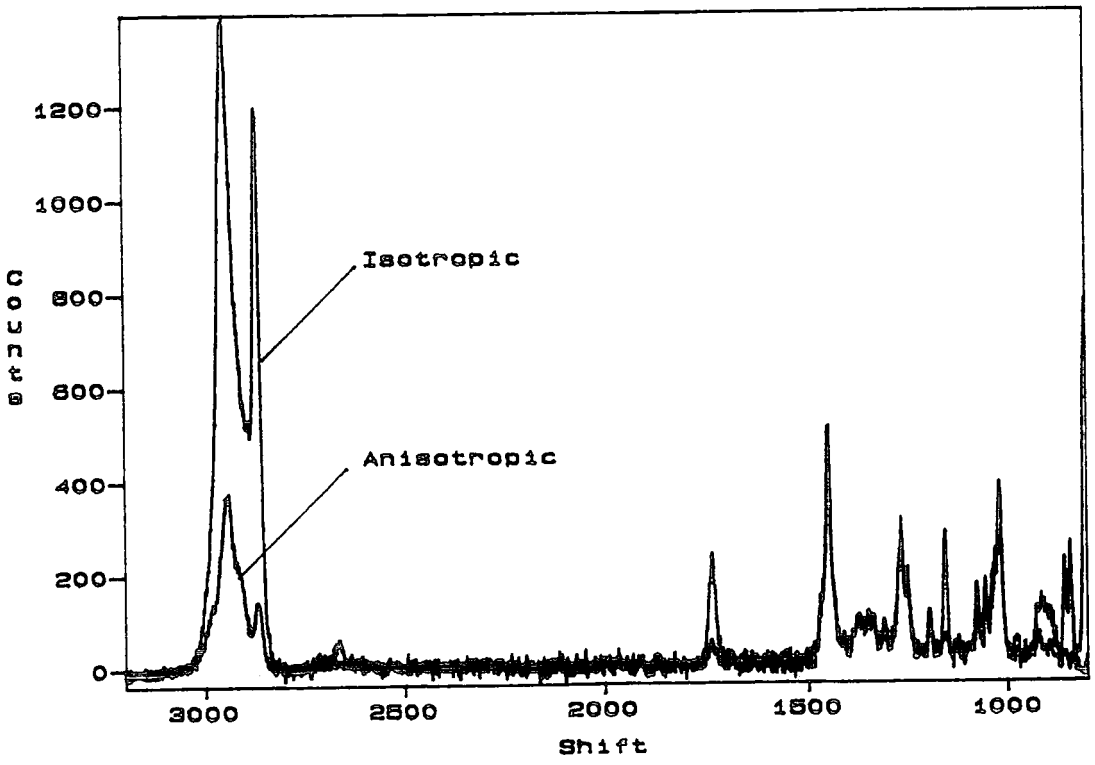

Figure 4.9. Isotropic and anisotropic Raman spectra of bis(cyclohexyl)-2-methyl succinate, BC2MS

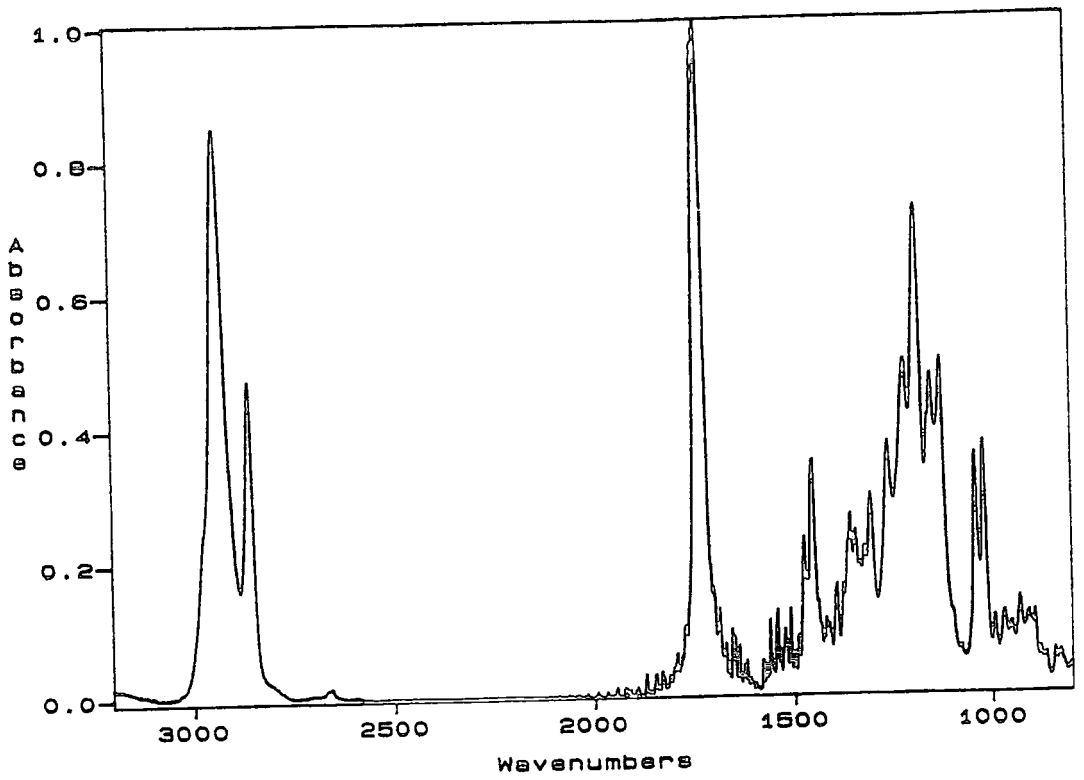

Figure 4.10. Infra red spectrum of bis(cyclohexyl)-2,2-dimethyl succinate, BC22DMS

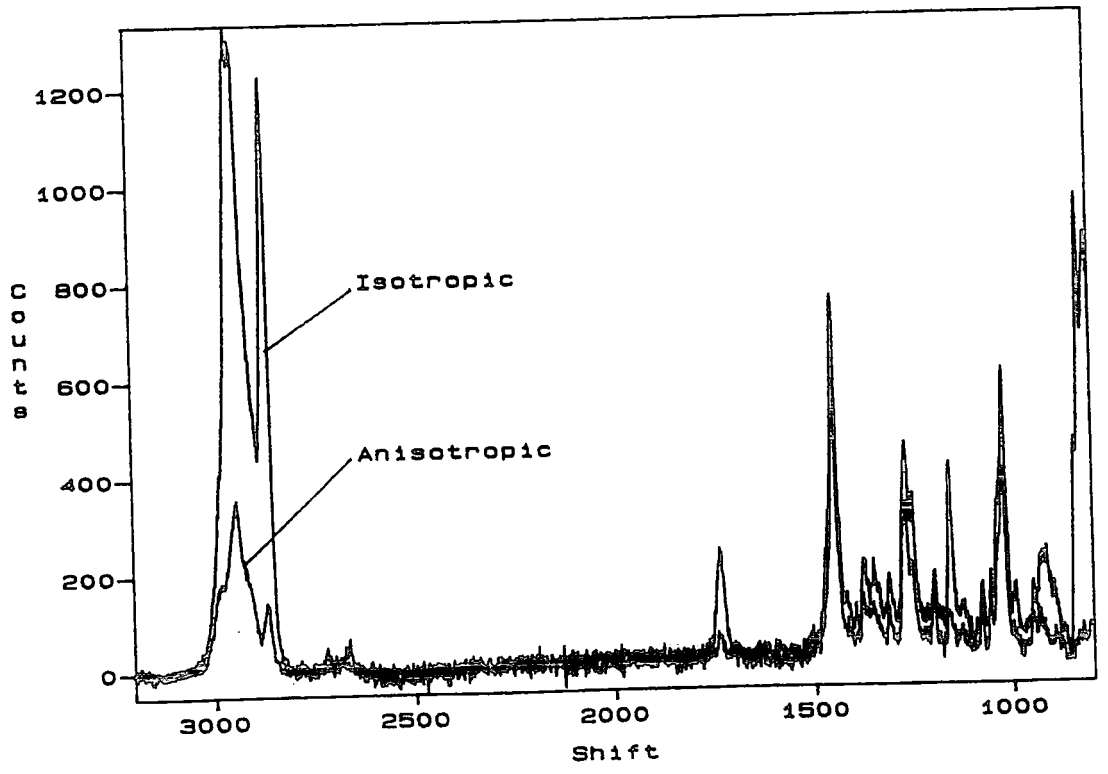

Figure 4.11. Isotropic and anisotropic Raman spectra of bis(cyclohexyl)-2,2-dimethyl succinate, BC22DMS

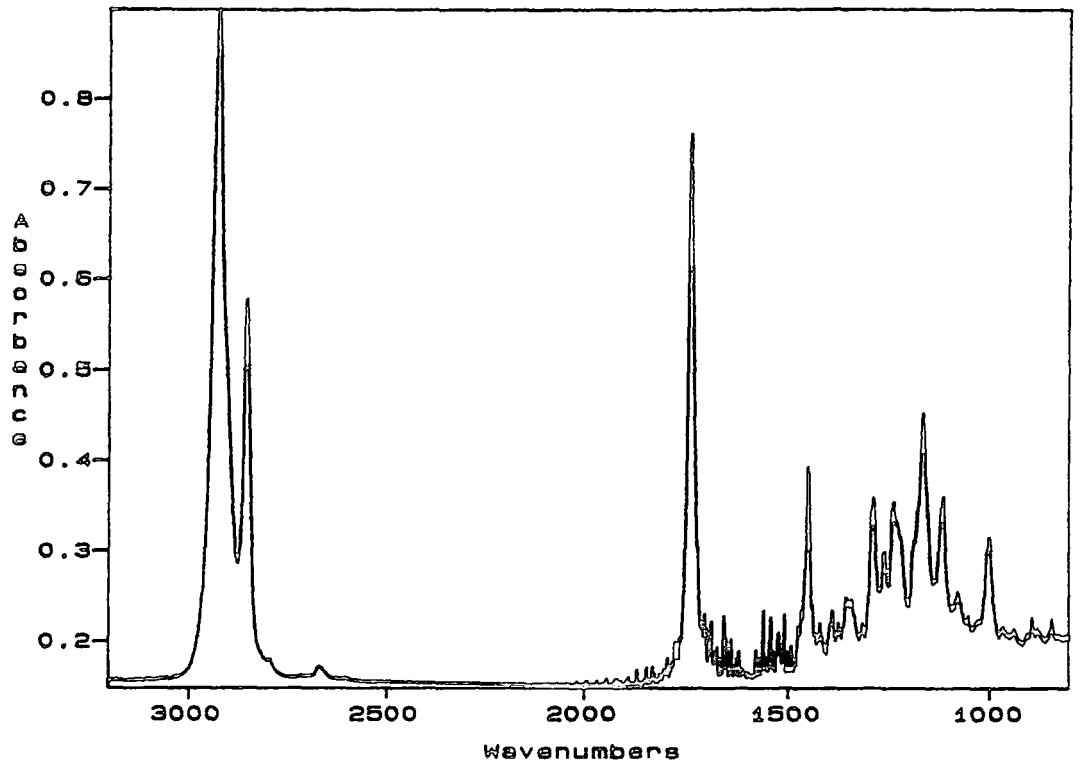

Figure 4.12. Infra red spectrum of cyclohexyl methyl cyclohexyl acetate, CMCA.

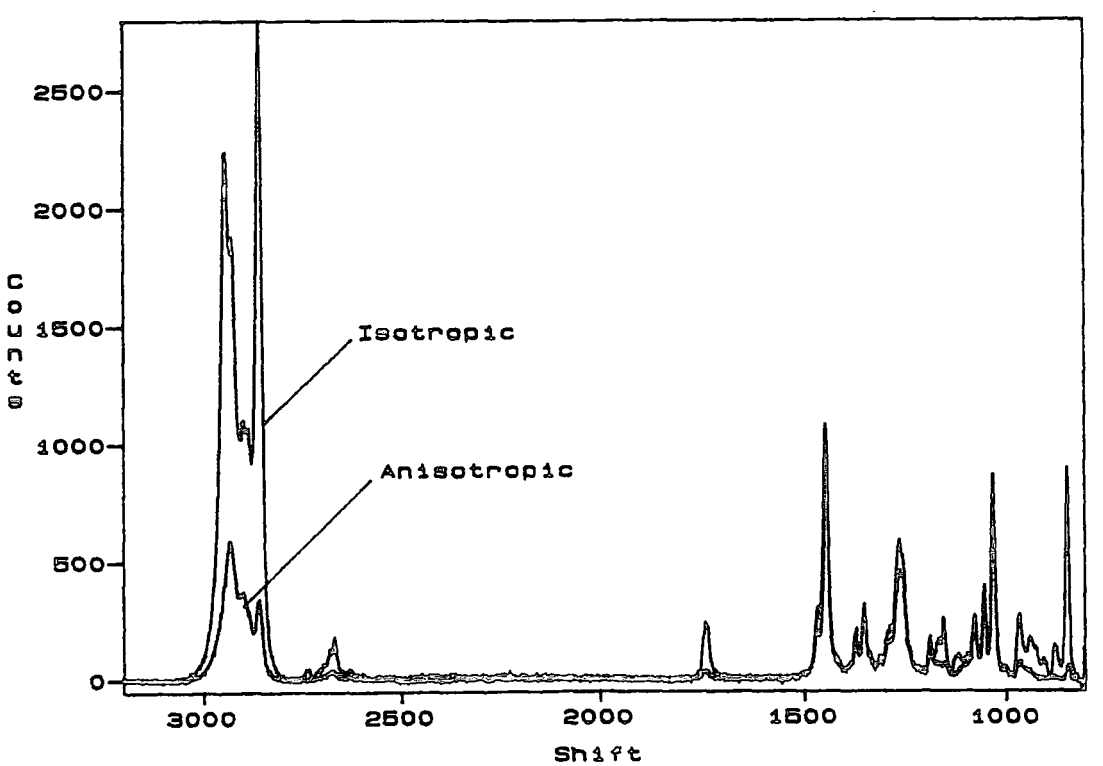

Figure 4.13. Isotropic and anisotropic Raman spectra of cyclohexyl methyl cyclohexyl acetate, CMCA.

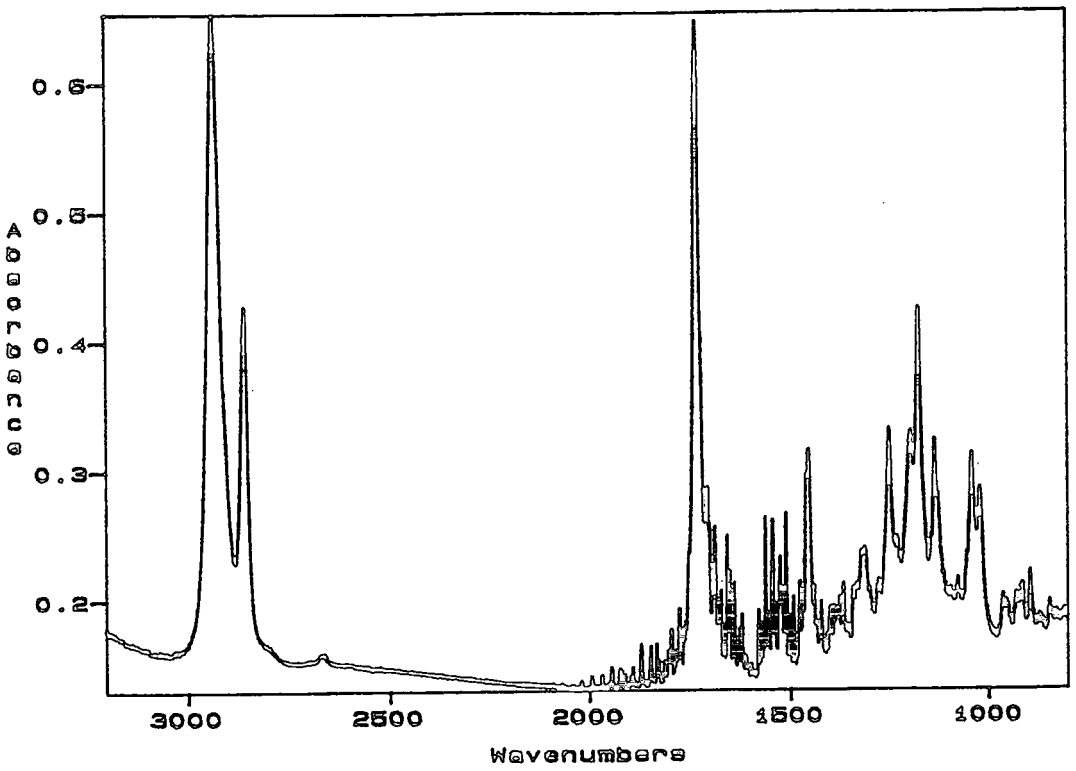

Figure 4.14. Infra red spectrum of cyclohexyl cyclohexane carboxylate, CCC.

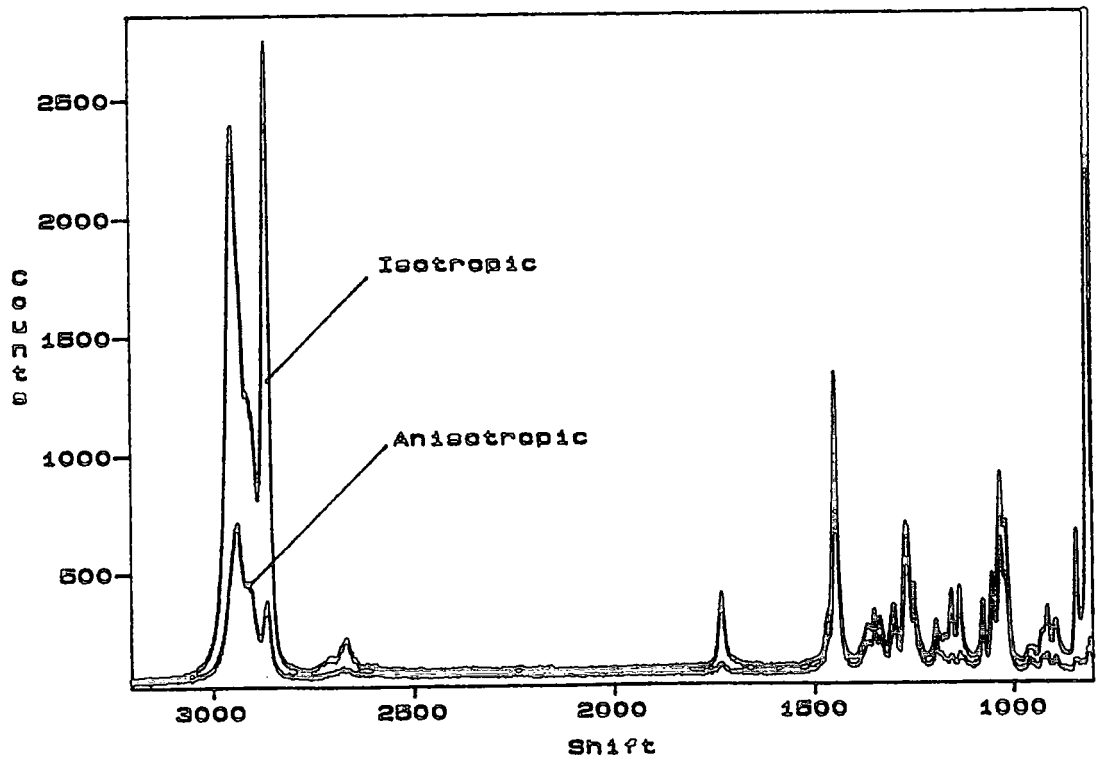

Figure 4.15. Isotropic and anisotropic Raman spectra of cyclohexyl cyclohexane carboxylate, CCC.

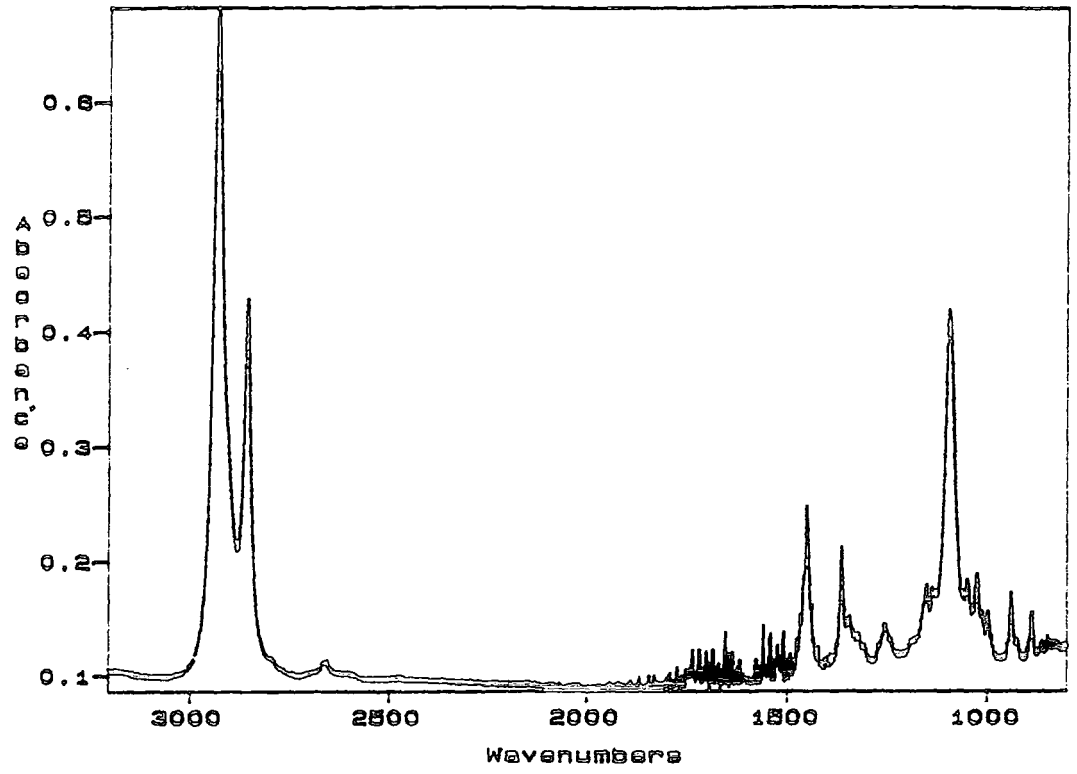

Figure 4.16. Infra red spectrum of Biscyclohexyl Ether BCE.

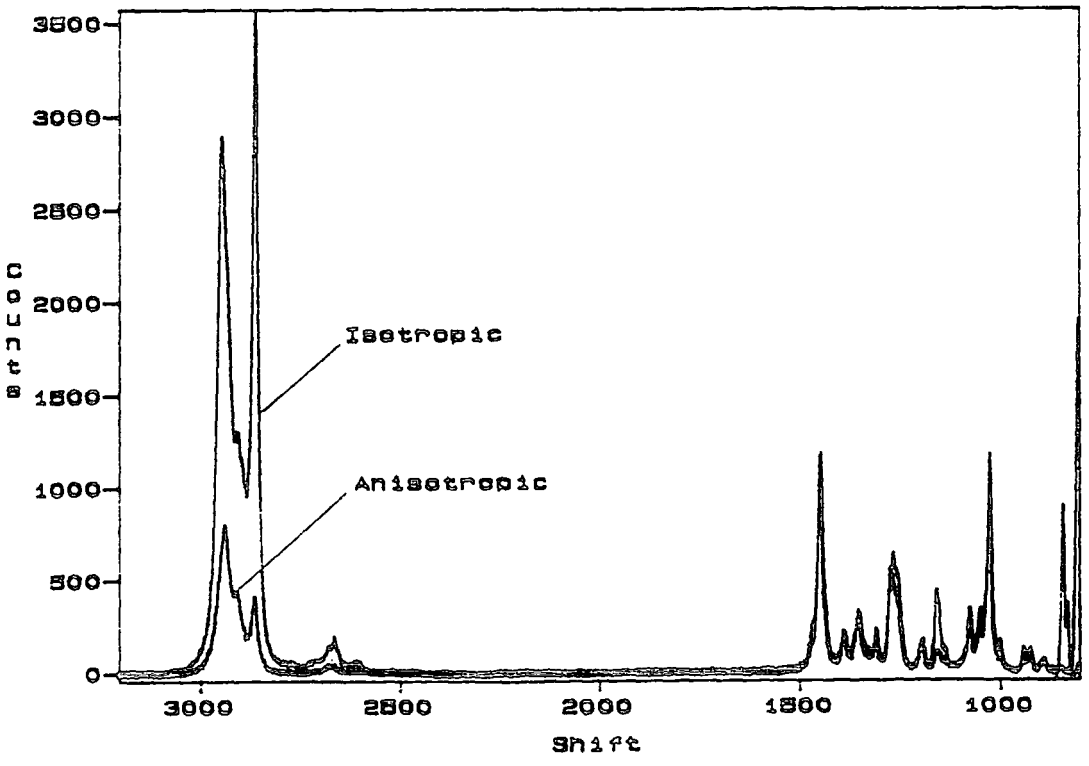

Figure 4.17. Isotropic and anisotropic Raman spectra of Biscyclohexyl Ether. BCE.

Table 4.1. Major bands and assignments for vibrational spectra of Bis(cyclohexyl) Succinate, BCS.

Frequency cm^{-1}		Functional Group	Symbol	Description
Raman	IR			
2944	2938	$-CH_2-$	$\nu_{as}(CH_2)$	Antisymmetric C-H Stretch
2864	2860	$-CH_2-$	$\nu_s(CH_2)$	Symmetric C-H Stretch
1735	1733	-C=O	$\nu_s(C=O)$	Carbonyl Stretch
1446	1451	$-CH_2-$	$\delta_s(CH_2)$ring	Symmetric C-H Bending of the cyclohexyl ring
1264	1261	$-CH_2-$	$\nu(CH_2)$	C-H Deformation
1153	1166	-C-O-	ν(C-O)	Skeletal C-O Stretch Ester
1079	1096	$-CH_2-$	$\nu(CH_2)$	C-H Deformation
1053	1041	-C-O-	ν(C-O)	Skeletal C-O Stretch
1019	1018	-C-O-	ν(C-O)	Skeletal C-O Stretch
	907	$-CH_2-$	$\nu(CH_2)$	C-H Rocking
866	866	-C-C-	ν(C-C)	Skeletal C-C Stretch
802	801	-C-C-	ν(C-C)	Skeletal C-C Stretch

Table 4.2. Major bands and assignments for vibrational spectra of bis(cyclohexyl)-2-Methyl Succinate, BC2MS

Frequency cm^{-1}		Functional Group	Symbol	Description
Raman	IR			
2946	2937	$-CH_2-$	$\nu_{as}(CH_2)$	Antisymmetric C-H Stretch
2866	2860	$-CH_2-$	$\nu_s(CH_2)$	Symmetric C-H Stretch
1741	1733	-C=O	$\nu_s(C=O)$	Carbonyl Stretch
1448	1453	$-CH_2-$	$\delta_s(CH_2)$ring	Symmetric C-H Bending of the cyclohexyl ring
1263	1258	$-CH_2-$	$\nu(CH_2)$	C-H Deformation
1153	1173	-C-O-	ν(C-O)	Skeletal C-O Stretch Ester
1074	1096	$-CH_2-$	$\nu(CH_2)$	C-H Deformation
1054	1039	-C-O-	ν(C-O)	Skeletal C-O Stretch
1017	1017	-C-O-	ν(C-O)	Skeletal C-O Stretch
	908	$-CH_2-$	$\nu(CH_2)$	C-H Rocking
865	864	-C-C-	ν(C-C)	Skeletal C-C Stretch
801	801	-C-C-	ν(C-C)	Skeletal C-C Stretch

Table 4.3. Major bands and assignments for vibrational spectra of bis(cyclohexyl)-2,2-Dimethyl Succinate, BC22DMS

Frequency cm^{-1}		Functional Group	Symbol	Description
Raman	IR			
2943	2937	$-CH_2-$	$\nu_{as}(CH_2)$	Antisymmetric C-H Stretch
2866	2860	$-CH_2-$	$\nu_s(CH_2)$	Symmetric C-H Stretch
1735	1731	-C=O	$\nu_s(C=O)$	Carbonyl Stretch
1448	1453	$-CH_2-$	$\delta_s(CH_2)$ring	Symmetric C-H Bending of the cyclohexyl ring
1264	1257	$-CH_2-$	$\nu(CH_2)$	C-H Deformation
1153	1183	-C-O-	ν(C-O)	Skeletal C-O Stretch Ester
1076	1096	$-CH_2-$	$\nu(CH_2)$	C-H Deformation
1053	1041	-C-O-	ν(C-O)	Skeletal C-O Stretch
1019	1019	-C-O-	ν(C-O)	Skeletal C-O Stretch
	907	$-CH_2-$	$\nu(CH_2)$	C-H Rocking
866	864	-C-C-	ν(C-C)	Skeletal C-C Stretch
805	801	-C-C-	ν(C-C)	Skeletal C-C Stretch

Table 4.4. Major bands and assignments for vibrational spectra of CMCA.

Frequency cm^{-1}		Functional Group	Symbol	Description
Raman	IR			
2944	2926	$-CH_2-$	$\nu_{as}(CH_2)$	Antisymmetric C-H Stretch
2864	2854	$-CH_2-$	$\nu_s(CH_2)$	Symmetric C-H Stretch
1735	1738	-C=O	$\nu_s(C=O)$	Carbonyl Stretch
1446	1452	$-CH_2-$	$\delta_s(CH_2)$ring	Symmetric C-H Bending of the cyclohexyl ring
1264	1262	$-CH_2-$	$\nu(CH_2)$	C-H Deformation
1153	1164	-C-O-	ν(C-O)	Skeletal C-O Stretch Ester
1079	1082	$-CH_2-$	$\nu(CH_2)$	C-H Deformation
1053	1032	-C-O-	ν(C-O)	Skeletal C-O Stretch
1019	1004	-C-O-	ν(C-O)	Skeletal C-O Stretch
	904	$-CH_2-$	$\nu(CH_2)$	C-H Rocking
866	866	-C-C-	ν(C-C)	Skeletal C-C Stretch
802	801	-C-C-	ν(C-C)	Skeletal C-C Stretch

Table 4.5. Major bands and assignments for vibrational spectra of CCC.

Frequency cm^{-1}		Functional Group	Symbol	Description
Raman	IR			
2948	2935	$-CH_2-$	$\nu_{as}(CH_2)$	Antisymmetric C-H Stretch
2864	2857	$-CH_2-$	$\nu_s(CH_2)$	Symmetric C-H Stretch
1729	1729	-C=O	$\nu_s(C=O)$	Carbonyl Stretch
1446	1452	$-CH_2-$	$\delta_s(CH_2)$ring	Symmetric C-H Bending of the cyclohexyl ring
1267	1276	$-CH_2-$	$\nu(CH_2)$	C-H Deformation
1153	1174	-C-O-	ν(C-O)	Skeletal C-O Stretch Ester
1074		$-CH_2-$	$\nu(CH_2)$	C-H Deformation
1053	1042	-C-O-	ν(C-O)	Skeletal C-O Stretch
1029	1021	-C-O-	ν(C-O)	Skeletal C-O Stretch
807	801	-C-C-	ν(C-C)	Skeletal C-C Stretch

Table 4.6. Major bands and assignments for vibrational spectra of BCE.

Frequency cm^{-1}		Functional	Symbol	Description
Raman	IR	Group		
2944	2931	$-CH_2-$	$\nu_{as}(CH_2)$	Antisymmetric C-H Stretch
2864	2857	$-CH_2-$	$\nu_s(CH_2)$	Symmetric C-H Stretch
1446	1451	$-CH_2-$	$\delta_s(CH_2)$ring	Symmetric C-H Bending of the cyclohexyl ring
1264	1256	$-CH_2-$	$\nu(CH_2)$	C-H Deformation
1153	1148	-C-O-	ν(C-O)	Skeletal C-O Stretch Ether
1079	1091	$-CH_2-$	$\nu(CH_2)$	C-H Deformation
1053	1041	-C-O-	ν(C-O)	Skeletal C-O Stretch
1019	1018	-C-O-	ν(C-O)	Skeletal C-O Stretch

References

1. F.R. Dolish. "Characteristic Raman Frequencies of Organic Compounds". Wiley and Sons, New York. (1974)

2. R.M. Silverstein, G.C. Bassler and T.C. Morrill, "Spectrometric Identification of Organic Compounds". Wiley and Sons, New York (1981)

3. L.J. Bellamy, "The Infra red Spectra of Complex Molecules", Third Edition, Chapman and Hall, London (1975)

CHAPTER 5

Variable Temperature Studies

5.1 Introduction

High temperature infra-red spectra of BCS and all the related molecules (see figure 4.1) were recorded using the apparatus described in 3.2. On viewing the spectra shown in figures 5.1-5.3, it is apparent that little change in peak frequency is observed, but there appears to be some change in band widths (i.e. Full Width at Half Maximum Height, FWHM), and the carbonyl band for BCS exhibits a large change in band shape. (figure 5.7). Tables 5.1-5.6 summarise the spectral details.

Table 5.1 FWHM for BCS
*Due to overlapping bands, the full width at 3/4's maximum height was measured.

Temperature °C	$\nu_a(CH_2)$ $cm^{-1}\pm0.5cm^{-1}$	$\nu_s(CH_2)$ $cm^{-1}\pm0.5cm^{-1}$	$\nu(C=O)$ $cm^{-1}\pm0.5cm^{-1}$	$\nu(C-O)$* $cm^{-1}\pm0.5cm^{-1}$
25	42.2	23.4	26.6	22.2
50	42.2	25.0	27.6	23.3
60	42.2	25.0	27.6	25.4
70	42.2	25.0	28.5	26.7
80	42.2	25.0	28.5	28.9
90	40.6	25.0	28.5	27.8
100	40.6	25.0	28.5	27.8
110	40.6	25.0	28.5	28.9
120	40.6	25.0	25.6	31.1
130	40.6	25.0	25.6	31.1
140	40.6	26.6	25.6	31.1
150	40.6	26.6	25.6	33.3

Table 5.2 FWHM for BC2MS.
*Due to overlapping bands, the full width at 3/4's maximum height was measured.

Temperature °C	$\nu_a(CH_2)$ $cm^{-1}\pm0.5cm^{-1}$	$\nu_s(CH_2)$ $cm^{-1}\pm0.5cm^{-1}$	$\nu(C=O)$ $cm^{-1}\pm0.5cm^{-1}$	$\nu(C-O)$* $cm^{-1}\pm0.5cm^{-1}$
25	40.6	23.4	25.6	20.0
50	39.1	23.4	25.6	20.0
60	39.1	23.4	25.6	20.0
70	39.1	23.4	25.6	22.2
80	39.1	23.4	25.6	22.2
90	39.1	23.4	25.6	22.2
100	39.1	23.4	25.6	22.2
110	39.1	23.4	25.6	22.2
120	39.1	25.0	25.6	22.2
130	39.1	25.0	25.6	25.4
140	39.1	25.0	25.6	25.4
150	39.1	25.0	25.6	25.4

Table 5.3 FWHM for BC22DMS.
*Due to overlapping bands, the full width at 3/4's maximum height was measured.

Temperature °C	$\nu_a(CH_2)$ $cm^{-1}\pm0.5cm^{-1}$	$\nu_s(CH_2)$ $cm^{-1}\pm0.5cm^{-1}$	$\nu(C=O)$ $cm^{-1}\pm0.5cm^{-1}$	$\nu(C-O)$* $cm^{-1}\pm0.5cm^{-1}$
25	43.8	25.0	30.5	20.0
50	43.8	25.0	31.5	22.2
60	46.9	26.6	33.5	22.2
70	46.9	26.6	33.5	22.2
80	45.3	26.6	33.5	22.2
90	45.3	26.6	32.5	25.4
100	43.8	26.6	32.5	25.4
110	43.8	26.6	31.5	25.4
120	42.2	26.6	31.5	25.4
130	42.2	26.6	31.5	25.4
140	42.2	26.6	31.5	25.4
150	42.2	26.6	31.5	26.7

Table 5.4 FWHM for CMCA
*Due to overlapping bands, the full width at 3/4's maximum height was measured.

Temperature °C	$\nu_a(CH_2)$ $cm^{-1}\pm0.5cm^{-1}$	$\nu_s(CH_2)$ $cm^{-1}\pm0.5cm^{-1}$	$\nu(C=O)$ $cm^{-1}\pm0.5cm^{-1}$	$\nu(C-O)$* $cm^{-1}\pm0.5cm^{-1}$
25	39.1	21.9	17.7	13.3
50	39.1	21.9	18.7	15.6
60	39.1	21.9	18.7	15.6
70	40.6	21.9	18.7	15.6
80	40.6	21.9	17.7	17.8
90	40.6	21.9	19.7	17.8
100	40.6	23.4	19.7	17.8
110	40.6	23.4	19.7	17.8
120	40.6	23.4	19.7	17.8
130	40.6	23.4	19.7	17.8
140	40.6	23.4	19.7	22.2
150	40.6	23.4	20.7	22.2

Table 5.5 FWHM for CCC

*Due to overlapping bands, the full width at 3/4's maximum height was measured.

Temperature °C	$\nu_a(CH_2)$ $cm^{-1}\pm0.5cm^{-1}$	$\nu_s(CH_2)$ $cm^{-1}\pm0.5cm^{-1}$	$\nu(C=O)$ $cm^{-1}\pm0.5cm^{-1}$	$\nu(C-O)$* $cm^{-1}\pm0.5cm^{-1}$
25	55.1	23.6	21.0	13.3
50	49.2	23.6	20.4	13.3
60	47.2	23.6	20.4	13.3
70	46.3	23.6	20.4	13.3
80	45.3	23.6	19.8	13.3
90	43.3	23.6	19.8	13.3
100	42.3	23.6	19.1	13.3
110	41.3	25.6	19.8	13.3
120	40.4	25.6	19.8	13.3
130	43.3	25.6	20.4	15.6
140	43.3	26.6	20.4	17.8
150	43.3	27.6	21.0	17.8

Table 5.6 FWHM for BCE

Temperature °C	$\nu_a(CH_2)$ $cm^{-1}\pm0.5cm^{-1}$	$\nu_s(CH_2)$ $cm^{-1}\pm0.5cm^{-1}$
25	32.8	23.4
50	32.8	23.4
60	32.8	23.4
70	32.8	25.0
80	32.8	25.0
90	32.8	25.0
100	32.8	25.0
110	32.8	26.6
120	32.8	26.6
130	32.8	26.6
140	32.8	28.1
150	32.8	28.1

5.2 Results

5.2.1. Bandwidths

5.2.1.1. CH_2 Stretching Region

From table 5.1. and figure 5.1. it can be seen that the width of the antisymmetric stretching band decreases, while that of the symmetric band increases. On adding a branching methyl group to the internal hydrocarbon chain, this broadening and narrowing is still apparent, but the changes are not as great. (table 5.2 and figure5.2) A similar observation follows for the dimethyl compound (table 5.3. and figure 5.3).

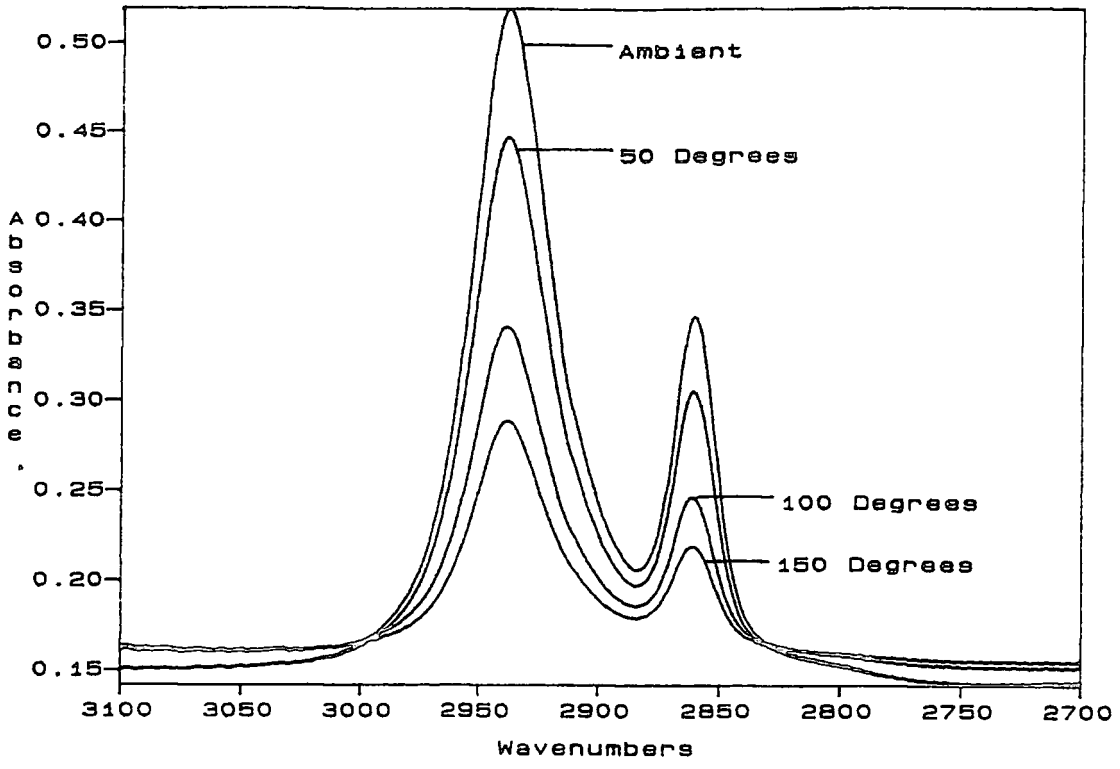

Figure 5.1. CH_2 stretching region for BCS with increasing temperature.

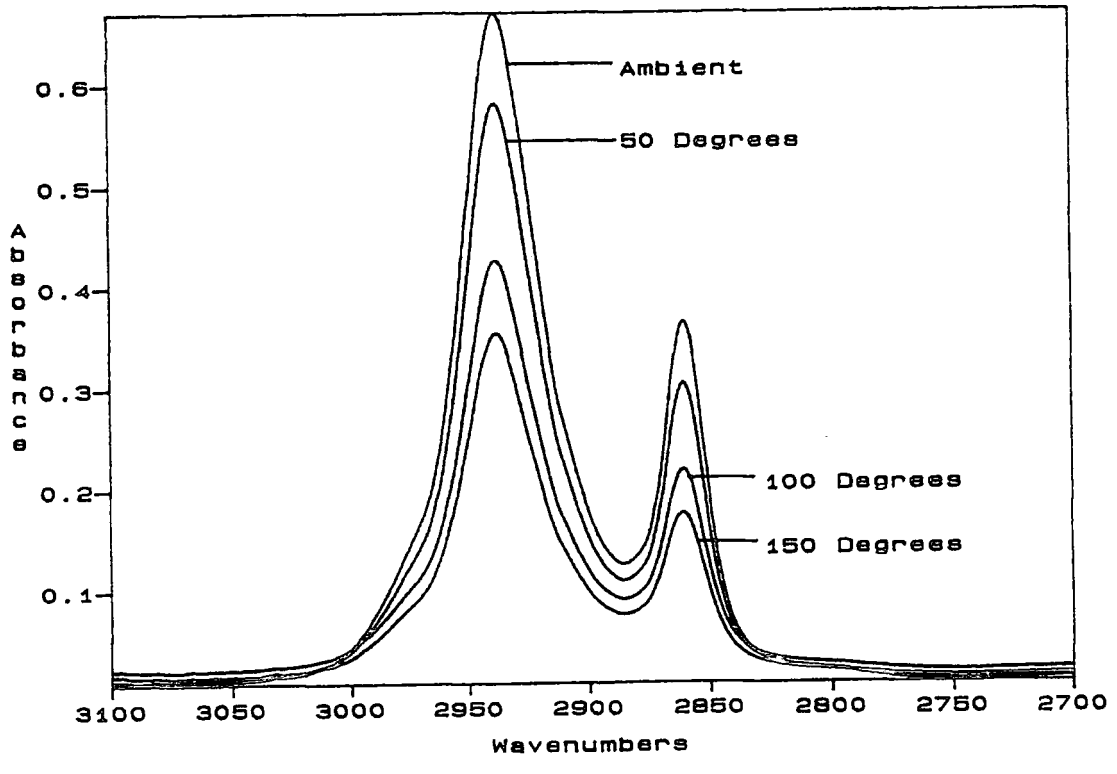

Figure 5.2. CH_2 stretching region for BC2MS with increasing temperature.

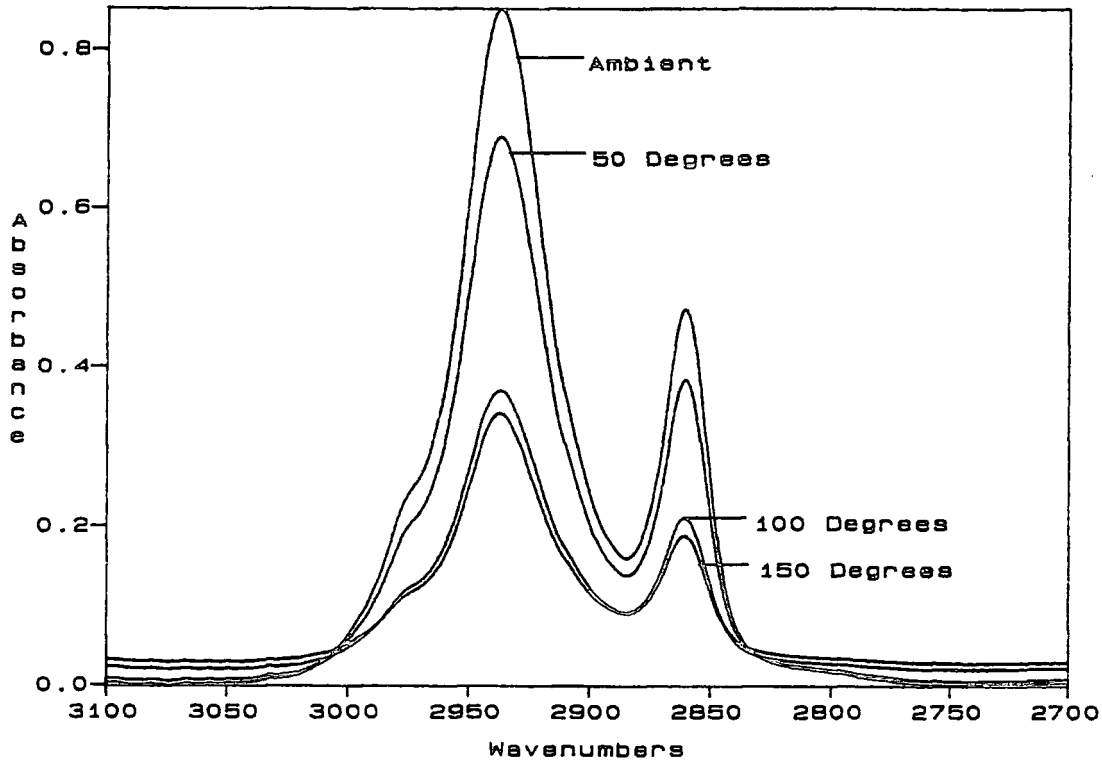

Figure 5.3. CH_2 stretching region for BC22DMS with increasing temperature.

The compounds with only one ester group show similar behaviour, with the most dramatic change being observed for CCC (figure5.4), whose antisymmetric stretching mode decreases by 10.8cm^{-1} while the symmetric mode increases by 4cm^{-1}.

The graph of relative intensities of the CH_2 stretching region compared to the carbonyl stretching region shows a negative gradient for all the molecules with the change for CCC being the greatest (figure 5.5). On ratioing peak heights, a positive gradient was observed when ratioing the antisymmetric CH_2 stretching region against the symmetric CH_2 stretch stretching region with CCC showing the largest change. (figure 5.6) Similar behaviour is seen when ratioing the antisymmetric stretching region against the CH_2 ring scissors mode and the ester stretching region with, once again, the largest change being exhibited by CCC.

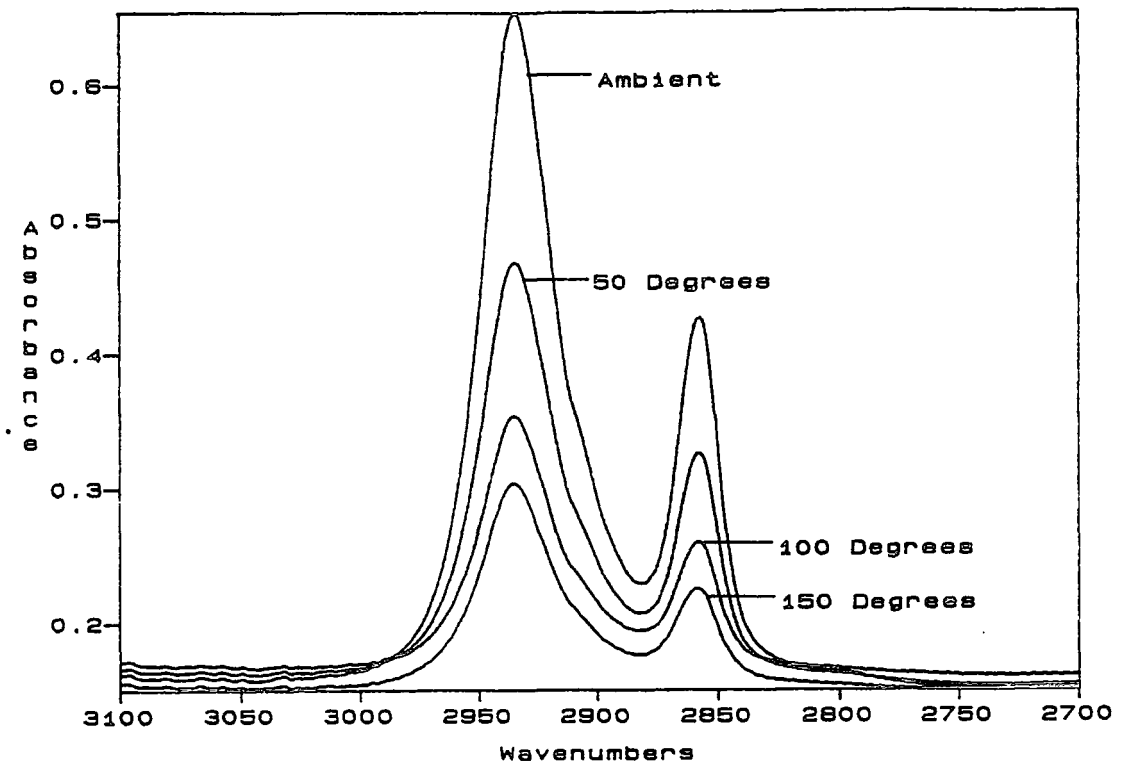

Figure 5.4. CH_2 stretching region for CCC with increasing temperature.

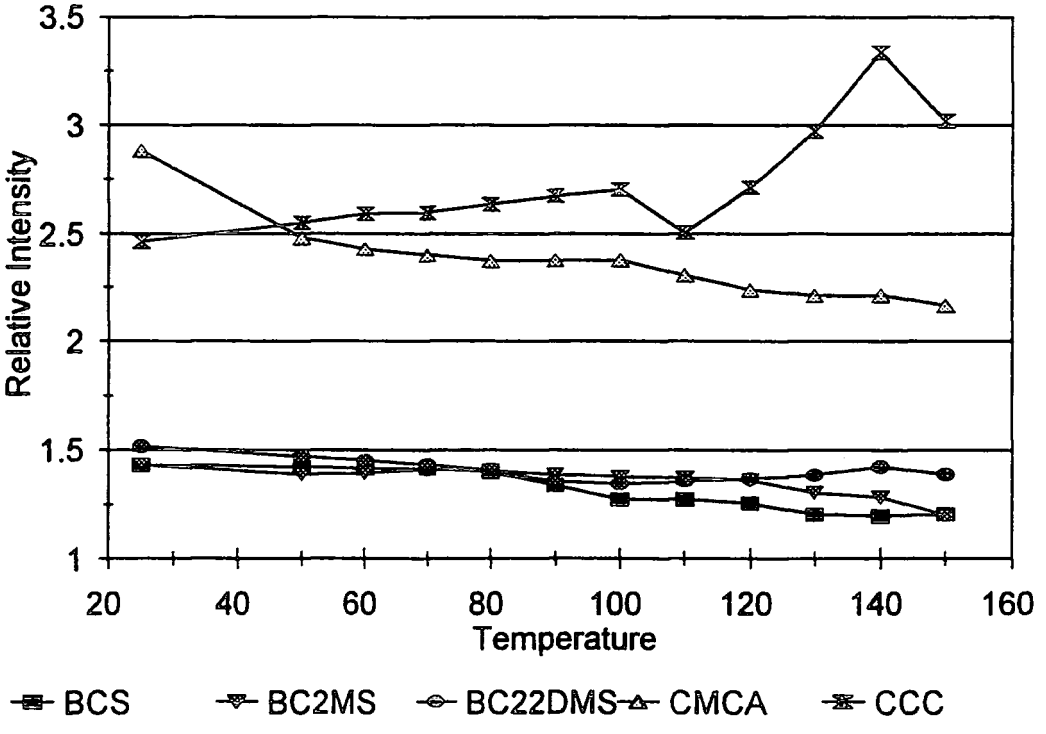

Figure 5.5. Graph of relative intensities of the CH_2 stretching region compared to the carbonyl stretching region for all molecules.

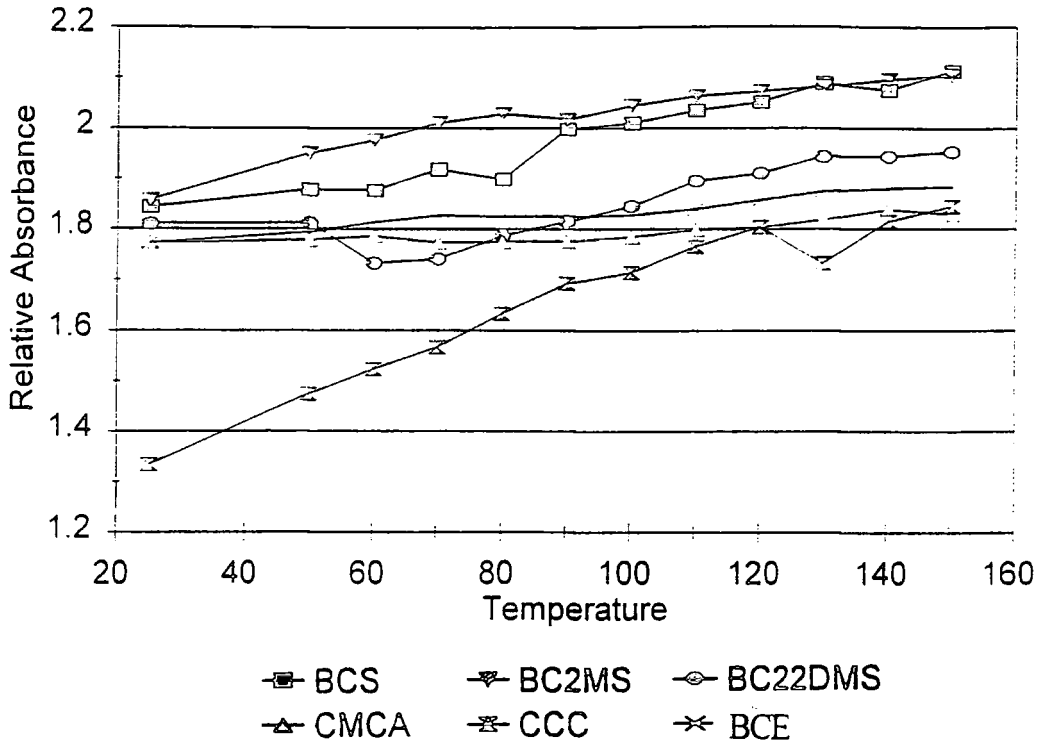

Figure 5.6. Relative peak heights of the antisymmetric CH2 stretch against the symmetric CH2 stretch for all molecules.

5.2.1.2. Carbonyl Stretching Region

The carbonyl stretching region for BCS shows an initial increase in width, followed by a period of no change, and then a decrease in width to below the initial value. (figure 5.7) There seems to be no change in width for BC2MS outside the experimental error (figure 5.8), and the changes for BC22DMS (figure 5.9) follow those for BCS. The bandwidths for CMCA show a steady increase (figure 5.10), and those for CCC show a decrease followed by no change followed by an increase to the original value (figure 5.11). This indicates a competition of effects. As can be seen from the spectra (figure 5.2, 5.4, 5.5) and from Fourier deconvolution (see section 5.3 and figure 5.16) there are at least two components to the carbonyl envelope for the diester compounds. If these two components show differing behaviour, then this will be reflected in the overall bandshape. Also, the BCS spectra exhibit a large change in band shape.

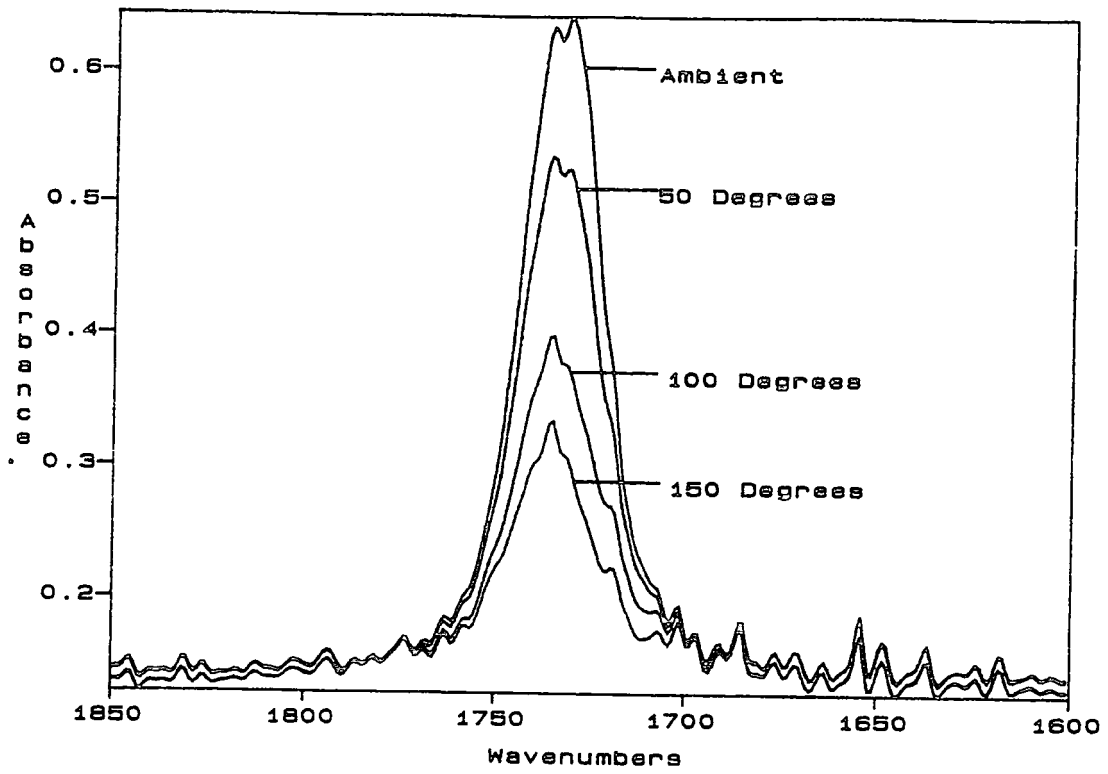

Figure 5.7. Carbonyl band for BCS with increasing temperature.

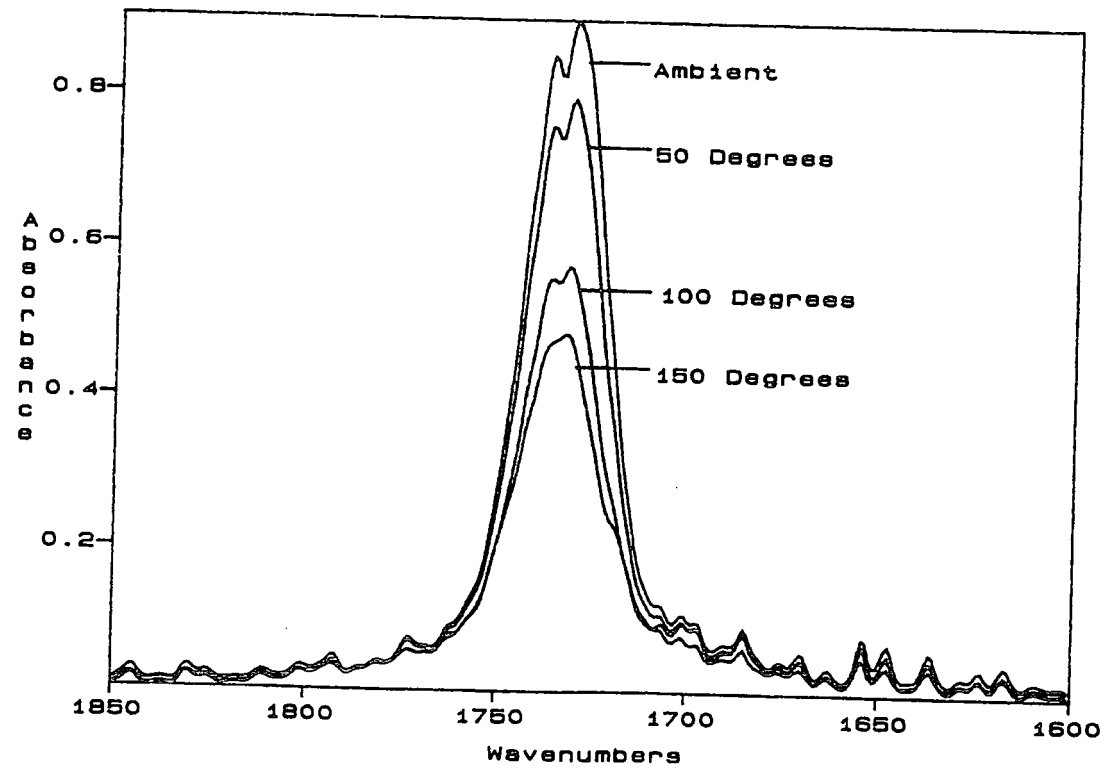

Figure 5.8. Carbonyl band for BC2MS with increasing temperature.

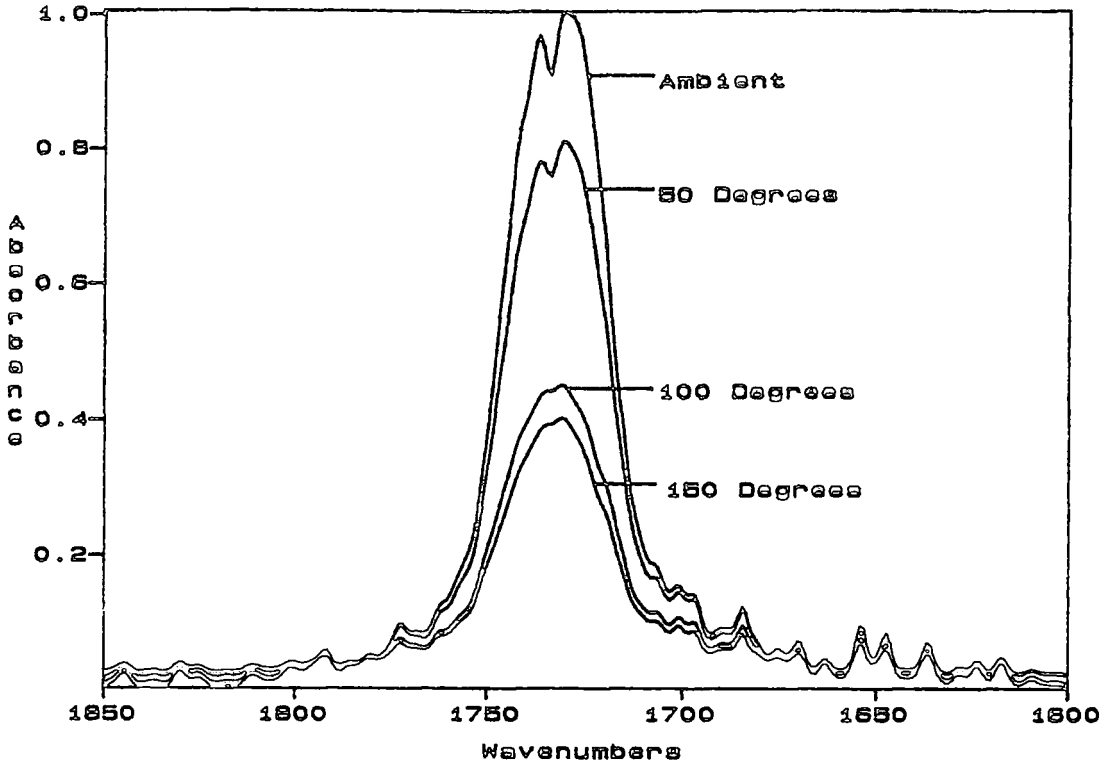

Figure 5.9. .Carbonyl band for BC22DMS with increasing temperature.

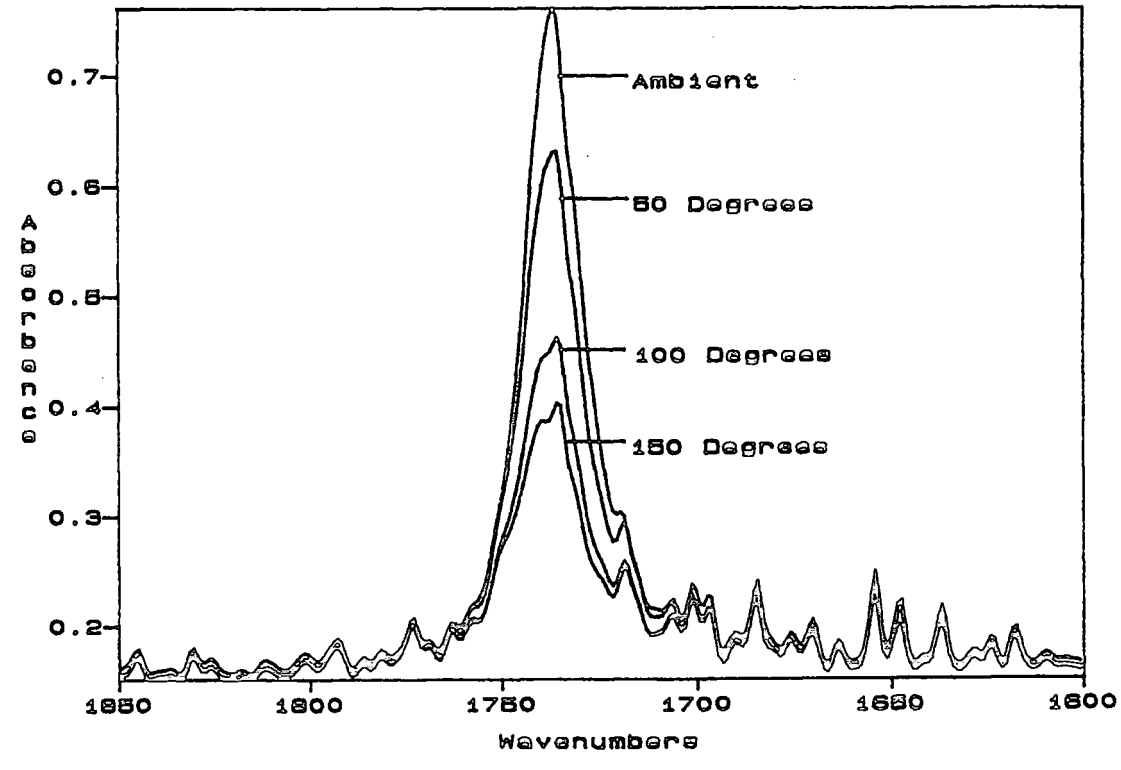

Figure 5.10. Carbonyl band for CMCA with increasing temperature.

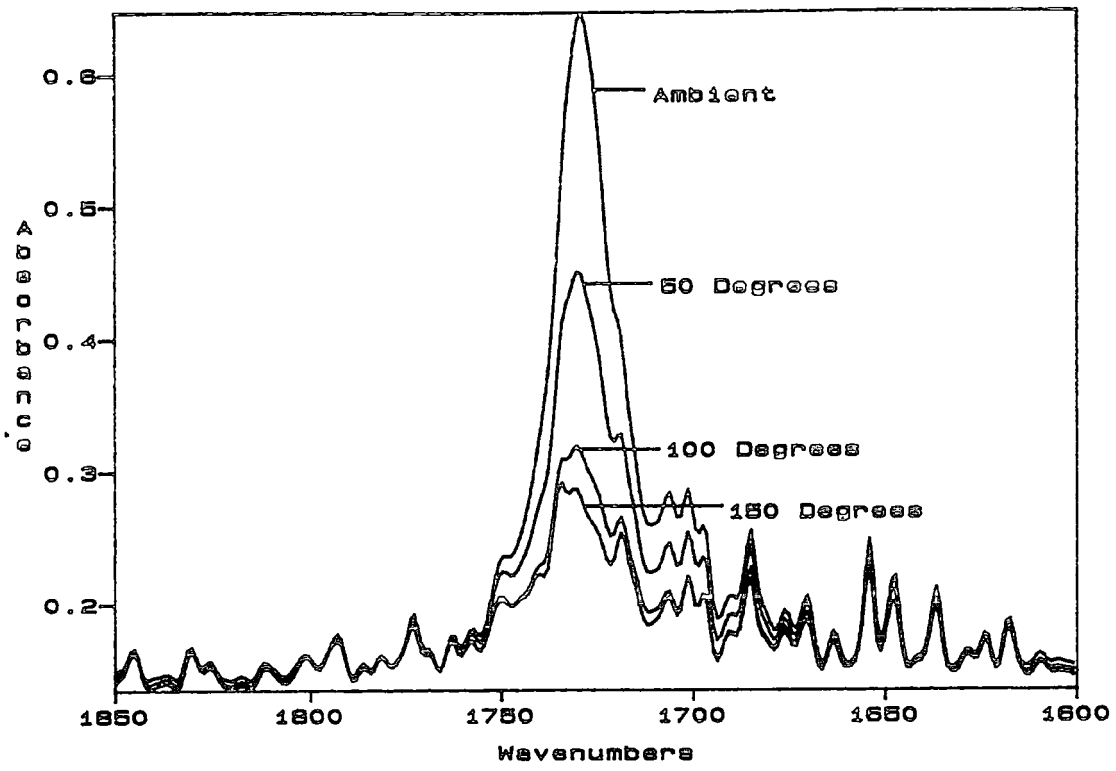

Figure 5.11. Carbonyl band for CCC with increasing temperature.

Using Fourier deconvolution and a band fitting program from the Mattson software package, an attempt has been made to monitor the changes that are occurring on increasing the temperature. This is discussed in 5.3.

The ratio of the overall carbonyl stretch against the ring scissors mode shows an increase for BCS, an increase followed by a decrease for BC2MS, a decrease followed by an increase for BC22DMS, little change is seen for CMCA, and an increase followed by a decrease for CCC (see figure 5.12). When using the the ester stretching region, positive gradients are seen. (figure 5.13)

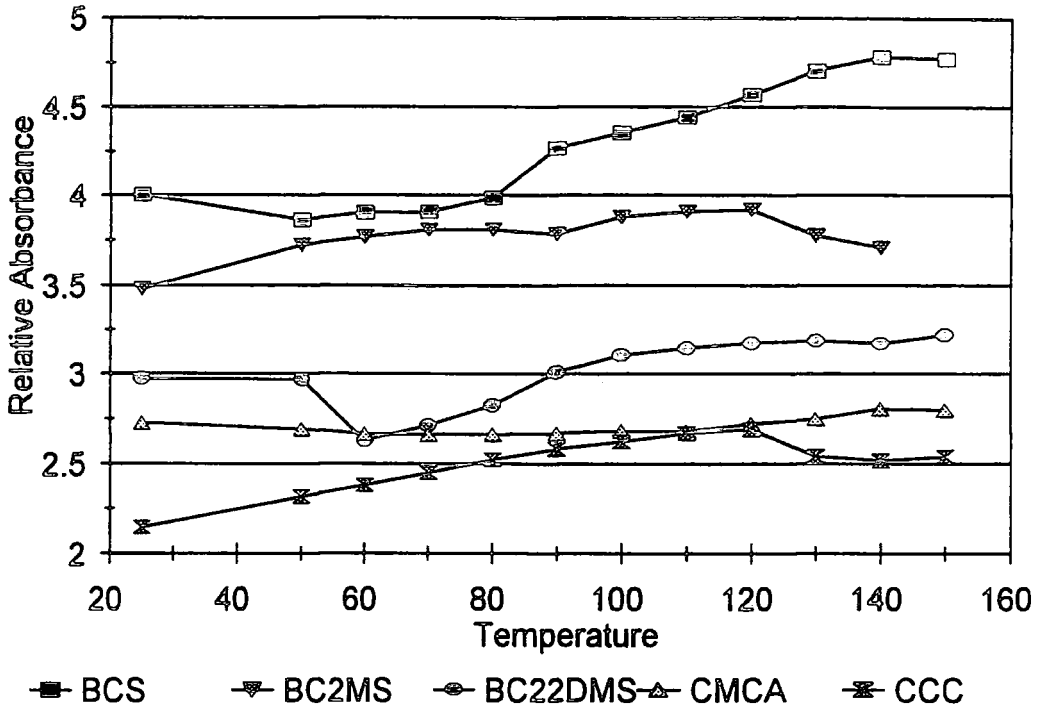

Figure 5.12. Peak height ratio of the carbonyl stretch against the CH_2 ring scissors mode.

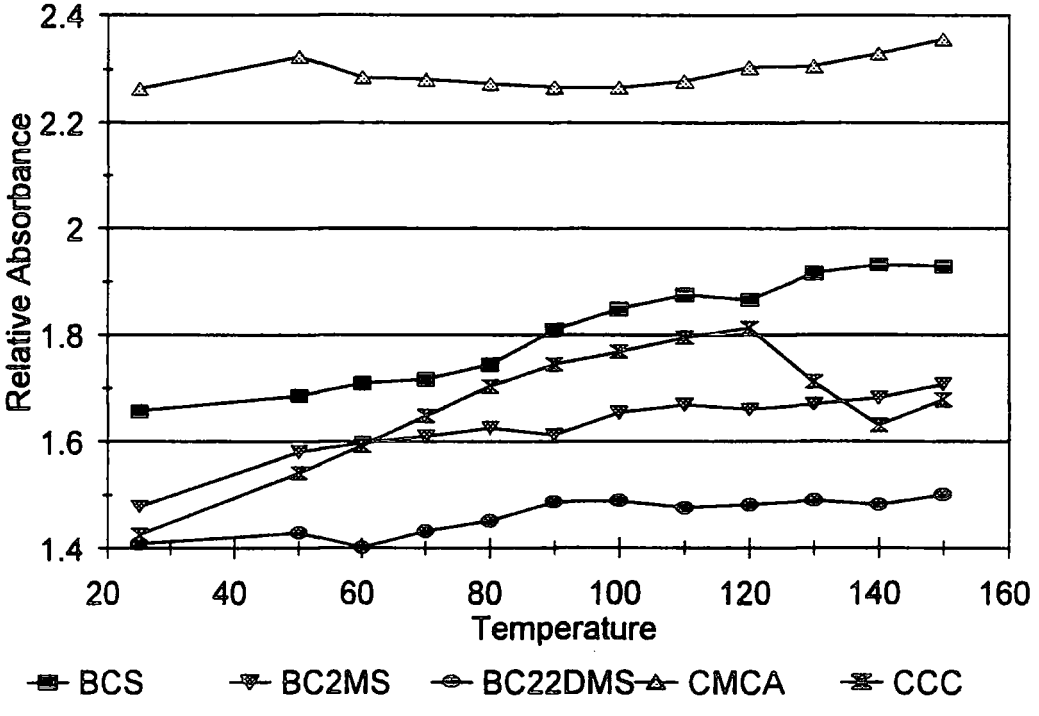

Figure 5.13. Peak height ratio of the carbonyl stretch against the ester stretching region.

5.2.3. Ester Stretching Region

All the measured widths (which were measured at 3/4's of the maximum height rather than half the height due to the problem of overlapping bands) can be seen to increase. Once more this indicates that the rate of relaxation is increasing with temperature. The change is quite dramatic for BCS (figure 5.14) and CMCA (figure 5.15) with the bandwidth increasing by fifty percent.

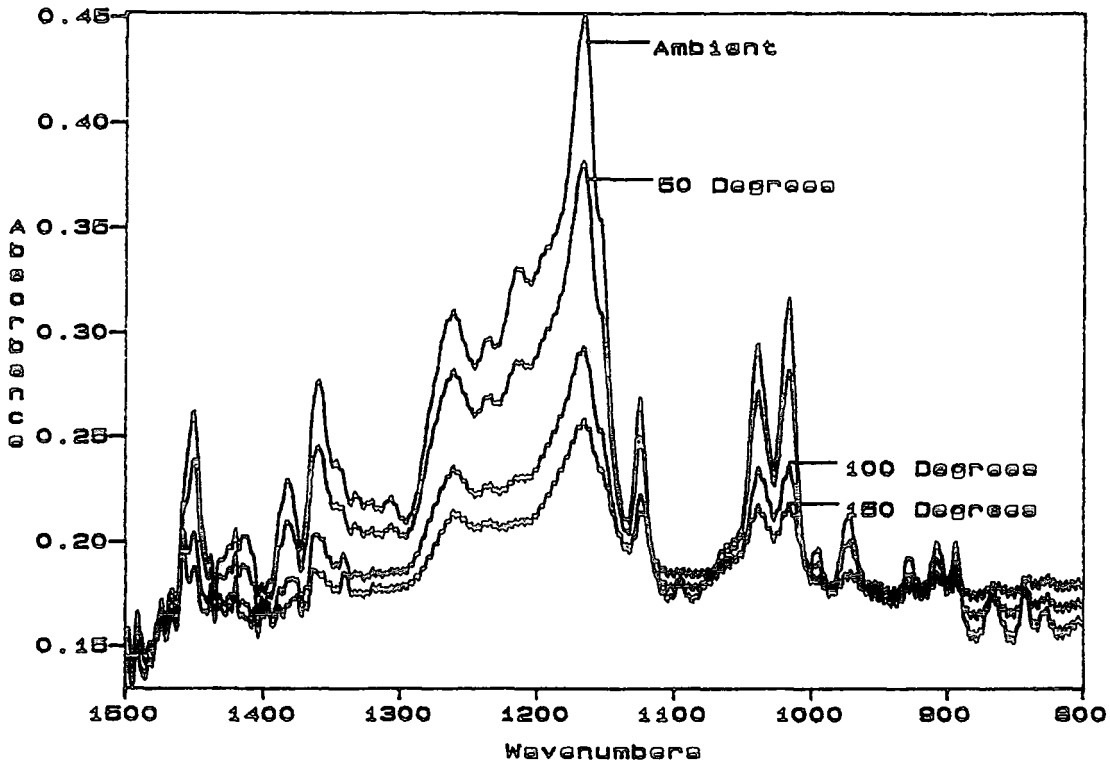

Figure 5.14. 1500-800cm^{-1} region for BCS.

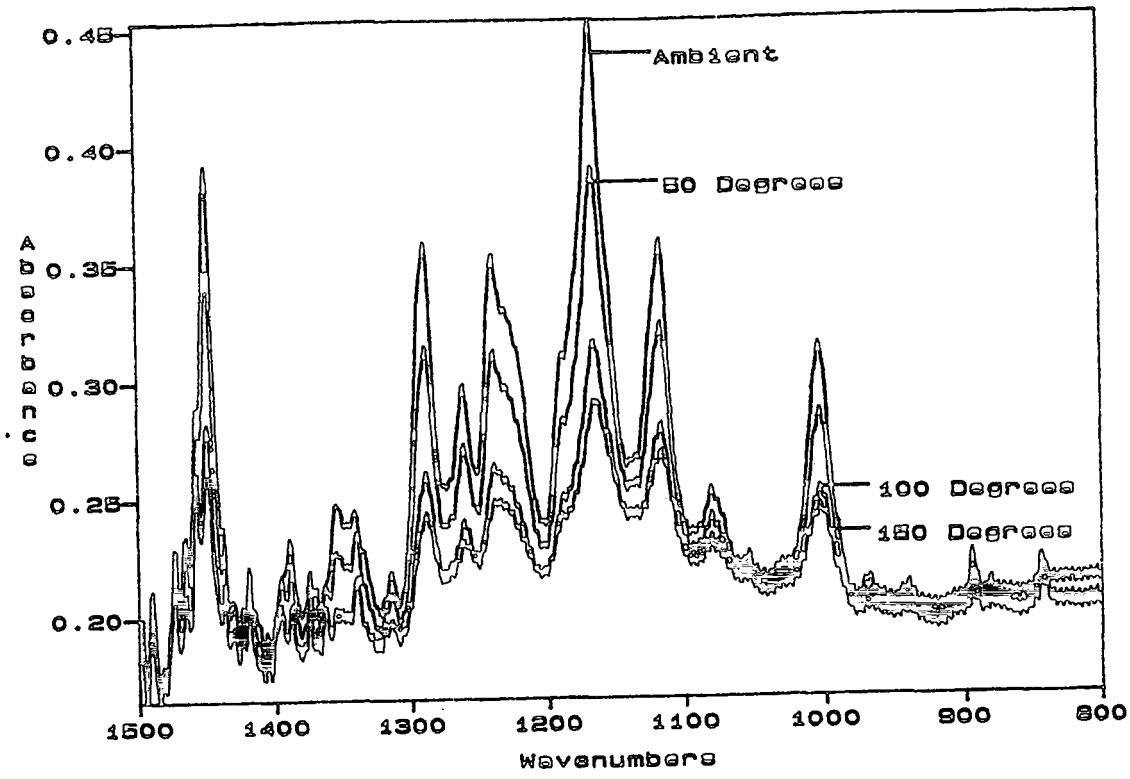

Figure 5.15. 1500-800cm^{-1} region for CMCA.

5.3. Discussion

5.3.1 Bandwidth Changes

As the temperature is increased, the kinetic energy of the system also increases (KE = 3/2kT, where k is the Boltzmann constant and T is the temperature), and the density decreases. As the energy is increased, the collisions between the molecules become "harder" and the molecules become further apart. Equation 2.41., states that for an infra-red band with normalised intensity $I_{ir}(\omega)$[1,2]

$$\phi_v(t)\phi_{IR}(t) = \langle Q_i(0)Q_i(t)\rangle\langle P_1[\bar{\mu}_i(0).\bar{\mu}_i(t)]\rangle = \int I_{ir}(\omega)\exp(i\omega t)\partial\omega \qquad (2.41)$$

where $\langle Q_i(0).Q(t)\rangle$ is the vibrational relaxation function,

$\langle P_l[\vec{\mu}_i(0).\vec{\mu}_i(t)]\rangle$ is the first order reorientational correlation function where $\vec{\mu}$ is the unit vector along the direction of the transition moment corresponding to the normal co-ordinate Q_i of the ith molecule.

On increasing the temperature, τ_{rot}^{-1}, the correlation rate corresponding to the rotational correlation function always increases.[1,2] However, the correlation rate that describes the vibrational correlation function, τ_{vib}^{-1}, can either increase or decrease. When the intermolecular forces are principally long range dipolar interactions, motional narrowing occurs, and τ_{vib}^{-1} is seen to decrease this can be explained using the Kubo model and produces a Lorentzian band shape. Whilst when the intermolecular forces are short range, τ_{vib}^{-1} is seen to increase and the bands are seen to broaden. This is explained more fully in chapter 6.

As the width of a particular vibrational band can be related to the correlation time using equation 2.55 ($\tau_x \cong (\pi c \Delta\nu_{1/2})^{-1}$) which assumes a Lorentzian band shape, some deductions can be made regarding the rate of relaxation.

The relaxation rate of the antisymmetric stretching band decreases whilst that of the symmetric stretch increases but the change is not very significant. Tables 5.7 and 5.8 show the corresponding correlation times calculated from the bandwidths.

Table 5.7 Correlation times for the antisymmetric CH2 stretching region. All data is quoted in psec. Error is ± 1.5psec.

Temp °C	BCS	BC2MS	BC22DMS	CMCA	CCC	CC
25	25.1	26.1	24.2	27.1	19.3	32.3
50	25.1	27.1	24.2	27.1	21.6	32.3
100	26.1	27.1	24.2	26.1	25.1	32.3
150	26.1	27.1	25.1	26.1	24.5	32.3

Table 5.8 Correlation times for the symmetric CH2 stretching region. All data is quoted in psec. Error is ± 1.5psec.

Temp °C	BCS	BC2MS	BC22DMS	CMCA	CCC	CC
25	45.3	45.3	42.4	48.4	45.0	45.3
50	42.4	45.3	42.4	48.4	45.0	45.3
100	42.4	45.3	39.9	45.3	45.0	42.4
150	39.9	42.4	39.9	45.3	38.4	37.8

As the rotational relaxation rate always increases, it seems apparent that the vibrational part of the relaxation function is increasing for the antisymmetric stretching band. For the symmetric stretching band, either the amount of motional narrowing is not significant enough compared to the rotational part to see an overall decrease in width, or the vibrational relaxation rate is increasing. Another possibility, and probably the more likely reason for the small changes seen arises from the balance between temperature and density effects. As the temperature is increased, the density decreases and hence the free volume will increase. So, the collisions between molecules are harder, but on average the molecules are further apart therefore, as there may be little change in the average interactions felt by the molecules, little change will be observed.

If the carbonyl bands are now considered, it is apparent that for the three diester compounds that changes are occurring.(figures 5.2., 5.5. and 5.5) The overall carbonyl band for BC22DMS is by far the broadest, indicating the influence of the branching methyl groups. If the change of the two components of the overall band are monitored the FWHM are seen to increase.(Tables 5.1. to 5.3.) However, if the change in intensity of both bands is monitored, it can be seen that, on ratioing the higher wavenumber component against the lower wavenumber component, that the behaviour of the three molecule's carbonyl bands is somewhat different. The intensity changes for the components of the carbonyl envelope give rise to there being little change observed in the overall band.

As mentioned previously Fourier deconvolution was used to separate the components from the overall carbonyl region for the diester compounds. This is a

procedure that carries out a reverse Fourier transform on a spectrum with the result being multiplied by an apodisation function. The data is then transformed forward into the frequency domain. This process has the effect of resolution enhancement[3-6]. The program requires an approximation of the FWHM of the bands, an enhancement factor, and the apodisation function required.

When peak fitting, it was assumed that the peak frequencies of the separate carbonyl bands did not vary with temperature as no variation of peak frequency was observed in any other vibrational bands in any of the molecules studied, and the percentage of Gaussian and Lorentzian components was constant.

It is apparent from figure 5.16. that there are two main bands within the carbonyl envelope for BCS. This also follows for BC2MS, and BC22DMS. Tables 5.9-5.11 summarise the peak fitted data and figures 5.17 and 5.18 show examples of the peak fitted data with the residual from the fitting procedure included.

Figures 5.19-5.21 show the variation in FWHM for the fitted bands as the temperature is increased.

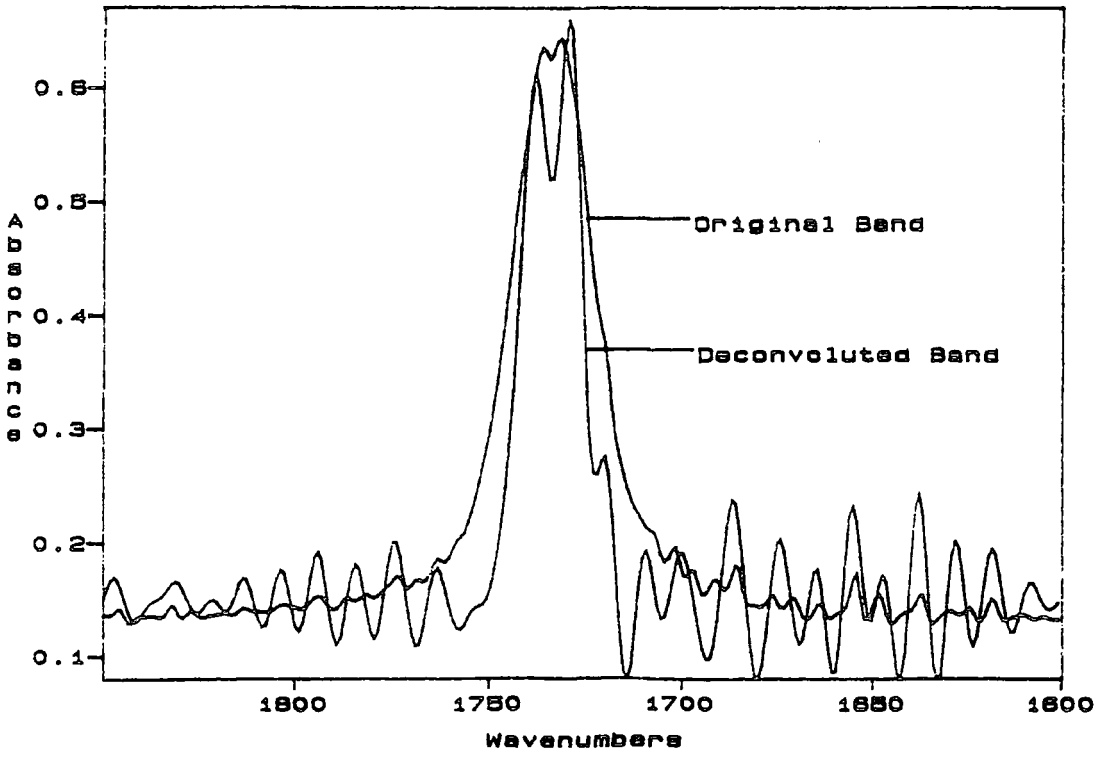

Figure 5.16. Fourier deconvoluted band for the carbonyl region of BCS.

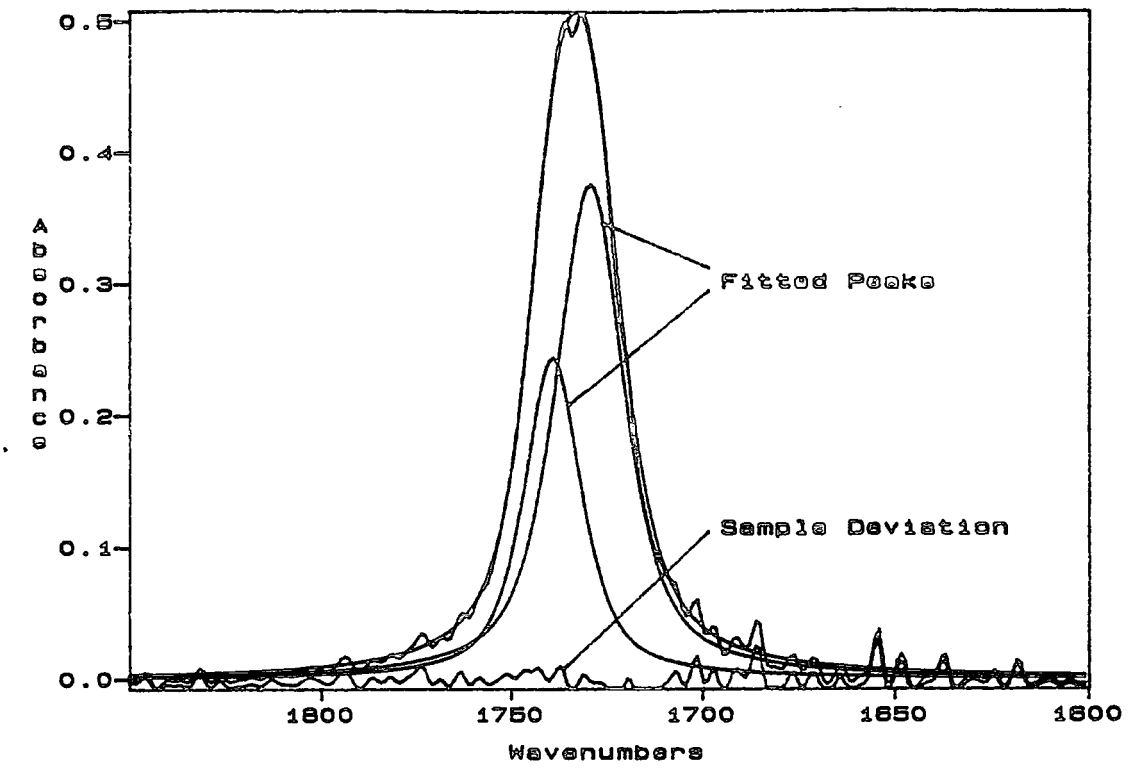

Figure 5.17. An example of peak fitted data. BCS at ambient temperature, 20°C.

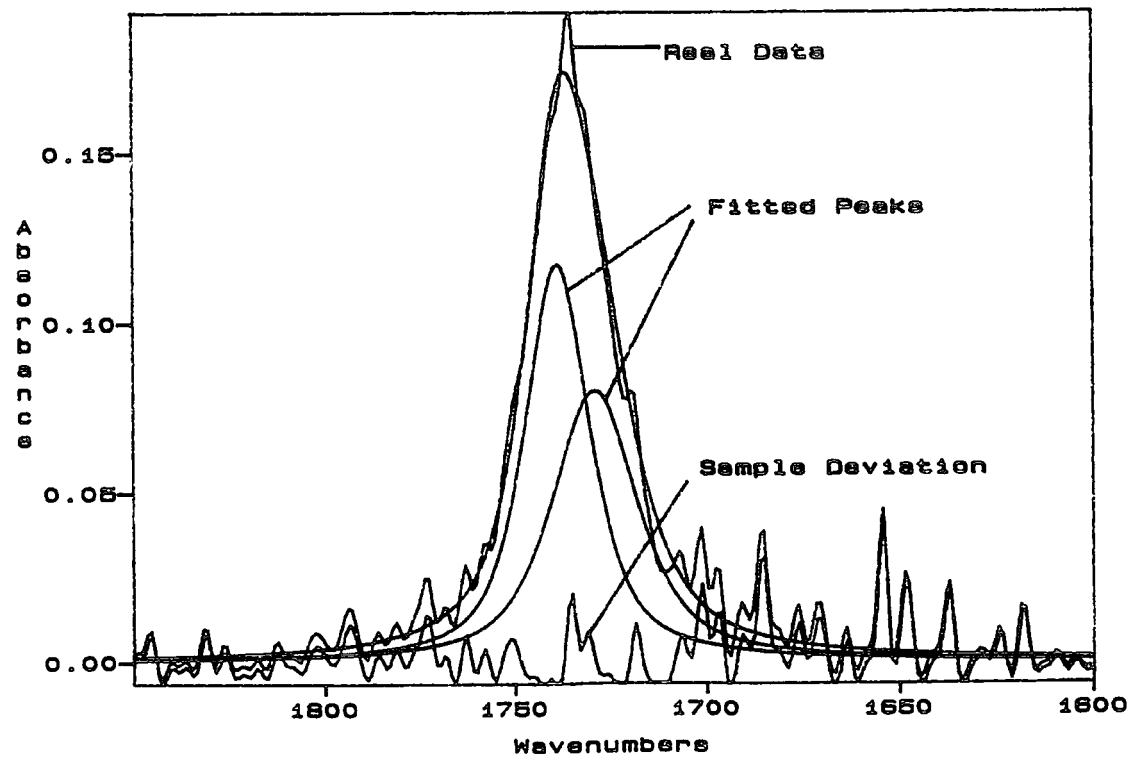

Figure 5.18. An example of peak fitted data. BCS at 150°C.

Table 5.9. Peak fitted data for the carbonyl stretch of BCS. The peak centres were fixed at the values given on Fourier deconvolution. i.e. 1738.72 and 1729.07.

Temp °C	Abs	Width cm^{-1}	Intensity	Abs	Width cm^{-1}	Intensity
25	0.24	17.79	6.12	0.38	21.27	11.32
50	0.20	19.22	5.63	0.26	23.45	8.78
60	0.20	19.00	5.26	0.24	23.34	7.77
70	0.19	19.99	5.31	0.21	25.70	7.52
80	0.18	19.94	5.20	0.20	25.12	6.68
90	0.15	18.98	5.08	0.17	25.71	6.15
100	0.13	18.29	3.38	0.15	26.76	5.72
110	0.13	18.48	3.39	0.13	25.40	5.73
120	0.13	19.02	3.37	0.12	25.54	5.20
130	0.12	19.64	3.40	0.10	25.43	3.45
140	0.12	19.77	3.37	0.09	25.77	3.23
150	0.12	20.18	3.34	0.08	26.34	2.98

Table 5.10. Peak fitted data for the carbonyl stretch of BC2MS. The peak centres were fixed at the values given on Fourier deconvolution. i.e. 1739.39 and 1728.50.

Temp °C	Abs	Width cm^{-1}	Intensity	Abs	Width cm^{-1}	Intensity
25	0.44	16.72	10.37	0.70	19.46	19.24
50	0.34	17.27	8.37	0.70	20.24	17.42
60	0.33	17.68	8.28	0.56	20.19	16.06
70	0.34	18.12	8.61	0.50	19.79	15.02
80	0.31	18.65	8.06	0.47	20.26	13.50
90	0.24	17.91	6.15	0.45	21.11	13.54
100	0.20	17.85	5.11	0.43	21.73	13.42
110	0.20	18.61	5.29	0.40	21.84	12.52
120	0.20	19.44	5.39	0.38	22.23	11.87
130	0.18	19.81	5.15	0.36	23.58	11.89
140	0.19	20.00	5.31	0.34	23.45	11.43
150	0.17	19.87	5.82	0.34	26.00	12.45

Table 5.11. Peak fitted data for the carbonyl stretch of BC22DMS. The peak centres were fixed at the values given on Fourier deconvolution. i.e. 1741.24 and 1727.77.

Temp °C	Abs	Width cm^{-1}	Intensity	Abs	Width cm^{-1}	Intensity
25	0.48	15.47	10.52	0.89	22.97	28.96
50	0.37	16.73	8.87	0.69	25.10	23.64
60	0.24	18.22	6.19	0.46	27.30	17.83
70	0.22	18.69	5.82	0.43	27.75	16.87
80	0.21	19.23	5.71	0.41	27.86	16.27
90	0.20	19.28	5.42	0.38	27.18	15.67
100	0.19	19.47	5.18	0.35	26.43	13.13
110	0.18	20.24	5.09	0.33	26.39	12.28
120	0.18	20.15	5.05	0.32	25.73	11.68
130	0.18	19.97	5.96	0.31	25.03	11.12
140	0.18	19.84	5.93	0.31	25.47	10.81
150	0.17	20.65	5.93	0.30	25.34	10.86

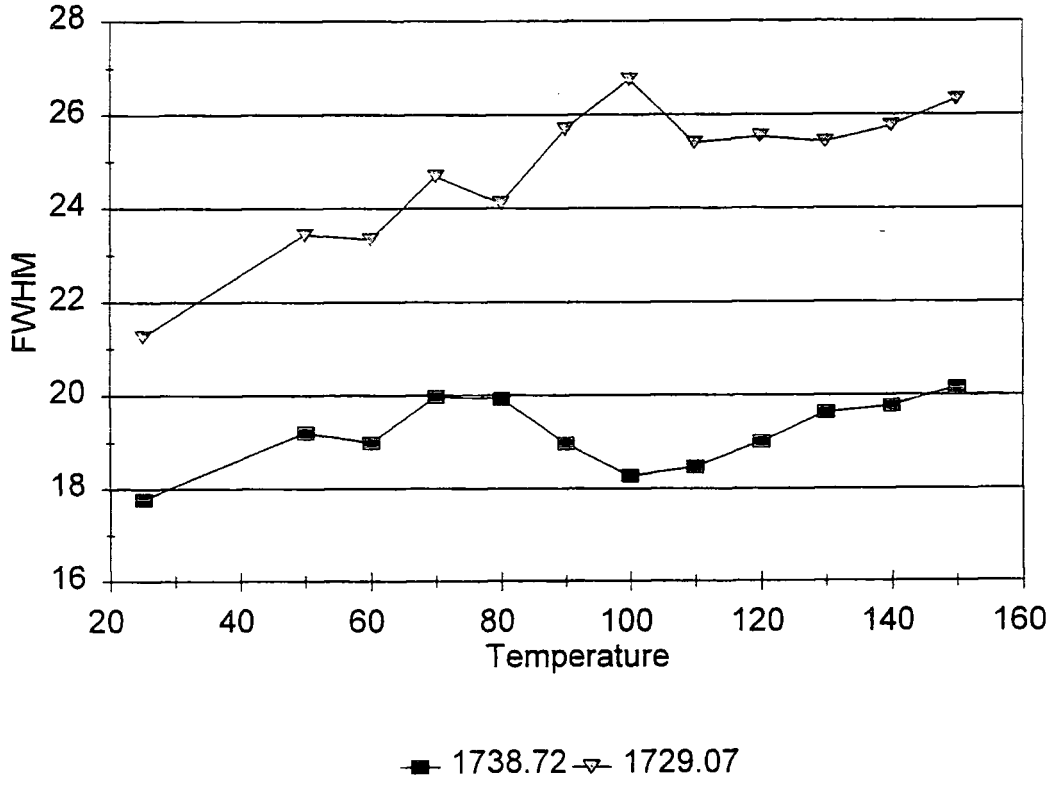

Figure 5.19. Graph showing the variation of FWHM for the fitted bands of the carbonyl band in BCS.

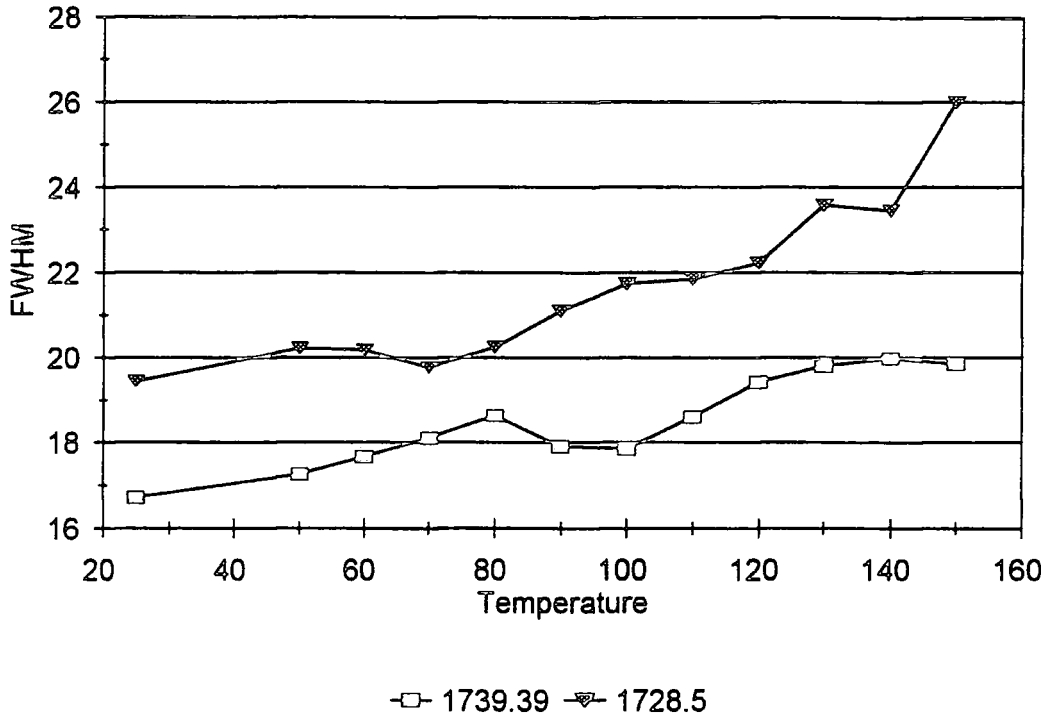

Figure 5.20. Graph showing the variation of FWHM for the fitted bands of the carbonyl band in BC2MS.

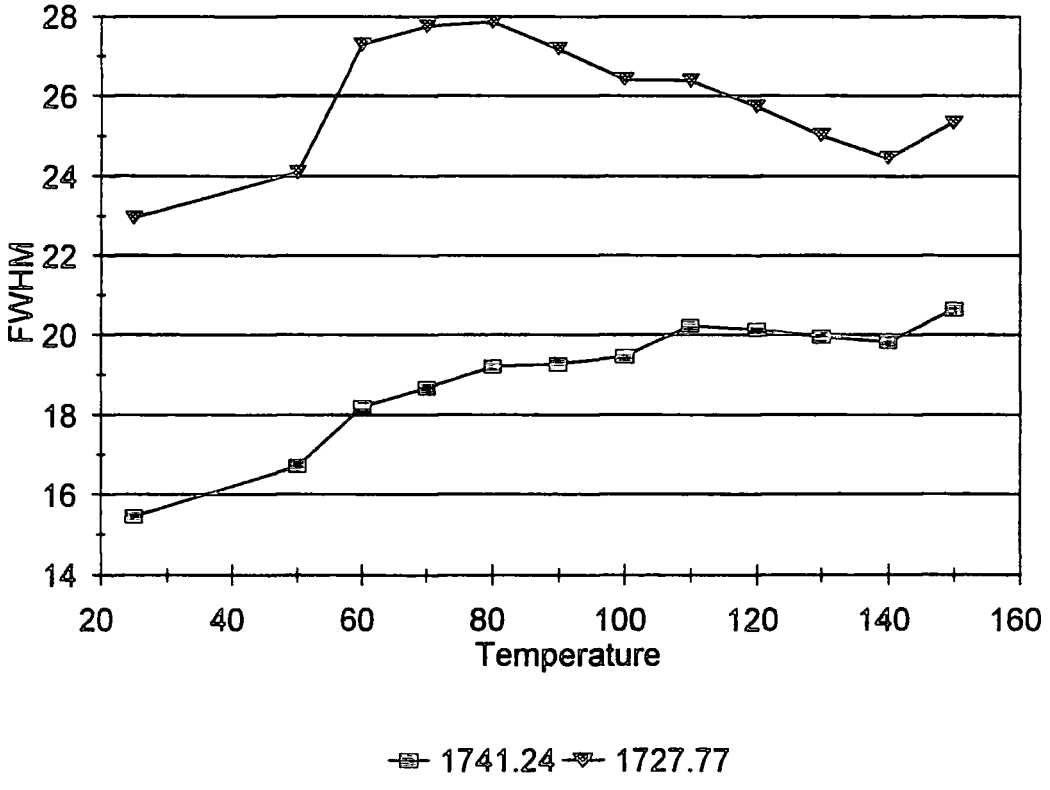

Figure 5.21. Graph showing the variation of FWHM for the fitted bands of the carbonyl band in BC22DMS.

It can be seen that both bands increase in width as the temperature is increased, with the width change of the higher wavenumber band being greatest. This is also true for the other two diester compounds. This indicates an increase in the relaxation rate for both components.

It is not surprising that two carbonyl bands are apparent in the infra-red spectra of BCS, as there are two carbonyl functional groups in the molecule. In fact, there may well be more bands in the overall carbonyl band (there appears to be shoulders on both the high and low frequency sides of the band), but due to the uncertainties involved in Fourier deconvolution and the peak fitting programmes, it was decided to only fit to two carbonyl bands. It can be seen from the residual left after peak fitting in figures 5.17 and 5.18 that there are errors involved with this procedure. Without a proper error analysis built into the fitting program itself, it is very difficult to put a figure to the inherent error. However, the procedure does give some definite trends as can be seen from figures 5.19-5.21.

There is now the question of how the different environments arise. From the data obtained, some deductions can be made. If an intermolecular process was responsible for the differing carbonyl environments, then as all the ester containing molecules are very similar in structure, it would seem likely that the monoester compounds would show evidence of different carbonyl environments in their spectra. This is not apparent (figures 5.11 and 5.12). Therefore, the differing carbonyl environments arise from intramolecular differences perhaps brought about by rotation of the hydrocarbon chain joining the cyclohexyl rings, with internal rigidity being responsible for the differences between the diester compounds.

The FWHM of the monoester compounds are also seen to increase indicating an increase in the rate of relaxation.

The FWHM for the ester stretch of all the molecules increase, with the change for BCS being the greatest. Table 5.12 shows the corresponding correlation times calculated from the bandwidths.

Table 5.12. Correlation times for the ester stretching region. All data is quoted in psec. Error is ± 1.5psec.

Temp °C	BCS	BC2MS	BC22DMS	CMCA	CCC
25	47.8	53.1	53.1	79.8	79.8
50	45.5	53.1	47.8	68.0	79.8
100	38.2	47.8	43.5	59.6	79.8
150	31.9	41.8	39.7	47.8	59.6

On observing the behavioural differences between the carbonyl and ester stretches, it may be possible to distinguish between intermolecular and intramolecular effects. The carbonyl bands will provide the intermolecular information due to the changes in the dipolar interactions between adjacent molecules, and the ester stretch will provide the intramolecular information.

If this is true, it seems that both intermolecular and intramolecular processes are effected in similar ways with the result being an increase in the relaxation rate.

5.3.2 Relative Intensities and Peak Heights

Wherever possible, relative intensities were calculated. (i.e. for the CH_2 and the carbonyl stretching regions) But, when it was impossible to measure the intensities due to overlapping bands, peak heights were measured and used to try and help with interpretation.

As was explained in chapter 2,

$$\text{Intensity} \propto \left| \partial\mu / \partial Q \right|^2 \qquad 5.1$$

which implies,

$$\text{Intensity} \approx \left| \Delta\mu / \Delta Q \right|^2 \qquad 5.2$$

where μ is the transition dipole of the molecule and is related to the electronic distribution in the molecule, and Q is the normal coordinate which is related to the atomic motions. Consequently, a change in intensity can be related to several phenomena including the following:

1. A change in the equilibrium process in the liquid.(e.g. a conformation process).

2. A change in the molecular interactions in the liquid.(e.g. changing the solvent or changing the temperature).

3. A change of phase. This can also be related to the change in molecular interactions.

As can be seen from figure 5.5, the intensity of the carbonyl band increases with temperature relative to the overall CH_2 stretching region for all the molecules, with the change for CCC being the greatest.

The change in relative intensity is not likely to be indicative of a change in phase as this would be very apparent in the spectra. Therefore, it is due to either a conformation change and/or a change in the molecular interactions in the liquid which might well be brought about by a change in conformation.

If the relative intensity changes of the fitted carbonyl groups are plotted, figure 5.22., it can be seen that for BCS the higher wavenumber band increases in intensity compared to the lower wavenumber band. This is also true for BC22DMS, but to a lesser extent. However, for BC2MS the opposite is seen. (i.e. the lower wavenumber band increases in intensity compared to that of higher wavenumber). This difference in behaviour must be due to the presence of the branching methyl groups in BC2MS and BC22DMS. It is also apparent that unsymmetric branching has a different effect to the symmetric branching of BC22DMS. The increase in one band and the decrease in another is indicative of a change in conformation.

It would be expected that the predominant attractive forces between the diester molecules would be dipolar interactions through the carbonyl groups. It might also be expected that BCS, which has no branching off the joining hydrocarbon chain and therefore little hindrance to packing, would have the strongest dipolar attraction

compared to BC2MS or BC22DMS, which do have branching off the joining chain. Hence, the observed changes would be greatest for BCS, as the change in interactive forces would be greatest for this molecule and this is apparent in the data. It also seems that unsymmetric branching of the joining hydrocarbon chain has a different effect to symmetric branching. This might be indicative of the differences in the way the two molecules pack in the liquid, or might indicate that some conformational change is occurring that is different for the two molecules.

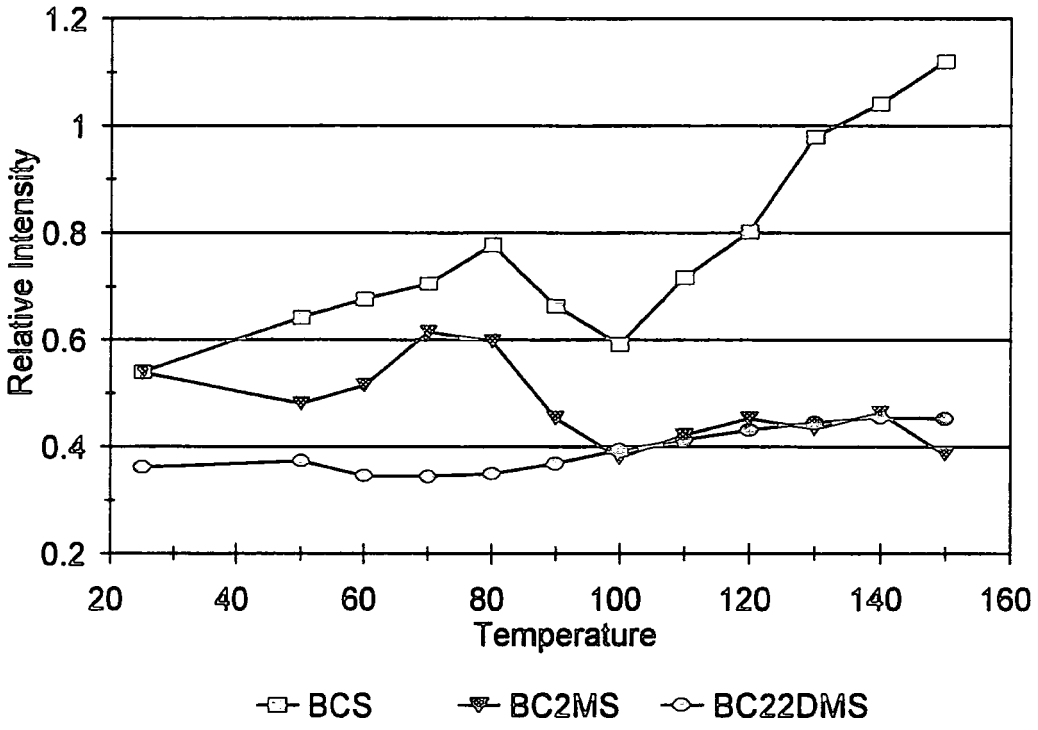

Figure 5.22. Relative intensity changes for the fitted carbonyl bands for BCS, BC2MS and BC22DMS. Ratio is higher wavenumber component:lower wavenumber component.

On ratioing peak heights, it is apparent that several changes are occurring. If peak heights are ratioed against the antisymmetric CH_2 stretching band then positive gradients are seen (figure 5.6). This is also true when ratioing the carbonyl stretching band against the ester stretching region (figure 5.13) and the CH_2 ring scissors band (figure 5.12). Again, these changes are indicative of conformation changes.

For all the peak height ratios mentioned, and indeed for the relative intensity measurement, CCC exhibits the largest change. This may well arise from the differences in internal flexibility of the molecules studied. Table 5.13 shows the kinematic viscosity of the ester compounds. As a high viscosity is required for a good traction coefficient, it appears that the viscosity measurements can be used as a measure of molecular rigidity.

Various theories have been proposed for the molecular features which may be associated with high fluid traction coefficients (μ's)[7]. In general the principle requirement for a high μ has been a high degree of molecular rigidity.

As mentioned in 1.2, viscosity is ultimately molecular in origin. Therefore, if internal rigidity is taken into account, it would be expected that the more flexible molecules would exhibit the greatest change due to the relative ease of molecular rotations and vibrations. From table 5.13, it can be seen that the less hindered molecule is CCC, followed by CMCA, BC2MS, BCS, and finally the most internally rigid molecule, BC22DMS. Hence, it might be expected that CCC would exhibit the largest changes, and indeed it does. It must be remembered that CCC only has CH_2 groups on the cyclohexyl rings while the other ester compounds have chain CH_2 groups. So, this might well contribute to the large differences in FWHM at elevated temperature. However, due to the greater proportion of ring CH_2 groups compared to chain CH_2 groups, it is likely that the overiding effect will be due to the cyclohexyl rings.

Table 5.13. Vk(T) is the kinematic viscosity in cSt at temperature °C.

	Vk(40)	Vk(100)
BCS	23.82	3.922
BC2MS	22.09	3.746
BC22DMS	27.04	5.062
CMCA	7.89	2.30
CCC	7.16	2.06

For measurements involving the carbonyl or ester vibrational modes, BCS and CCC show the largest changes. The packing of BCS and CCC in the liquid is likely to be very similar due to the similarity in the structures, even though BCS has two carbonyl functional groups rather than the one in CCC. (This is shown in the differences in FWHM of the two molecules carbonyl bands, with the band for BCS being wider.(Tables 5.1. and 5.4)) However, the packing for BC2MS and BC22DMS will be different due to the presence of branching methyl groups on the interjoining hydrocarbon chain. With the molecules moving faster due to the increased energy, the packing i.e. the intermolecular forces will be disrupted. Due to the branching methyl groups in BC2MS and BC22DMS it would be expected that the molecules would not be "held" as strongly by their surrounding neighbours as in the case of BCS and CMCA. Consequently, the change in forces felt by the molecules of BCS and CMCA would be greater than for BC2MS and BC22DMS and this would be apparent in the spectra.

Therefore, although intramolecular rigidity plays an important part in the behaviour of the molecules, intermolecular interactions also assist in providing the observed effects.

References

1. J. Yarwood and R. Arndt, "Study of Intermolecular Interactions in the Liquid Phase", Chapter 4 of "Molecular Association", Vol. 2, ed. R. Foster, Academic Press (1979)

2. R. Arndt and G. Doge, "Infra red and Raman Studies on Molecular Dynamics in Liquids", Chapter 6 of "Spectroscopy and Dynamics of Molecular Liquids", Ed. D. Steele and J. Yarwood, Elsevier (1991)

3. J.K. Kauppinen, D.J. Moffatt, H.H. Mantsch, D.G. Cameron, Anal. Chem, 53, 1454 (1981)

4. J.K. Kauppinen, D.J. Moffatt, H.H. Mantsch, D.G. Cameron, Appl. Optics, 20, 1866 (1981)

5. J.K. Kauppinen, D.J. Moffatt, H.H. Mantsch, D.G. Cameron, Appl. Spectrosc. 35, 271 (1981)

6. D.G. Cameron and D.J. Moffatt, J. Testing and Evaluation, 12, 78 (1984)

7. M.P. Dare-Edwards, Synth. Lubr., 8, 197 (1991)

CHAPTER 6

Variable Pressure Studies

6.1 Introduction

Variable pressure data was recorded using the diamond anvil cell (figure 3.7). A resolution of $4cm^{-1}$ was employed for all the data obtained. Figure 6.1 shows the spectra of BCS at 5kbar and 35kbar. Unlike the variable temperature data, there are some changes in peak frequency (tables 6.1-6.6) as well as for bandwidths (tables 6.7-6.12).

N.B. 1kbar ≡ 0.1 GPa

Table 6.1. Peak frequency variation with pressure for BCS

Pressure kbar	$\nu_a(CH_2)$ cm^{-1} $\pm0.5cm^{-1}$	$\nu_s(CH_2)$ cm^{-1} $\pm0.5cm^{-1}$	ν(C=O) cm^{-1} $\pm0.5cm^{-1}$	$\delta(CH_2)$ cm^{-1} $\pm0.5cm^{-1}$	ν(C-O) cm^{-1} $\pm0.5cm^{-1}$
0	2937	2860	1732	1450	1167
5	2937	2860	1732	1450	1167
10	2937	2860	1732	1450	1167
15	2937	2860	1732	1450	1167
20	2939	2860	1732	1452	1167
25	2943	2862	1730	1450	1168
30	2947	2866	1730	1450	1170
35	2951	2868	1732	1452	1172

Table 6.2. Peak frequency variation with pressure for BC2MS

Pressure kbar	$\nu_a(CH_2)$ cm^{-1} $\pm0.5cm^{-1}$	$\nu_s(CH_2)$ cm^{-1} $\pm0.5cm^{-1}$	ν(C=O) cm^{-1} $\pm0.5cm^{-1}$	$\delta(CH_2)$ cm^{-1} $\pm0.5cm^{-1}$	ν(C-O) cm^{-1} $\pm0.5cm^{-1}$
0	2939	2860	1732	1454	1174
5	2939	2860	1732	1456	1172
10	2937	2860	1732	1454	1172
15	2939	2860	1734	1456	1174
20	2937	2860	1734	1456	1174
25	2937	2860	1734	1456	1174
30	2939	2860	1734	1458	1174
35	2943	2862	1734	1458	1178

Table 6.3. Peak frequency variation with pressure for BC22DMS.

Pressure kbar	$\nu_a(CH_2)$ cm^{-1} $\pm0.5cm^{-1}$	$\nu_s(CH_2)$ cm^{-1} $\pm0.5cm^{-1}$	$\nu(C=O)$ cm^{-1} $\pm0.5cm^{-1}$	$\delta(CH_2)$ cm^{-1} $\pm0.5cm^{-1}$	$\nu(C-O)$ cm^{-1} $\pm0.5cm^{-1}$
0	2936	2860	1732	1456	1184
5	2947	2866	1730	1456	1190
10	2949	2870	1732	1456	1192
15	2956	2872	1730	1456	1194
20	2959	2876	1730	1458	1196
25	2960	2878	1732	1458	1197
30	2962	2881	1734	1458	1200
35	2970	2887	1738	1458	1201

Table 6.4. Peak frequency variation with pressure for CMCA.

Pressure kbar	$\nu_a(CH_2)$ cm^{-1} $\pm0.5cm^{-1}$	$\nu_s(CH_2)$ cm^{-1} $\pm0.5cm^{-1}$	$\nu(C=O)$ cm^{-1} $\pm0.5cm^{-1}$	$\delta(CH_2)$ cm^{-1} $\pm0.5cm^{-1}$	$\nu(C-O)$ cm^{-1} $\pm0.5cm^{-1}$
0	2926	2854	1738	1450	1167
5	2928	2854	1736	1450	1168
10	2928	2854	1736	1450	1170
15	2928	2854	1736	1448	1174
20	2932	2856	1734	1448	1174
25	2932	2857	1734	1448	1174
30	2936	2858	1734	1448	1174
35	2937	2858	1734	1448	1176

Table 6.5. Peak frequency variation with pressure for CCC

Pressure kbar	$\nu_a(CH_2)$ cm^{-1} $\pm0.5cm^{-1}$	$\nu_s(CH_2)$ cm^{-1} $\pm0.5cm^{-1}$	$\nu(C=O)$ cm^{-1} $\pm0.5cm^{-1}$	$\delta(CH_2)$ cm^{-1} $\pm0.5cm^{-1}$	$\nu(C-O)$ cm^{-1} $\pm0.5cm^{-1}$
0	2936	2858	1730	1452	1174
5	2937	2858	1734	1448	1174
10	2937	2858	1734	1448	1172
15	2937	2860	1734	1450	1172
20	2937	2860	1734	1446	1174
25	2939	2860	1734	1448	1174
30	2937	2860	1734	1448	1174
35	2939	2860	1734	1450	1174

Table 6.6. Peak frequency variation with pressure for BCE

Pressure kbar	$\nu_a(CH_2)$ cm^{-1} $\pm 0.5cm^{-1}$	$\nu_s(CH_2)$ cm^{-1} $\pm 0.5cm^{-1}$	$\delta(CH_2)$ cm^{-1} $\pm 0.5cm^{-1}$
0	2932	2856	1458
5	2933	2858	1458
10	2936	2858	1458
15	2936	2858	1458
20	2939	2860	1458
25	2939	2860	1458
30	2939	2860	1458
35	2939	2860	1458

Table 6.7. FWHM variation with pressure for BCS

*Due to overlapping bands, the full width at 3/4's maximum height was measured.

Pressure kbar	$\nu_a(CH_2)$ cm^{-1} $\pm 0.5cm^{-1}$	$\nu_s(CH_2)$ cm^{-1} $\pm 0.5cm^{-1}$	$\nu(C=O)$ cm^{-1} $\pm 0.5cm^{-1}$	$\delta(CH_2)$ cm^{-1} $\pm 0.5cm^{-1}$	$\nu(C-O)$ cm^{-1} $\pm 0.5cm^{-1}$
0	40.3	22.6	24.0	16.1	22.6
5	38.7	22.6	23.0	17.7	22.6
10	38.7	22.6	22.0	17.7	26.8
15	38.7	22.6	23.0	19.4	41.9
20	38.7	22.6	24.0	19.4	46.2
25	41.9	26.8	26.0	26.8	46.2
30	46.8	29.0	26.0	26.8	51.6
35	53.2	32.3	28.0	29.0	54.8

Table 6.8. FWHM variation with pressure for BC2MS

*Due to overlapping bands, the full width at 3/4's maximum height was measured.

Pressure kbar	$\nu_a(CH_2)$ cm^{-1} $\pm 0.5cm^{-1}$	$\nu_s(CH_2)$ cm^{-1} $\pm 0.5cm^{-1}$	$\nu(C=O)$ cm^{-1} $\pm 0.5cm^{-1}$	$\delta(CH_2)$ cm^{-1} $\pm 0.5cm^{-1}$	$\nu(C-O)$ cm^{-1} $\pm 0.5cm^{-1}$
0	38.7	24.2	24.0	26.8	22.6
5	38.7	26.8	22.0	29.0	26.8
10	38.7	26.8	21.0	29.0	26.8
15	41.9	27.4	22.0	29.0	29.0
20	41.9	29.0	22.0	29.0	32.3
25	41.9	29.0	23.0	29.0	36.5
30	46.8	32.3	24.0	29.0	41.9
35	56.5	38.7	29.0	29.0	48.4

Table 6.9. FWHM variation with pressure for BC22DMS.

*Due to overlapping bands, the full width at 3/4's maximum height was measured.

Pressure kbar	$\nu_a(CH_2)$ cm^{-1} $\pm 0.5cm^{-1}$	$\nu_s(CH_2)$ cm^{-1} $\pm 0.5cm^{-1}$	$\nu(C=O)$ cm^{-1} $\pm 0.5cm^{-1}$	$\delta(CH_2)$ cm^{-1} $\pm 0.5cm^{-1}$	$\nu(C-O)$ cm^{-1} $\pm 0.5cm^{-1}$
0	41.1	27.4	28.0	19.4	24.2
5	54.8	37.1	27.0	26.8	26.8
10	59.7	41.9	28.0	26.8	29.0
15	67.7	48.4	31.0	29.0	30.6
20	74.2	51.6	32.0	29.0	32.3
25	77.4	61.3	33.0	30.6	36.5
30	86.5	71.0	34.0	30.6	37.1
35	91.9	77.4	36.0	30.6	38.7

Table 6.10. FWHM variation with pressure for CMCA.

*Due to overlapping bands, the full width at 3/4's maximum height was measured.

Pressure kbar	$\nu_a(CH_2)$ cm^{-1} $\pm 0.5cm^{-1}$	$\nu_s(CH_2)$ cm^{-1} $\pm 0.5cm^{-1}$	$\nu(C=O)$ cm^{-1} $\pm 0.5cm^{-1}$	$\delta(CH_2)$ cm^{-1} $\pm 0.5cm^{-1}$	$\nu(C-O)$ cm^{-1} $\pm 0.5cm^{-1}$
0	46.0	29.0	22.0	22.6	46.2
5	50.0	32.3	24.0	22.6	51.6
10	50.0	32.3	26.0	22.6	54.8
15	54.8	33.9	33.0	22.6	64.5
20	62.9	37.9	34.0	22.6	67.7
25	67.7	41.9	36.0	22.6	74.2
30	71.0	41.9	36.0	22.6	80.6
35	74.2	41.9	36.0	29.0	83.9

Table 6.11. FWHM variation with pressure for CCC

*Due to overlapping bands, the full width at 3/4's maximum height was measured.

Pressure kbar	$\nu_a(CH_2)$ cm^{-1} $\pm 0.5cm^{-1}$	$\nu_s(CH_2)$ cm^{-1} $\pm 0.5cm^{-1}$	$\nu(C=O)$ cm^{-1} $\pm 0.5cm^{-1}$	$\delta(CH_2)$ cm^{-1} $\pm 0.5cm^{-1}$	$\nu(C-O)$ cm^{-1} $\pm 0.5cm^{-1}$
0	47.8	33.0	41.7	19.1	27.0
5	69.6	36.5	56.7	17.4	46.2
10	87.0	38.3	58.3	17.4	56.7
15	87.0	56.7	59.1	17.4	59.1
20	92.2	56.7	60.0	17.4	66.1
25	93.9	57.4	61.7	17.4	67.8
30	93.9	59.1	62.6	17.4	71.3
35	93.9	59.1	62.6	17.4	76.5

Table 6.12. FWHM variation with pressure for BCE

Pressure kbar	$\nu_a(CH_2)$ cm^{-1} $\pm 0.5cm^{-1}$	$\nu_s(CH_2)$ cm^{-1} $\pm 0.5cm^{-1}$
0	31.5	26.8
5	54.8	37.1
10	66.1	40.3
15	76.8	46.2
20	87.1	48.4
25	96.8	51.6
30	96.8	53.2
35	100.0	54.8

6.2. Results

6.2.1. CH_2 Stretching Modes

For all molecules both the antisymmetric modes and the symmetric modes increase in frequency, with the antisymmetric mode increasing more than the symmetric mode. BC22DMS exhibits the greatest increase in frequency for both modes. (figure 6.1.) The increase in frequency arises from the effect of hard core repulsive forces which increase rapidly with density. Figure 6.2 shows this region for BCS.

There is a large pressure induced broadening for both modes for all the molecules. This is consistent with an increase in the number of vibrational environments for the CH_2 stretching region (i.e. inhomogeneous broadening) with increased pressure.

The graph of relative intensities of the CH_2 region ratioed against the overall carbonyl band shows a positive gradient for BC2MS and a negative gradient for the other molecules studied. (figure 6.3.)

On ratioing the peak heights, a positive gradient was observed for the ratio of the antisymmetric CH_2 stretching region against the symmetric CH_2 region for BCS and BC22DMS whereas for the other molecules, this behaviour is reversed with a negative gradient being observed. (figure 6.4.) The latter behaviour is also observed when the antisymmetric CH_2 stretching mode is ratioed against the overall carbonyl band, the CH_2 ring scissors mode (~$1450cm^{-1}$), and the ester C-O stretching mode.

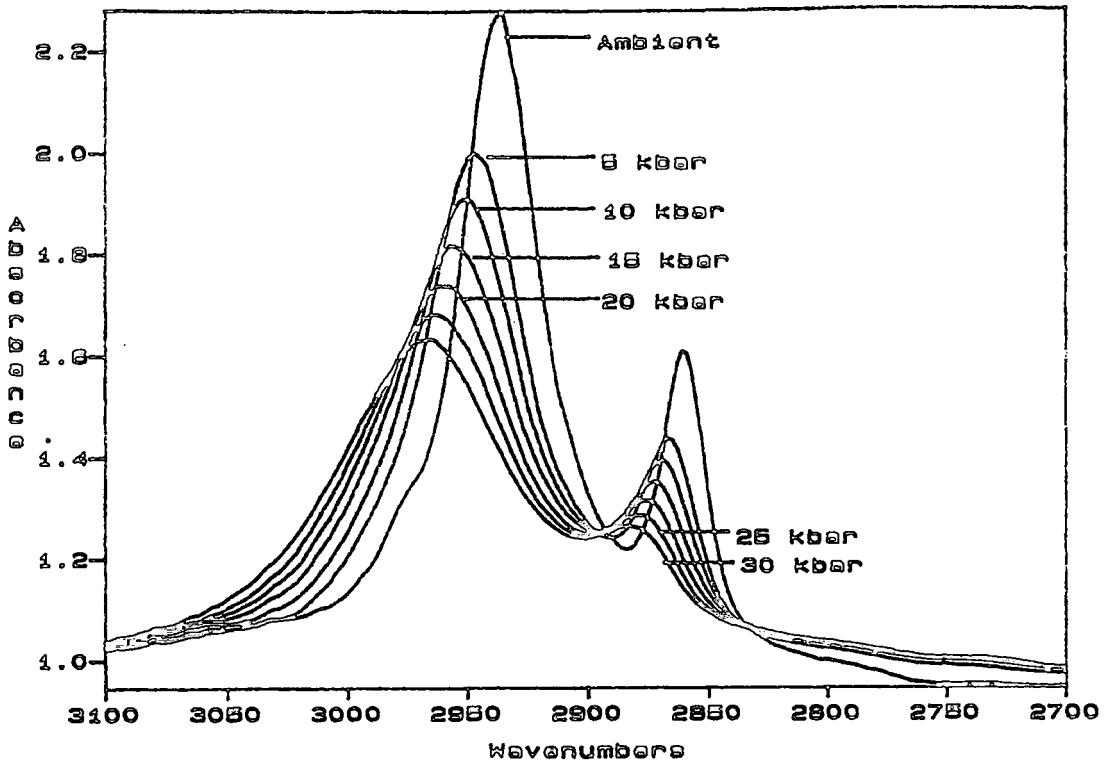

Figure 6.1. The CH_2 stretching region with increasing pressure for BC22DMS.

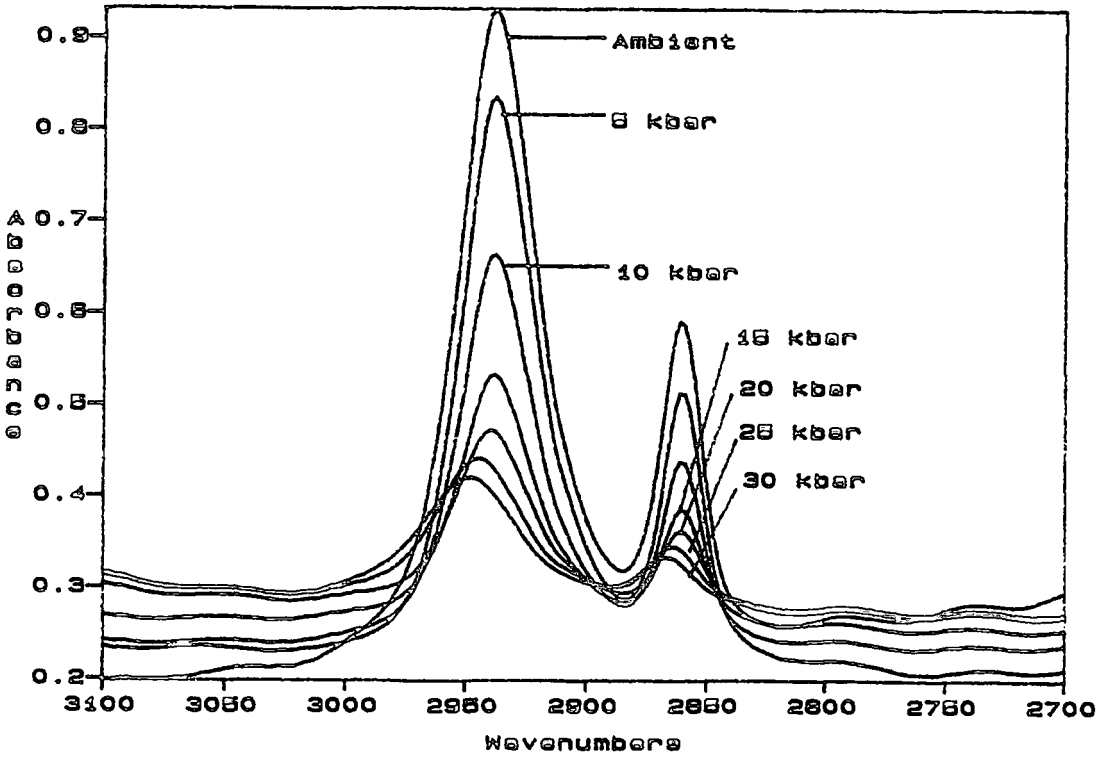

Figure 6.2. The CH_2 stretching region with increasing pressure for BCS.

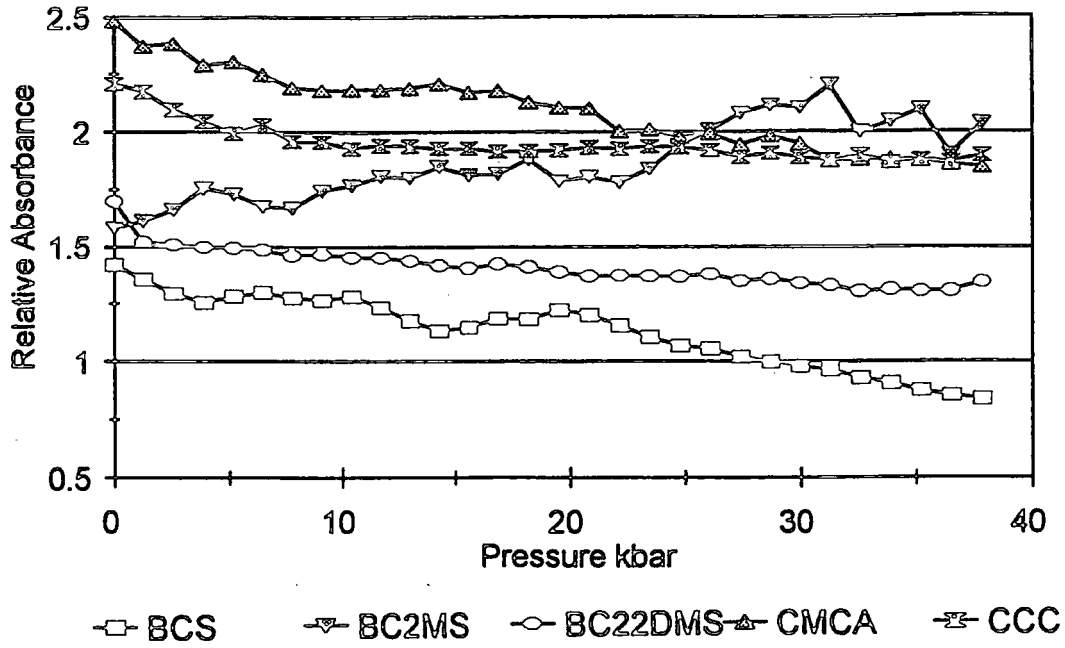

Figure 6.3. Intensity ratio of the CH_2 stretching region against the overall carbonyl stretching region with increasing pressure.

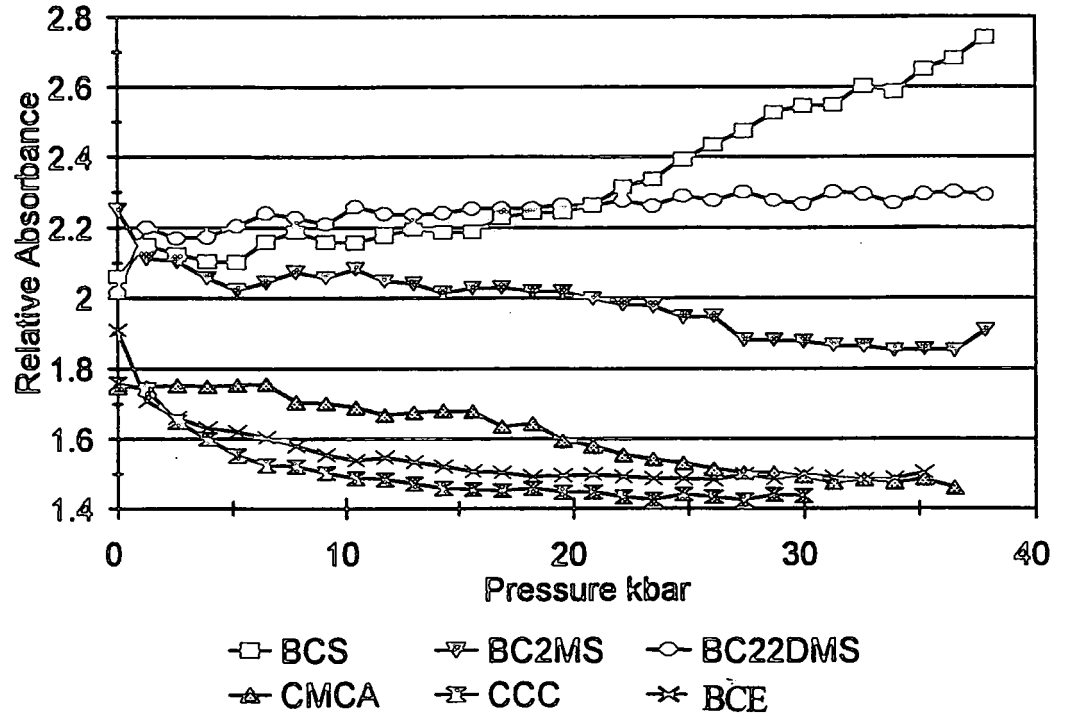

Figure 6.4. Peak height ratio of the antisymmetric CH_2 stretching region against the symmetric CH_2 stretching region with increasing pressure.

6.2.2. Carbonyl Stretching Region

There is very little change in the peak frequency of the carbonyl region for the studied molecules as a function of pressure. However, BC22DMS (figure 6.5) shows an increase of $6cm^{-1}$ and CMCA shows a decrease of $4cm^{-1}$ (figure 6.6.). This indicates a competition of effects. For BC22DMS, it seems that the repulsive part of the potential is dominating the frequency shift for the overall band, whereas for CMCA the attractive part of the potential is dominating. The apparent lack of shift for the other molecules may indicate a cancelling of the attractive potential by the repulsive part which would provide no visible change.

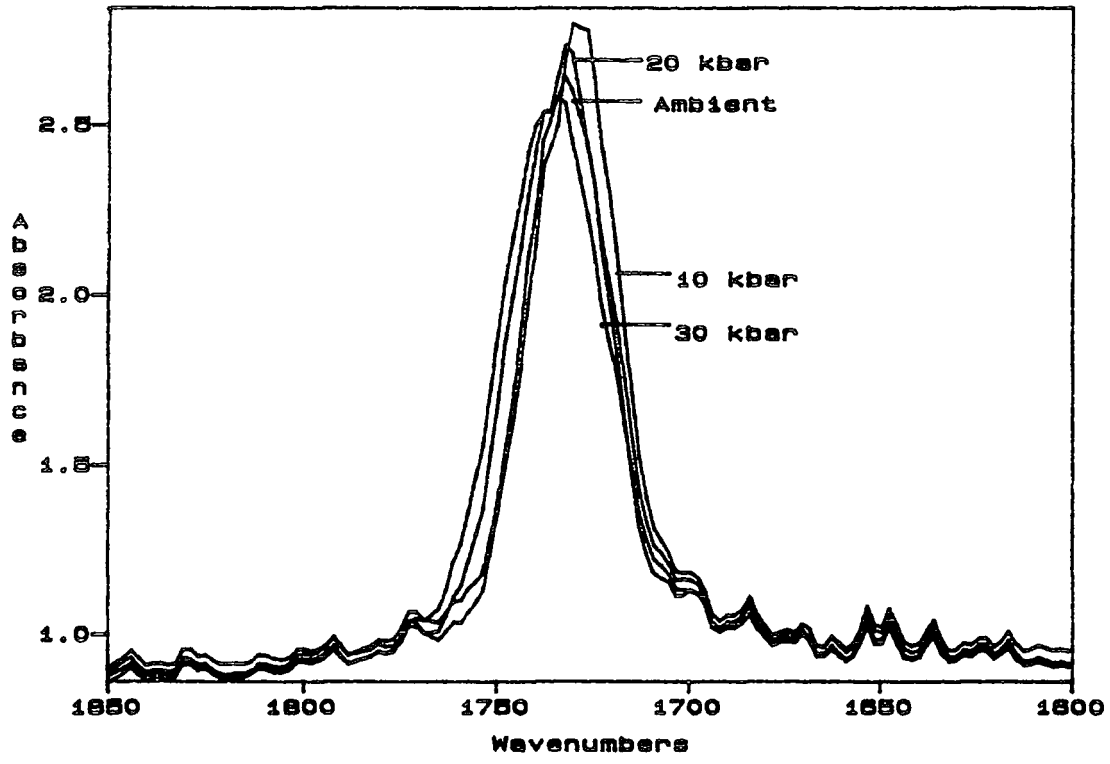

Figure 6.5. The carbonyl stretching region for BC22DMS.

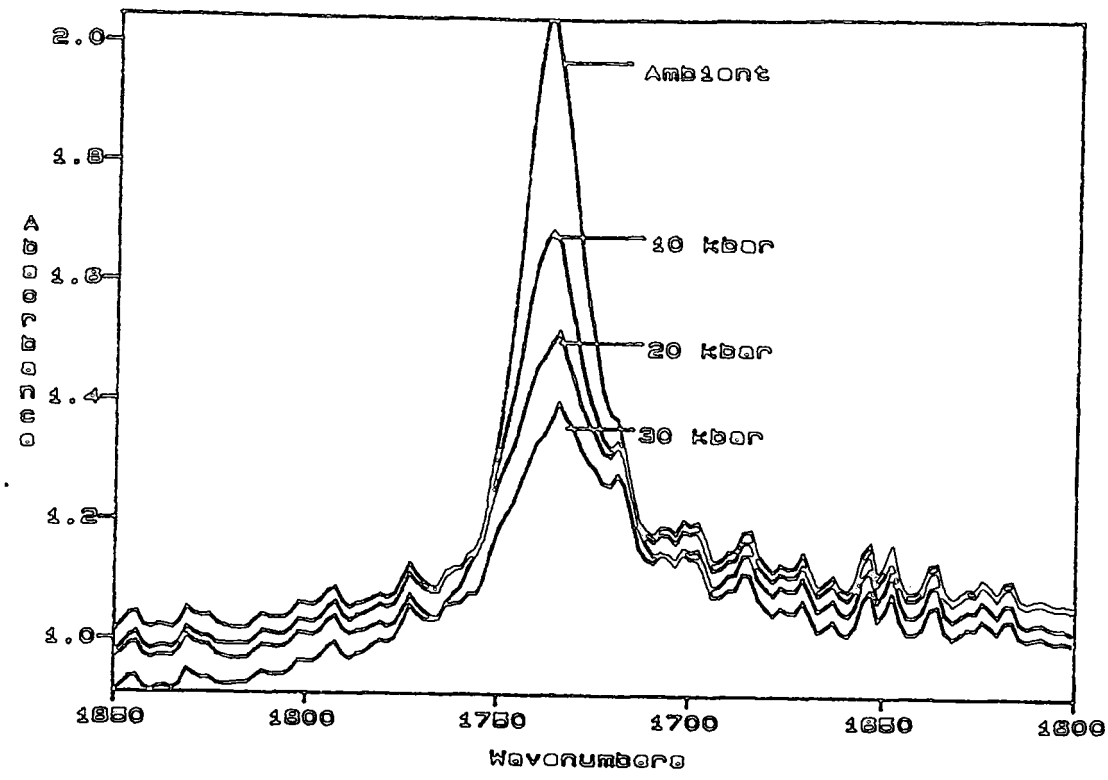

Figure 6.6. The carbonyl stretching region for CMCA

The bandwidths of the carbonyl bands all increase with the molecules only containing one carbonyl group exhibiting the largest change. It should be noticed that there is a difference in widths of this band between the diester compounds and the monoester compounds, with the width of the former (due to the presence of at least two bands) being somewhat larger. This again might be indicative of a cancellation of effects. If the bands within the overall carbonyl envelope for the diester compounds exhibit different behaviour when compressed, (which is likely) then the overall effect may well be one of no change to the overall band. It is also possible that the behaviour is a consequence of the competing effects of an increase in environmental modulation time and the alignment of the carbonyl groups. A decrease in the rate of modulation of a vibration will effectively increase the vibrational relaxation rate, and thus the bandwidth. Whilst the relaxation rate and the bandwidth will decrease with increased alignment, due to the fewer environments for the vibrational mode.

On ratioing the overall peak heights, interesting behaviour is seen on ratioing the carbonyl stretching region against the CH_2 ring scissors band for BCS. The graph increases to a maximum and is then seen to decrease to its original value at which point a positive gradient is seen. The other molecules all exhibit little change. (figure 6.7) The ratio of the carbonyl stretching region against the ester stretching band again shows different behaviour when compared to the other molecules. BC22DMS shows a positive gradient whilst the other molecules give negative gradients. (figure 6.8)

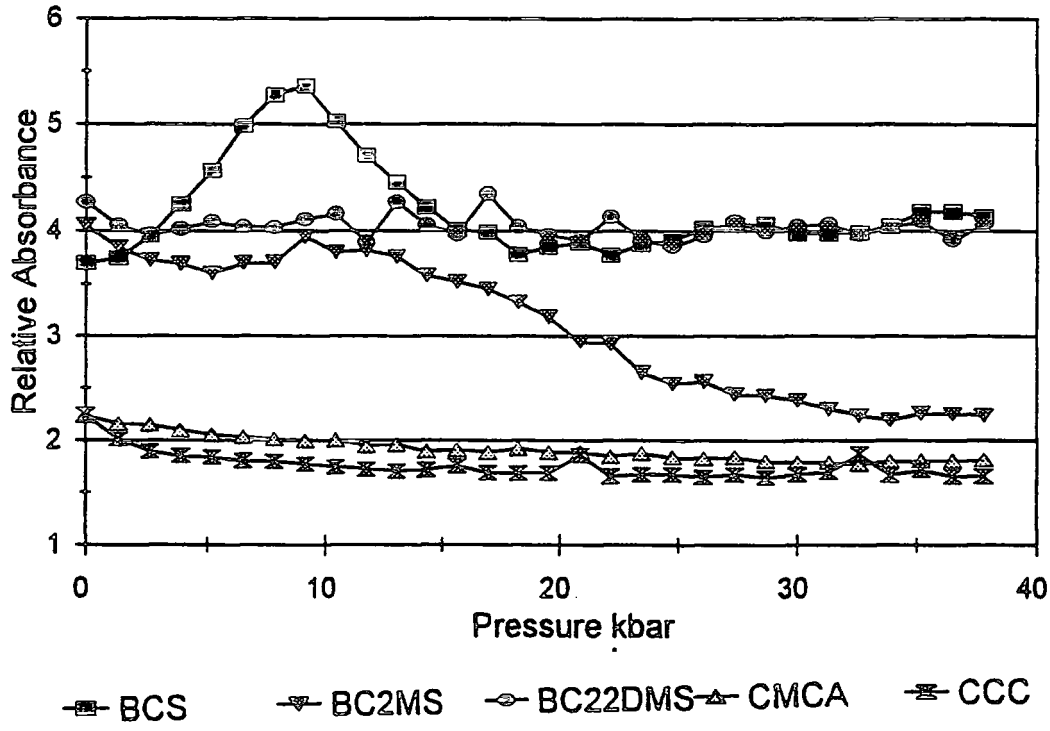

Figure 6.7. Peak height ratio of the carbonyl stretching region against the CH_2 ring scissors region with increasing pressure.

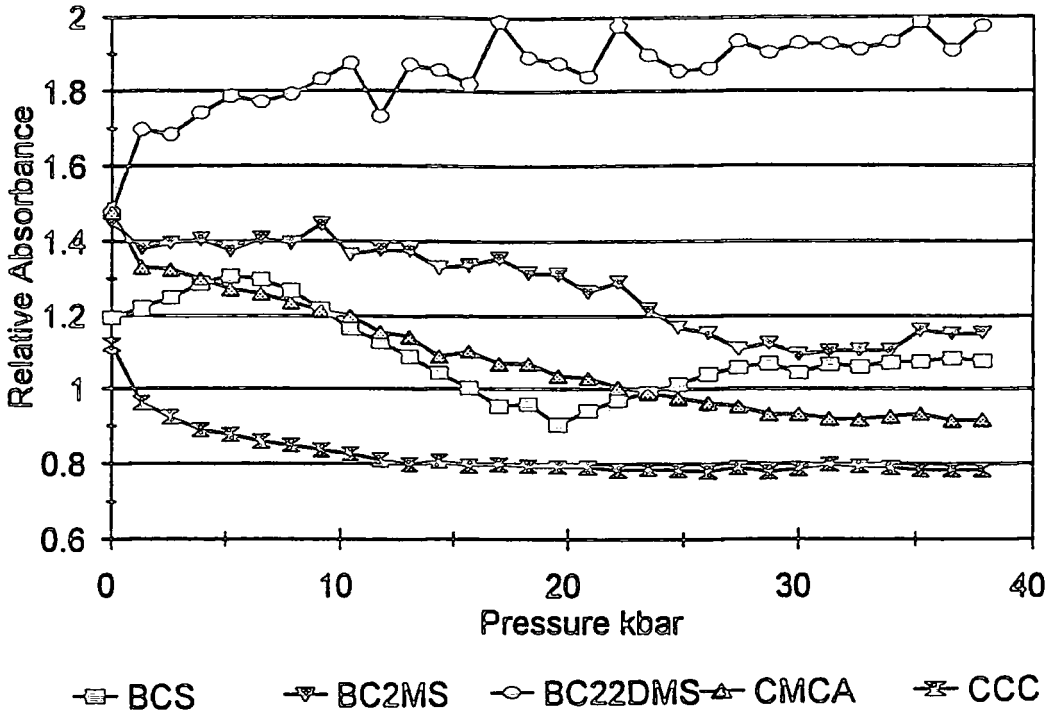

Figure 6.8. Peak height ratio of the carbonyl stretching region against the ester stretching region with increasing pressure.

6.2.3. CH_2 Ring Scissors Band

Little change is exhibited in the peak frequencies of the CH_2 ring scissors mode. With a slight increase being exhibited by the diester compounds indicating that the repulsive part of the potential is again more dominant than the attractive part. Figure 6.9 shows the 1500-800cm^{-1} region for BCS.

BCS and BC22DMS show similar behaviour to one another with regards to bandwidth changes, both giving an increase of ~10cm^{-1} over the pressure range. The other molecules show relatively little change.

It proved very difficult to resolve this band accurately at high pressures due to the presence of water vapour. Although spectral subtraction was attempted, reliable data was hard to achieve.

The peak height ratios exhibiting any change using this band have already been mentioned. (i.e. using the antisymmetric CH_2 stretching mode and the carbonyl regions).

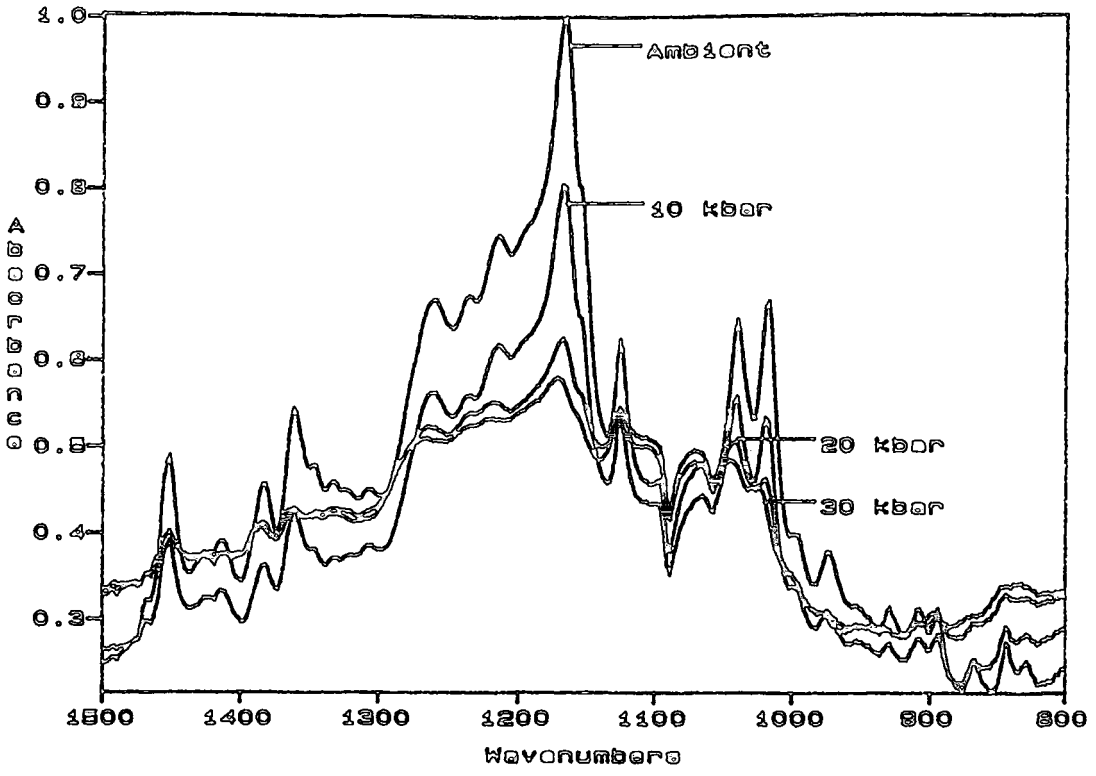

Figure 6.9. 1500-800cm^{-1} region with increasing pressure for BCS.

6.2.4. Ester Stretching Region

All the peak frequencies for the ester stretching region exhibit an increase with BC22DMS (figure 6.10.) showing the largest change. The interactions controlling the frequency of this band are obviously localised in the repulsive part of the potential for all the molecules.

There is a dramatic increase in the bandwidth of this mode for all molecules indicating an increase in the vibrational relaxation rate of this mode.

Again, all the observations when ratioing peak heights have already been made in previous sections.

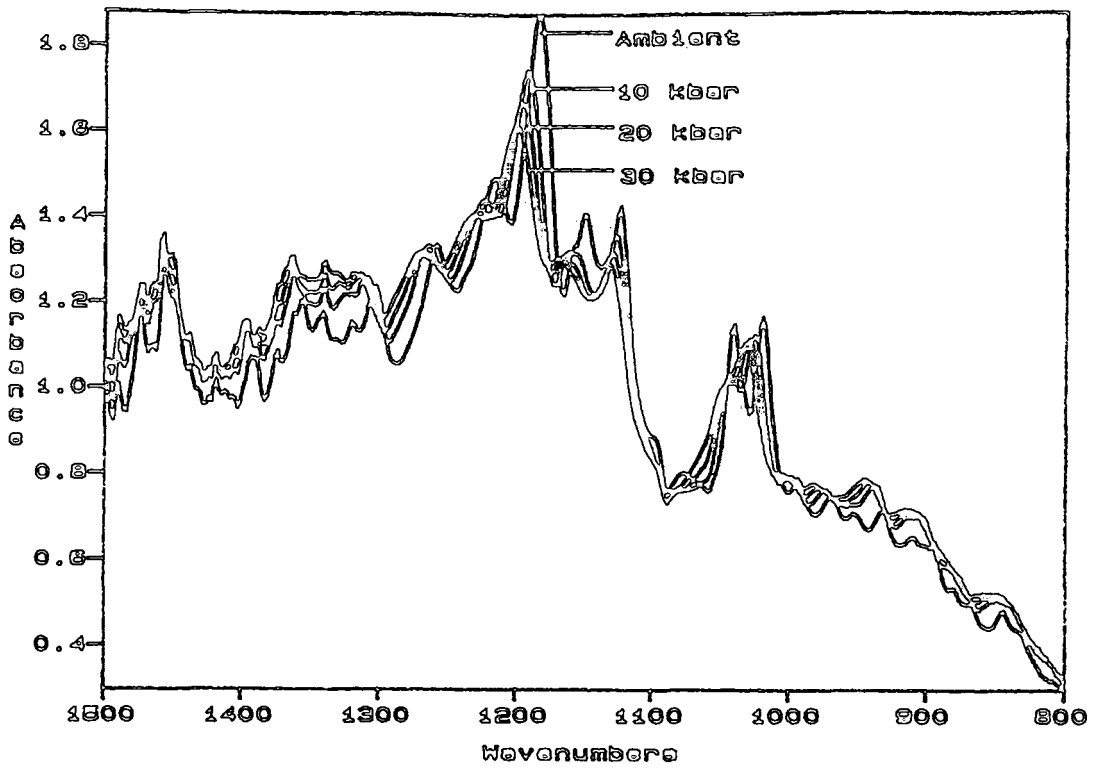

Figure 6.10. 1500-800cm^{-1} region with increasing pressure for BC22DMS.

6.2.5. Other Bands

All other bands show a slight increase in frequency with pressure as would be expected, and they all broaden as pressure is increased.

6.3. Discussion

The application of pressure to molecules in the condensed phase has been shown to give a red shift (i.e. to lower frequency), a blue shift (i.e. to higher frequency), or little change in behaviour.[1-4] A delicate balance exists between the opposing effects of repulsive and attractive interactions which is altered by the increased pressure.

Relaxation processes in a liquid are dependent on intermolecular and intramolecular interactions. This implies that on increasing the pressure it would be expected that the bandwidths would exhibit some change. A change in intermolecular and intramolecular interactions can also cause conformational changes, which can result in the suppression or enhancement of any bands dependent on the conformation of the molecule.[5]

If the magnitude of the transition dipole moment of a vibrational mode is altered by increased pressure this will also effect the absolute intensity of a band.

Due to the closeness of many of the bands, a reliable quantification of the relative band intensities or band widths was not possible, especially at high pressures when band overlap becomes more significant.

6.3.1 Peak Frequencies

6.3.1.1 CH_2 Stretching Region

The antisymmetric stretching region and the symmetric stretching region exhibit the largest frequency shifts for all molecules, with the change for the antisymmetric band being the greatest.

It is well known in the literature[7] that normal modes of each CH_2 group can couple with the corresponding modes of neighbouring CH_2 groups according to various phase angles. Most of these coupled modes are weak in the infra red and Raman spectra[6] except for those with $\phi=0$ (Raman active, in phase) and $\phi=\pi$ (infra red active, out of phase). In order to understand the effect of pressure on the CH_2 modes the volume change during the stretching cycle with $\phi=0$ and $\phi=\pi$ needs to be assessed.

For the symmetric stretch when $\phi=0$, all the CH_2 groups are stretching symmetrically in phase, which induces a large volume change between the maximum and minimum amplitudes of the CH bonds during each stretching cycle.

For the symmetric stretching region when $\phi=\pi$, any of the CH_2 groups increases its volume by the maximum stretching of the CH bonds within each half of the stretching cycle, while the neighbouring CH_2 group decreases its volume at the same time by the maximum contraction of the CH stretch. Thus, the net volume change associated with the symmetric CH_2 mode for $\phi=\pi$ is significantly smaller.

For the antisymmetric mode, the volume change during each CH_2 stretch is approximately the same for both $\phi=0$ and $\phi=\pi$. Therefore, for Raman bands it would be expected that the symmetric stretch would exhibit a large frequency change and this would be larger than for the corresponding antisymmetric mode. For infra red bands the symmetric mode would exhibit a small frequency change with increased pressure which would be expected to be less than for the antisymmetric stretch. This has been shown to be true, by Wong et al, for n-hexadecane.[7]

Therefore, the difference between the symmetric and antisymmetric modes can be readily explained as being due to the effect of the intramolecular vibrational coupling of these modes with the corresponding modes on adjacent CH_2 groups.

The large shift for BC22DMS (figure 6.1.) might also be attributed to the presence of the branching methyl groups on the hydrocarbon chain between the cyclohexyl rings. It was noted by Wong[7] that for n-hexadecane, the largest pressure/frequency shift of all the modes was exhibited by the antisymmetric CH_3 stretching region.

There may well be significant contributions from Fermi resonance (FR) effects. These arise largely from FR interaction between the symmetric C-H stretching fundamentals and a dispersion of overtones of the C-H bending fundamentals. Increasing the pressure changes the contributions from FR to the CH stretching region, due to changes in the frequency range of the CH bending overtones.[6] These changes will effect the intensities and bandwidths of the symmetric CH stretching bands and CH bending overtones, and to a lesser extent the frequencies of these bands.

Changes in the dispersion of the CH bending overtones are caused by conformational changes which effect both intermolecular and intramolecular CH coupling. Observations of these changes in FR with increased pressure are more noticeable with the Raman spectra of the CH stretching region[8] because the overtone bands are more intense than in the infra red. However, the changes in FR are reflected in the infra red spectra of the region. These changes can manifest themselves as a loss of intensity of the symmetric CH_2 stretching band as a direct consequence of changes in FR with increased interaction. This causes a redistribution of intensity between the symmetric CH_2 stretching mode and the CH overtones brought about by increased FR.

6.3.1.2. Carbonyl Stretching Region

As mentioned previously, there is no change in the peak frequencies for the carbonyl envelopes of BCS and BC2MS. There is however an increase in frequency seen for BC22DMS, but it is difficult to interpret this as there are obviously at least two contributions to the overall band.

The monoester compounds (i.e. CMCA and CCC) do not have this difficulty. There is a shift to low frequency for CMCA (figure 6.6.). The sum of attractive forces (which produce a negative frequency shift) and repulsive forces (which produce a positive shift) can result in an overall positive or negative shift. Both types of forces should increase with increasing density in the bulk fluid, because the intermolecular distance decreases.

The repulsive interactions are usually[9] assumed to vary with R_{AB}^{-12}. However, from the Lennard-Jones potential (figure 2.6) it is seen that the attractive forces vary more noticably and R_{AB}^{-6} is usually taken to be the average value, but it can vary between R_{AB}^{-3} and R_{AB}^{-8}. Therefore, it is more usual to see increased vibrational frequencies with increased density, indicating that repulsive interactions increase more rapidly than the attractive interactions. However, if there is an additional variable that affects the attractive interaction energy which is altered by increased density, e.g. rotational alignment, then the attractive interactions can increase more rapidly with pressure than the repulsive interactions, because the dipoles are more effectively aligned.

It is likely that attractive interactions, most probably dipole-dipole, localised at the carbonyl groups play an important role in determining the spectroscopic properties of the carbonyl stretching mode of all the molecules studied. Observations of a decrease in frequency for CMCA with increased pressure suggest that the dipole interactions for this group increase with pressure. This gives an increased alignment of the dipoles and a consequently large increase in the interaction energy with decreasing intermolecular distance. However, CCC exhibits an increase in frequency with increased pressure. This implies that for this molecule, that repulsive interactions are dominant. The differences in behaviour of the two molecules may well be explained by the longer chain separating the cyclohexyl rings for CMCA. For CCC, with the longer chain separating the cyclohexyl rings, there is more chance of the internal movement of the chain disrupting the dipole-dipole interactions of the carbonyl group. This will result in an overall increase in repulsive interactions and will give a blue shift in frequency.

It is also possible that as the pressure is increased, the compounds undergo a phase change.

A decrease in peak frequency has been observed for acetone[3] and Wong et al[5] observed that the frequency of their ester carbonyl in dioleoyl phosphatidylethanolamine decreased. However, after these initial decreases, an increase then occurred indicating that the repulsive part of the potential became more important. This is not observed for the molecules studied in this thesis, although there is no way of proving this for the diester compounds due to the presence of at least two separate bands in the carbonyl band.

6.3.1.3. Ester Stretching Region

The ester stretching region exhibits an increase in peak frequency (figures 6.9 and 6.10) apart from CCC which shows no shift at all. The relatively large shift may indicate that the C-O vibration is strongly influenced by the change in repulsive potential. The close proximity of the carbonyl group may also influence the frequency shift. If an increase in the density causes a conformational change, then it may also effect the intramolecular coupling between the C-O and the carbonyl group. A decrease in the

in the dipolar coupling would cause a blue frequency shift. Such a change in coupling would also effect the carbonyl mode.

As mentioned in chapter 5, the difference in behaviour between the carbonyl stretch and the ester stretch may well be attributed to the difference between intermolecular interactions and intramolecular interactions. If this is true, it seems that there is a large difference. The increasing pressure and hence the density has little visible effect on the carbonyl peak frequency for the diester compounds, although this may be due to the different behaviour of the bands contained in this mode. There is a slight decrease in frequency for CMCA indicating that the attractive potential is dominant and hence the intermolecular interactions are enhanced. However, for the ester stretch there is an increase in peak frequency indicating that the repulsive part of the potential is the dominant factor in the intramolecular interactions. This may well arise from interactions with the carbonyl group or some involvement with the bulky cyclohexyl rings. As the largest change is exhibited by BC22DMS, it seems that the branching methyl groups also play an important part in intramolecular interactions.

6.3.1.4 Other Modes

All other modes, apart from the CH_2 ring scissors mode which exhibits little change, show an increase in frequency with pressure. This implies that the interactions of the vibrational modes with the repulsive potential dominates the frequency shift. The extent of this shift is dependent on how much a vibration interacts with the changing potential. Modes involving a large volume change should show a greater increase in frequency over modes involving a smaller amplitude of vibration. This has been observed in many studies[4,7,10]. It should be noted that the extent of any shift will also be affected by the change in attractive interactions, which like the repulsive interactions vary from mode to mode.

6.3.2 Vibrational Relaxation as a Function of Pressure

In relatively complicated molecules, e.g. BCS, it can be expected that many different relaxation processes contribute to the observed relaxation rates of the vibrational modes. Provided that these are statistically uncorrelated then each of these processes contributes a bandwidth increment to the overall bandwidth. The vibrational relaxation rate τ_v^{-1} can be represented by

$$\tau_v^{-1} = \tau_1^{-1} + \tau_2^{-1} + \tau_3^{-1} + \ldots\ldots \qquad 6.1$$

where τ_1^{-1}, τ_2^{-1} and τ_3^{-1} represent the contributions from the separate relaxation processes. It is usual[9,11-13] to assume that the vibrational dissipative energy transfer contributes a negligible amount to the overall vibrational relaxation.

It is reasonable to discount vibrational population relaxation since the vibrational energy in the process is transferred to the rotational and translational energy of the molecules. This is an ineffective mechanism since the Fourier frequency components of the effective motions match poorly with the vibrational frequencies involved in infra red and Raman spectroscopy. ($\hbar\omega \rangle\rangle k_b T$)

Only molecular collisions of particularly high energy are able to cause vibrational

de-excitation and the probability of such high energy events is low[14]. Therefore, even in a regime of short-range rapidly fluctuating intermolecular forces vibrational energy dissipation should contribute considerably less to vibrational relaxation than vibrational dephasing.

From the Raman measurements (see chapter 4 and equation 2.38), it can be seen that the reorientational motion of BCS at ambient temperature does not contribute significantly to the vibrational bandwidths of BCS. Assuming that reorientational motions will become even more restricted at high densities ($\tau_{rot} \propto \eta$)[9,15,16], then any contribution to the band widths from reorientational motion can be ignored without bringing any errors into the interpretation. Therefore, it is assumed that for BCS that the bands are broadened by vibrational dephasing alone.

Vibrational dephasing contains contributions from inhomogeneous and homogeneous broadening processes.

Inhomogeneous broadening gives rise to a broadening due to a certain distribution of frequencies around a mean value, which is a consequence of the interaction of the individual molecules with the surrounding bulk. The homogeneous contribution to the dephasing is caused by short range rapidly varying dynamical processes. This is a consequence of loss of phase due to molecular "collisions." (see chapter 2)

For phase relaxation, the Kubo model for vibrational dephasing is frequently employed[18,19]. The relaxation function $\phi_{pp}(t)$ is expressed as

$$\phi_{pp}(t) = \exp\{-\langle \Delta\omega^2 \rangle [t\tau_m + \tau_m^2 [\exp(-t/\tau_m) - 1]]\} \qquad 6.2$$

where $<\Delta\omega^2>$ is the mean square frequency fluctuations (shift) due to the different interactions of a particular mode with the surrounding "potentials" (equivalent to the vibrational second moment $M2_v$), and τ_m is the modulation (or correlation) time which is related to the time scale of these "bulk" fluctuations. The subscript pp indicates a pure phase relaxation process. Both homogeneous and inhomogeneous dephasing mechanisms can be considered in terms of the Kubo stochastic line shape theory. If the dephasing process is a rapid modulation process then a Lorentzian line shape will occur, whilst if slow modulation is occurring a Gaussian line shape will be produced. If the overall process is a mixture of both processes then an intermediate or Voigt line shape will occur.

Vibrational dephasing arising from a distribution of frequencies that are modulated by translational or reorientational motion is referred to as inhomogeneous broadening. Whilst if the modulation process is vary rapid i.e. due to collisions, the dephasing process is considered to be homogeneous. Therefore for very fast modulations, the effects of the (inhomogeneous) environment are diminished and the process is mainly dependent on the modulation rate. Homogeneous broadening is

therefore in the rapid modulation limit. Whilst inhomogeneous broadening can, depending on the conditions, be in the fast or slow modulation limit, or be intermediate between the two.

6.3.2.1. Vibrational Dephasing of the Carbonyl Stretching Mode

The infra red band of the carbonyl stretching region for all the molecules studied exhibits an increase in width with increasing pressure (see figures 6.5., 6.6., 6.11. and 6.12). As in the previous chapter, the carbonyl band for the diester molecules was fitted to two bands, their peak frequencies being given by Fourier deconvolution. The fitted bands data is given in tables 6.13-6.15.

Table 6.13. Peak fitted data for the carbonyl stretch of BCS. The peak centres were fixed at the values given on Fourier deconvolution. i.e. 1738.72 and 1729.07.

Pressure kbar	Abs	Width cm^{-1}	Intensity	Abs	Width cm^{-1}	Intensity
0	0.56	13.36	10.89	0.78	16.30	16.87
5	0.65	16.06	14.74	0.65	13.60	12.61
10	0.44	14.47	8.96	0.48	14.00	9.59
15	0.32	16.91	7.69	0.29	13.73	6.54
20	0.20	18.75	6.39	0.21	14.35	4.29
25	0.14	19.79	3.99	0.24	16.77	6.79
30	0.14	21.35	4.24	0.23	17.67	6.76
35	0.16	23.63	6.33	0.19	18.50	6.04

Table 6.14. Peak fitted data for the carbonyl stretch of BC2MS. The peak centres were fixed at the values given on Fourier deconvolution. i.e. 1737.98 and 1728.33.

Pressure kbar	Abs	Width cm^{-1}	Intensity	Abs	Width cm^{-1}	Intensity
0	1.07	18.82	28.70	0.78	16.30	16.87
5	0.84	16.06	19.08	0.65	13.60	12.61
10	0.66	16.24	14.28	0.48	14.00	9.59
15	0.52	16.57	12.22	0.29	13.73	6.54
20	0.39	17.92	9.82	0.21	14.35	4.29
25	0.29	22.90	9.24	0.24	16.77	6.79
30	0.25	24.35	8.51	0.23	17.67	6.76
35	0.29	28.65	11.69	0.19	18.50	6.04

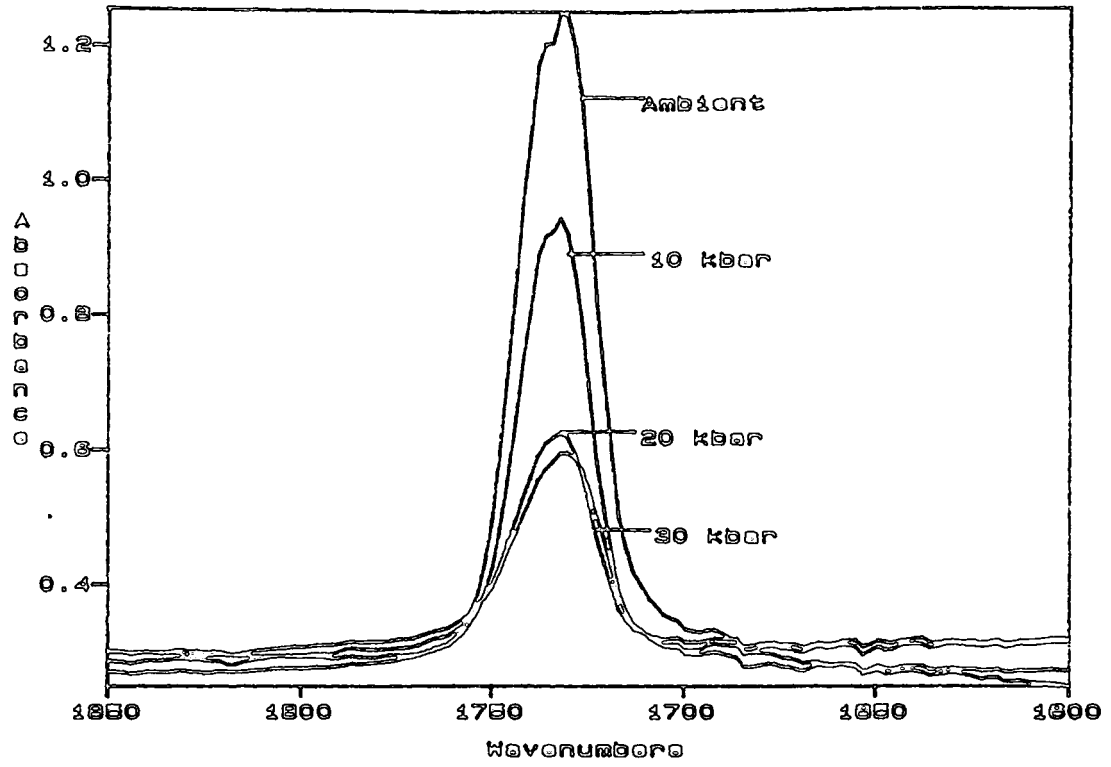

Figure 6.11. The carbonyl stretching region for BCS.

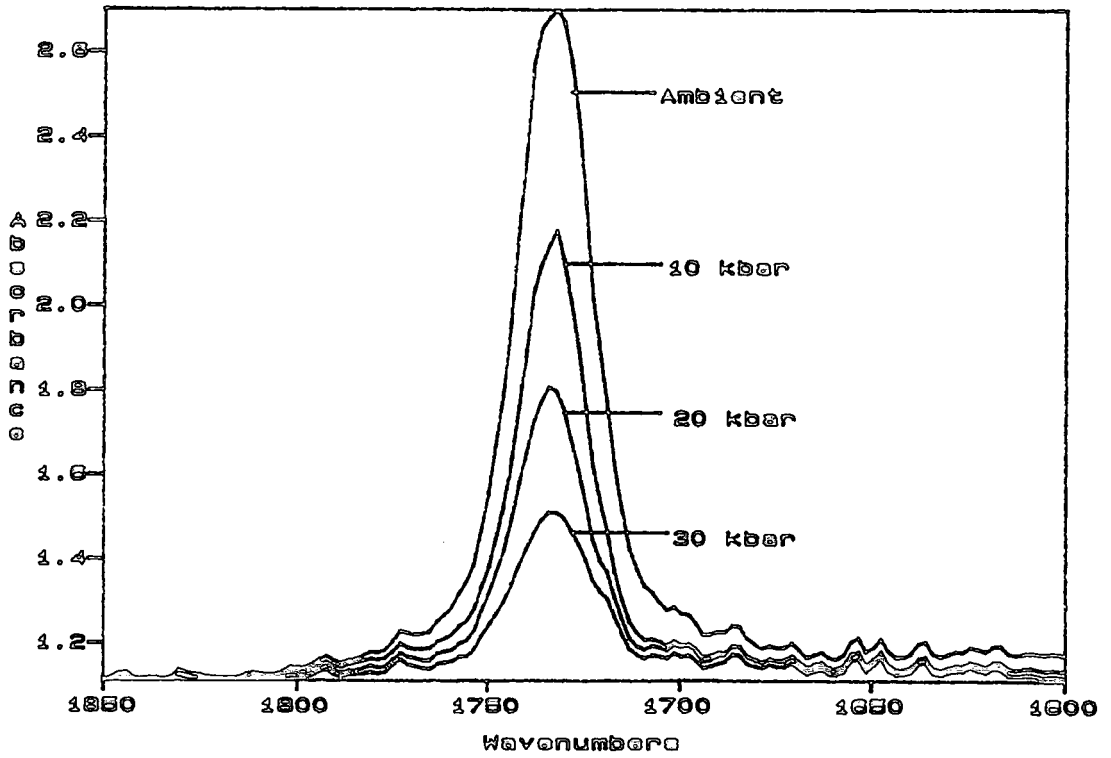

Figure 6.12. The carbonyl stretching region for BC2MS.

Table 6.15. Peak fitted data for the carbonyl stretch of BC22DMS. The peak centres were fixed at the values given on Fourier deconvolution. i.e. 1739.69 and 1727.16.

Pressure kbar	Abs	Width cm^{-1}	Intensity	Abs	Width cm^{-1}	Intensity
0	0.88	16.39	19.28	1.40	19.75	39.42
5	0.52	13.28	9.76	1.78	22.08	56.82
10	0.64	16.21	14.81	1.67	22.91	54.14
15	0.81	17.56	20.17	1.46	23.70	49.17
20	0.94	20.57	27.37	1.24	26.40	44.67
25	1.03	21.56	31.64	1.10	26.73	41.88
30	1.19	23.95	40.42	0.88	27.36	33.98
35	1.32	27.47	51.72	0.58	30.85	26.56

As can be seen from figures 6.13-6.15, the fitted data also show an increase in bandwidth with the high frequency part exhibiting the greatest increase. This increased bandwidth indicates an increase in the vibrational relaxation rate (FWHM $\propto \tau_v^{-1}$). It was seen that this mode for CMCA was effected by an increase in attractive interactions with increased pressure, most probably due to a significant relative increase in the alignment of the dipoles. Although it was not apparent from the data, it is likely that this is also true for the other molecules up to a certain pressure, after which an increase in the repulsive part of the potential is usually seen, as it is well known that this occurs for molecules containing a carbonyl group.[3,7,20]

It should be noted that CCC exhibited an increase in repulsive interactions (i.e. a shift in frequency to higher wavenumber). If the structures of the studied molecules are observed, it can be seen that CCC has only the ester functionality separating the cyclohexyl rings whereas the other ester containing molecules contain methylene groups in the joining chain. Therefore, as there is relatively less chance of the internal motions of the chain preventing repulsive interactions of the CCC molecules, a blue frequency shift would be expected for this band. As the length of the joining chain for the other molecules is similar in size to that of CMCA, it would be expected that the behaviour of the diester compounds would follow that of CMCA.

If inhomogeneous broadening, due to attractive force frequency fluctuations, of this mode is considered to be in the fast modulation regime (Lorentzian line shape), then in accordance with the Kubo model

$$FWHM \propto \tau_v^{-1} = M2_v \tau_m \qquad 6.3$$

and the product $M2_v\tau_m$ (see equation 6.2 for definitions) must be increasing with pressure. In contrast, if the dephasing is assumed to be in the slow modulation limit (Gaussian line shape), then

$$FWHM \propto \tau_v^{-1} = 2(2\ln 2)^{1/2}(M2_v)^{1/2} \qquad 6.4$$

and $M2_v$ must be increasing.

For the interpretation of the changes in bandwidths it is necessary to consider the effect of pressure on the vibrational first (frequency shift) and second moment ($M2_v$). It has been shown[21,22] that in the Kubo model for vibrational dephasing the first moment, arising from dipole-dipole interactions (which dominate the interaction of the carbonyl groups), may be written as

$$\langle \Delta\omega \rangle_{dd} = (NM_{tt}/R_0^3)\langle K_{ij} \rangle \qquad 6.5$$

where N is the mean number of nearest neighbours (within the first solvation shell), M_{tt} is related to the transition dipole ($\partial\mu/\partial Q$), K_{ij} is the orientation function given in the binary point dipole approximation[22] by

$$K_{ij} = -2\mathrm{Cos}\theta_i\mathrm{Cos}\theta_j + \mathrm{Sin}\theta_i\mathrm{Sin}\theta_j\mathrm{Cos}\phi_{ij} \qquad 6.6$$

θ_i and θ_j are the angles made by the two dipoles i and j with an axis through their centres and ϕ_{ij} is the dihedral angle between them (figure 6.16.), and R_0 is the distance to the first peak in the radial distribution function.

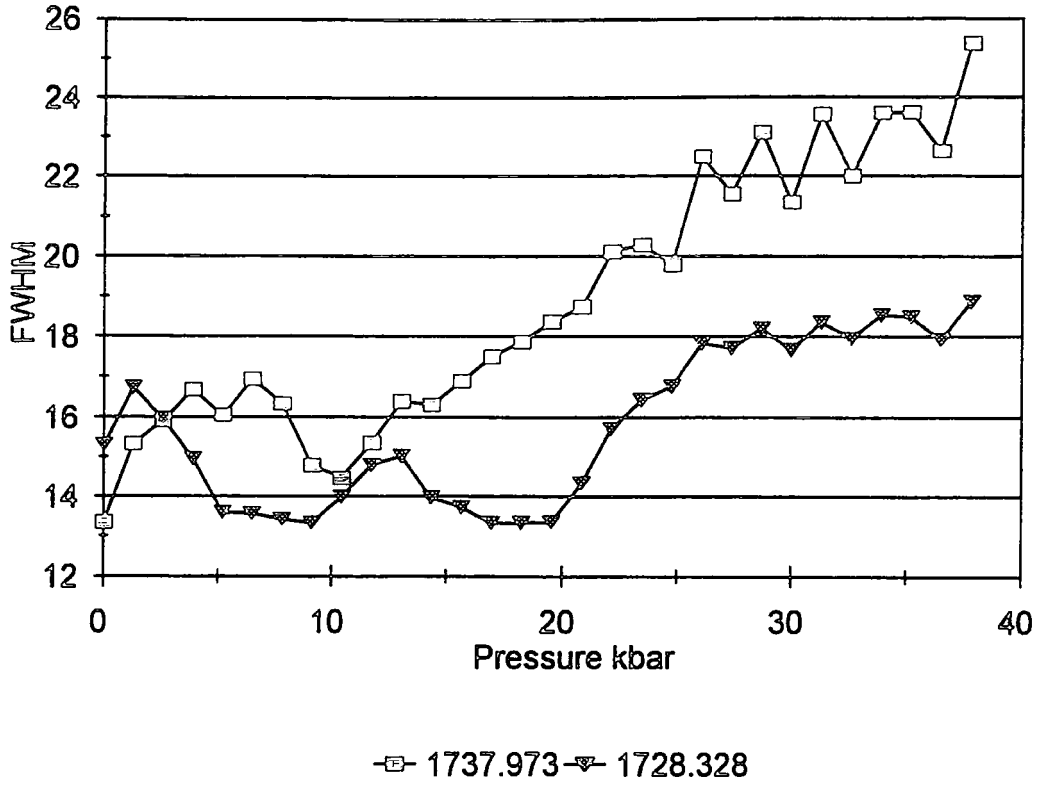

Figure 6.13. FWHM for the fitted bands of the carbonyl stretching region for BCS.

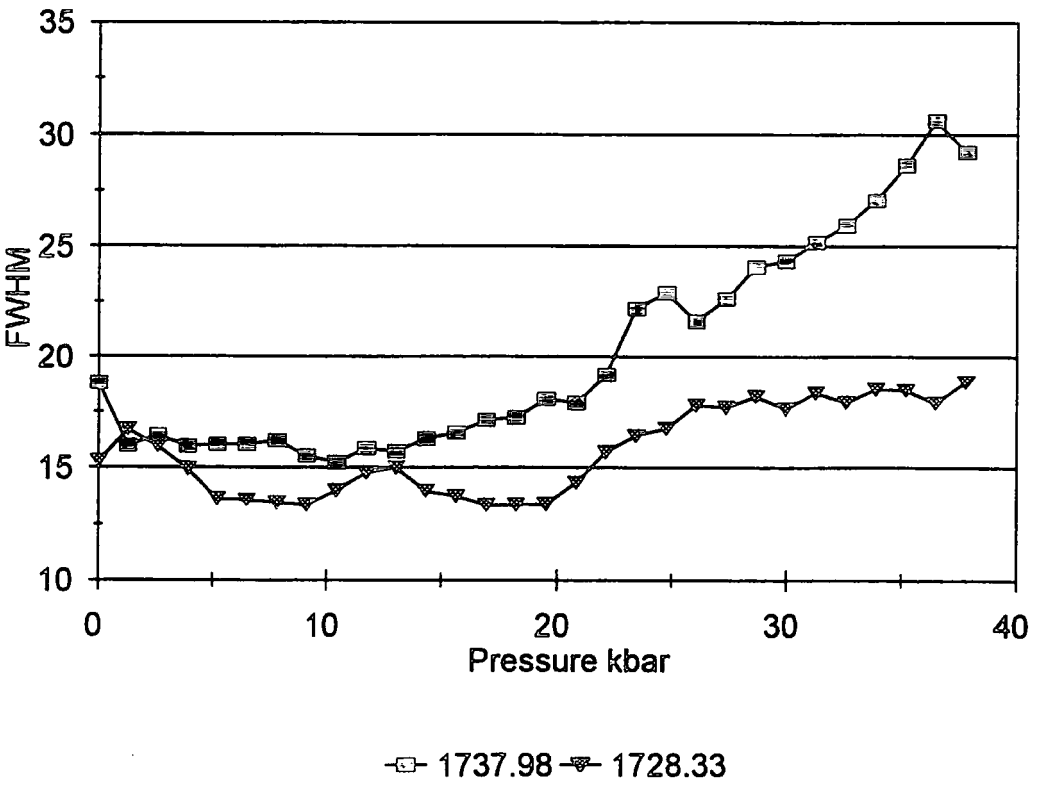

Figure 6.14. FWHM for the fitted bands of the carbonyl stretching region for BC2MS.

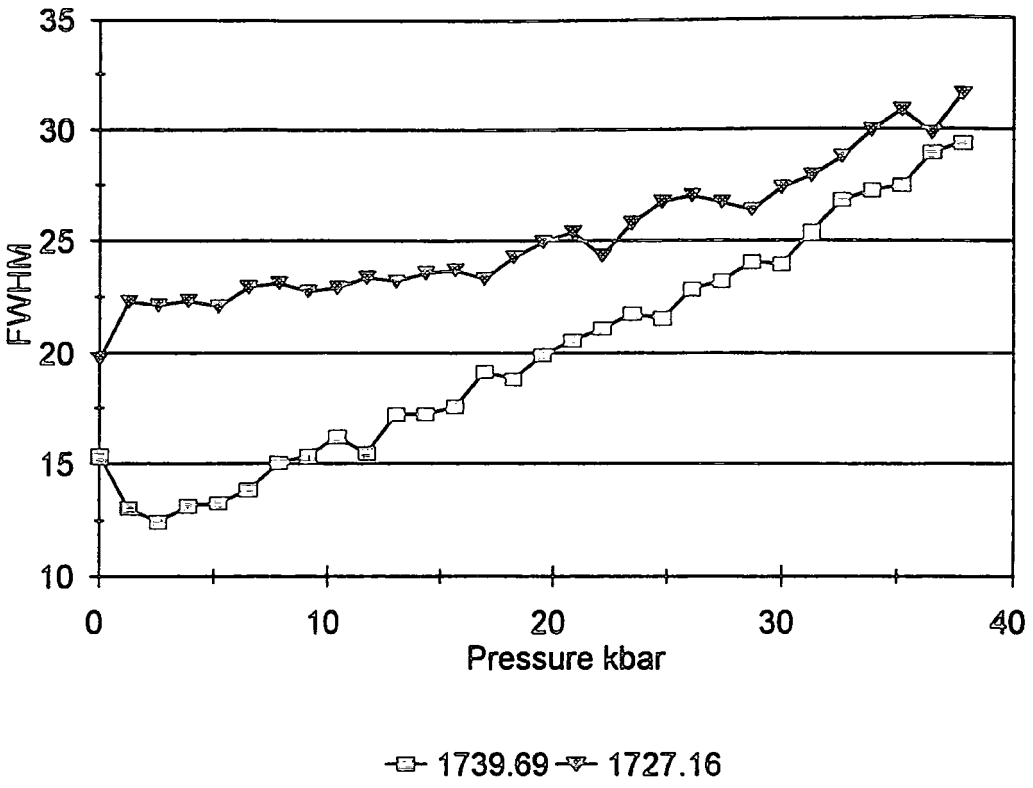

Figure 6.15. FWHM for the fitted bands of the carbonyl stretching region for BC22DMS.

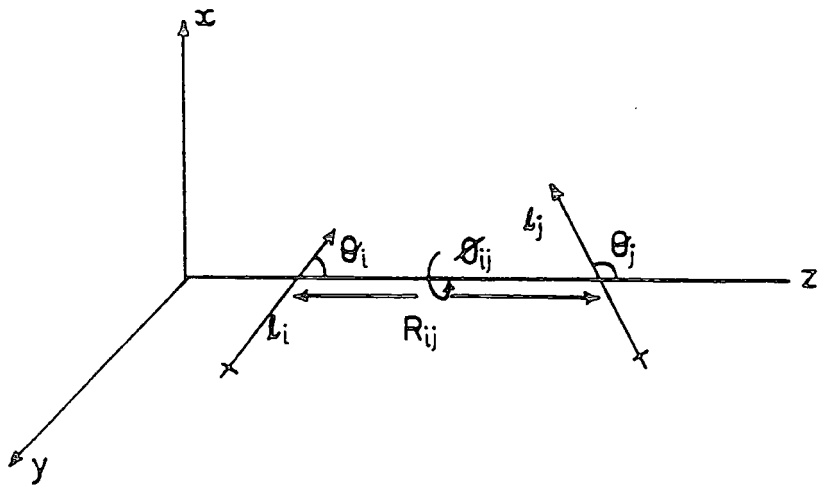

Figure 6.16. Geometrical configuration of the pair of transition dipoles μ_i and μ_j which defines the parameter K_{ij}

The first moment or frequency shift is related to the orientational ordering in the first solvation shell e.g. K_{ij} becomes more negative as for example, θ_i and θ_j approach zero and the two dipoles become aligned with each other. The contribution to the first moment from dipole-dipole interactions vanishes in the absence of orientational order. Consequently, it is expected that a negative frequency shift is induced by increased alignment.

The second moment is given by

$$\left\langle \Delta\omega^2 \right\rangle_{dd} = (NM_{tt}^2 / R_o^6)\left\langle K_{ij}^2 \right\rangle \qquad 6.7$$

This is related to the distribution of dipoles (oscillators) in the first solvation shell. It is largely determined by the width of the first peak in the radial distribution function and therefore is expected to decrease as local order increases and vice versa.

If the system is in the fast modulation limit, then because $M2_v\tau_m$ increases with pressure for BCS, τ_m must be increasing at a faster rate than the rate of decrease of $M2_v$. It is not surprising that τ_m would increase significantly with pressure for BCS. For long ranged attractive potentials, τ_m may be identified with a rotational or translational correlation time. Therefore, it would follow

$$\tau_m (\equiv \tau_{rot} \text{ or } \tau_{trans}) \propto \eta/T \qquad 6.8$$

and provided that the system is in rapid modulation limit[15,16,23], $M2_v \propto \rho$

$$\tau_v^{-1} \propto \frac{\rho\eta}{T} \qquad 6.9$$

For short range potentials τ_m may be identified with a time between collision and homogeneous broadening. It has been shown[24] that

$$(\tau_{ph})^{-1} = \frac{9}{2}\cdot\frac{\mu\gamma^2}{M^2}\frac{kT}{\omega^2 L^2}\frac{1}{\tau_c} \qquad 6.10$$

where M is the reduced mass of the oscillator with frequency ω, L measures the range of the interaction[25], γ is a mass factor, μ is the reduced mass of the system involved in the collision, and τ_c may be identified as the "time between collisions"[15,18,27]. It has been argued by many people, using an isolated binary collision (IBC) model, that τ_c should be approximated to an Enskog time (τ_E) for the rate of binary collisions with small spheres[27,28]

$$\tau_E = \left\{\frac{8}{3}\left(\frac{k_b T}{\pi m}\right)^{1/2}\pi\rho\sigma^2 g(\sigma)\right\}^{-1} \qquad 6.11$$

where $g(\sigma)$ is the radial distribution function

$$g(\sigma) = \frac{(Z-1)}{4n_p} \qquad 6.12$$

and

$$Z = 1 + n_p + n_p^2 + \frac{n_p^3}{(1-n_p)^3} \qquad 6.13$$

n_p is the solvent packing fraction an is equal to $(\pi\rho\sigma^3)/6$.

Collision theory can also be approximated using a "cell" model

$$\tau_c = \frac{\rho d^2}{6\eta} \qquad 6.14$$

where d is the distance between the molecules which can be estimated from the molar volume. τ_c can also be obtained using the Gordon J diffusion (collision interrupted free rotation) model.[18] In all three methods, the collision rate increases with increasing density which results in an increase in the dephasing rate as estimated by the IBC model. To a first approximation, the time between the collisions is proportional to the inverse of viscosity[28,29]. Therefore the increase in vibrational dephasing with density is proportional to the increase in viscosity. This implies that, the τ_v^{-1} values, in the rapid modulation limit, should show some viscosity dependence, regardless of whether the model employed is one for homogeneous and inhomogeneous dephasing.

For BCS and for BC22DMS the viscosity increases with pressure (figures 6.17 and 6.18) implying that τ_m should also increase with pressure for these molecules.

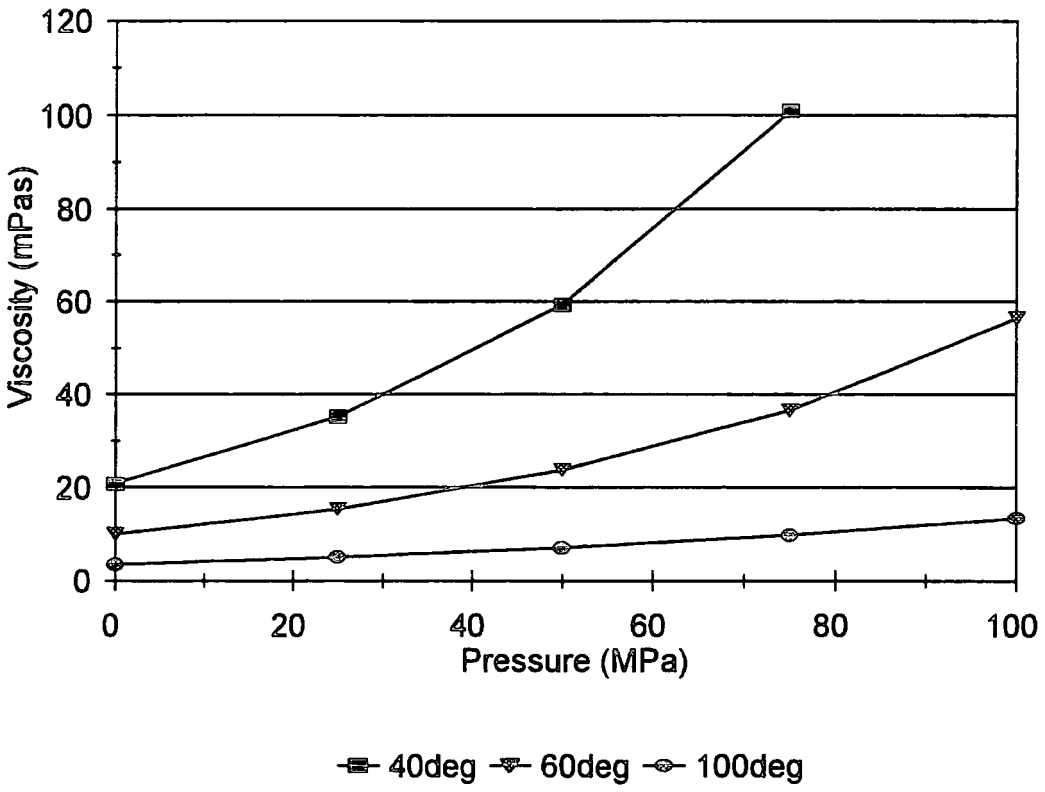

Figure 6.17. Viscosity versus pressure for BCS.

It has been found to be true for many molecules containing a carbonyl group that the modulation of attractive forces are likely to be very slow.[3,20]. It is therefore highly likely that this band, for BCS, is formed in the slow modulation limit if dipolar interactions dominate the potential. The assumption of being in the slow modulation

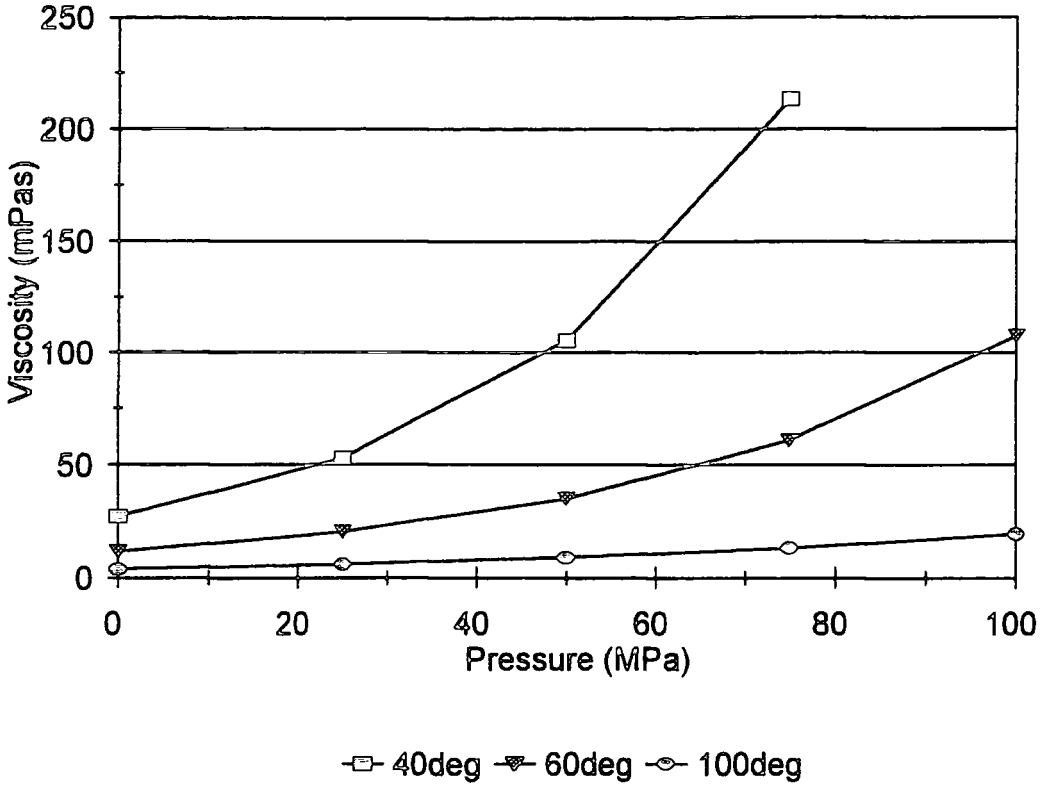

Figure 6.18. Viscosity versus pressure for BC22DMS.

limit was used by Chandler et al[23] to interpret the acetone data of Schindler and Jonas[3]. For polyatomic molecules the dephasing time was short when compared to the attractive force relaxation time T_a

$$T_a = \frac{\sigma^2}{\pi^2 D} \qquad 6.15$$

where σ is the molecular diameter and D is the translational diffusion constant which decreases with increasing molecular size. Hence, the attractive forces will generally relax more slowly as the polyatomic molecule becomes increasingly more complex. The dephasing time often decreases because the pertubation effectively lasts for a long time and the phase of the oscillators is rapidly lost. Therefore, compared to simpler molecules, the contribution from inhomogeneous broadening arising from the attractive force fluctuations should increase with the complexity of the molecule. Using these facts, Chandler argues that for polyatomics, inhomogeneous broadening arising from the

slowly varying attractive forces should be considered to be in the slow modulation regime.

It was then shown by Chandler that the attractive force, inhomogeneous broadening, contributions dominate the dephasing of the carbonyl stretching mode of acetone. Their calculated line width contributions from attractive forces (LW_a) decrease with increasing density and consequently the overall bandwidth of the mode was predicted to decrease as density increases which agreed with the experimental data. It was shown that

$$LW_a \propto (\rho.\chi)^{1/2} \qquad 6.16$$

where ρ is the density and χ is the isothermal compressibility which is related to the distribution of local environments due to solvent number density fluctuations.[29] LW_a would normally be expected to decrease with increasing pressure, since χ decreases rapidly with pressure. However, it is also necessary to consider changes in density. Figure 6.19 shows how the density of BCS varies over the pressure range 0-200 MPa (0-2kbar). This is not in the correct range for the results obtained, but it shows the general shape of the line. If this is compared to figure 6.20 which shows the variation of the relaxation rate of the fitted carbonyl bands for BCS, it can be seen that the general shapes of the line are very similar. If figure 6.21, which plots $\rho\eta$ against pressure is now compared to figure 6.19, it can be seen that the general shapes of the lines are different. From equation 6.9, it can be seen that the vibrational relaxation rate is proportional to the kinematic viscosity. Therefore, if the system was in the rapid modulation regime, it would be expected that figures 6.20 and 6.21 would show similar line shapes. This is not the case, and it is therefore concluded that the modulation of the carbonyl group is in the slow modulation regime. For BCS the vibrational dephasing due to attractive force frequency distribution should be considered to be in the very slow modulation regime. Therefore an increase in bandwidth with pressure implies an increasing second moment.

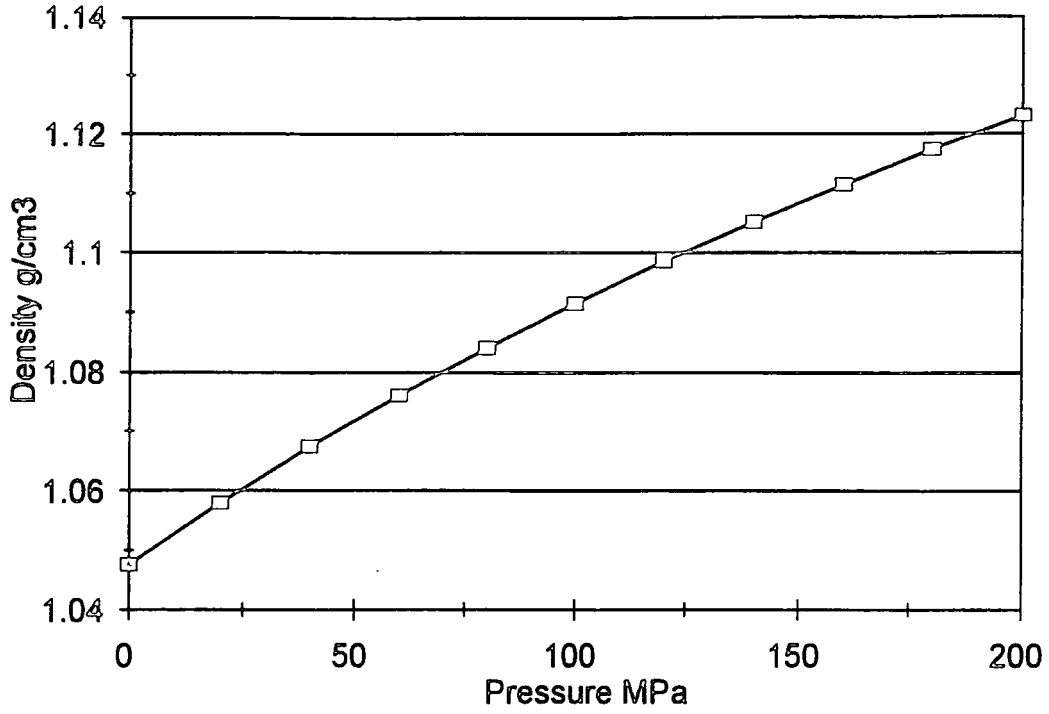

Figure 6.19. Density against pressure at 40°C for BCS.

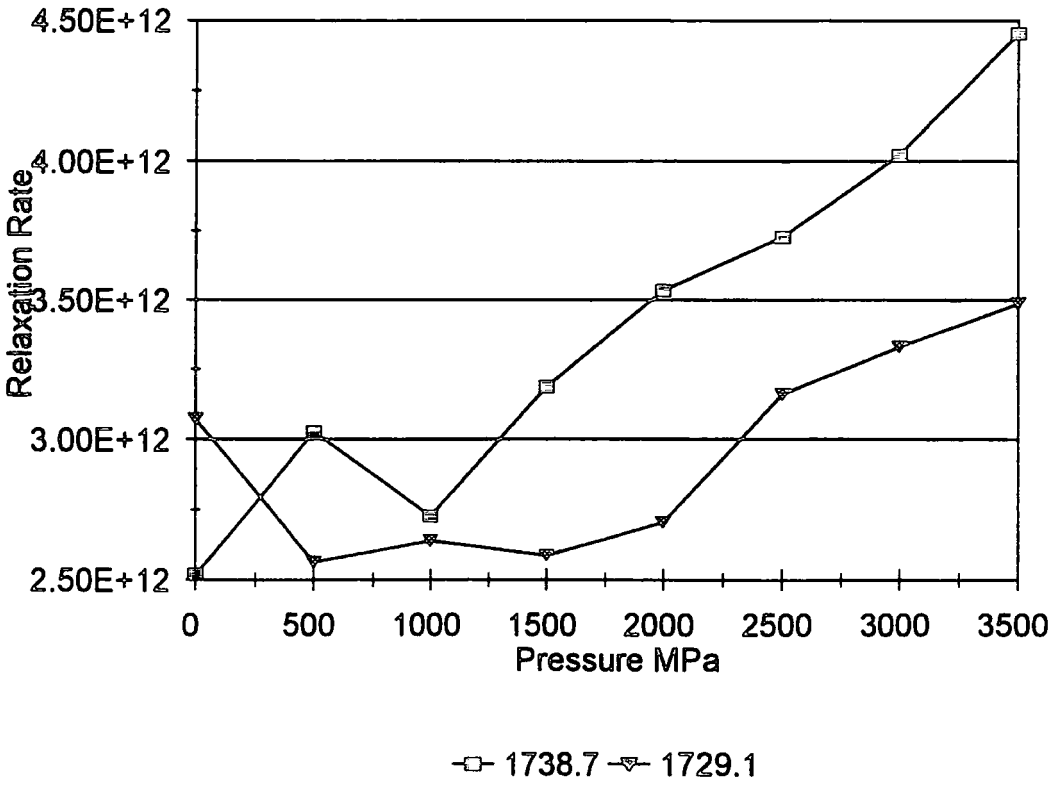

Figure 6.20 Variation in vibrational relaxation rate with pressure for BCS

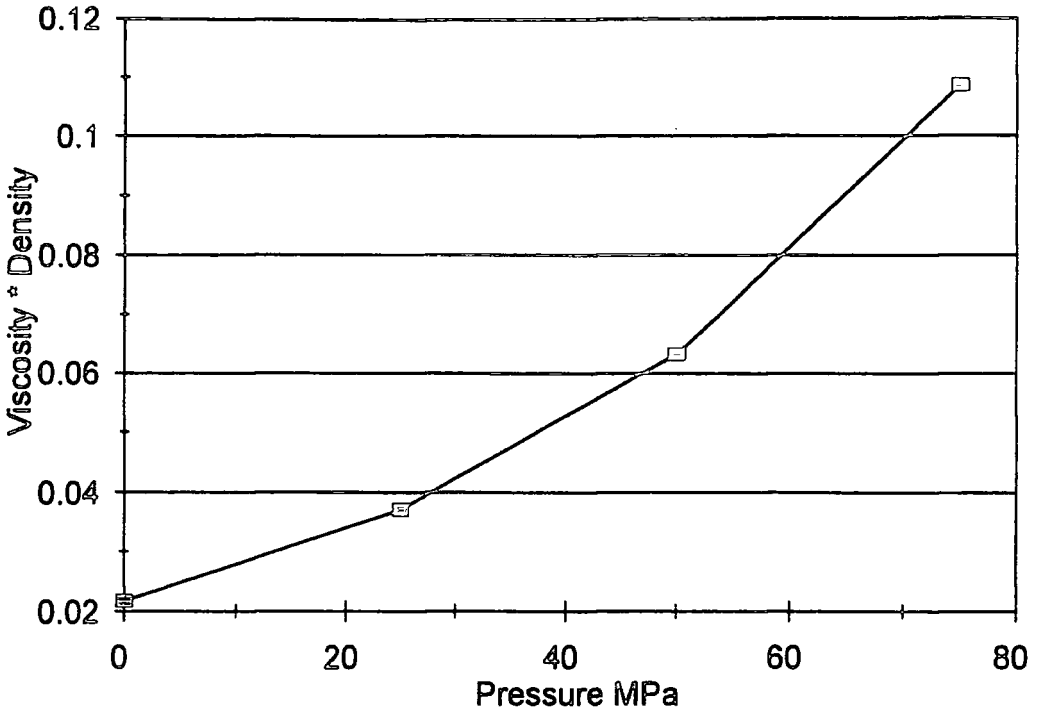

Figure 6.21 ρη against pressure for BCS at 40°C.

This leaves a problem of interpreting a set of data for CMCA which indicates an increase in ordering of the molecules (in the first solvation shell) and second moment data which show that the width of the distribution of molecular oscillations (in the first solvation shell) increases with pressure. There is a possibility that there is a short range disorder and a longer range ordering of the molecular dipoles. The short range forces ought to be rapidly modulated and a significant spectral wing associated with short time contributions to the band profile should be observed. This is not seen, but overlapping bands in the spectra would prevent detection. It might be that ordering in one part of the molecule is associated with disordering as a whole. Due to the flexibility of the molecule, changes in intermolecular potentials with pressure, due to intramolecular conformational changes may occur. It may also be possible that the carbonyl modes normal co-ordinate is distributed among vibrational displacements other than the ester grouping as is the case for dimethylformamide[30]. This may lead to a carbonyl band profile that reflects interactions in other parts of the molecule well away from the carbonyl group.

6.3.2.2. Vibrational Dephasing of the Ester Stretching Mode

A large increase in bandwidth is exhibited in the infra red spectra of the ester stretching mode for all the molecules. The corresponding vibrational correlation times are shown in table 6.17.

Table 6.17. Correlation times, obtained from equation 2.55, for the ester stretching region. All data is quoted in psec. Error is ± 1.5 psec.

Pressure kbar	BCS	BC2MS	BC22DMS	CMCA	CCC
0	46.9	46.9	43.8	23.5	39.3
5	46.9	41.1	41.1	20.6	23.5
10	41.1	41.1	36.6	19.4	19.0
15	25.3	36.6	34.7	16.5	18.0
20	23.5	32.8	32.8	15.7	16.1
25	23.5	29.9	29.9	14.3	15.6
30	20.6	25.3	28.6	13.2	14.9
35	19.4	21.9	27.4	12.6	13.9

The broadening of these bands reflects an increase in vibrational dephasing rates. The increase in FWHM (or decrease in correlation times) is also accompanied by a shift to higher frequency, which suggests that they are dominated by the repulsive part of the potential. This indicates that the vibrational second moment of these two modes increases with density. Therefore, it is expected that the vibrational dephasing rate of both these modes would increase with pressure. As was shown previously, in the rapid modulation limit, both vibrational dephasing rates from inhomogeneous and homogeneous broadening are proportional to viscosity. If the dephasing is occurring in the slow modulation regime, the bandwidth would also increase with pressure proportional to the increase in $M2_V$, and this has been shown to be the case for the carbonyl stretching band.

As mentioned in chapter 5, differences in behaviour between the ester stretching region and the carbonyl stretching region could be indicative of differences between the intramolecular and intermolecular interactions. The ester stretching band broadens dramatically with pressure, far more than the individual components of the carbonyl stretching region. Therefore, either the number of vibrational environments for the ester

stretching band have increased dramatically, or the internal motions of the all the molecules are such that a large increase in the vibrational correlation rate is seen. As the pressure is increased, the density increases, and it would be expected that molecular motions would become constrained as the molecules were forced closer together. As the cyclohexyl rings are bulky, it might be expected that motions of the ring about the C(=O)-O-ring bond might be the most hindered due to an increased number of interactions and this would manifest itself in changes in the ester stretching band. If this is true, it is likely that a 'cog-like' interaction of the cyclohexyl rings is occurring at elevated pressures. This is given in the literature[31] to be one of the reasons why cyclohexyl rings are thought to be important in the design of traction fluids.

6.3.2.3. Vibrational Dephasing of the CH_2 Stretching Mode

Due to the complicated nature of the CH stretching region (with both cyclohexyl ring CH_2 and chain CH_2 groups and also for BC2MS and BC22DMS, branching CH_3 groups), there will be no extensive attempt to quantitatively explain the observed changes in bandwidth. The antisymmetric and symmetric bands both exhibit an increase with that for the antisymmetric stretch being the greatest in all cases. Tables 6.18 and 6.19 show the vibrational correlation times for these bands.

Table 6.18. Correlation times, obtained from equation 2.55, for the antisymmetric CH_2 stretching region. All data is quoted in psec. Error is ± 1.5 psec.

Pressure kbar	BCS	BC2MS	BC22DMS	CMCA	CCC
0	26.3	27.4	25.8	23.1	22.2
5	27.4	27.4	19.4	21.2	15.2
10	27.4	27.4	17.8	21.2	12.2
15	27.4	25.3	15.7	19.4	12.2
20	27.4	25.3	14.3	16.9	11.5
25	25.3	25.3	13.7	15.7	11.3
30	22.7	22.7	12.4	14.9	11.3
35	19.9	18.8	11.5	14.3	11.3

Table 6.19. Correlation times, obtained from equation 2.55, for the antisymmetric CH_2 stretching region. All data is quoted in psec. Error is ± 1.5 psec.

Pressure kbar	BCS	BC2MS	BC22DMS	CMCA	CCC
0	46.9	43.8	38.7	36.6	32.2
5	46.9	41.1	28.6	32.8	29.1
10	46.9	41.1	25.3	32.8	27.7
15	46.9	38.7	21.9	31.3	19.0
20	46.9	36.6	20.6	28.0	19.0
25	41.1	36.6	17.3	25.3	18.5
30	36.6	32.8	14.9	25.3	18.0
35	32.8	27.4	13.7	25.3	18.0

Such observations depend on a complicated mixture of phenomena. These include variations in intramolecular and intermolecular CH coupling due to changes in conformation and packing of the molecules, changes in Fermi resonance contributions and changes in the intermolecular and intramolecular potentials.

An increase in bandwidth could reflect an increase in the modulation time τ_c, which as explained earlier is expected to increase with increased viscosity. If however, the relaxation is in the slow modulation regime, as has been suggested for the carbonyl mode, the bandwidth is independent of the modulation time and should decrease with a decreasing second moment. Therefore, as can be seen the interpretation of the changes for this envelope is difficult.

However, the changes for CCC and CC are totally dependent on the CH_2 groups on the cyclohexyl rings. Therefore, it seems reasonable to assume that these groups will

behave in a similar fashion for the other molecules as well. Thus, the ring CH_2 groups exhibit a large broadening with pressure. This might well indicate a change in the packing of the molecules when under pressure. It is known that the presence of cyclohexyl rings aids in the performance of a traction fluid[31], and it is perhaps some sort of "locking" of these rings that produces both the change in FWHM and the change in frequency. This will be further examined in chapter 9.

The initial lack of bandwidth change with pressure may be due to the ordering of the molecules. Further increases in pressure force the molecules closer together and may cause local disorder of the C-H interactions, producing the increase in bandwidth.

6.3.3. Relative Intensities and Peak Heights

There are many changes seen when ratioing intensities and peak heights as a function of pressure. However, it is only possible to interpret these changes rather speculatively due to the changing pathlength of the D.A.C. during the experiments.

As seen in figure 6.3, the relative intensity of the CH_2 stretching region compared to the overall carbonyl region exhibits different behaviour for the molecules studied. For BC2MS the graph shows a positive gradient, whilst for the other molecules, a negative gradient is seen. As for the changes with temperature, BCS and CMCA exhibit the largest changes. This is explained by the similarity in structure of these two molecules and their ability to pack more closely together than BC2MS and BC22DMS. Consequently when pressure is applied the change in interactions will be greatest for these two molecules.

This change is not likely to be the result of a change in phase, as this would be seen in the spectra. It is likely that the changes are indicative of a change in conformation.

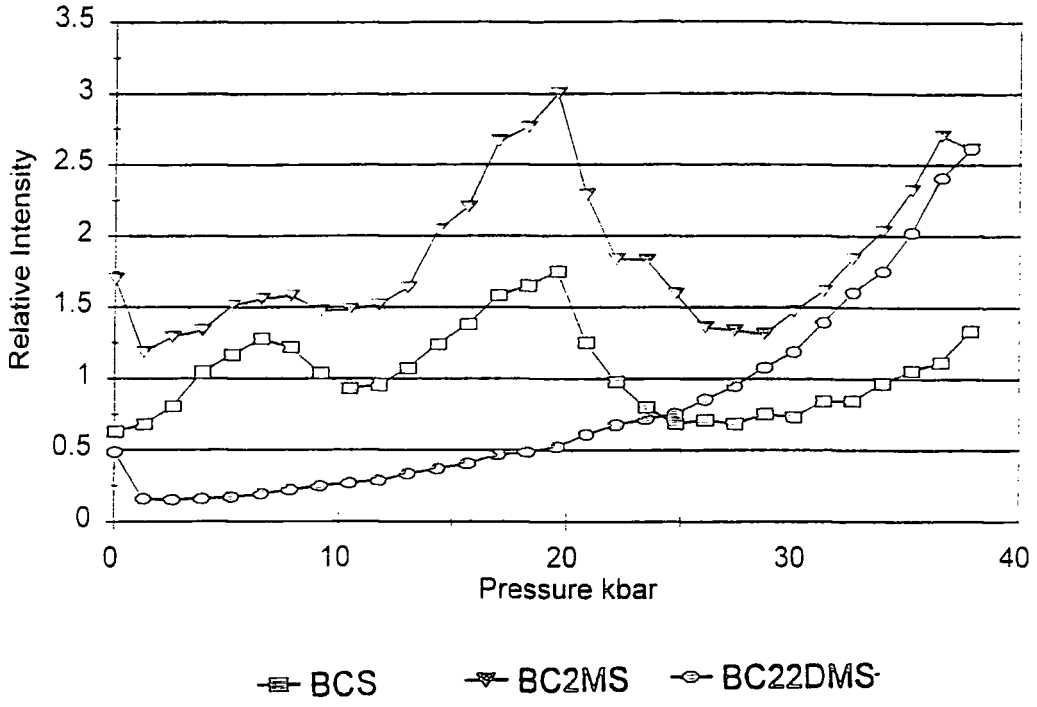

Figure 6.22 Relative Intensity changes for the fitted carbonyl bands. High frequency component is ratioed against the low frequency component.

If the intensity changes for the fitted carbonyl bands are observed (figure 6.22), the overall effect is an increase in the higher wavenumber band. (Without further experimental measurements, it is not clear whether the apparent maxima reached by the graphs for BCS and BC2MS is a real effect, so no interpretation for this is given.) This is the same effect that was observed with temperature. It seems that intramolecular changes are causing a conformational change in the diester molecules with unsymmetric branching exhibiting a different effect to symmetric branching.

It could also be argued that due to increased density with pressure, the modes requiring most volume will be seen to diminish. This would the behaviour of all the molecules apart from BC2MS, so it seems that a conformational change brought about by increased pressure and the molecular rigidity of the molecules is more likely.

It is also apparent that when ratioing the intensities of the fitted carbonyl bands that BC22DMS exhibits the greatest change. This is not unexpected as the presence of two branching methyl groups will make the carbonyl groups in the same molecule more different in the case of BC22DMS than for BCS or BC2MS.

References

1. A.M. Benson, Jr. and H.G. Drickamer, J. Chem. Phys., 27, 1164 (1957)
2. R.R. Wiederkehr and H.G. Drickamer, J. Chem. Phys., 28, 311 (1958)
3. W. Schindler, P.T. Sharko and J. Jonas, J. Chem. Phys., 76, 3493 (1982)
4. W. Schindler, and J. Jonas, J. Chem. Phys., 72, 5019 (1980)
6. S.L. Wunder, Macromolecules 14, 1024 (1981)
6. P.T.T. Wong, T.E. Chagwedera and H.H. Mantsch, J. Chem. Phys., 87, 4487 (1987)
7. P.T.T. Wong, S.F. Weng and H.H. Mantsch, W. Schindler, J. Chem. Phys., 85, 2315 (1986)
8. N.A. Walker, PhD Thesis Newcastle-Upon-Tyne Polytechnic, (1986)
9. W.G. Rothschild, "Dynamics of Molecular Liquids", John Wiley and Sons (1984)
10. A. Whitley, J. Yarwood and D.J. Gardiner, J. Chem. Soc. Faraday Trans., 89, 881 (1993)
11. S. Bratos, J. Chem. Phys., 63, 3499 (1975)
12. W.G. Rothschild, G.J. Rosaro and R.C. Livingstone, J. Chem. Phys., 62, 2553 (1975)
13. J. Schroeder, V.H. Schiemann, P.T. Sharko and J. Jonas, J. Chem. Phys., 66, 3215 (1977)
14. B. Hartmann and Z.I. Slawsky, J. Chem. Phys., 47, 2491 (1967)
15. R.M. Lynden-Bell, Mol. Phys., 33, 907 (1977); Faraday Symp. Chem. Soc., 11, 167 (1978)
16. G.C. Tabisz and R.M. Lynden-Bell, Chem. Phys. Letts., 46, 175 (1977)
17. D.C.M. van Woerkom, J. de Bleijer, M. de Zwart and J.C. Leyte, Chem. Phys., 4, 236 (1974)
18. J. Yarwood and R. Arndt, "Study of Intermolecular Interactions in the Liquid Phase", Chapter 4 of "Molecular Association", Vol. 2, ed. R. Foster, Academic Press (1979)
19. R. Kubo, in "Fluctuations, Relaxation and Resonance in Magnetic Systems", Ed. D.Ter. Haar), Plenum, New York (1962)
20. A. Whitley, PhD Thesis, Durham University (1990)
21. G. Doge, Z. Naturforsch. Teil., A28, 919 (1973)
22. A. Khuen, G. Doge and J. Yarwood, Mol. Phys., 52, 399 (1984)

23. K.S. Schweizer and D. Chandler, J. Chem. Phys., 76, 2296 (1982)

24. S.F. Fischer and A. Laubreau, Chem. Phys. Lett., 35, 6 (1975)

25. K.F. Herzfeld and T.A. Litovitz, "Absorption and Dispersion of Ultrasonic Waves", Academic Press, New York (1959)

26. J. Yarwood and R. Arndt, "Study of Intermolecular Interactions in the Liquid Phase", Chapter 6 of "Molecular Association", Vol. 2, ed. R. Foster, Academic Press (1979)

27. J. Schroeder, V.H. Schiemann and J. Jonas. Mol. Phys., 34, 1501 (1977)

28. R.M. Lynden-Bell and P.-O. Westlund, Mol. Phys., 61, 1541 (1987)

29. T.A. Litovitz, J. Chem. Phys., 26, 469 (1957); W.M. Madigosks and T.A. Litovitz, J. Chem. Phys., 34, 489 (1961)

30. D. Steele, T.C. Jao and I. Scott, J. Mol. Spectrosc., 92, 1 (1982)

31. K.H. Hentschel, J. Synth. Lubr., 2, 143 (1985)

CHAPTER 7

Dynamic Pressure Studies Using the EHD Rig.

7.1 Introduction

Using the EHD rig (figure 3.10), infra red spectra of BCS were obtained at different loads and speeds.(Table 7.1) The remaining molecules were not studied using this technique due to time considerations and quantity of the liquids available.

Table 7.1. The conditions used for obtaining the spectra of BCS.

Load in Newtons	Pressure, GPa	RPM	ms^{-1}
3.8	0.4015	150	0.2
3.8	0.4038	200	0.3
6.5	0.3951	150	0.2
6.5	0.3978	200	0.3
7.3	0.3944	150	0.2
7.3	0.3970	200	0.3
8.1	0.3936	150	0.2
8.1	0.3966	200	0.3
8.1	0.4068	600	0.8
8.1	0.4090	700	0.9
8.1	0.4105	800	1.1
8.1	0.4124	900	1.2
10.1	0.4053	600	0.8
10.1	0.4064	700	0.9

N.B. 1kbar ≡ 0.1GPa

The spectra were acquired every 24μm from the centre of the contact towards the inlet along the centre line of the contact and also offset from the centre line. Figure 7.1 shows the areas from which measurements were taken.

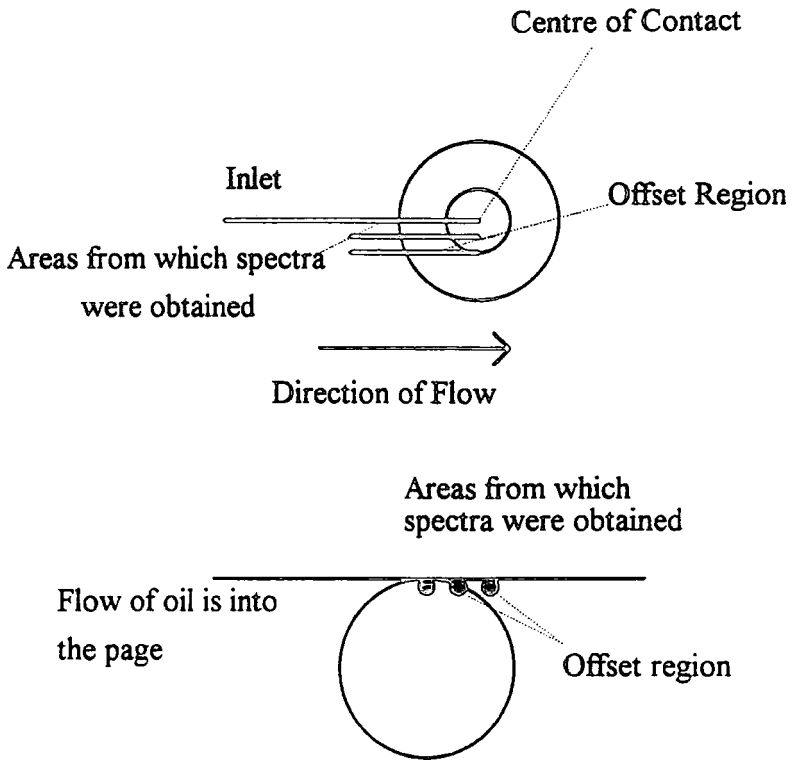

Figure 7.1. Schematic plans of the EHD contact showing the areas from which spectra were obtained. The offset lines are at 48 and 120μm from the centre line.

No spectra were obtained moving towards the outlet due to the effect of cavitation. The usual form of cavitation in lubricating films is the liberation of dissolved gases. Mineral oils contain between 8 and 10 percent of dissolved air. When the pressure in the oil film falls below ambient, some of the air is liberated in the form of bubbles. This tends to maintain the oil film pressure near the level of the saturation pressure. For most lubrication conditions, the saturation and ambient pressures will be almost equal. These observations suggest that the pressure in the cavitated region of lubricating films will be approximately constant and will be near atmospheric or ambient pressure.[1] The photographs in figure 7.2. show the centre of the contact and the outlet. The process of cavitation can be clearly seen.

The load in Newton's in table 7.1 was calculated by measuring the diameter of the Hertzian contact zone and then using[1]

$$a = \left(\frac{6k^2 \varepsilon FR}{\pi E'} \right)^{1/3} \qquad 7.1$$

or

$$b = \left(\frac{6\varepsilon FR}{\pi k E'}\right)^{1/3} \qquad 7.2$$

where a and b are the radii of the contact zone (they are both equal for these studies, but if the contact zone was an ellipse they would be inequivalent), E' is the reduced Young's modulus

$$E' = \frac{2}{\frac{1-\nu_a^2}{E_a} + \frac{1-\nu_b^2}{E_b}} \qquad 7.3$$

where ν_a^2 and ν_b^2, and E_a and E_b are the Poisson ratios and Young's modulus of the diamond window and the steel ball respectively, R is the sum of curvature

$$R = \frac{1}{R_x} + \frac{1}{R_y} \qquad 7.4$$

where R_x and R_y are the radii of the ball, k is the ellipticity parameter a/b (in this case assumed to be =1), ε=1.0003+(0.5968/(R_y/R_x)) and F is the applied load.

The regions studied were chosen for various reasons. Firstly in order to perhaps be able to relate the changes in the spectra with the pressure or film thickness in the contact it was necessary to conduct the experiments within a region for which computer modelled pressure profiles and film thicknesses could be obtained. There was also the problem of the stability of the apparatus. If a low load was used at a high speed, the diamond window was forced off the rotating ball, and no spectra were obtained. Vibrations from the driving motor also proved problematic. Therefore the conditions for the experiments were governed by the values for which the pressure profiles and film

thicknesses could be modelled which coincided with the values for which measurable spectra could be obtained.

The pressure and film thickness profiles are calculated from and quoted in dimensionless units. The following equations represent the five dimensionless groupings that were established by Dowson and Higginson[2]

i) Dimensionless speed parameter

$$U = \frac{\eta_0 u}{E' R_x} \qquad 7.5$$

where η_0 is the atmospheric viscosity, u is the surface velocity in the direction of motion $u = \frac{u_a + u_b}{2}$. The subscript a denotes motion in the transverse direction and b motion in the direction of motion.

ii) Dimensionless load parameter

$$W = \frac{w}{E' R_x^2} \qquad 7.6$$

where w is the normal applied load.

iii) Dimensionless materials parameter

$$G = \alpha E' \qquad 7.7$$

where α is the pressure viscosity coefficient of lubrication.

iv) Ellipticity parameter

$$k = \frac{a}{b} \qquad 7.8$$

where a is the semiaxis in the transverse direction and b the semiaxis in the direction of motion.

v) Dimensionless film thickness

$$\overline{H}_c = \frac{h_c}{R_x} = 2.69U^{0.67}G^{0.53}W^{-0.067}(1-0.61\exp(-0.73k)) \qquad 7.9$$

where h_c is the central film thickness. This equation can be used to explain the differences in intensity of the spectra. As can be seen the change in load on the contact has little effect on the central film thickness when compared to speed. Therefore, as the speed of the ball is increased, the central film thickness would be expected to increase and this should be apparent in the spectra. To a lesser extent, as the normal applied load is increased, the central film thickness would be expected to decrease.

In addition to the five dimensionless groupings, there are two other quantities that are required to be able to model the pressure and film thickness. These are represented below.

$$M = \frac{W}{(2U)^{0.75}} \qquad 7.10$$

$$L = G\sqrt[4]{2U} \qquad 7.11$$

M is a variation of the dimensionless load parameter, and L represents the lubricant properties[3].

Finally, the dimensionless pressure, P can be represented as

$$P = \frac{p}{E'} \qquad 7.12$$

where p is the pressure in the contact at any one point.

Few changes were observed in peak frequencies or bandwidths, so these results are not tabulated. Any specific changes will be outlined in the results section. However, unusual band shapes are observed and negative going bands are also apparent in one instance. All spectra show a decrease in intensity as the sampling region moves towards the centre of the contact. This is due to the decreasing pathlength of the oil film.

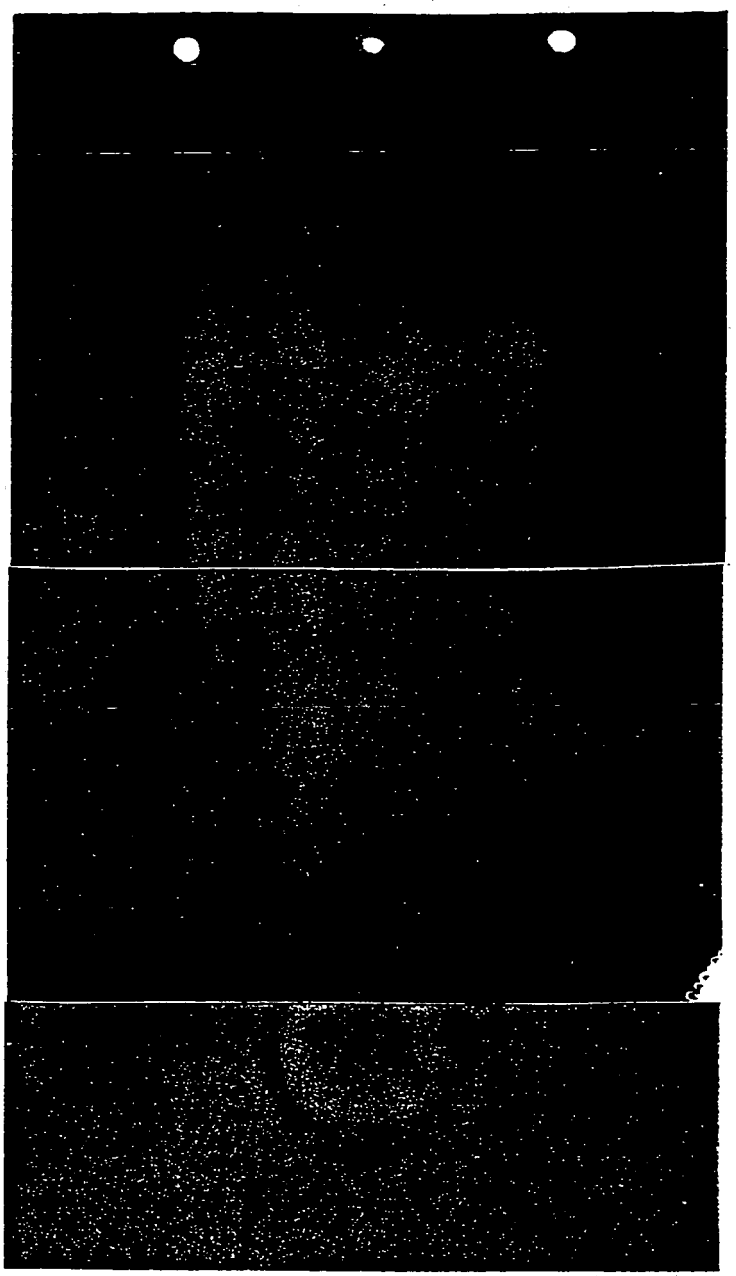

Figure 7.2. The Hertzian contact zone and the outlet. The process of cavitation can be clearly seen.

7.2 Results

7.2.1 CH_2 Stretching Region

There is no change in bandwidths or peak frequencies exhibited by the spectra obtained at any one speed and load. When the load is varied at constant speed some changes become noticeable. For the spectra obtained at 150rpm, there is little change exhibited in the bandwidths or peak frequencies in this region when sampled along the centre line of the contact (figure 7.3). However, when the sampling window is moved off this line, the bandwidths of the stretching bands are seen to decrease as the applied load is increased (figure 7.4). Similar behaviour is shown by the spectra obtained at 200rpm, with the narrowing of both the antisymmetric and symmetric stretching bands being apparent for the spectra obtained along the centre line as well (figure 7.5).

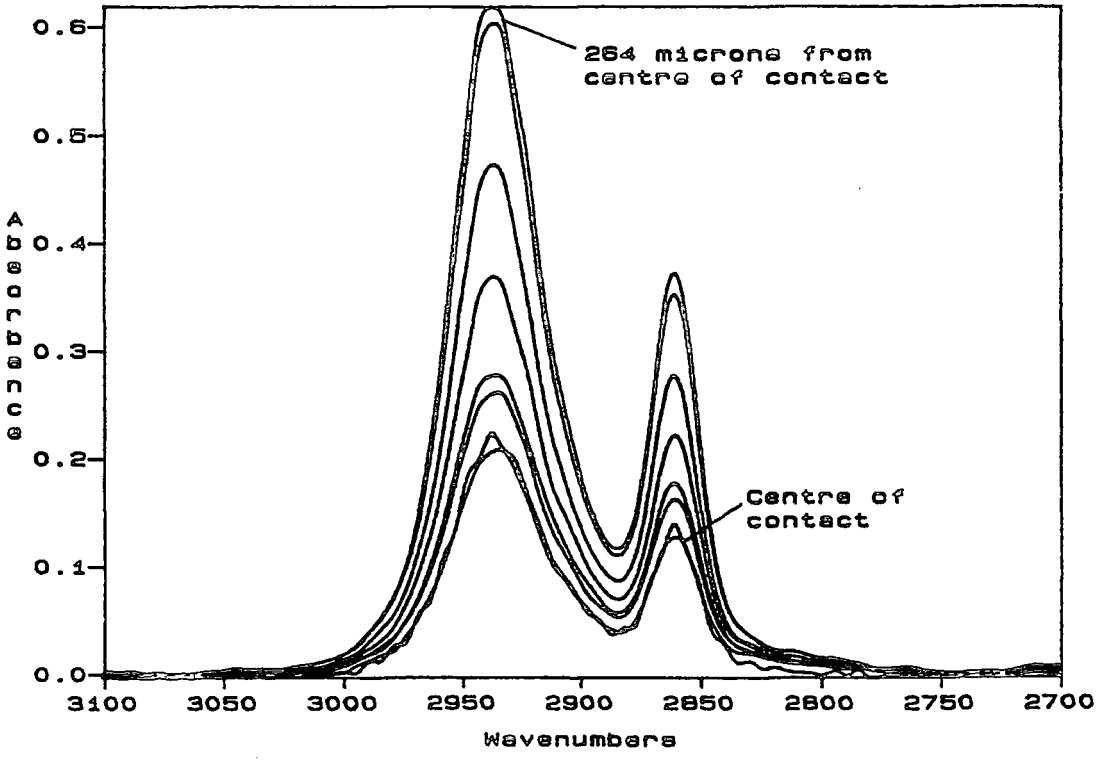

Figure 7.3. The CH_2 stretching region for BCS at 150rpm and 3.8N load. Data obtained from the centre line of the contact moving towards the inlet.

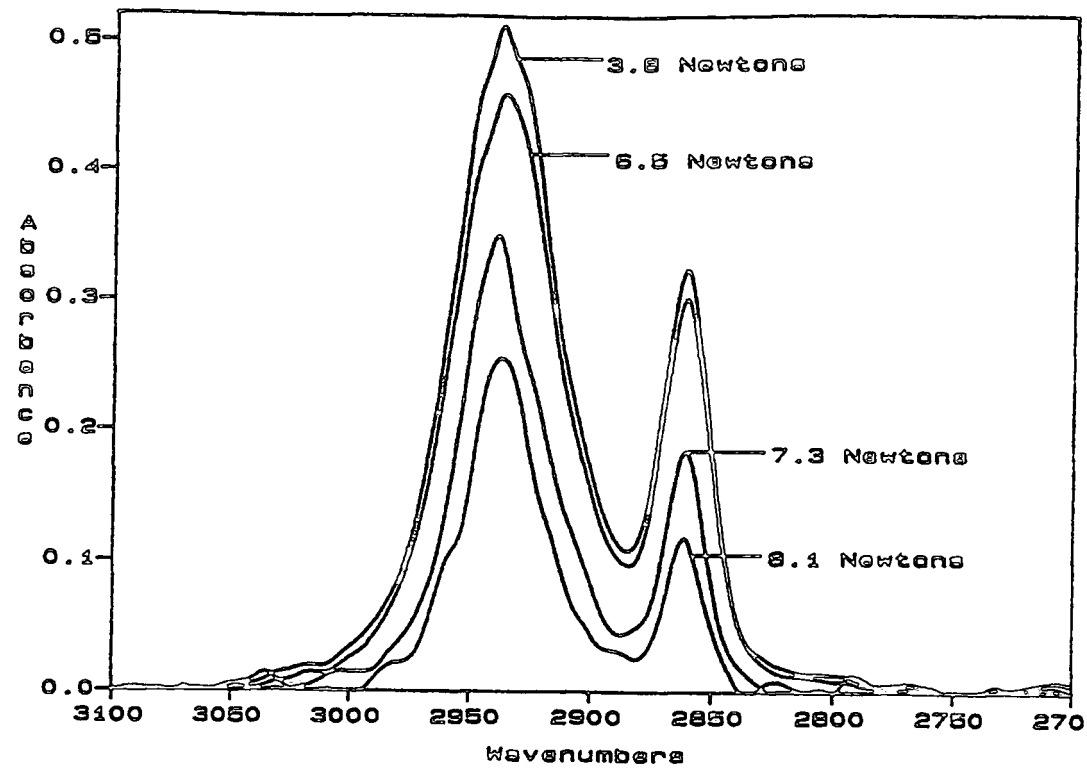

Figure 7.4. The CH_2 stretching region for BCS at 150rpm and increasing load. Data obtained offset by 48μm from the centre line of the contact.

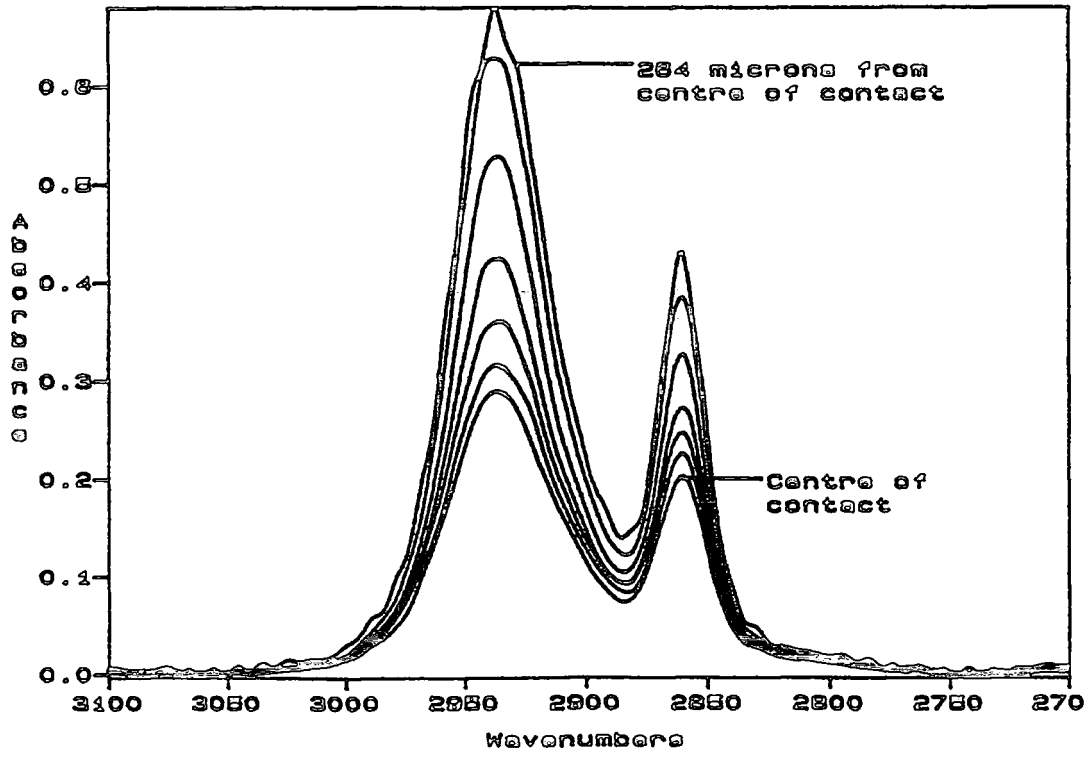

Figure 7.5. The CH_2 stretching region for BCS at 200rpm and 3.8N load. Data obtained from the centre line of the contact moving towards the inlet region.

If the load is held constant and the speed varied, the CH_2 stretching bands are seen to broaden on going from 150rpm to 200rpm.(Figure 7.6) The level of absorbance is also seen to increase as the speed is increased. This is due to film thickness increases.

If the data obtained at 8.1 Newtons is examined some remarkable changes are observed at higher speeds. At 600rpm, the region is seen to broaden as the IR window is moved towards the inlet. At 264 microns from the centre of the contact the spectra become very different (figure 7.7). At 700rpm, there is no visible change seen for the behaviour of this region, whilst for 800rpm and 900rpm the unusual behaviour is again seen.

There are very few conclusive changes in relative intensities or peak heights using this region. However it does seem that the spectra obtained for 150rpm and 200rpm at the higher loads exhibit some changes. These will be mentioned in section 7.3.. For the spectra obtained at 8.1 Newtons, all the relative intensity and peak height ratios exhibit negative gradients as a function of distance from the centre of the contact.

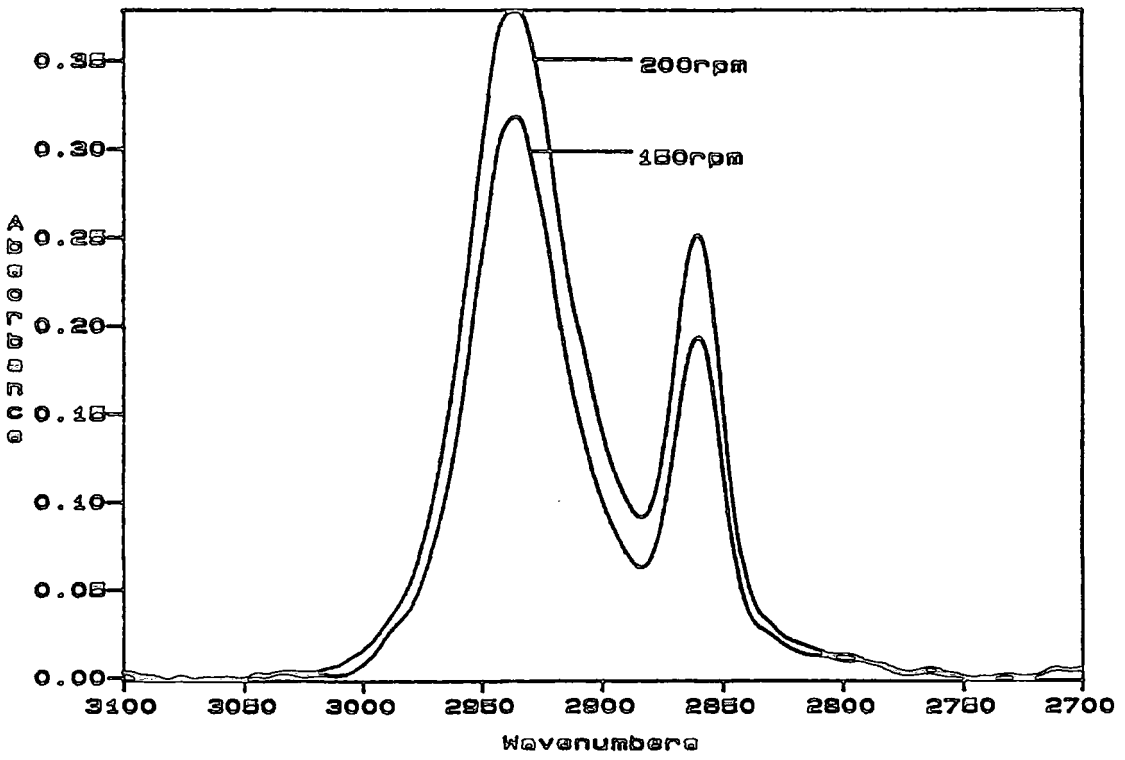

Figure 7.6. The CH_2 stretching region for BCS at 150rpm and200rpm at 3.8N load. Data obtained from the centre line of the contact at 96μm from the centre.

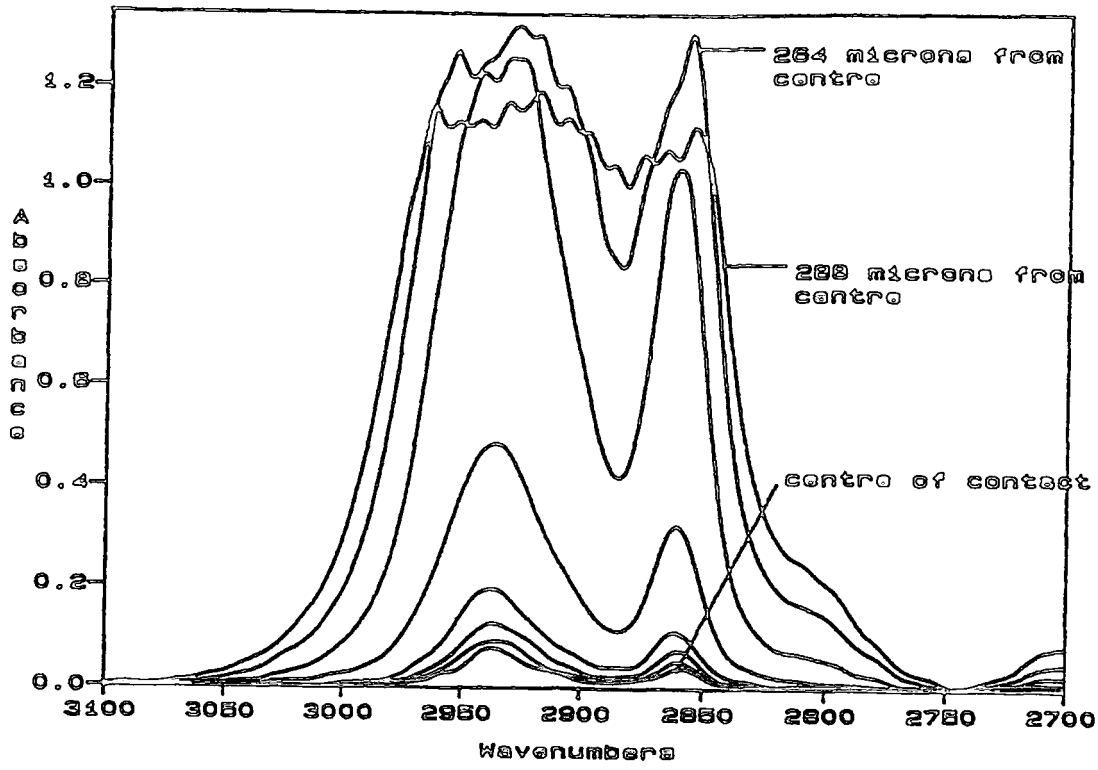

Figure 7.7. The CH_2 stretching region for BCS at 600rpm and 8.1N load. Data obtained from the centre line of the contact moving towards the inlet region.

7.2.2 Carbonyl Stretching Region

For spectra obtained at a single load at 150rpm and at different distances from the centre of the contact along the centre line, there is some indication of the presence of at least two carbonyl stretching bands by the appearance of a shoulder on the high frequency side of the overall band (figure 7.8). However when offset from the centre line, a distinct appearance of two bands is seen, and it seems noticeable that the higher frequency component of the envelope decreases with respect to the lower frequency component as the sampling region is moved towards the inlet (figure 7.9). As the sampling window is further offset from the centre line, this splitting increases. If the load is then increased at 150rpm, again few changes are seen along the centre of the contact. If the IR window is then offset from the centre line the splitting again becomes visible. The two distinct bands are most visible at 6.5 Newtons, and the immediate recognition of two bands diminishes at 7.3 and 8.1 Newtons (figure 7.10)

For 200rpm, there is a slight decrease in the overall width of the carbonyl stretching band as the load is increased. As the load is increased the shoulder on the

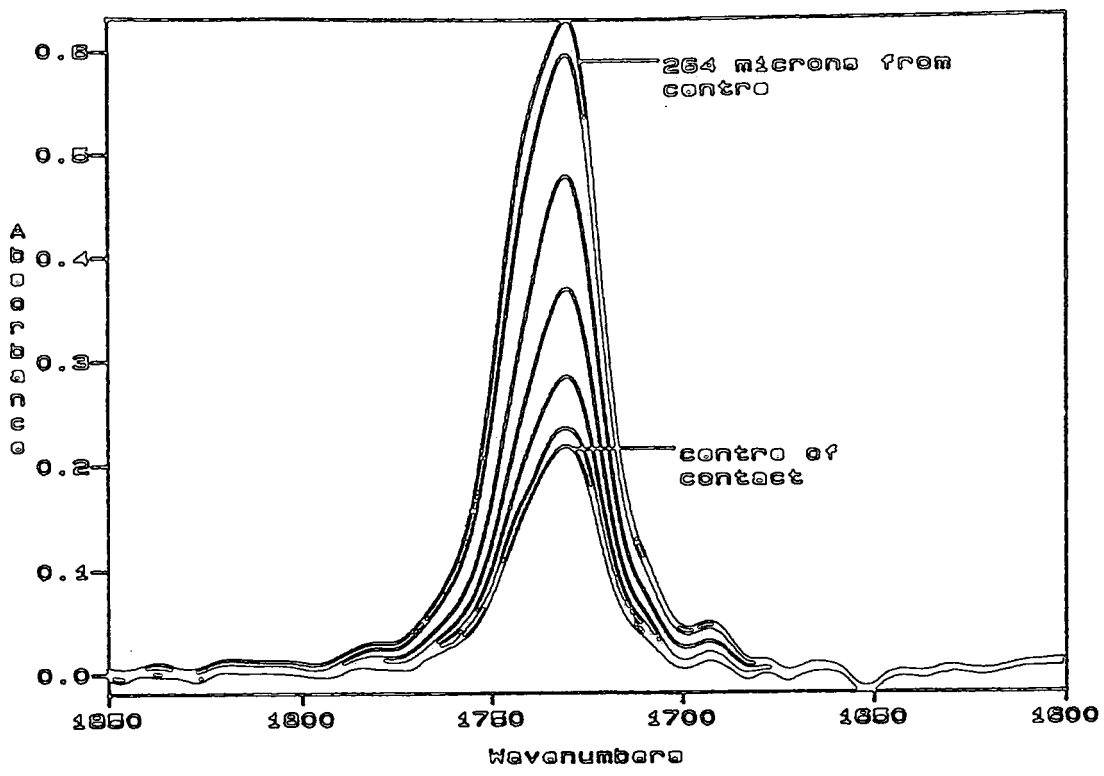

Figure 7.8. The carbonyl stretching region for BCS at 150rpm and 3.8N load. Data obtained from the centre line of the contact moving towards the inlet region.

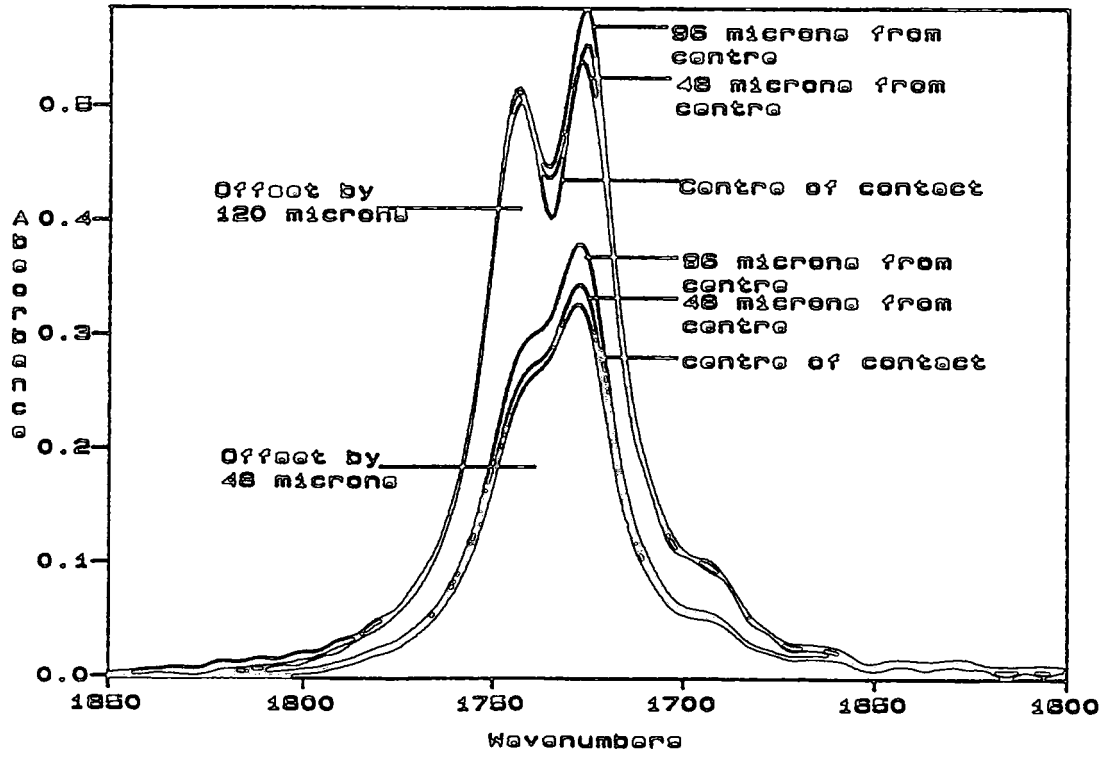

Figure 7.9. The carbonyl stretching region for BCS at 150rpm and 3.8N load. Data obtained offset from the centre line of the contact moving towards the inlet region.

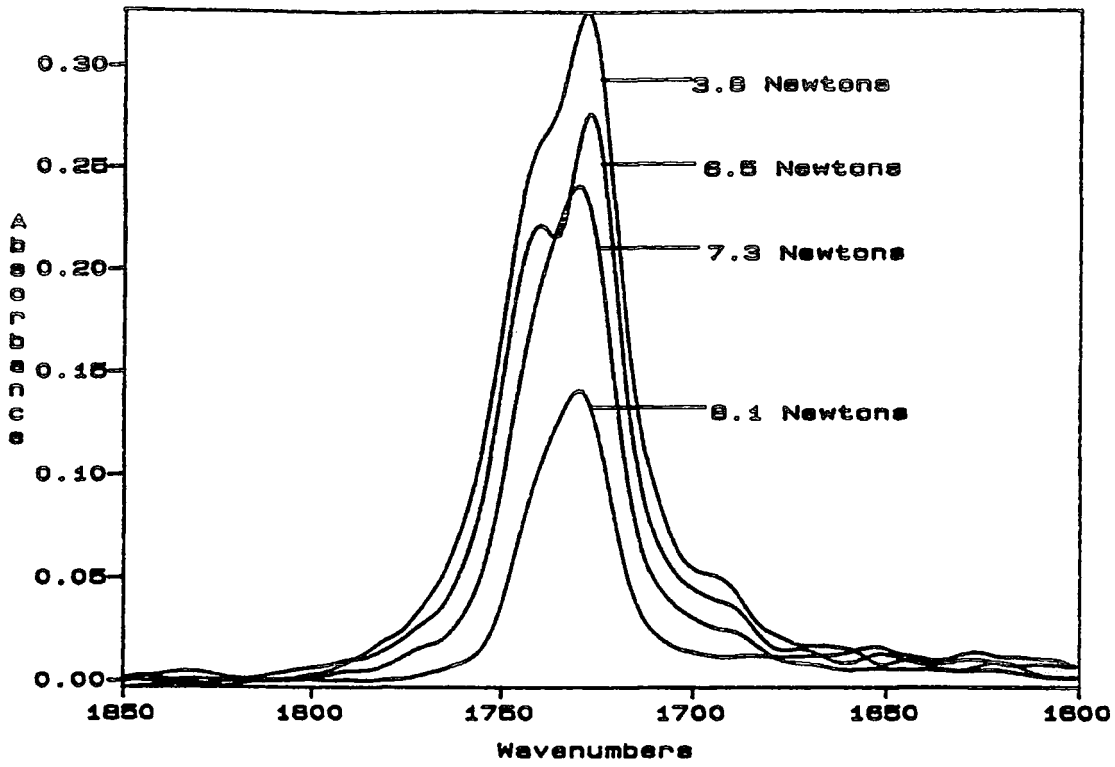

Figure 7.10. The carbonyl stretching region for BCS at 150rpm and varying load. Data obtained offset by 48μm from the centre line of the contact.

high frequency side of the band is less apparent and there is a slight shift to higher frequency.

Again, the offset spectra display the splitting of the carbonyl band, but there is also a shift to higher frequency and a bandwidth narrowing as the load is increased.(Figure 7.11)

For the data obtained at 8.1 Newtons very unusual behaviour is again seen at high speeds. The behaviour for 600rpm (figure 7.12), 800rpm and 900rpm is very similar with the region broadening considerably and the observation of unusual bands. However, for 700rpm, whilst there is a broadening of the region seen, two distinct bands are seen, and no unusual behaviour is apparent (figure 7.13).

As mentioned previously, the relative peak height changes will be explained in 7.3.

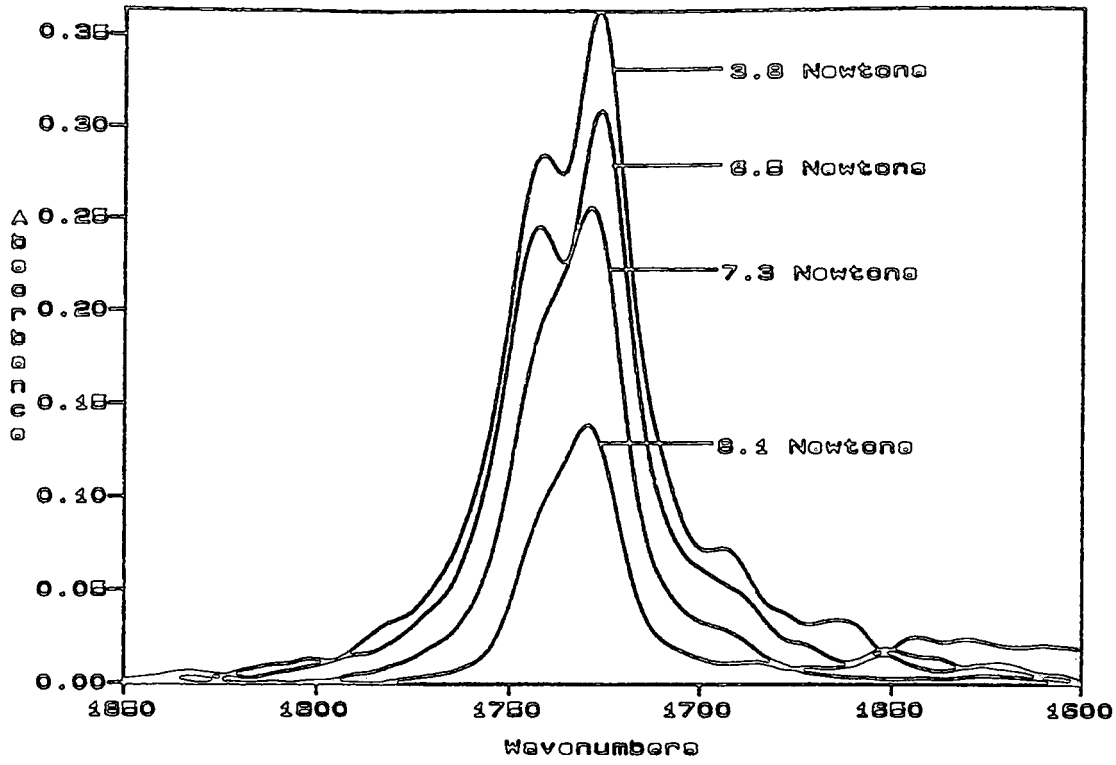

Figure 7.11. The carbonyl stretching region for BCS at 200rpm and varying load. Data obtained offset by 48μm from the centre line of the contact.

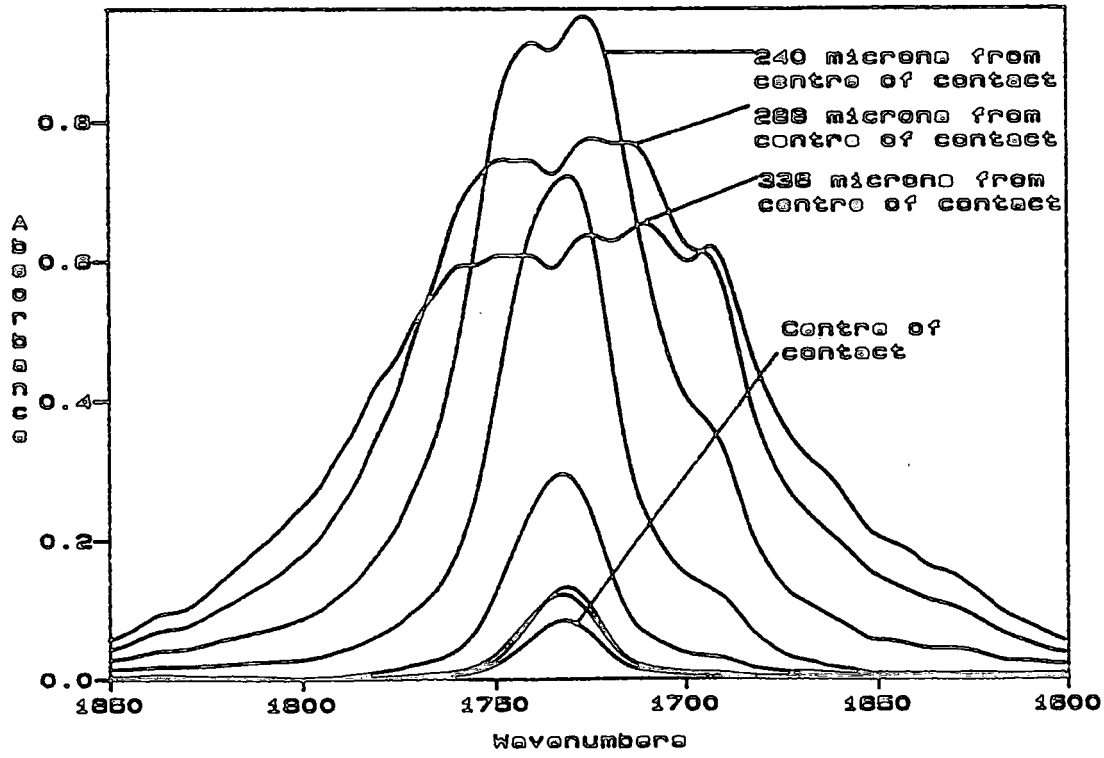

Figure 7.12. The carbonyl stretching region for BCS at 600rpm and 8.1N load. Data obtained from the centre line of the contact moving towards the inlet region.

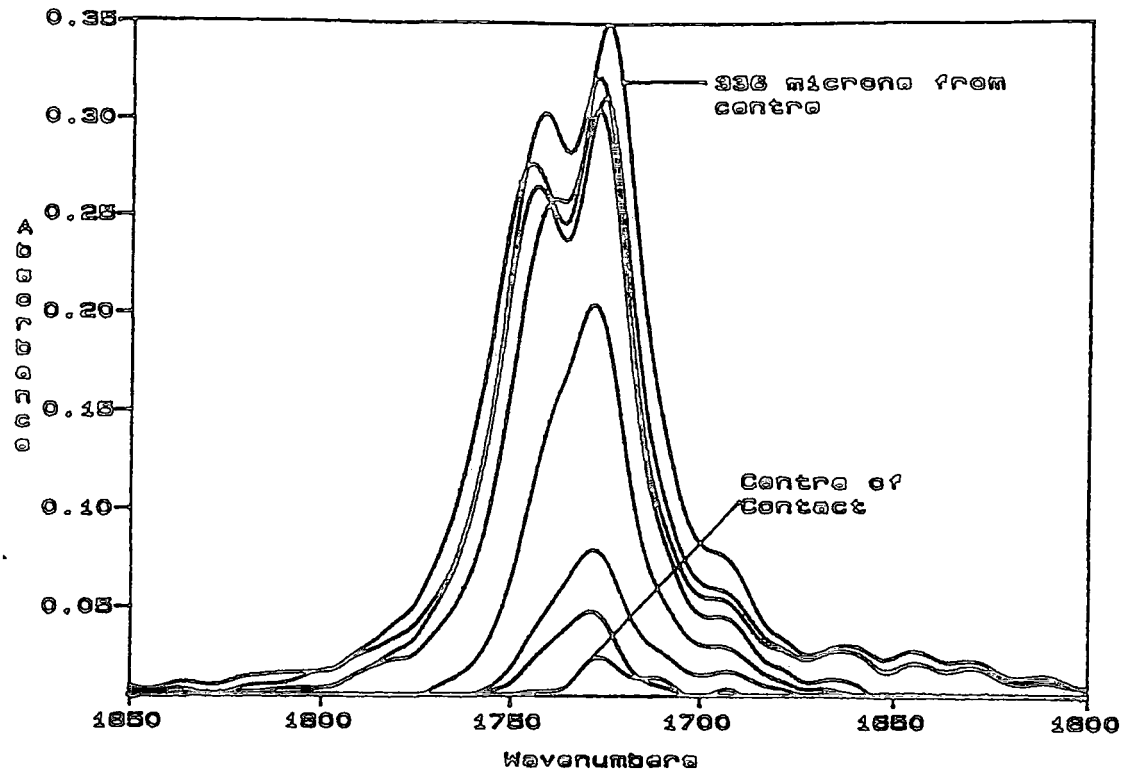

Figure 7.13. The carbonyl stretching region for BGS at 700rpm and 8.1N load. Data obtained from the centre line of the contact moving towards the inlet region.

7.2.3 CH_2 Ring Scissors Region

Little change is seen in this region even when offset from the centre of the contact. However as with all the other regions, unusual behaviour is seen for the spectra obtained at 8.1 Newtons at higher speeds (figure 7.14).

7.2.4 Ester Stretching Region

As with the other regions little change is seen when in the centre of the contact apart from the data obtained at 8.1 Newtons. However, on offsetting the IR window, the ester stretching region is seen to broaden as it is offset (figure 7.15), and then narrow as the window is moved towards the inlet (figure 7.16). This band system is also seen to narrow as the load is increased and broaden as the speed is increased.

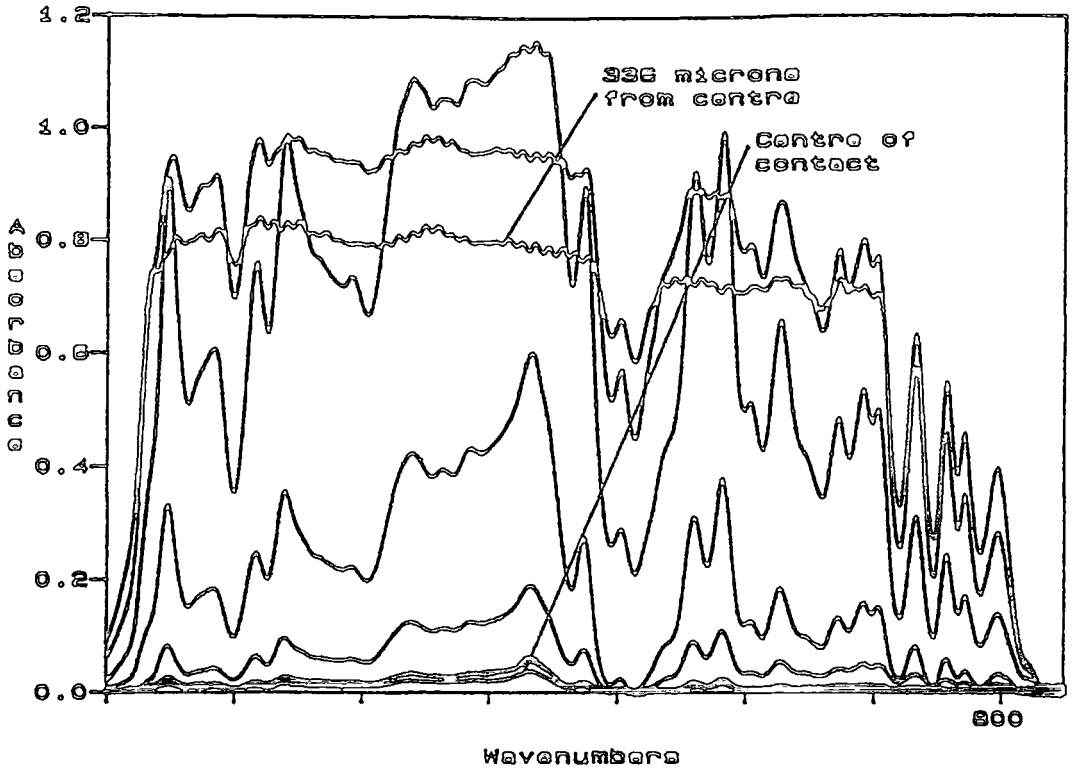

Figure 7.14. 1500-750cm^{-1} region for BCS at 600rpm and 8.1N load. Data obtained from the centre line of the contact moving towards the inlet region.

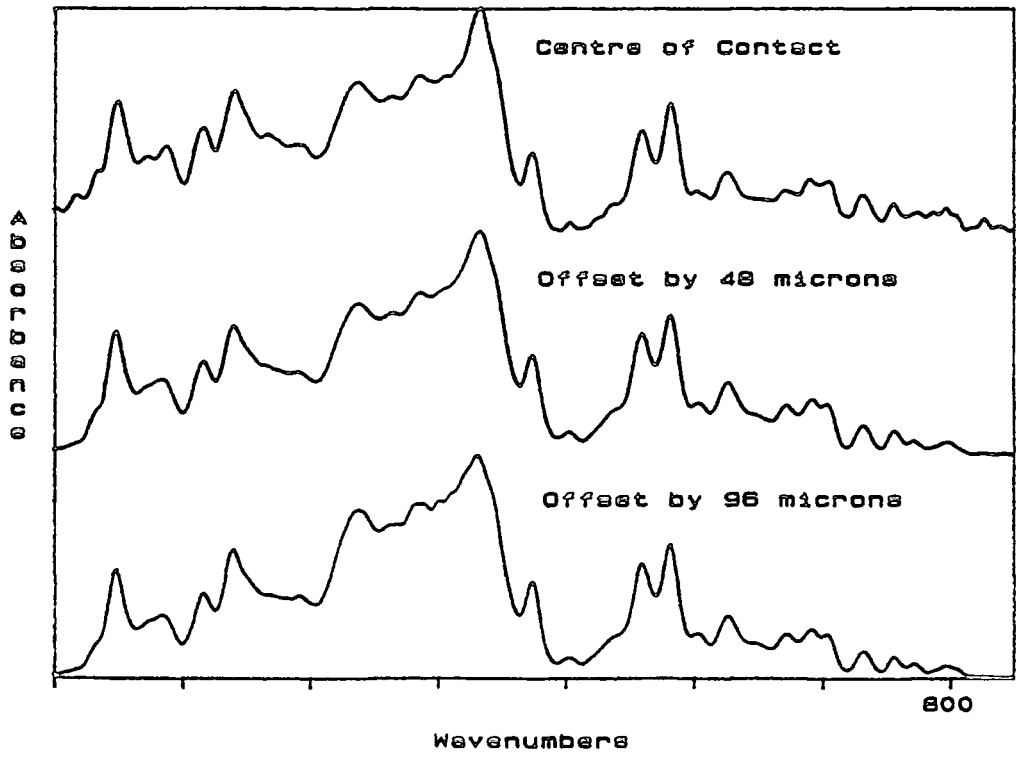

Figure 7.15. 1500-750cm^{-1} region for BCS at 150rpm and 3.8N load. Data obtained offset from the centre line of the contact.

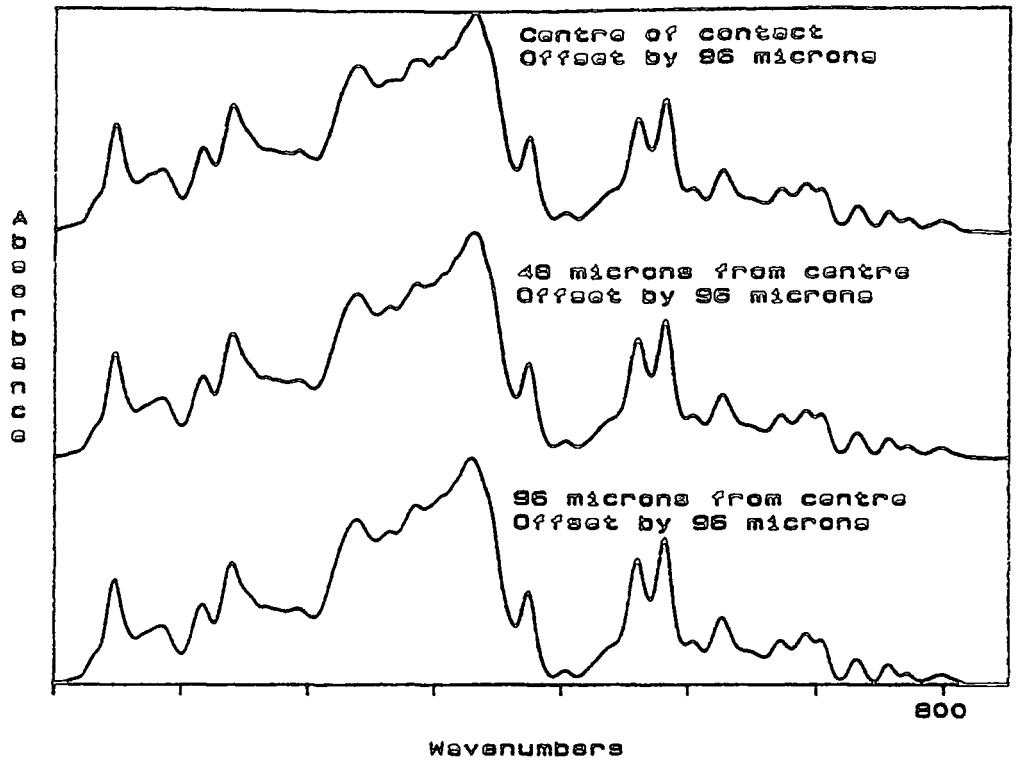

Figure 7.16. 1500-750cm^{-1} region for BCS at 150rpm and 3.8N load. Data obtained offset from the centre line of the contact moving towards the inlet region.

7.3 Discussion

In recent years there has been increasing interest and concern about the friction resistance to shear of lubricant films in elastohydrodynamic (EHD) contacts, as found in gears and cams. This friction, or "traction", plays an important role in determining the efficiency of transmissions and other lubricated systems and thus, for most applications, should have as low a value as possible. However, there is also interest in producing lubricants which give very high traction, for use in traction drives.

A number of studies have examined the general relationship between traction and molecular structure, mostly in the quest for high traction fluids. These have shown that lubricants based upon molecules with a large degree of internal flexibility tend to give low traction behaviour, whereas bulky, relatively rigid molecules produce fluids with high traction in EHD.

Unfortunately, although this ground rule is well established, little is yet known about the detailed influence of molecular structure on traction. One of the main reasons for this is that the conditions in EHD contacts are so severe that conventional rheological models have doubtful validity. The mechanisms by which lubricant films yield in an EHD contact are not yet sufficiently well understood for tests made under different conditions to be interpreted in a unified way.

It was hoped that using infra red spectroscopy would provide a molecular picture of the processes occurring within an EHD contact. These could then be used with the bulk fluid properties to help deduce what molecular interactions provide a good traction fluid.

7.3.1 Change in Bandwidths

As mentioned earlier, there are only very small changes in the bandwidths of the spectra. However, there are some definite trends in the small changes seen. For constant speed and load, most of the vibrational bands are seen to broaden as they are offset from the centre line and narrow as the IR window is moved towards the inlet region. If the pressure profiles and film thicknesses are examined, (see figures 7.17-20

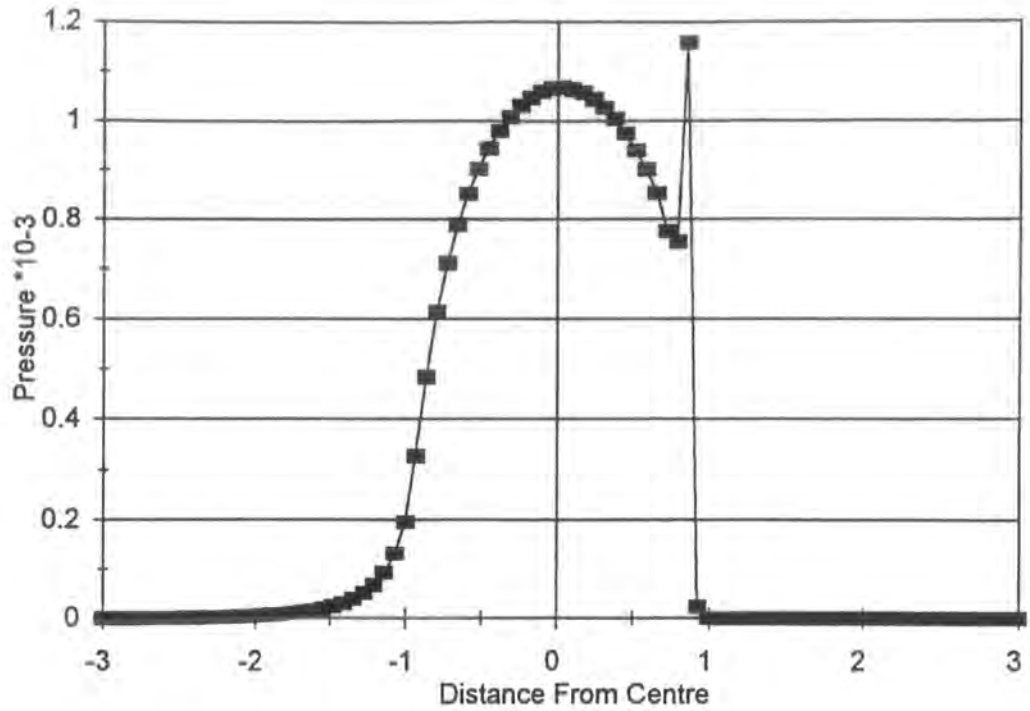

Figure 7.17. Pressure profile for 150rpm at 3.8N load. Units are non-dimensional.

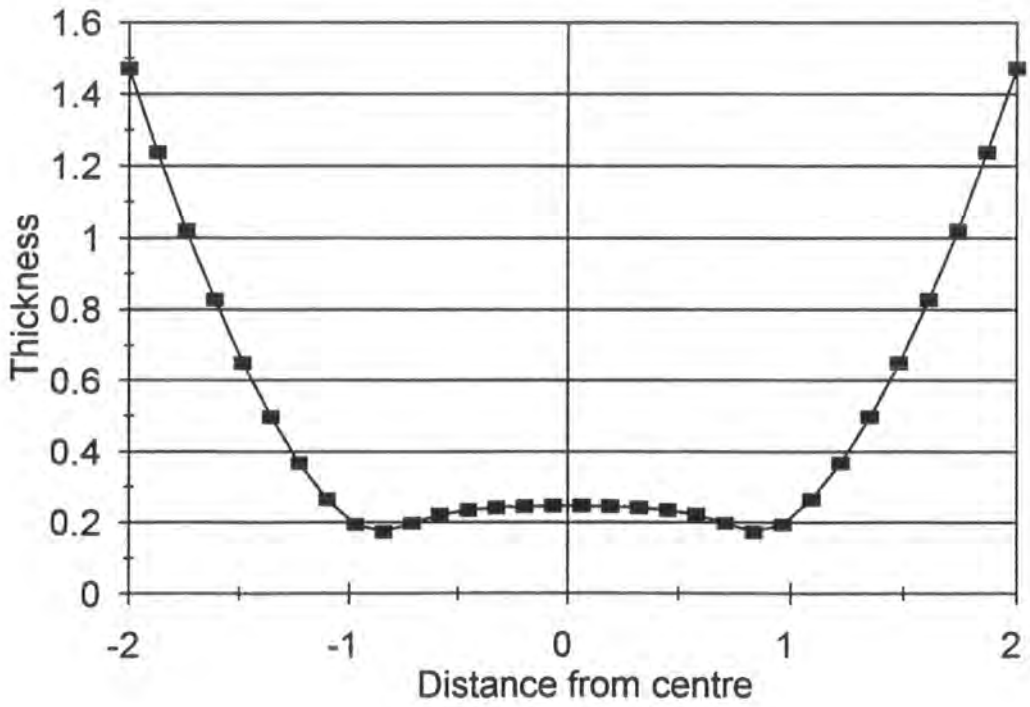

Figure 7.18. Film thickness perpendicular to direction of flow for 150rpm at 3.8N load. Units are non-dimensional

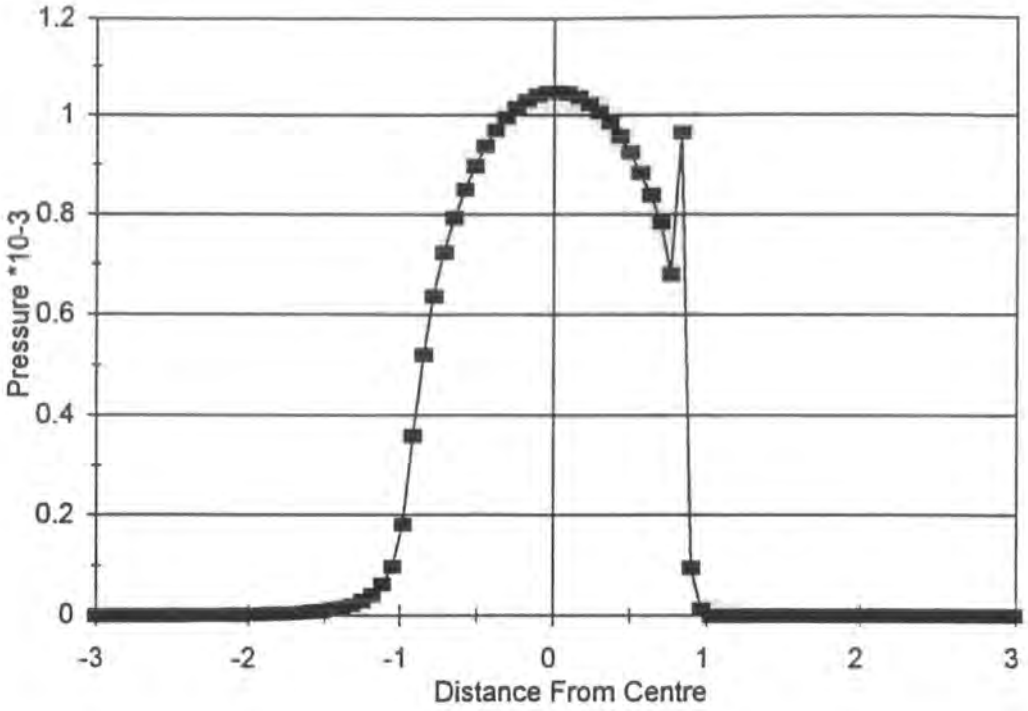

Figure 7.19. Pressure profile for 150rpm at 8.1N load. Units are non-dimensional.

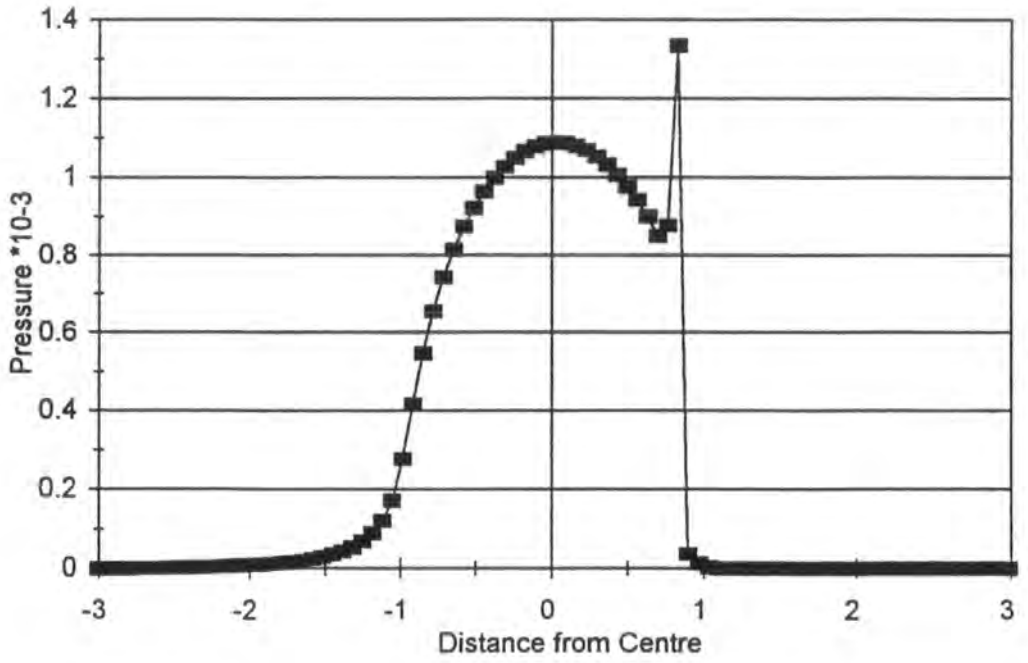

Figure 7.20. Pressure profile for 700rpm at 8.1N load. Units are non-dimensional.

for some examples. The remaining pressure and film thickness profiles are included in appendix 2.) it is evident that as the IR window is moved towards the inlet, the pressure decreases and it would be expected that the bands would narrow due to the decrease in interactions as the compression of the molecules is lessened. If the film thickness is now examined, it can be seen that the thickness of the fluid decreases as it is offset from the centre (i.e. moved perpendicularly to the direction of flow). Therefore, the average distances between the molecules decreases, with a consequent increase in molecular interactions which leads to, in this case a broadening of the bands (see chapter 6). The vibrational bands are also seen to broaden as the speed is increased and narrow as the load is increased. Again, these changes can be explained with reference to the pressure profiles. As the load is increased, the maximum pressure at the centre of the contact is seen to decrease, thus reducing the molecular interactions and therefore the rate of relaxation will be seen to decrease. As the speed is increased, it is evident that the maximum pressure increases indicating a possible increase in relaxation rate due to the increased molecular interactions.

7.3.2. Changes in the Carbonyl Stretching Region

As in previous chapters, the carbonyl stretching region was fitted to two bands. Figure 7.21 shows that the data obtained from the fitting program shows very little changes in bandwidth along the centre line at 150rpm and 3.8N load. This is also true when load is increased at 150rpm and 200rpm. When offset, the splitting of the two bands is evident (figures 7.10 and 7.11), and this varies as the sampling window is moved towards the inlet region, but once again there is little variation in bandwidths of the fitted bands. When the load is held constant, there is little change in the spectra at low speeds, but at higher speeds there is a small increase in width for both components as the sampling window is moved towards the inlet. (figures 7.12 and 7.13)

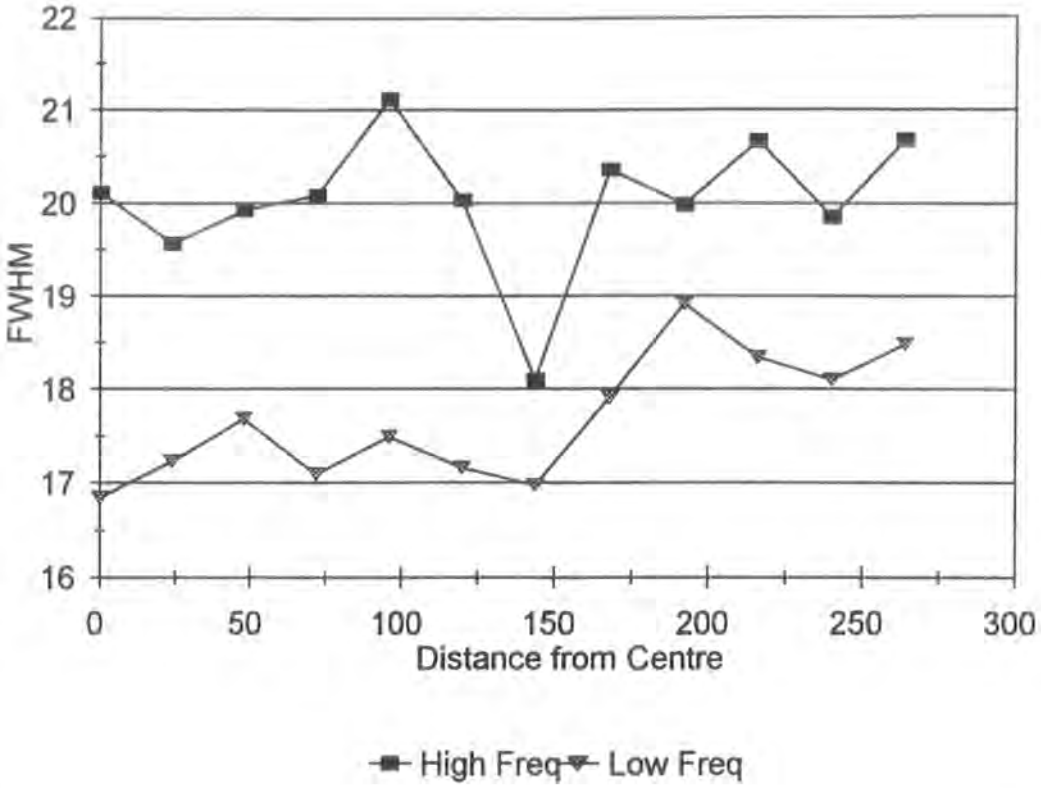

Figure 7.21. Graph showing the variation in bandwidth for the fitted carbonyl bands Data obtained at 150rpm and 3.8N load along centre line of the contact moving towards the inlet region.

If the pressure profiles and film thicknesses are examined, see appendix 2, in detail the following is seen:

1. Constant speed, increasing load.

a) The pressure spike towards the outlet decreases with respect to the pressure in the centre of the contact.

b) The pressure spikes offset from the centre line increase with respect to the pressure in the centre of the contact.

c) The shape of the overall pressure profile changes. The shape becomes more rounded.

d) Both the centre film thickness and the minimum film thickness decrease.

e) The difference between the minimum film thickness and that in the centre decreases.

2. Constant load, increasing speed.

a) The pressure spike towards the outlet increases with respect to the pressure in the centre of the contact.

b) The pressure spikes offset from the centre line decrease and then increase again with respect to the pressure in the centre of the contact. e.g. There are no pressure spikes for 600rpm at 8.1N, but at 800rpm and 8.1N the spikes are visible again.

c) The shape of the overall pressure profile changes. The shape is more rounded at lower speeds.

d) The film thickness increases with increasing speed.

As mentioned previously, for the data obtained at 150 and 200rpm offset from the centre line, changes occur. For the data at 48 microns offset from the centre line, the splitting of the two bands is evident at 3.8N and 6.5N, but at 7.3N and 8.1N the immediate appearance of the two bands is not clear. There is however a high frequency shoulder on these two bands and there appears to be a slight shift to high frequency. It is also noticeable that the intensity of the overall carbonyl stretching band decreases as the load is increased. This is expected and is explained due to the decreasing film thickness predicted from equation 7.9. From the spectra offset 120 microns from the centre line, the high frequency component is seen to increase with respect to that of low frequency. If figures 7.22-23 are examined it can be seen that the film thickness decreases with respect to load and on moving away from the centre of the contact. At the same time, the pressure also decreases and then increases to a maximum before it falls away. Therefore, it is likely that there is a subtle combination of the effects of decreasing film thickness and pressure changes. If for example the set of data offset by 120 microns coincide with the minimum film thickness and the pressure spike, then it would be expected that, as in chapter 6, the molecules would be perturbed by considerable intermolecular forces and this would drive them into different conformations. This is apparent as the high frequency component is obviously increasing. It should also be remembered that the molecules are being sheared at considerable rates and this is likely to have a considerable effect on any changes seen.

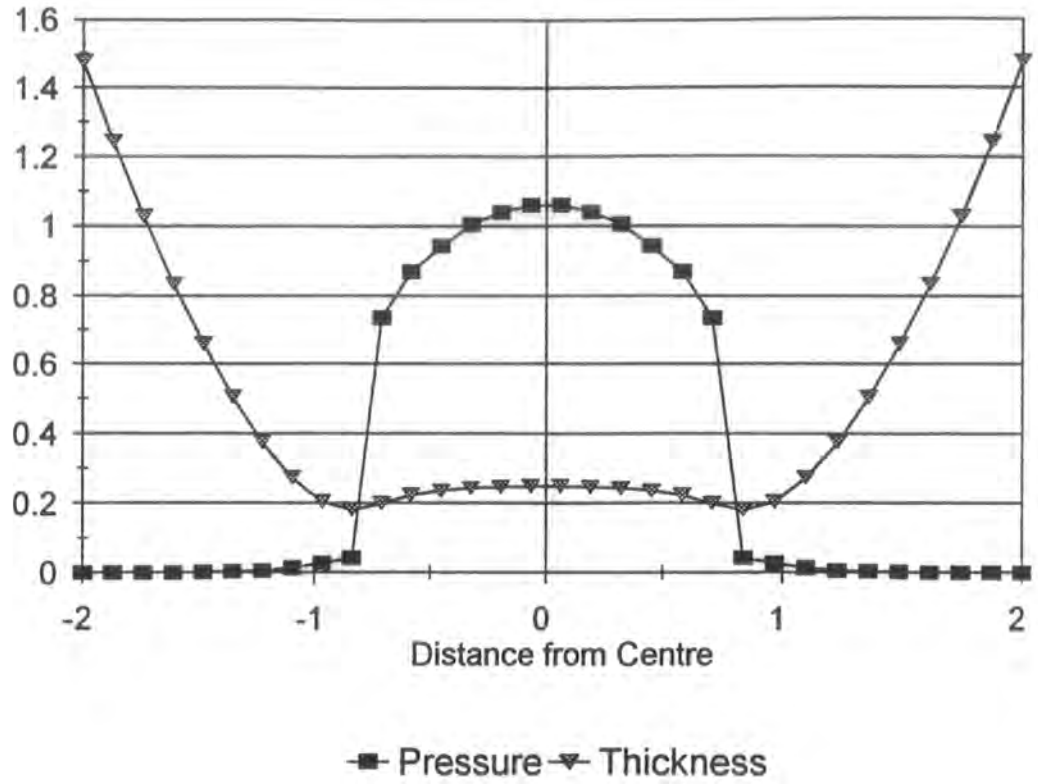

Figure 7.22. Variation of pressure and thickness perpendicular to the direction of flow for 150rpm at a load of 3.8N. Units are non-dimensional.

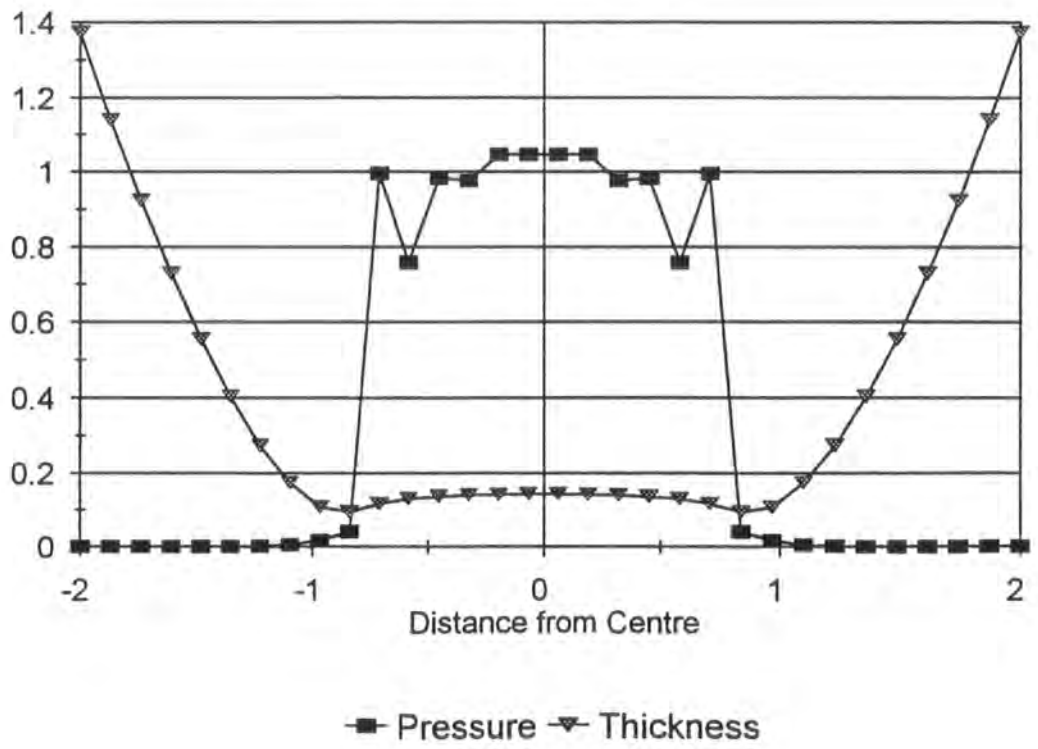

Figure 7.23. Variation of pressure and thickness perpendicular to the direction of flow for 150rpm at a load of 8.1N. Units are non-dimensional.

We now move on to the data obtained at a constant load of 8.1N. At 150rpm and 200rpm, as mentioned earlier the data taken along the centre of the contact towards the inlet show little changes, but when offset, due to combinations of shear, pressure and film thickness, changes become apparent. As higher speeds are reached, the two carbonyl band components are apparent and broadening occurs as the sampling window moves from the centre of the contact towards the inlet. At a distance from the centre, all the sets of spectra show very unusual changes apart from the set obtained at 700rpm. The broadening of the bands occurs due to the difference in intermolecular forces experienced by molecules in the centre of the contact and molecules some distance away from the centre. In the centre, if the molecules are forced to approach each other to van der Waals distances by very high forces, then the shearing of adjacent molecular layers will be hindered by strong steric interactions most likely to involve the cyclohexyl rings. As the IR window is moved away from the centre, the pressure and the shearing force decrease somewhat and fewer molecular interactions will occur. In order to obtain high traction coefficients, the single molecules must interact strongly. Hentschel[4], used a cog like interaction to explain the behaviour of the cyclohexyl compounds he studied. Molecules containing cyclohexyl rings can be imagined as shapes having both teeth and indentations (see figure 7.24) fitting them. At certain pressure values, the molecular layers will approach each other to such an extent that the teeth can lock into the indentations. Thus considerable resistance is offered to a shearing stress across the direction of the molecular layers. This model conception also allows the prediction that molecules shaped approximately like balls, ellipsoids, or even threadlike hydrocarbons have low traction coefficients because they are susceptible to molecular rotations and vibrations. This theory also ties in with that of molecular rigidity[5]. If the internal motions of a molecule are hampered by the inclusion of rigidity enhancing substituents, then it is very unlikely that a "ball" shape will be obtained through intramolecular motions. Therefore a high traction coefficient will result.

It could be that these processes occur in BCS at the higher speeds, but it would be expected that the unusual behaviour would be seen in all the data as there are no big differences in either the film thickness or the pressure profile.

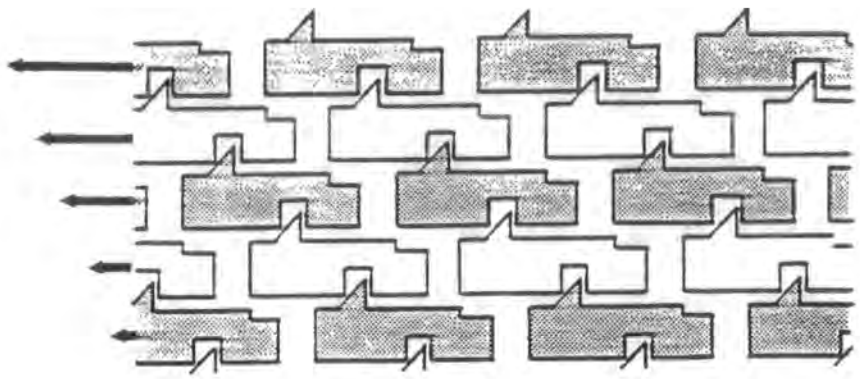

Figure 7.24. The "cog" like interactions of a single molecular shape forming high traction coefficients.

Temperature effects will also play a part in the molecular dynamics, as with the ball rotating at high speeds, heat will be evolved. There is no satisfactory way of measuring the temperature of the fluid in the contact. A thermocouple could be placed to measure the temperature of the oil bath, but this would give no indication of the temperature in the contact. Raman spectroscopy could also be used to deduce the temperature, but with the very small thicknesses and the motion of the liquid this would prove very difficult.

Throughout this discussion it has been evident that there seems to be no explanation of why such unusual bands are seen in the spectra. Are the changes seen real? It is likely that they are, as the unusual bands appear in three separate sets of data. Whether the bands arise from molecular effects i.e. change in molecular conformation and/or dramatic increase in molecular environments due to the extreme conditions of high shear and pressure, or whether they represent an external mechanical process it is impossible to tell. There are many possibilities for such mechanical processes. The rotating ball could be slightly eccentric which would cause a raising and lowering process of the window and indeed the film thickness, the vibrations of the driving motor could

have an adverse effect on the system, or the force of the rotating ball could be so great that liquid could be forced out of the join between the plate holding the diamond window and the metal top plate thus producing several changes of refractive index. All these effects might well play a part in producing the unusual bands, but without further study, there is no way of interpreting this data.

7.3.3. Unusual Behaviour of Data Obtained at 10.1 Newtons and 700rpm

In addition to the very unusual bandshapes seen for the data at 8.1 Newtons load and 600, 800 and 900rpm, there is also the appearance of negative absorption bands for the data obtained at 10.1 Newtons and 700rpm (figure 7.25). It can be seen that the spectra taken from the centre of the contact show negative absorption peaks. As the spectra move further away from the centre, the absorption bands become less negative and eventually become positive. An attempt has been made to model the behaviour exhibited using a computer program developed in Durham by Dr. Y.P.Song[6] with no success. This program solves Maxwell's equations using wave propagation matrices for a multilayered system (figure 7.26) for a particular vibrational band. The general principles of the procedure are outlined below.

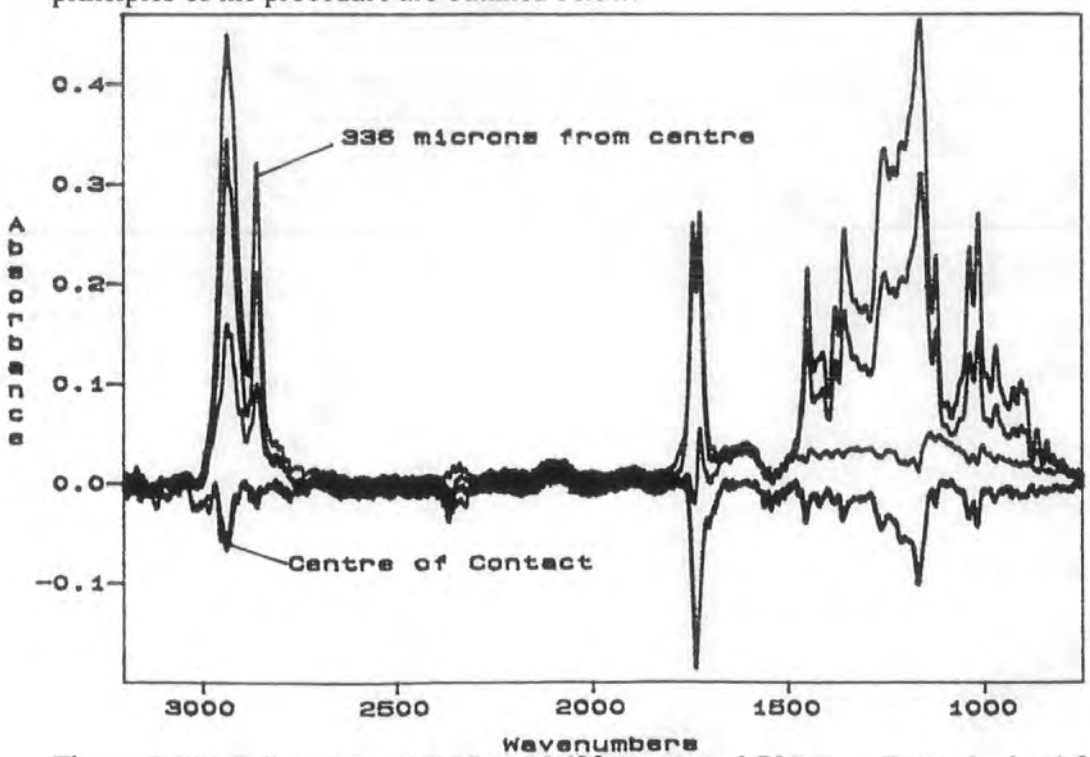

Figure 7.25. Full spectra of BCS at 10.1Newtons and 700rpm. Data obtained from the centre line of the contact moving towards the inlet region.

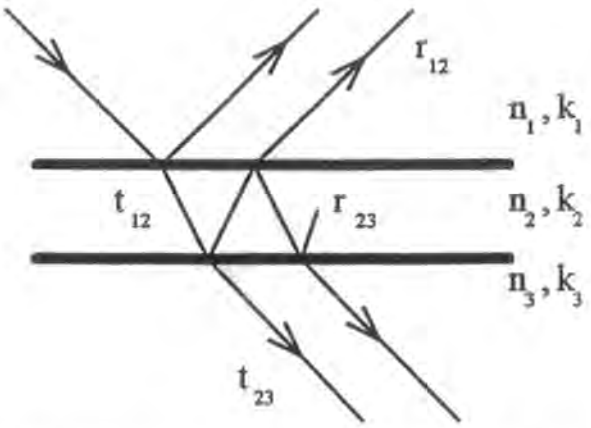

Figure 7.26. Schematic ray representation of reflection by a thin film on a substrate. n and k represent the imaginary and real parts of the refractive indices, with the subscript 1 referring to the superstrate, 2 to the film and 3 to the substrate. t represents the transmitted beam, and r the reflected beam.

As schematically shown in figure 7.26, the reflection of infra red electromagnetic waves by a film is a complicated process. In the neighbourhood of a vibrational band of the film, the complex refractive indices of the superstrate (usually air), film and substrate are schematically shown by figure 7.27

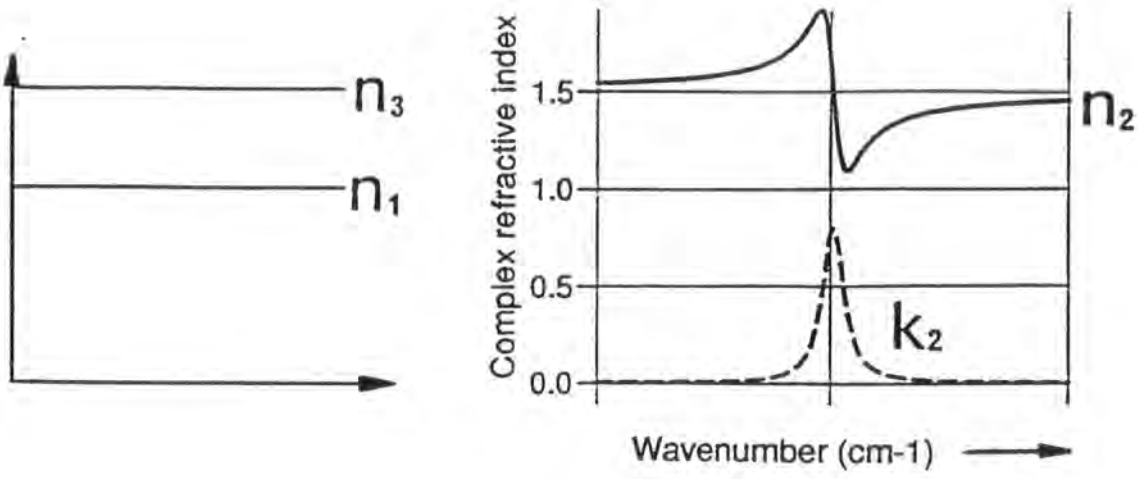

Figure 7.27. Refractive indices of the superstrate n_1, film n_2, and substrate n_3 at the neighbourhood of a vibrational band of the film.

The reflection coefficient of an interface is well known to be proportional to the difference between the complex refractive indices of the media surrounding the interface. In figure 7.28. the interfacial reflection coefficients, r_{12} for the superstrate/film interface and r_{23} for the film/substrate interface are shown.

The overall reflection coefficient of the system depends on the two interfacial reflection coefficients. phase changes at the interfaces. absorption in the film. and phase retardation for the beam to travel through the film. The last factor may be negligible if the film is very much thinner than the wavelength.

The real part of r_{12} and r_{23} may compensate each other and produce a constant contribution to the real part of the overall reflection coefficient. The imaginary parts of the interfacial reflection coefficients would cancel each other if the film were infinitely thin. For finite thickness. the contribution from r_{23} will suffer from absorption during its travelling through the film. and therefore it can not completely cancel the contribution from r_{12}. As a result. the imaginary part of the overall reflection coefficient will peak at the molecular vibration frequency. The overall reflectivity of the system is equal to the square of the real part. which is a constant. plus the square of the imaginary part. which is peaked. Therefore. the total reflection may appear to be peaked at the molecular vibrational frequency. giving an impression that a negative absorption has occurred.

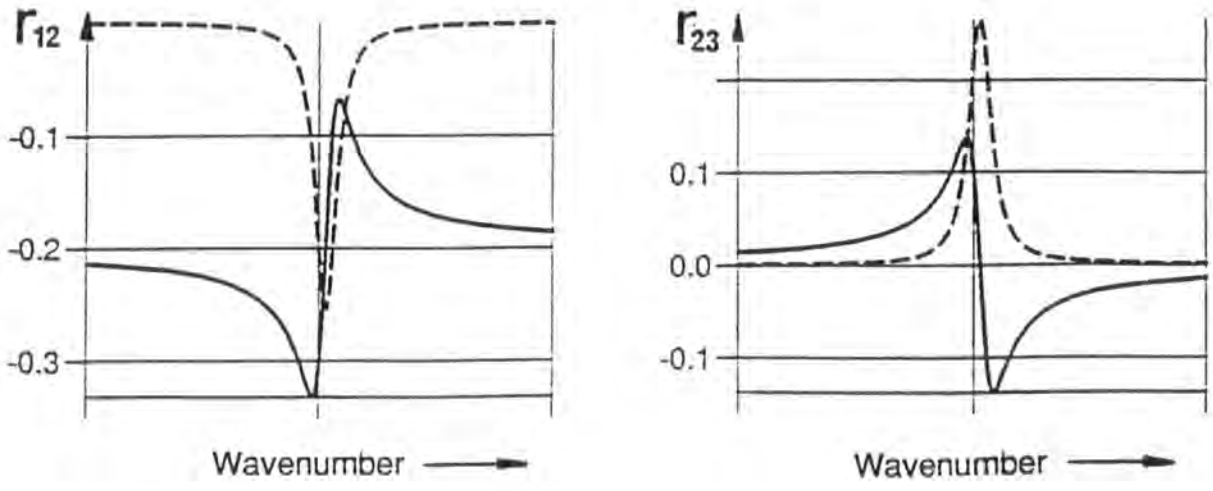

Figure 7.28. Interfacial reflectivities.

The above qualitative description is purely designed for illustrative purposes. A quantitative description of such a system can only be achieved by numerical simulations and by fitting the numerically simulated results to experimental data. In order to do so, the complex refractive indices of the films and the substrates need to be known.

In addition to the differences between the imaginary and real parts of the refractive indices combining to produce negative absorption bands, it is also evident that these bands do not arise from reflections of the metal ball. It is well known that only positive absorption bands can be obtained from a metal surface, so the spectra are not being dominated by this surface. Therefore these bands must arise from some other optical components.

If a four layered system for the EHD rig system is considered (figure 7.29), it is evident that the negative absorption bands must be caused by reflection at the diamond/oil interface or reflection at an oil/metal oxide layer on the steel ball bearing.

Spectral responses are more complicated on nonmetallic substrates than on metallic ones[7]. Such responses can include polarisation scrambling[7] and severe bandshape distortion[8,9]. (N.B. This might also explain the very unusual bandshapes seen at 8.1 Newtons and 600, 800, and 900rpm) In general, polarisation scrambling can be neglected in organic films[7].

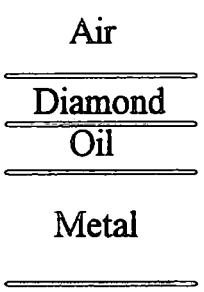

Figure 7.29. Schematic diagram of the interfaces within the EHD contact.

Using the carbonyl stretching band, an attempt was made to simulate the unusual spectra. Various parameters were calculated from the band in order to model the exact conditions apparent in the EHD. These relate to the refractive index, the peak

frequency, the intensity of the band, the width of the band and the shape of the band. In the simulations, it was assumed that the unusual behaviour arose from reflection at an oil/metal oxide layer. Various thicknesses of oil were tried, but this proved to have little effect on the simulated spectra. Figure 7.30 gives an example of the output from the simulations.

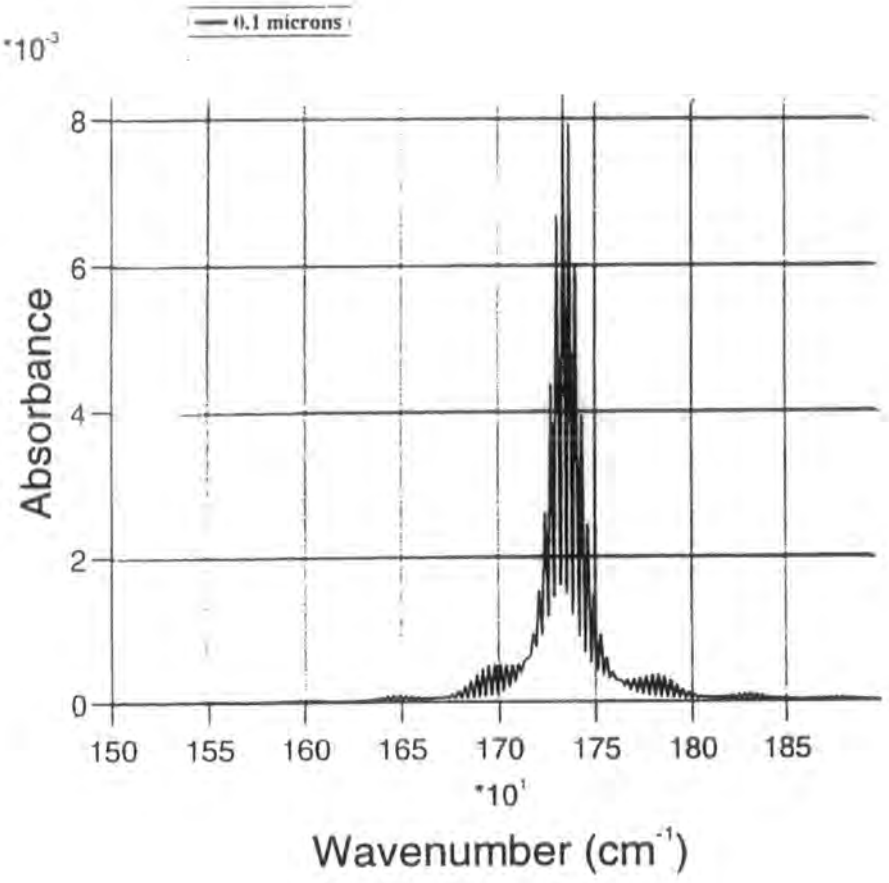

Figure 7.30. Simulation of the carbonyl stretching band at 10.1 Newtons and 700rpm.

As can be seen, there is little comparison with the experimental data.

Finally, the unusual bands may arise from the optical set up of the microscope used. If there are reflections off mirrors or distortions off interfaces, these could cause distortions that would be apparent in the spectra.

References

1. B.J. Hamrock and D. Dowson, "Ball Bearing Lubrication- The Elastohydrodynamics of Elliptical Contacts" John Wiley and Sons, New York (1981)
2. D. Dowson and G.R. Higginson, "Elastohyrdrodynamic Lubrication, the Fundamentals of Roller and Gear Lubrication" Pergamon, Oxford (1966)
3. A.A. Lubrecht. W.E. ten Napel and R. Bosma, J. Tribol., 109, 437 (1987)
4. K.-H. Hentschel, J. Synth. Lubr., 2, 165 (1985)
5. M.P. Dare-Edwards, Synth. Lubr., 8, 197 (1991)
6. Y.P. Song. Personal Communication.
7. A.N. Parikh and D.L. Allara, J. Chem. Phys., 96, 927 (1992)
8. M.D. Porter, T.B. Bright, D.L. Allara and T. Kuwana, Anal. Chem., 58, 2461 (1986)
9. D.L. Allara, A. Baca and C.A. Pryde, Macromolecules 11, 1215 (1978)

CHAPTER 8

Solution Studies

8.1 Introduction

In order to obtain some indication of the strength of intermolecular interactions between the molecules, infra red spectra were obtained at 0.5 and 0.05 mole fraction in hexane, carbon tetrachloride and carbon disulpide, for all the molecules. Tables 8.1-4 summarise the spectral changes for BCS (the remaining ester compounds exhibited exactly the same behaviour so that data is not tabulated). Raman spectra were also obtained for all the molecules at the same concentrations for heptane, tables 8.5-6 summarise the changes.

Table 8.1. Peak frequency variation for 0.5 mole fraction BCS

Solvent	$\nu_a(CH_2)$ $cm^{-1}\pm0.5cm^{-1}$	$\nu_s(CH_2)$ $cm^{-1}\pm0.5cm^{-1}$	ν(C=O) $cm^{-1}\pm0.5cm^{-1}$	ν(C-O)* $cm^{-1}\pm0.5cm^{-1}$
None	2937	2861	1733	1166
C_7H_{16}	-	-	1735	1166
CS_2	2935	2856	1732	1166
CCl_4	2938	2858	1733	1166

Table 8.2. Peak frequency variation for 0.05 mole fraction BCS

Solvent	$\nu_a(CH_2)$ $cm^{-1}\pm0.5cm^{-1}$	$\nu_s(CH_2)$ $cm^{-1}\pm0.5cm^{-1}$	ν(C=O) $cm^{-1}\pm0.5cm^{-1}$	ν(C-O)* $cm^{-1}\pm0.5cm^{-1}$
None	2937	2861	1733	1166
C_7H_{16}	-	-	1741	1165
CS_2	2933	2859	1733	1165
CCl_4	2936	2855	1733	1165

Table 8.3. FWHM variation for 0.5 mole fraction BCS

Solvent	$\nu_a(CH_2)$ $cm^{-1}\pm0.5cm^{-1}$	$\nu_s(CH_2)$ $cm^{-1}\pm0.5cm^{-1}$	ν(C=O) $cm^{-1}\pm0.5cm^{-1}$	ν(C-O)* $cm^{-1}\pm0.5cm^{-1}$
None	35.3	17.2	26.2	22.3
C_7H_{16}	-	-	20.6	18.5
CS_2	34.9	18.4	20.7	18.3
CCl_4	33.1	17.6	19.5	17.9

Table 8.4. FWHM variation for 0.05 mole fraction BCS

Solvent	$\nu_a(CH_2)$ $cm^{-1}\pm0.5cm^{-1}$	$\nu_s(CH_2)$ $cm^{-1}\pm0.5cm^{-1}$	ν(C=O) $cm^{-1}\pm0.5cm^{-1}$	ν(C-O)* $cm^{-1}\pm0.5cm^{-1}$
None	35.3	17.2	26.2	23.3
C_7H_{16}	-	-	15.3	14.2
CS_2	27.5	16.7	17.3	15.3
CCl_4	30.1	16.5	18.5	16.2

Table 8.5. Peak frequency variation for 0.5 mole fraction in heptane. Raman data for all molecules.

Compound	ν(C=O) $cm^{-1}\pm0.5cm^{-1}$	ν(C-O)* $cm^{-1}\pm0.5cm^{-1}$
BCS	1734	1152
BC2MS	1733	1151
BC22DMS	1732	1153
CMCA	1735	1151
CC	1726	1151

Table 8.6. FWHM variation for 0.5 mole fraction in heptane. Raman data for all molecules.

Compound	ν(C=O) $cm^{-1}\pm0.5cm^{-1}$	ν(C-O)* $cm^{-1}\pm0.5cm^{-1}$
BCS	21.2	8.5
BC2MS	18.0	8.2
BC22DMS	20.3	12.5
CMCA	18.5	11.0
CC	22.7	8.4

Table 8.7. Peak frequency variation for 0.05 mole fraction in heptane. Raman data for all molecules.

Compound	ν(C=O) $cm^{-1}\pm0.5cm^{-1}$	ν(C-O)* $cm^{-1}\pm0.5cm^{-1}$
BCS	1738	1152
BC2MS	1736	1153
BC22DMS	1737	1152
CMCA	1739	1152
CC	1732	1153

Table 8.8. FWHM variation for 0.05 mole fraction. Raman data for all molecules.

Compound	ν(C=O) cm^{-1}±0.5cm^{-1}	ν(C-O)* cm^{-1}±0.5cm^{-1}
BCS	16.2	6.2
BC2MS	14.0	7.4
BC22DMS	18.2	9.1
CMCA	12.6	8.0
CC	12.2	7.5

8.2. Results

8.2.1. CH_2 Stretching Modes

The frequencies of the antisymmetric and symmetric modes of the CH_2 bands, for the infra red measurements decrease in solution, with the change in dilution with CCl_4 being the greatest(figure 8.1). The red shift in frequency increases as the liquid becomes more dilute. (figure 8.2). This region can not be studied in heptane due to the overlapping bands from the heptane vibrational modes.

The FWHM also decrease in solution, with the bands further narrowing on dilution (tables 8.3-4)

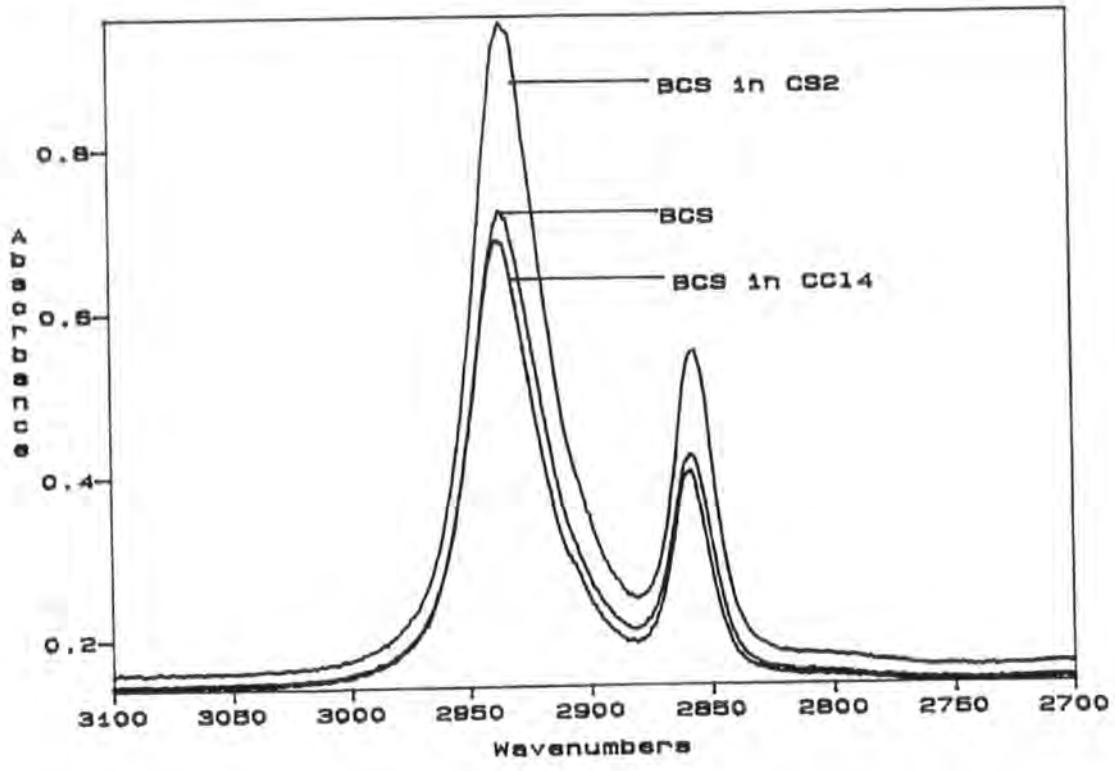

Figure 8.1. Infra red spectra of the CH_2 stretching region for 0.5 mole fraction BCS in CS_2 and CCl_4

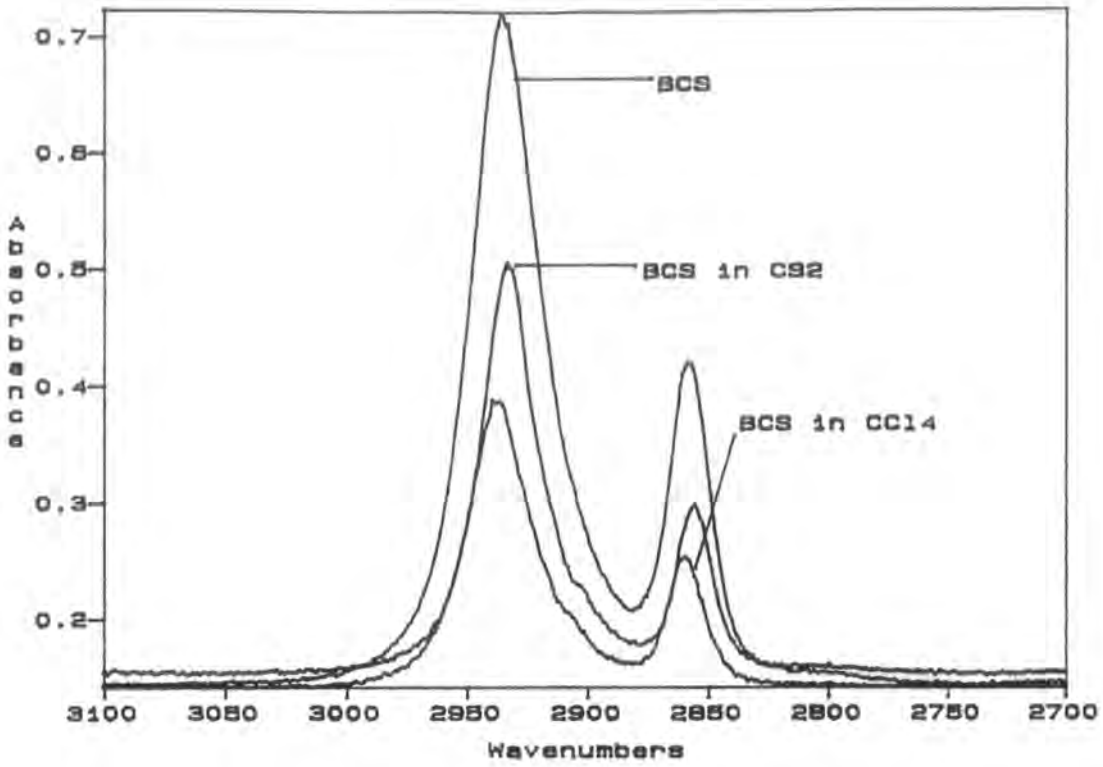

Figure 8.2. Infra red spectra of the CH_2 stretching region for 0.05 mole fraction BCS in CS_2 and CCl_4

8.2.2. Carbonyl Stretching Region

The infra red bands in CS_2 and CCl_4 exhibit little change in frequency, whilst that in heptane shifts to higher frequency. (figure 8.3). The carbonyl stretching region in the Raman experiments is relatively small in intensity for the diester compounds (figure 8.4), but is more apparent for CMCA and CC. (figure 8.5). Again, for both infra red and Raman measurements, the blue shift in heptane increases as the solution becomes more dilute. (figure 8.6).

All the FWHM decrease in solution.(figure 8.3) Once again, the bands narrow further on dilution, with the change in heptane being the greatest. (figure 8.6)

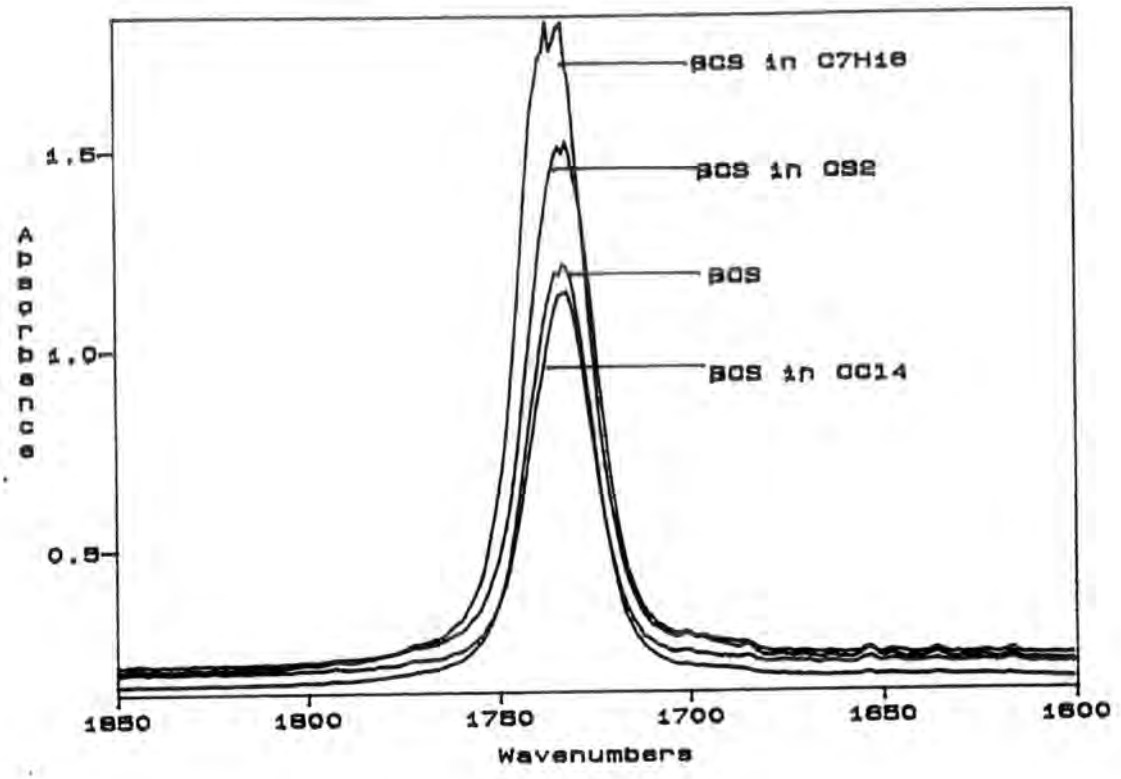

Figure 8.3. Infra red spectra of the carbonyl stretching region for 0.5 mole fraction BCS in CS_2, CCl_4 and heptane.

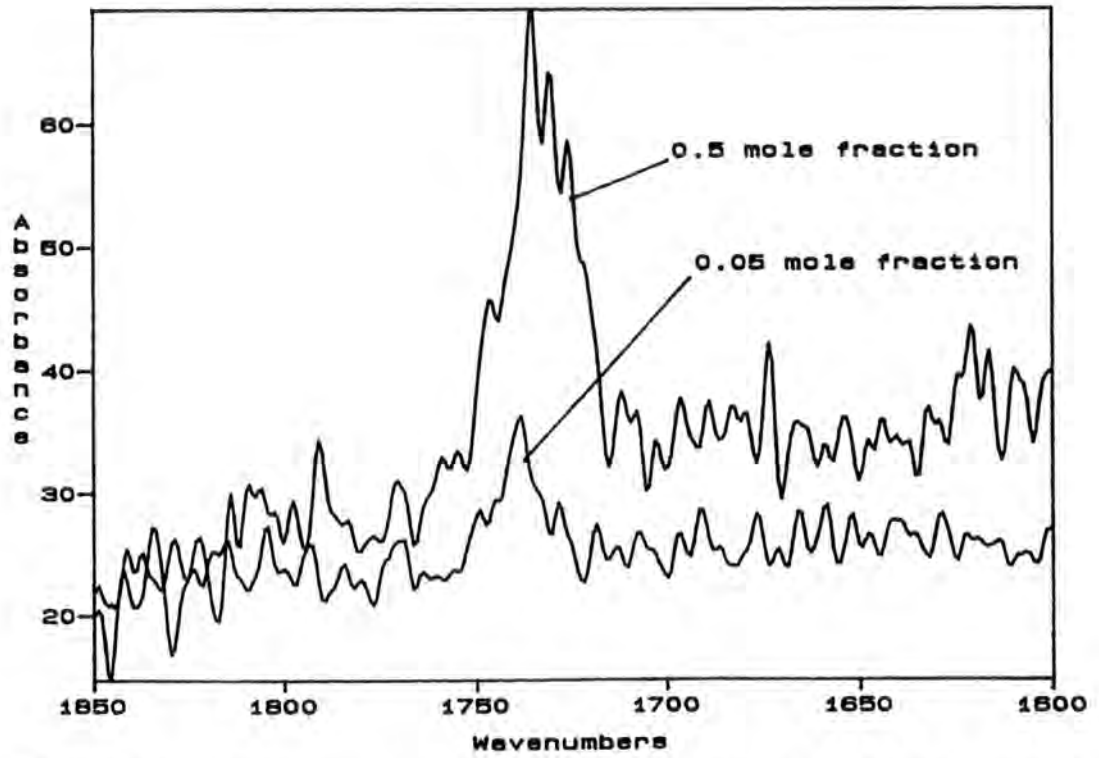

Figure 8.4. Raman spectra of the carbonyl stretching region for 0.5 and 0.05 mole fraction BCS in heptane.

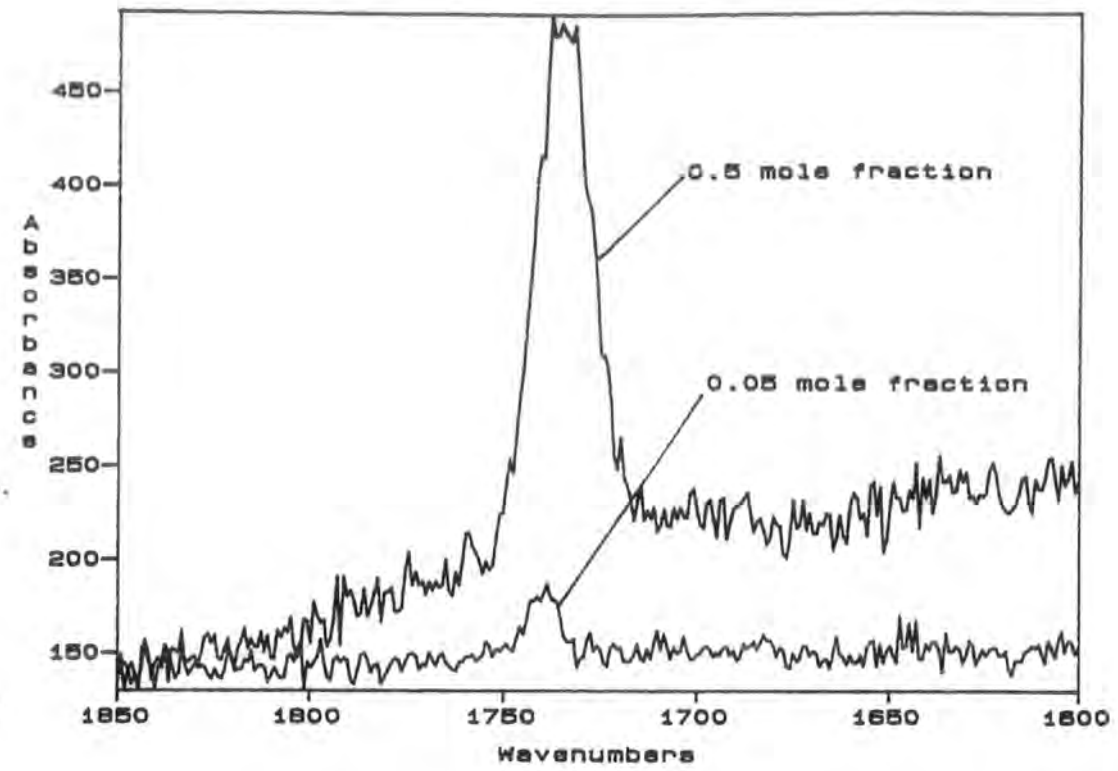

Figure 8.5. Raman spectra of the carbonyl stretching region for 0.5 and 0.05 mole fraction CMCA in heptane

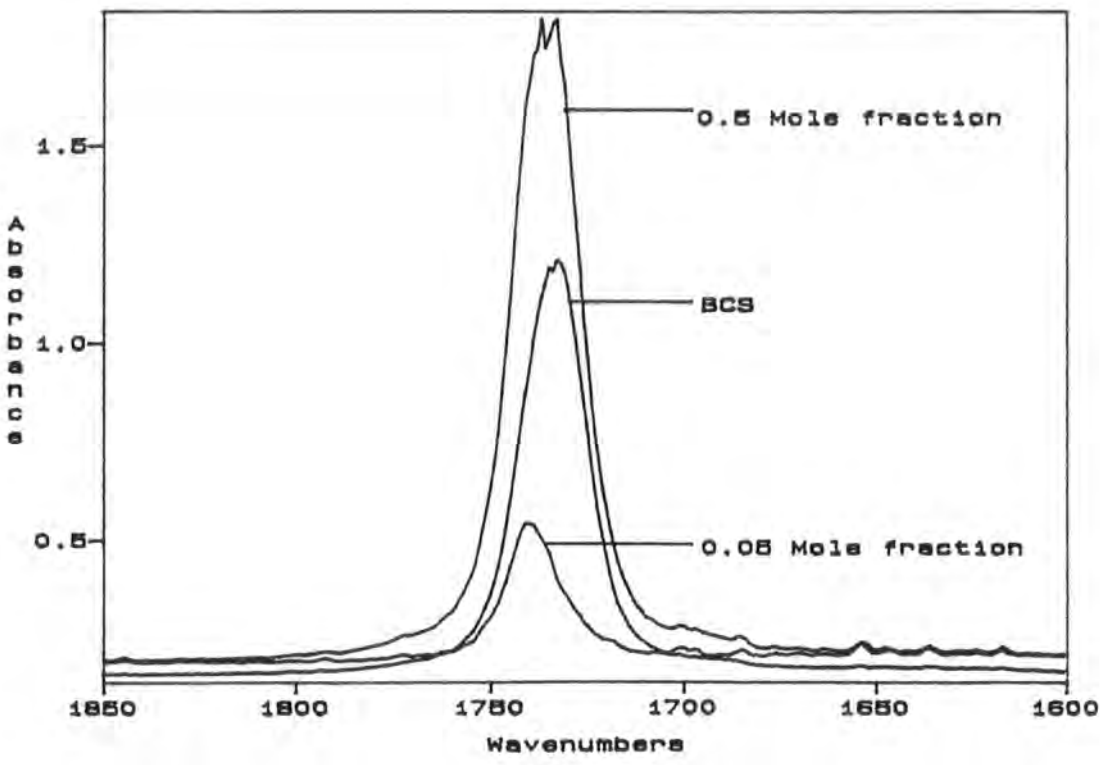

Figure 8.6. Infra red spectra of the carbonyl stretching region for BCS in heptane.

8.2.4. Ester Stretching Region

There is little change exhibited in the infra red peak frequency for the ester stretching region for all molecules. However, there is a narrowing of the ester stretching band on dilution, with the change in heptane being the greatest (figure 8.7 and tables 8.3 and 8.4)

8.2.5. Other Bands

All other bands exhibit similar changes to the ones mentioned previously, with the changes in heptane being the greatest.

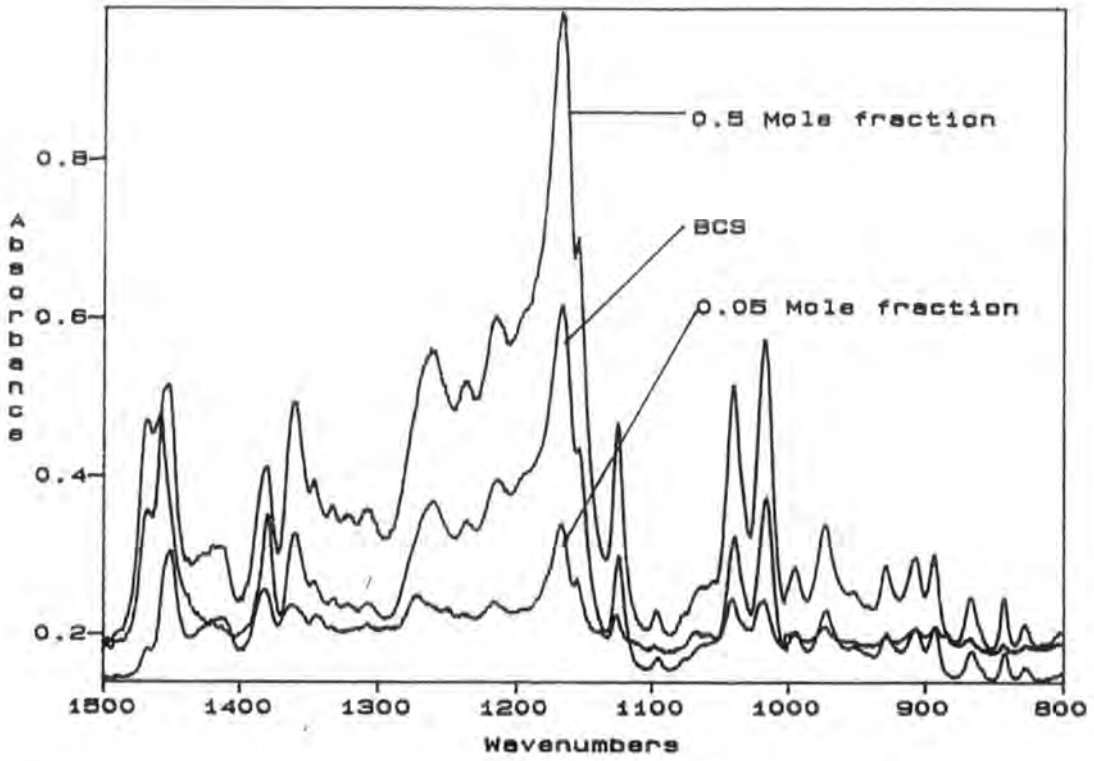

Figure 8.7. Infra red spectra of the 1500-800cm^{-1} for 0.5 and 0.05 mole fraction BCS in and heptane.

8.3 Discussion

8.3.1 Frequency Shifts

When molecules are placed in solution, the intermolecular forces on the solute molecules change with respect to those felt by molecules in the pure solute. This change in forces is felt by the bonds of the molecules and causes a change in frequency of the vibrational modes of the molecule.

Intermolecular forces can be expressed as the interaction of two molecules in terms of their intermolecular potential energy, U(r), which results from their separation at a distance r. (See chapter 2) Several different types of interaction contribute to the intermolecular potential energy e.g. dipole-dipole (and/or higher multiple interactions), dispersive, inductive and repulsive interactions. The first three types involve attractive forces which are long range and slowly varying, whilst repulsive interactions are short range and rapidly varying.

As mentioned previously Drickamer and et al have studied the influence of different types of intermolecular interactions on vibrational frequencies[1,2].They found that repulsive forces give a blue frequency shift whilst attractive forces give a red shift. This has been supported by molecular dynamics simulations.[3]

The frequency shift $\Delta\nu_2$ on going from an isolated molecule to the liquid phase is given by[1,2]

$$\Delta\nu_2 = A(\gamma e'_{i2} + e''_{i2}) \qquad 8.1$$

where $A = (8\pi^2c^2m\nu^g)^{-1}$, m is the reduced mass of the chemical oscillator, ν^g is the frequency of the isolated molecule, $\gamma=(-3f_{111}/f_{11})$ where f_{111} is the anharmonic and f_{11} is the harmonic force constant in the vibrational potential, e'_{i2} is the first derivative and e''_{i2} is the second derivative of the intermolecular interaction energies with respect to a displacement from the equilibrium position. The index 2 indicates solute molecules, and i indicates solvent molecules. The presence of the term $\gamma=(-3f_{111}/f_{11})$ allows for variation in the magnitude of the frequency shift for each different vibrational mode of a molecule. This is essentially a measure of how much a vibration modifies the intermolecular

potential. For instance, usually the carbonyl stretching vibration greatly modifies the large attractive intermolecular potential localised at the carbonyl group. Therefore, it can be expected that a relatively large frequency shift will be observed when molecules containing the carbonyl functionality are dissolved in solution.

In dilute solutions in heptane, the frequencies of the bands for BCS increase whilst very little change is seen in the peak frequencies for BCS in CS_2 or CCl_4. BCS will have a large dipole moment located in the carbonyl group and consequently it will be expected that attractive interactions will dominate in the pure liquid and probably in solution. By dissolving BCS in various solvents the intermolecular potential felt by the molecules will change. Attractive interactions between BCS molecules will be disrupted and new solvent-solute interactions will occur.

In CS_2 or CCl_4, observation of little overall change in vibrational frequency, for all modes for BCS could be due to the solvent -solute interactions causing a large enough red frequency shift to offset the blue frequency shift caused by the separation of BCS molecules. In heptane, the interactions of BCS with the heptane molecules does not alter the intermolecular potential in a manner which cancels the shift due to the reduction in BCS-BCS attractive interactions. Therefore, the overall effect seen for BCS is a blue frequency shift. It is also possible that the repulsive interactions in heptane are more significant than in CS_2 or CCl_4. However, there is no reason to expect that BCS-heptane repulsive interactions are any greater than BCS-BCS repulsive interactions.

If it is assumed that attractive interactions do dominate the frequency shifts observed for BCS in solution, then it appears that heptane is showing a greater tendency to separate the BCS molecules than CS_2 or CCl_4. Thus producing the different behaviour in solution. Molecules like BCS are never expected to be packed randomly even in the liquid state. Therefore, with heptane being more "like" the chain structure of BCS, it might be expected that heptane would find it easier to associate with BCS and separate the BCS molecules. In addition, heptane has the greater molecular volume (M/ ρl) 147cm^3mole^{-1} as compared to 60cm^3mole^{-1} and 96cm^3mole^{-1} for CS_2 or CCl_4. So, it might be expected, considering the size alone, that heptane would be better at

separating the BCS molecules, for BCS at the same mole fraction concentration in the three solvents.

Another explanation for the difference in behaviour of the vibrational modes for BCS in heptane than for BCS in CS_2 or CCl_4 could be that solvent molecules in CS_2 or CCl_4 are interacting in some specific manner with the functional groups of BCS, in particular the carbonyl group. These interactions may cause significant red shifts.

Finally, it is necessary to consider the dependence of the frequency shift on intramolecular interactions. For rigid molecules, the frequency shift compared to the gas phase depends solely on the changes in intermolecular potential. For larger molecules like BCS, there may also be significant contributions from changes in the intramolecular potential. If the intramolecular interactions of BCS change, for instance because of a shape change or change in molecular flexibility, then this can significantly effect the frequencies of the vibrational modes. This may be occurring for BCS in heptane, explaining the large frequency shifts compared to those seen for BCS in CS_2 or CCl_4.

8.3.2 Bandwidths

There is a decrease in all the bandwidths measured. This implies that BCS-BCS interactions provide more efficient vibrational relaxation then BCS-solvent interactions. If inhomogeneous broadening is assumed to be the major cause of vibrational relaxation, and applying the Kubo line formalism[4] in the rapid modulation limit ($FWHM \propto \tau_v^{-1} = M2v\tau_m$, see chapter 6), then to observe a decrease in bandwidth, either the vibrational second moment or the environmental modulation time, or both, must decrease. A decrease in attractive interactions by solvation is predicted, from vibrational dephasing theory[5,6], to reduce both the second moment and the environmental modulation time. The environmental modulation time decrease due to the removal of attractive interactions between BCS molecules allowing for greater molecular flexibility, which will have the effect of motionally narrowing any broadening due to intramolecular inhomogeneous dephasing.

The greatest bandwidth change is seen in heptane. This provides evidence that the changes in molecular interactions which cause frequency shifts also modulate relaxation processes. The change in attractive interactions, particularly dispersive interactions, on going from BCS liquid to solution are mainly responsible for the observed frequency shifts. Therefore, it is probable that the width changes in solution arise from modulations to the relaxation processes caused by changes in the attractive intermolecular potential.

From these studies, it is apparent that the molecules are held together by quite strong intermolecular forces, probably dipolar interactions through the carbonyl functional groups.

References

1. A.M. Benson, Jr. and H.G. Drickamer, J. Chem. Phys., 27, 1164 (1957)
2. R.R. Wiederkehr and H.G. Drickamer, J. Cem. Phys., 28, 311 (1958)
3. D. Levesque, J.J. Weiss and D. Oxotoby, J. Chem. Phys., 68, 5528 (1978); ibid., 72, 2744 (1980).
4. R. Kubo, in "Fluctuations, Relaxation and Resonance in Magnetic Systems", Ed. D.Ter. Haar), Plenum, New York (1962)
5. J. Yarwood and R. Arndt, "Study of Intermolecular Interactions in the Liquid Phase", Chapter 4 of "Molecular Association", Vol. 2, ed. R. Foster, Academic Press (1979)
6. W.G. Rothschild, "Dynamics of Molecular Liquids", John Wiley and Sons (1984)

CHAPTER 9

Summary and Conclusions

9.0 Introduction

The aim of this project was to investigate the molecular behaviour of a model traction fluid (BCS) under conditions of high temperature and variable pressure. It was also hoped that by studying molecules similar in structure to BCS (figure 4.1) some deductions could be made regarding the intermolecular and intramolecular processes which lead to the required properties for a traction fluid. Infra red micro-reflectance absorption spectroscopy[1], a modern technique, has been used to try and simulate the operating conditions found in traction drives. In addition, in an attempt to learn more about the intermolecular interactions in the fluids, various solution spectra have been examined.

Vibrational frequency shifts and changes in bandwidths and intensities have yielded information on the intermolecular and intramolecular dynamics in BCS, and attempts have been made to link this information with the macroscopic behaviour of the fluid.

This chapter will first summarise the work completed in this thesis and will then draw some overall conclusions.

9.1 Summary of Results

9.1.1 Variable Temperature Studies

Few significant changes are observed on varying the temperature. However, this is common with the competing effects of temperature and density combining to cancel any variation.

There is some correlation between the viscosity of the molecules studied and the changes observed, with the more internally rigid molecules exhibiting the smallest changes.

On examination of the carbonyl stretching region, at least two separate bands are observed, with that of higher frequency becoming more prevalent at higher temperatures. This indicates an intramolecular process, probably coupled with a change in conformation.

It is postulated that some indication of intramolecular and intermolecular processes can be deduced from the differences between the ester stretching region and the carbonyl stretching region respectively. It is likely that the ester stretching band is heavily influenced by the close proximity of the cyclohexyl ring structures.

9.1.2 Variable Pressure Studies

There is considerable broadening of all the vibrational bands of the molecules studied as the pressure is increased. This is consistent with an increase in the vibrational relaxation rate.

All bands show a blue frequency shift, of varying degree, with increasing pressure, indicating that repulsive forces are dominating the observed changes for these bands. The same behaviour is observed for n-hexadecane[2].

The carbonyl stretching region of the diester compounds contains at least two bands, with the high frequency component becoming more dominant as pressure is increased. This indicates a change in conformation. Observations of the differences in the changes of peak frequency for CMCA and CC indicate that a competition of effects is occurring between the increased alignment of the carbonyl dipoles and the increase in

repulsive interactions. Analysis using the Kubo model[3] has shown that this band is more likely to be formed in the slow modulation regime.

The ester stretching region exhibits an increase in vibrational relaxation rate. The presence of the bulky cyclohexyl ring manifests itself in the behaviour of this region, with perhaps a "cog-like" interaction of the cyclohexyl rings of adjacent molecules occurring at elevated pressures.

9.1.3 Dynamic pressure Studies Using the EHD Rig

Unusual behaviour is exhibited in some of the spectra obtained from the dynamic pressure studies. This includes unusual band shapes and negative going bands. Little explanation can be given for this behaviour, although negative going bands are common in some studies with a film on a non-metallic substrate[5]. (See chapter 7)

There is a distinct appearance of two separate carbonyl stretching bands for some experimental conditions. This splitting increases as the sample area is moved towards the inlet or offset from this central line of the contact. This behaviour is somewhat unexpected as the conditions are most severe in the contacts' centre. In fact, it is likely that the severity of the conditions produces this effect. The combination of high pressure, high shear rate and temperature in the centre of the contact only allows the BCS molecules to assume a single conformation. As these conditions lessen i.e. moving towards the inlet, the molecules become less constrained and different behaviour is observed. The high frequency component of the carbonyl stretching region increases as the sampling area is moved towards the inlet.

Despite the very unusual behaviour under some conditions, very little change is seen in the peak frequencies or bandwidths of the "normal" BCS spectra.

With the assistance of three dimensional pressure and film thickness profiles, some attempt has been made to explain the observed changes in terms of a combination of pressure and film thickness changes.

9.1.4 Solution Studies

A blue shift and a narrowing of the carbonyl stretching region, of all the ester molecules studied, was apparent in heptane for both Raman and infra red spectra. This behaviour increases as the dilution increases. The large increase in frequency for this band, compared with the other vibrational bands, suggests that strong attractive, probably dipole-dipole, interactions are localised at the carbonyl group.

All the bands have a decreased band width in solution (heptane, carbon disulphide and carbon tetrachloride), showing that the vibrational relaxation rate is slower on dilution. Therefore, relaxation arising from BCS-BCS interactions is more efficient than that arising from BCS-solvent interactions.

It was suggested from the solution experiments that heptane is better at separating the BCS molecules than carbon disulphide or carbon tetrachloride. Heptane which is more similar to the overall structure of BCS is therefore more able to separate the BCS molecules.

9.2 Conclusions

It is common practice[5] to describe the shear behaviour of the oil in full EHD conditions by a traction curve in which the coefficient of traction is plotted against the slide/roll ratio. At small slide/roll ratios, the coefficient of traction first increases linearly as the slide/roll ratio is increased and then it gradually becomes non linear. After reaching a maximum, it turns to decrease by a thermal effect caused by viscous shearing of a fluid film at higher slide/roll ratios. These are labelled as the linear, the non-linear and the thermal region respectively.[6]

In order to explain this characteristic behaviour in oils in EHD contacts a number of rheological models have been proposed in which oils are assumed to behave as non-Newtonian viscous fluids, elastic or plastic solids.[7-12] It has generally been accepted that oils are practically Newtonian liquids under low pressures or high temperatures, while they behave as elastic solids under high pressures or low temperatures at low rates of shear. At high rates of shear, however, the Eyring[13] fluid model seems to have given the most reasonable explanation of the experimental results for a wide variety of fluid compositions over a wide range of operating conditions.

As outlined in chapter 1, in this theory, the movement of a molecule from one equilibrium position to the next is regarded as equivalent to the passage of the system over a potential energy barrier. This movement requires the expenditure of energy as work is done in "pushing back" the other molecules, and this energy is dependent on viscosity.

For a small shearing force, the viscosity can be expressed in terms of $\Delta G^{\#}$ the Gibbs Free Energy of activation for viscous flow, the molar volume V, Avogadro's number N, the gas constant R, Planck's constant h, the molecular weight M, and the temperature T

$$\eta \frac{V}{N} h = \nu \frac{M}{N} h = \exp\left(\frac{\Delta G^{\#}}{RT}\right) \qquad 1.7$$

where η is the viscosity and ν the kinematic viscosity.

It follows from simple transition state theory that:

$$\Delta V^{\#} = RT\left(\frac{\partial \ln \nu}{\partial P}\right)_T \qquad 1.8$$

$$\Delta H^{\#} = R\left(\frac{\partial \ln \nu}{\partial T^{-1}}\right)_p \qquad 1.9$$

$$\Delta S^{\#} = R \ln\left(\frac{Nh}{M\nu}\right) + \frac{\Delta H^{\#}}{T} \qquad 1.10$$

$\Delta V^{\#}$ and $\Delta H^{\#}$ are convenient measures of the pressure and temperature dependence of kinematic viscosity, and $\Delta V^{\#}$ alone can be regarded as a kind of pressure-viscosity coefficient.[14,17].

The values for $\Delta V^{\#}$ and $\Delta H^{\#}$ for BCS were obtained using table 9.1 and equations 1.8-1.10 and these are listed in table 9.2 along with other data for comparison obtained from the literature.[16] The structures of molecules 1-4 are shown in figure 9.1.

Table 9.1. Temperature and Pressure Dependence of Kinematic Viscosity of BCS

Temp	Measured Viscosity mPas				
°C	0MPa	25MPa	50MPa	75MPa	100MPa
40	27.34	53.29	105.5	213.5	442.4

Table 9.2 Flow activation quantities.

Fluid	Temperature °C	$\Delta V^{\#}$ cm^3/mol	$\Delta H^{\#}$ $kJmol^{-1}$	$\Delta S^{\#}$ $kJmol^{-1}$
BCS	40	54.67	28.3	
1	40	35.1	16.2	7.5
2	40	50.6	25.9	13.8
3	40	67.8	36.9	39.3
4	40	94.4	56.1	89.5

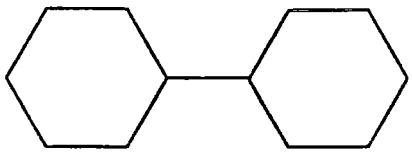

Compound 1

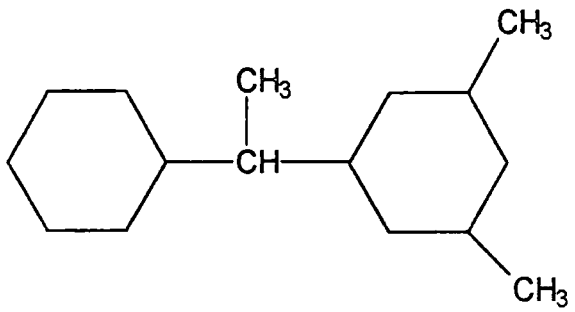

Compound 2

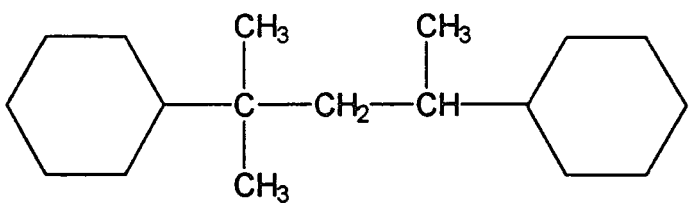

Compound 3

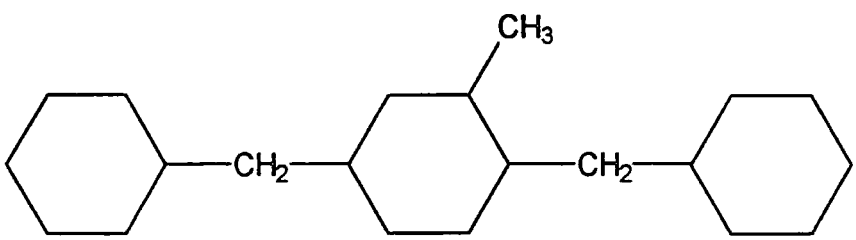

Compound 4

Figure 9.1. The structures of the alicyclic compounds in table 9.2.

The physical meaning of $\Delta V^{\#}$ has been interpreted as follows.[16] $\Delta V^{\#}$ is the volume change in the process of activation for viscous flow and is a measure of the size of the "hole" required for the activated jump. If the flow process is composed of segmental movements to adjacent "holes", figure 9.2, $\Delta V^{\#}$ is determined by averaging the contributions of various flow modes, i.e. the way in which the flow segments move into the "holes". For example, figure 9.3 shows a few typical examples of flow modes of n-alkane. Therefore, $\Delta V^{\#}$ is a measure of the averaged size of the "hole" sizes into which the segments are required to move. The more flexible the chemical structure of a molecule, the more flow modes the molecule has and the smaller the "hole" size the segments require in order to move.

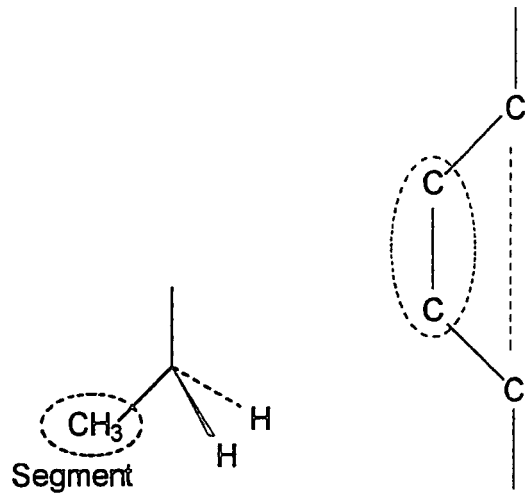

Figure 9.2. Examples of segmental flow.

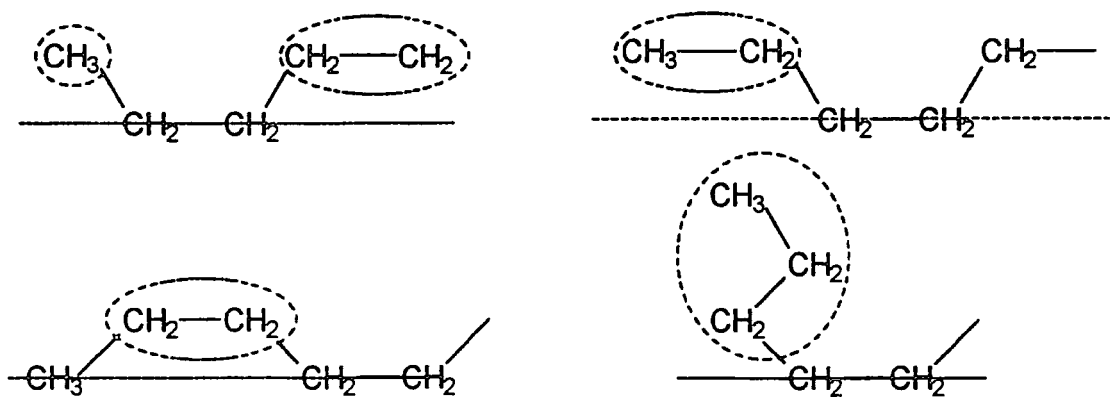

Figure 9.3. Various flow modes of n-alkane. The flow segments are represented by the dotted circles.

It has been suggested that the flow behaviour of mineral oils and synthetic ester lubricants is determined by the independent movement of the segments of a molecule[16,17]. Griest et al have also shown that the viscous flow of pure hydrocarbons which contain several cyclohexyl groups can be regarded as segmental flow[18]. Therefore, it seems reasonable to assume segmental movements for BCS.

As can be seen from table 9.2 adding more cyclohexyl groups to the molecule, increases the value of $\Delta V^{\#}$. This might indicate that the rigid cyclohexyl ring becomes more rigid due to bonding at both sides of the ring, as in compound 5, and the cyclohexyl group bonded only at one side can flow as if it were one molecule .i.e. the flow of bicyclohexane is composed of almost mutually independent flows of two cyclohexyl groups. However, this must depend on the functional groups between the cyclohexyl rings. If these in turn are rigidity enhancing, then the flow of the molecule will be more difficult.

$\Delta H^{\#}$ is the energy required for the flow process to occur. It has been suggested that $\Delta H^{\#}$ consisted of two terms, $\Delta H_h^{\#}$, the heat of "hole" formation and $\Delta H_j^{\#}$, the heat of activation for molecular or segmental translation[19]. If the process of activation for viscous flow proceeds at a constant pressure, the work required to create a "hole", $\Delta H_h^{\#}$, is proportional to $\Delta V^{\#}$. Therefore, $\Delta H^{\#}$, can be expressed approximately as[16]

$$\Delta H^{\#} = \Delta H_h^{\#} + \Delta H_j^{\#} = (P + P_i)\Delta V^{\#} + \Delta H_j^{\#} \qquad 9.1$$

where Pi is the internal pressure. According to the thermodynamic equation of state, P_i is expressed[16] as

$$P_i = T(\partial P/\partial T)_v - P = T(\alpha/\beta) - P \qquad 9.2$$

where α is the thermal expansion coefficient and β is the isothermal compressibility.

Using this equation the internal pressures of alicyclic compounds have been calculated, and from these, the values for $\Delta H_h^{\#}$ and $\Delta H_j^{\#}$ for the compounds[16]. A linear

relationship between $\Delta H_j^{\#}$ and $\Delta V^{\#}$ was found. This is not surprising, as they both effectively measure the flexibility of the molecule.

It can be seen that the fluids with large $\Delta V^{\#}$ show large $\Delta S^{\#}$. This increase can be thought of as arising from an increase in available volume due to "hole" formation.

Figure 9.4 shows the potential energy versus the torsion angle for the central CH_2-CH_2 bond of BCS, produced[20] using a computer-aided molecular mechanics system (U-MICRO 'CHEMMOD'). A Newton-Raphson energy minimisation procedure was used to determine the minimum energy conformational state (or states) for the molecule. For the minimum energy conformer, the rotational rigidity of each significant skeletal bond in the molecule was determined by potential energy calculations as a function of torsion angle, showing that potential energy barriers greater than ca. 5kcalmol^{-1} (19.8kJmol^{-1}) (≈8RT at 298K) are considered to be sufficient to confer significant rigidity into the molecular structure[20].

As can be seen from figure 9.4, there are two conformers that are very close to each other in terms of minimum energy. The energy barrier for conversion from the minimum energy conformer to the next closest is ca. 7.1kcalmol^{-1} (28.1kJmol^{-1}). This compares well with the value calculated for $\Delta H^{\#}$, the energy required for the flow process to occur, for BCS. This may indicate that a "flow" process arising from the rotation about the bond shown in figure 9.4 is occurring under conditions of high temperature and pressure, providing different molecular conformations that are visible in the spectra obtained.

The predominant attractive forces in BCS are located in the carbonyl group. Therefore, it would be expected that changing the molecular environment by altering the temperature or pressure of the system would have a large effect on the carbonyl stretching band. This is not apparent from the peak frequency or bandwidth changes, but it is evident from the peak fitted data. For the variable (static) pressure and temperature data, it is evident that as the pressure or temperature is increased, the higher frequency component becomes more dominant in the spectra. This change is indicative of a conformation change and as mentioned previously (chapter 6) it is more likely to occur as a result of intramolecular changes. The higher frequency component of the carbonyl

stretching region also increases for the dynamic pressure data, but this occurs as the sampling area is moved towards the inlet from the centre of the contact (i.e. as the pressure is reduced).

It is reasonable to assume that the application of temperature will provide enough energy for a proportion of the molecules to cross this barrier and fall into the conformer with a torsion angle of 300°. Indeed at 150°C, the energy provided to the system is equal to 7.1kcalmol^{-1} (28.1kJmol^{-1}).

Therefore as the temperature is increased, the proportion of molecules in this higher energy confomer would increase, and this would be apparent in the spectra.

The static high pressure spectra show similar behaviour to the temperature data. As the pressure is increased, the density increases and the molecules are forced into conformers that require less free volume. It seems that the conformer requiring the least free volume is in fact the same conformer as was apparent for the temperature data. Perhaps this is the conformer with a torsion angle of 300°. From figure 9.4, it can be seen that as the energy of the molecules is raised, they would first change in conformation from the conformer with a torsion angle of 180° to that with a torsion angle of ~70°. However, this is relatively unstable with a small energy barrier needed to be overcome for the molecules to return to their original conformation. As the energy is raised further, the conformer with a torsion angle of 300° would be attainable. This is a relatively stable conformation, so it might be expected that a greater proportion of the molecules would remain in this conformation than in that with a torsion angle of ~70°. Perhaps the conformer with a torsion angle of 300° has a flatter structure with the cyclohexyl rings being planar with respect to one another as compared to the minimum energy conformer.

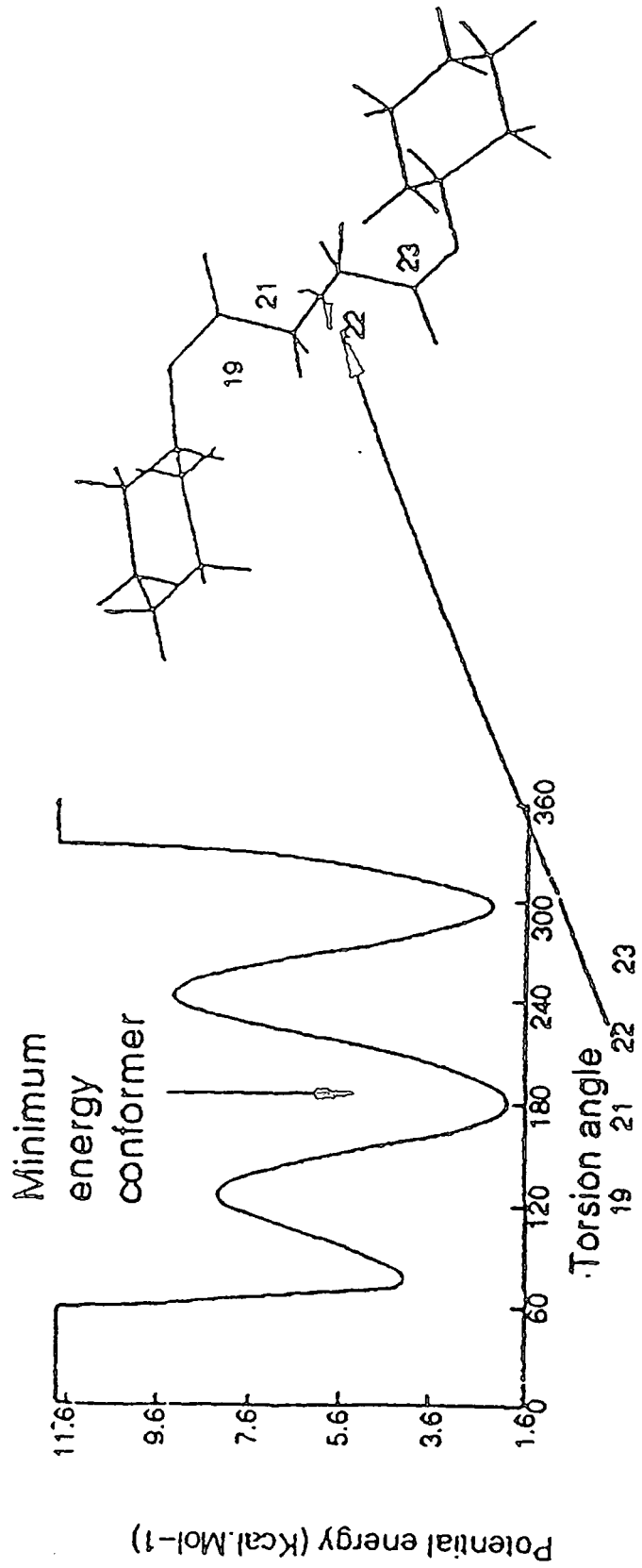

Figure 9.4 Potential energy vs. torsion angle plot of the central CH2-CH2 bond of BCS. The minimum energy conformer is identified on the plot and by the structural representation. Reproduced from reference 20.

There is now the problem of how to explain the dynamic pressure data. There are no significant changes in peak frequency or bandwidths, and the changes in the spectra are more apparent away from the centre of the contact. As mentioned previously, this is not expected. It is assumed that the conditions in the centre of the contact are so severe that the molecules have no "space" to move freely, and consequently no changes are observed. This must be as a consequence of shear rate, as this behaviour was not exhibited by the temperature or static variable pressure data. It is also evident that the high frequency component of the carbonyl region becomes more visible as the sampling area is moved away from the contact centre. Therefore the appearance of this band might suggest that the pressure gradient coupled with the high shear rate and temperature combines to force the molecules into different conformations.

The lack of changes in bandwidth and peak frequency are not surprising. If the pressures in chapters 6 and 7 are compared, it is evident that for the dynamic pressure data, the pressures reached are of the order of 3-4kbar, and no change in bandwidth or peak frequency was observed for the static pressure data for BCS until a pressure of at least 10kbar (1GPa) was reached. This again reinforces the fact that the shearing of the molecules is producing the changes seen.

Fluids are known to have excellent traction properties if they contain cyclohexyl rings. It is thought that the "locking" of these in a cog-like interaction at high pressure contributes greatly to the traction coefficient[21]. If this is coupled with molecular rigidity as shown in figure 9.4, then this property will be further enhanced. This locking of the molecules is quite likely to be occurring in the centre of the contact. As the fluid is drawn into the contact, the conditions of shear and pressure it experiences are tremendous. The molecules change from being in an easy flowing liquid to almost a pseudosolid (with pressures reaching typically $10^9 N/m^2$), and then back to an easy flowing liquid within a matter of milliseconds. The sudden change of conditions must influence the behaviour of the molecules. Perhaps it is these dramatic changes of conditions that are providing the changes in the conformation of the molecules, and once the fluid reaches the centre of the contact, the molecules are locked into a single conformation so therefore no changes are seen.

9.3 Concluding Remarks

Many factors complicate a quantitative understanding of traction in a practical device. Not only must the metallurgy and the topology of the contact surfaces play an important role, but also the nature of the adsorbed surface layer, which may be entirely different in composition from the fluid, has been shown to have a profound influence.[22] Furthermore, the properties of the fluid film through which the torque is transferred, must vary in a complex way because of the variation in temperature and pressure across the contact zone. Finally, the movement of the contacting surfaces influences the traction considerably.

In a hope to gain an insight into the molecular properties of a traction fluid, variable temperature and static pressure data was obtained with a view to comparing this with dynamic pressure data. From the results obtained, the shear rate seems to be important, and this coupled with the sudden changes in conditions as the molecules pass through the contact produces the behaviour seen.

9.4 Suggestions For Future Work

Throughout these studies, there has been the constant problem of separating the cyclohexyl ring CH_2 and the chain CH_2 vibrational modes. The obvious solution to this problem is to use some partially deuterated material. Not only would this assist in the interpretation of internal molecular rigidity about the chain CH_2-CH_2 bond, it might well provide some indication of the locking of the molecules under high pressures. Consequently this might well confirm the cog-like interactions of the molecules under traction conditions.

It is obvious that the in-situ measurements using the EHD rig need far more examination than was possible in this thesis. The data obtained for BCS needs to be extended and with a full study of the other molecules examined in this thesis and additionally the partially deuterated material in order to monitor the behaviour of the cyclohexyl rings. A problem with obtaining data from the EHD rig is that ≈60cm3 of liquid is required to fill the oil bath, and this may prove expensive especially for the partially deuterated materials. With continuing improvements in the computer modelling

of pressure and film thickness profiles it will be possible to examine a greater range of conditions and correlate changes in the spectroscopic behaviour with the corresponding pressure and film thicknesses.

It would also be very useful to conduct pressure measurements under constant density conditions.

As well as modelling the pressure and film thickness profiles, the constant advancement of computer technology, will lead to improved procedures to model the change in the conformation of molecules when they experience the conditions of high temperature and pressure.

In conclusion, interpretting the data from an in situ study has proved troublesome largely due to practical problems and the number of different variables the traction conditions provide. However, these studies show that conformational changes are apparent under both static pressure and temperature studies, and dynamic presuure studies. These changes are brought about by intramolecular processes as the Eyring model and the computer aided molecular graphics package have proven. It is these intramolecular conformational changes that are responsible for the traction properties of the fluids studied.

References

1. P.M. Cann and H.A. Spikes, Tribol. Trans., 3, 248, (1991)
2. P.T.T. Wong, S.F. Weng and H.H. Mantsch, W. Schindler, J. Chem. Phys., 85, 2315 (1986)
3. R. Kubo, in "Fluctuations, Relaxation and Resonance in Magnetic Systems", Ed. D.Ter. Haar), Plenum, New York (1962)
4. A.N. Parikh and D.L. Allara, J. Chem. Phys., 96, 927, (1992)
5. M. Muraki, Trib. Int. 20, 347, (1987)
6. A. Dyson, Phil. Trans. R. Soc. Lond., Ser. A, 266, 1 (1970)
7. A.W. Crook, Phil. Trans. R. Soc. Lond., Ser. A. 255, 281 (1963)
8. K.L. Johnson and R. Cameron, Proc. Inst. Mech. Eng., 182, 307 (1967-68)
9. S. Lingard, Tribology Int., 7, 228 (1974)
10. K.L. Johnson and A.D. Roberts, Proc. R. Soc. Lond., Ser. A, 337, 217 (1974)
11. K.L. Johnson and J.L. Tevaarwerk, Proc. R. Soc. Lond., Ser. A, 356, 215 (1977)
12. J.L. Tevaarwerk and K.L. Johnson, Trans. ASME, F, 101, 266 (1979)
13. S. Glasstone, K.J. Laidler, H. Eyring, "The Theory of Rate Processes", McGraw-Hill Book Co., New York (1941)
14. T. Kyotani, Y. Tamai and Y. Horita, A.S.L.E. Trans., 26, 538-44, (1983)
15. T. Kyotani, H. Yoshitake, T. Ito and T. Tamai, A.S.L.E. Trans., 29, 102-6, (1986)
16. Y. Tamai and T. Yoneda, Bull. Japan Petrol. Inst., 18, 9 (1976)
17. Y. Tamai and T. Kyotani, J. Japan Petrol. Inst., 25, 94 (1982)
18. E.W. Griest, W. Webb and R.W. Schiessler, J. Chem. Phys., 29, 711 (1958)
19. A. Bondi, Ann. N.Y. Acad. Sci., 53, 870 (1951)
20. M.P. Dare-Edwards, Synth. Lubr., 8, 197 (1991)
21. K.-H. Hentschel, J. Synth. Lubr., 2, 165 (1985)
22. Hammann, ASLE Trans, 13, 105 (1970)

APPENDICES

I. The C.C.D (Charge Coupled Device) Detector.

II. Pressure and Film Thickness Profiles For The EHD Rig.

III. Lectures Attended October 1991 - September 1994.

I. The C.C.D (Charge Coupled Device) Detector.

The C.C.D. (Charge Coupled Device) is a form of integrated circuit, having a metal-oxide semiconductor structure. The surface of the C.C.D. can be thought of as an array of photosensitive pixels. When a photon of light is incident on one of these pixels a photo electron is generated in the Silicon. This is trapped on the pixel and as more photons are incident more electrons are generated, and so a charge builds up on the pixel. For a given exposure time this charge is proportional to the intensity of the light (photons/unit time) incident on that pixel. Therefore, the distribution of charge on the C.C.D. at the end of an exposure corresponds to the distribution of light intensity across the surface of the chip.

At the end of the exposure, once the shutter has been closed, the charge needs to be moved off the chip and translated into a digital format, to enable processing and display of the image (the electronic equivalent of developing a negative, with the distribution of charge on the C.C.D. being analogous to the negative.). To achieve this 'read out' process, the C.C.D. has an array of electrodes which may be switched on or off by the computer. By switching the electrodes on and off in an appropriate fashion it is possible to move the packets of charge around the chip.

During a normal image readout each column of charge packets is moved one pixel column at a time so that each is moved onto the 'serial output register'. Once a column of charge is on this register it is moved down, one charge packet at a time, off the chip and through an amplifier which converts the charge to a voltage signal. This process is repeated until all the columns of charge have been read out through the amplifier. This systematic shifting enables the signal generated by each packet of charge to be related to its original position on the C.C.D.. Using this information a personal computer can produce a two dimensional plot of intensity versus position which is of course an image.

The C.C.D. chip in the C.C.D. camera in the Ramascope has an array of 385 by 578 pixels with the long axis lying vertically when mounted in the system. The chip is thermo-electrically cooled by a four stage Peltier cooler to approximately 200K (-78°C). The Peltier cooler is housed in the camera head, as is a fan to remove the waste heat

produced and an electro-mechanical shutter. The bulk of the associated electronics are housed in a remote electronics module which is housed in the Raman system.

II. Pressure and Film Thickness Profiles For The EHD Rig.

For a description of the units used in the profiles, refer to section 7.1.

Figure Number	Description
II.1	3-Dimensional Pressure Profile, 150rpm and 3.8 Newtons.
II.2	3-Dimensional Film Thickness Profile, 150rpm and 3.8 Newtons.
II.3	Pressure and Film Thickness Along Centre Line of Contact in Direction of Flow, 150rpm, 3.8 Newtons.
II.4	Pressure and Film Thickness Along Centre Line of Contact Perpendicular to Direction of Flow, 150rpm, 3.8 Newtons.
II.5	Pressure and Film Thickness Along Centre Line of Contact in Direction of Flow, 150rpm, 6.5 Newtons.
II.6	Pressure and Film Thickness Along Centre Line of Contact Perpendicular to Direction of Flow, 150rpm, 6.5 Newtons.
II.7	Pressure and Film Thickness Along Centre Line of Contact in Direction of Flow, 150rpm, 7.3 Newtons.
II.8	Pressure and Film Thickness Along Centre Line of Contact Perpendicular to Direction of Flow, 150rpm, 7.3 Newtons.
II.9	Pressure and Film Thickness Along Centre Line of Contact in Direction of Flow, 150rpm, 8.1 Newtons.
II.10	Pressure and Film Thickness Along Centre Line of Contact Perpendicular to Direction of Flow, 150rpm, 8.1 Newtons.
II.11	Pressure and Film Thickness Along Centre Line of Contact in Direction of Flow, 200rpm, 3.8 Newtons.
II.12	Pressure and Film Thickness Along Centre Line of Contact Perpendicular to Direction of Flow, 200rpm, 3.8 Newtons.
II.13	Pressure and Film Thickness Along Centre Line of Contact in Direction of Flow, 200rpm, 6.5 Newtons.
II.14	Pressure and Film Thickness Along Centre Line of Contact Perpendicular to Direction of Flow, 200rpm, 6.5 Newtons.

II.30 Pressure and Film Thickness Along Centre Line of Contact Perpendicular to Direction of Flow, 700rpm, 9.1 Newtons.

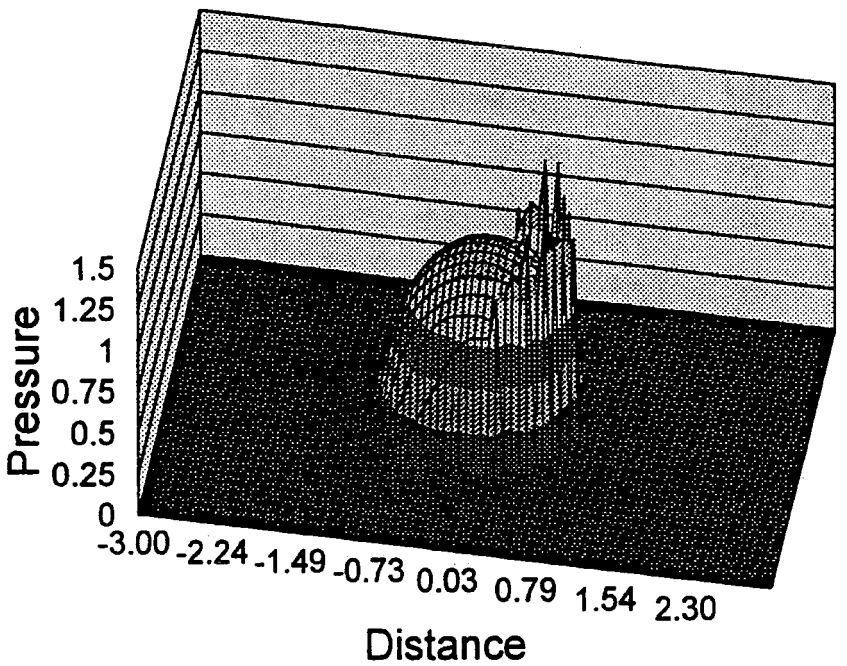

Figure II.1. 3-Dimensional Pressure Profile, 150rpm and 3.8 Newtons.

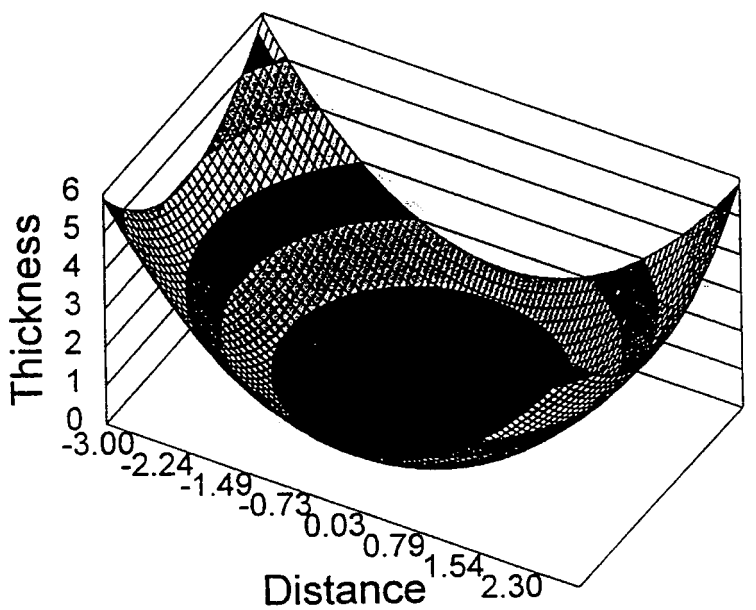

Figure II.2. 3-Dimensional Film Thickness Profile, 150rpm and 3.8 Newtons.

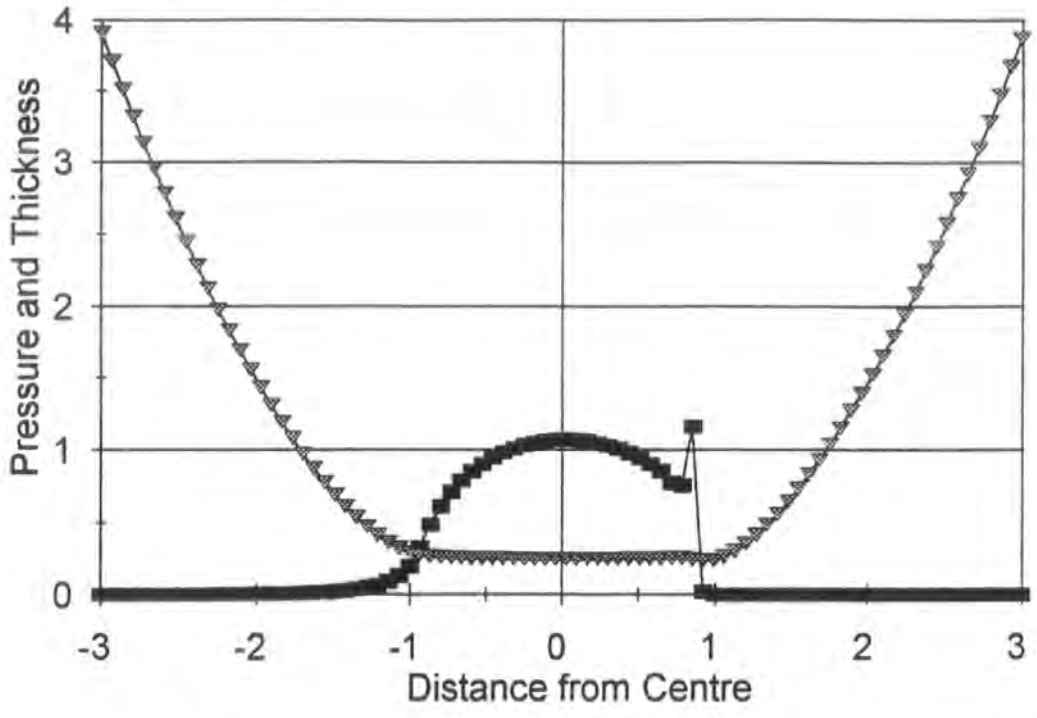

Figure II.3. Pressure and Film Thickness Profile Along Centre Line of Contact in Direction of Flow, 150rpm, 3.8 Newtons.

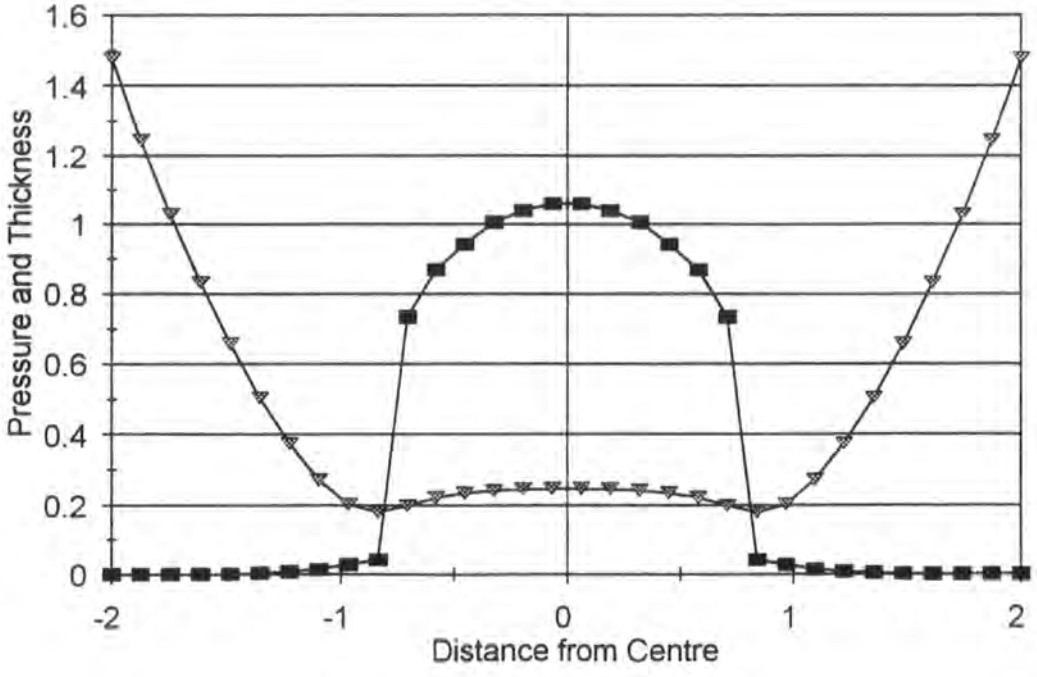

Figure II.4. Pressure and Film Thickness Profile Along Centre Line of Contact Perpendicular to Direction of Flow, 150rpm, 3.8 Newtons.

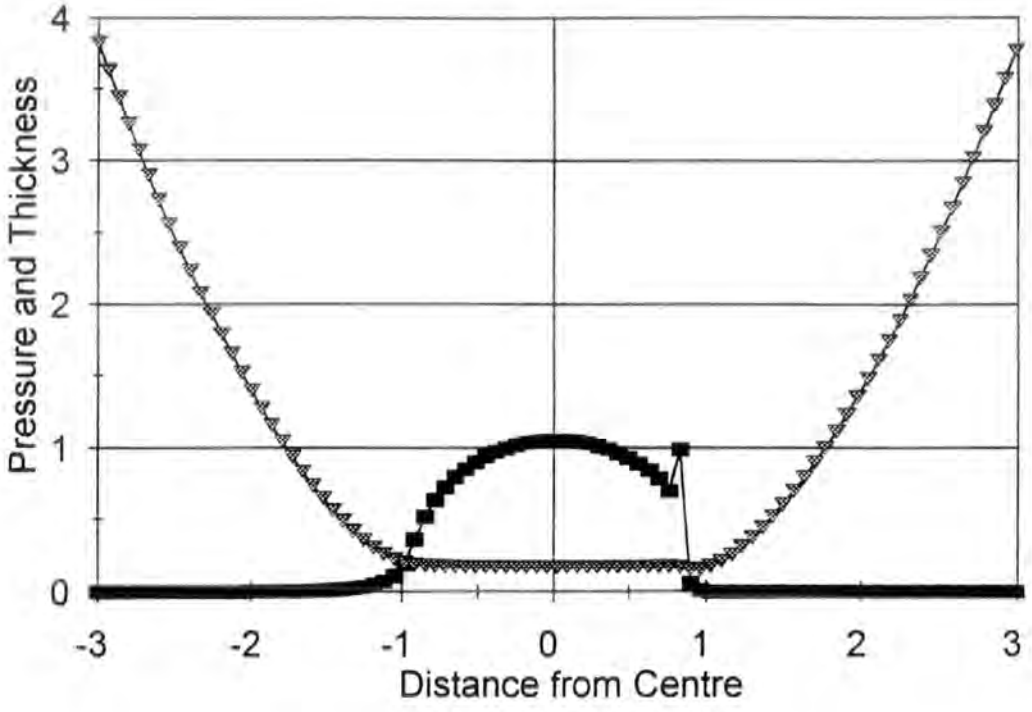

Figure II.5. Pressure and Film Thickness Profile Along Centre Line of Contact in Direction of Flow, 150rpm, 6.5 Newtons.

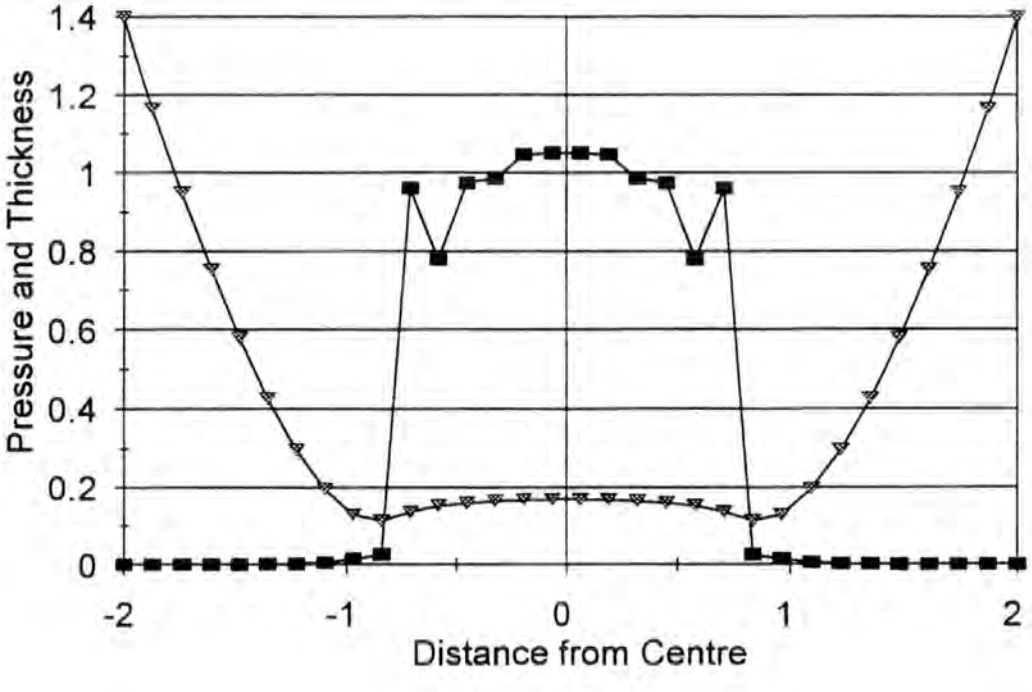

Figure II.6. Pressure and Film Thickness Profile Along Centre Line of Contact Perpendicular to Direction of Flow, 150rpm, 6.5 Newtons.

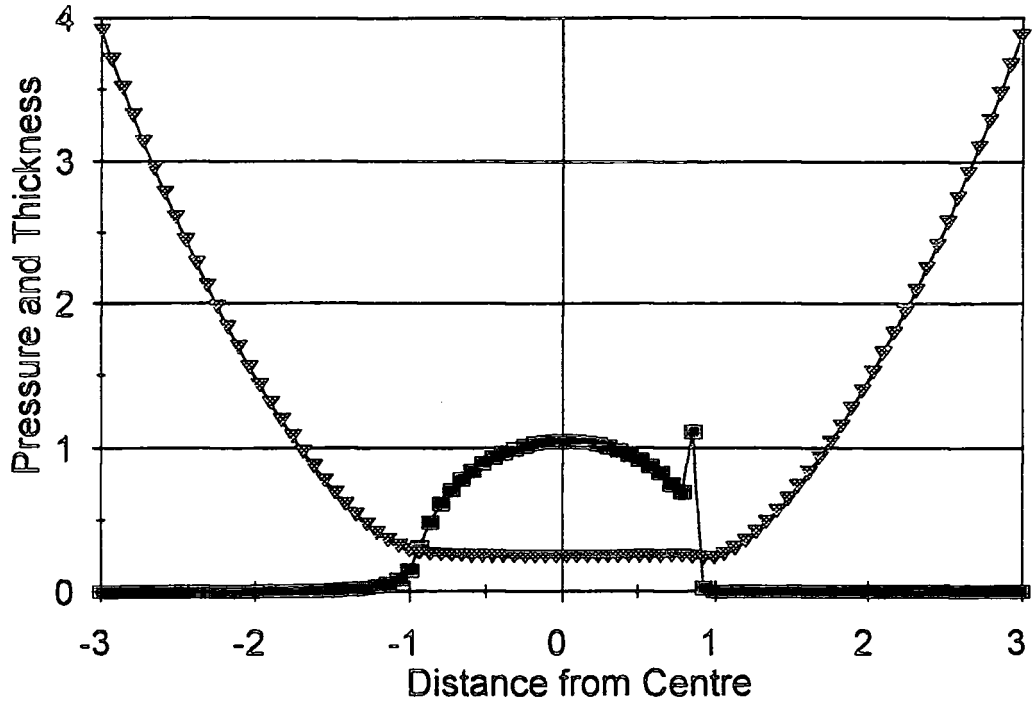

Figure II.7. Pressure and Film Thickness Profile Along Centre Line of Contact in Direction of Flow, 150rpm, 7.3 Newtons.

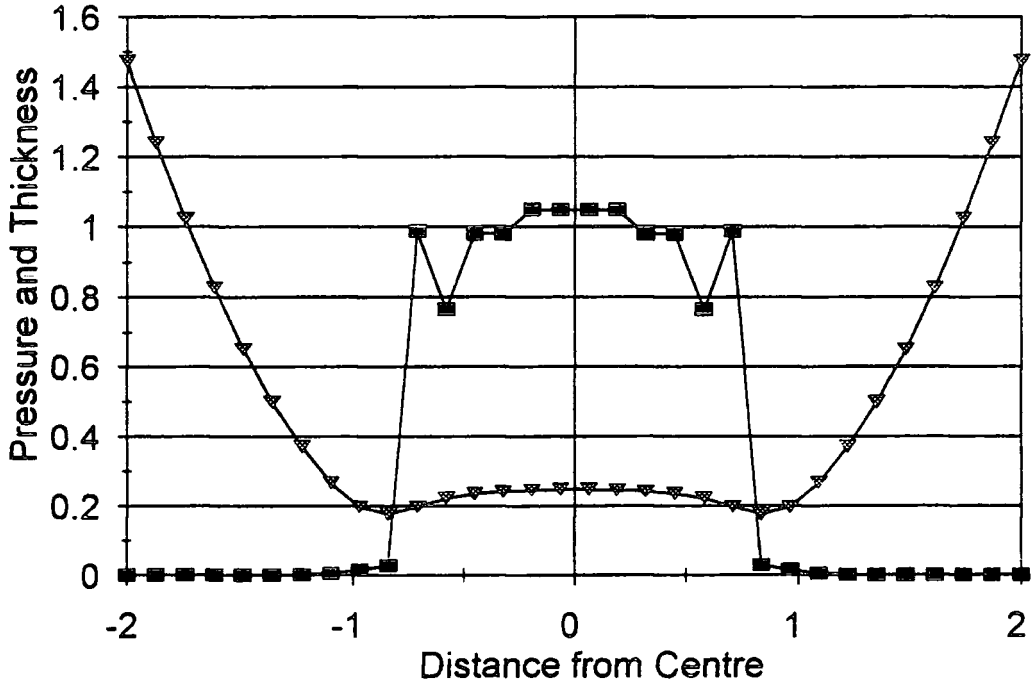

Figure II.8. Pressure and Film Thickness Profile Along Centre Line of Contact Perpendicular to Direction of Flow, 150rpm, 7.3 Newtons.

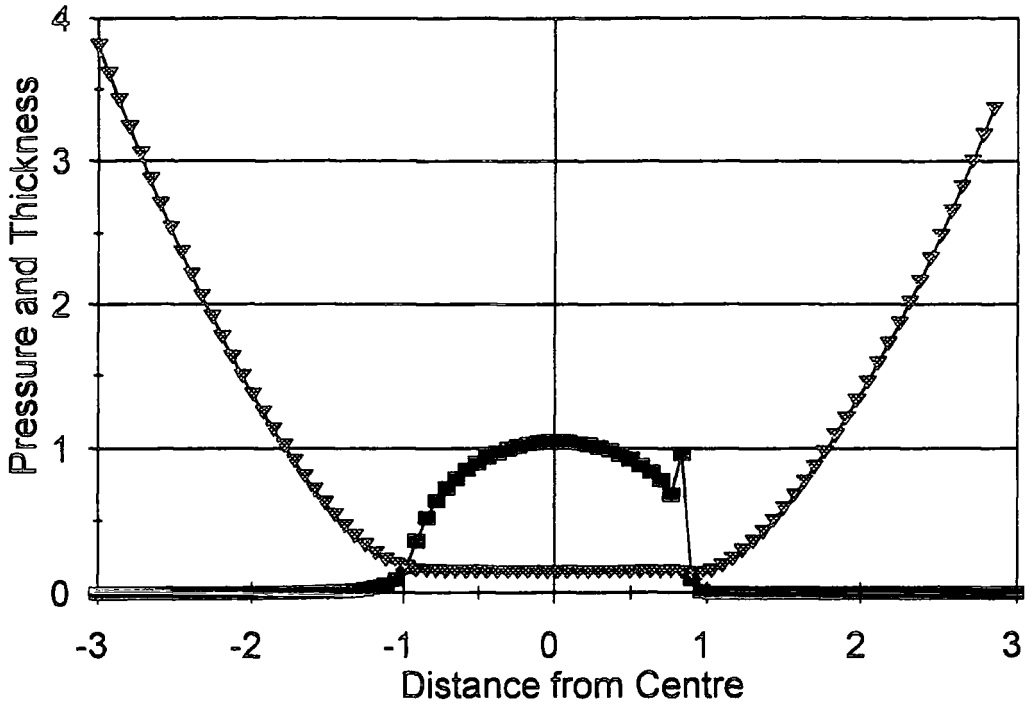

Figure II.9. Pressure and Film Thickness Profile Along Centre Line of Contact in Direction of Flow, 150rpm, 8.1 Newtons.

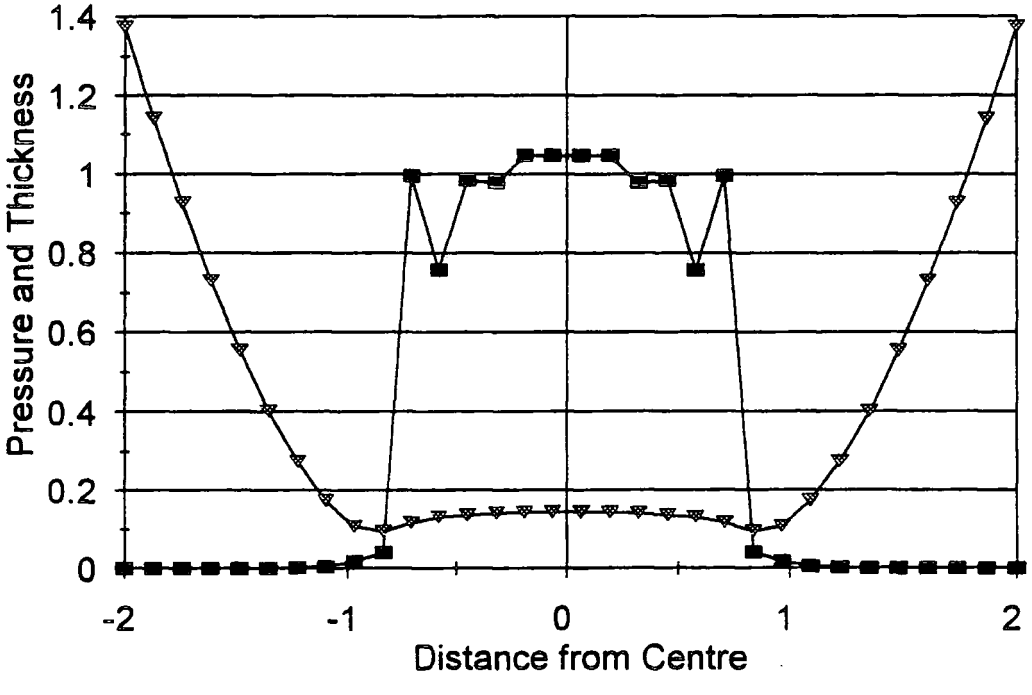

Figure II.10. Pressure and Film Thickness Profile Along Centre Line of Contact Perpendicular to Direction of Flow, 150rpm, 8.1 Newtons.

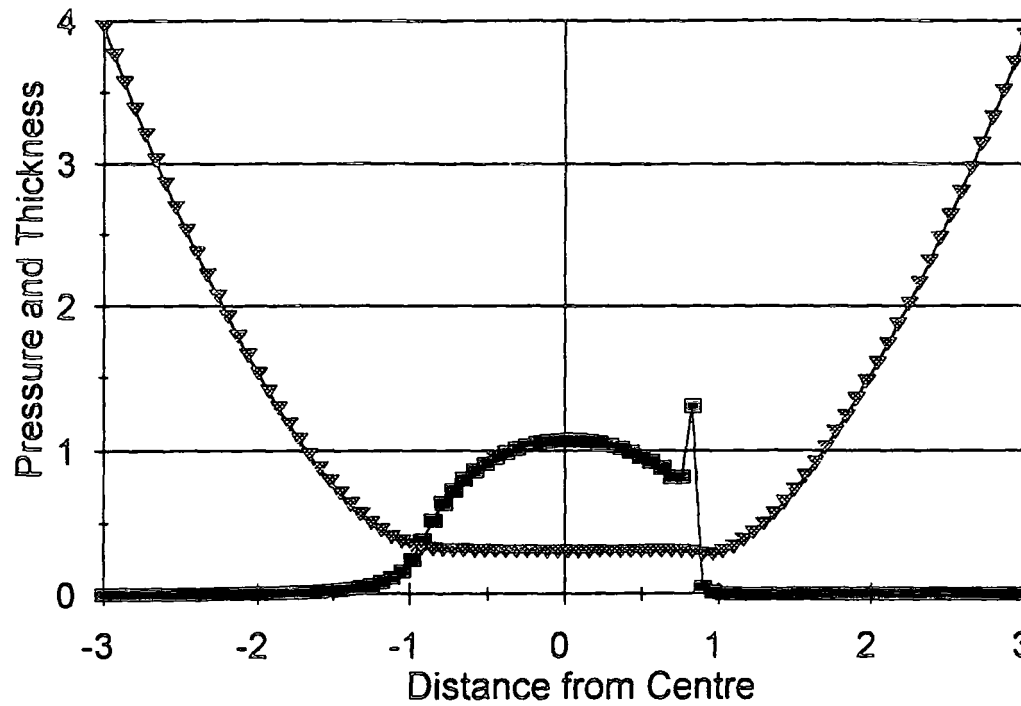

Figure II.11. Pressure and Film Thickness Profile Along Centre Line of Contact in Direction of Flow, 200rpm, 3.8 Newtons.

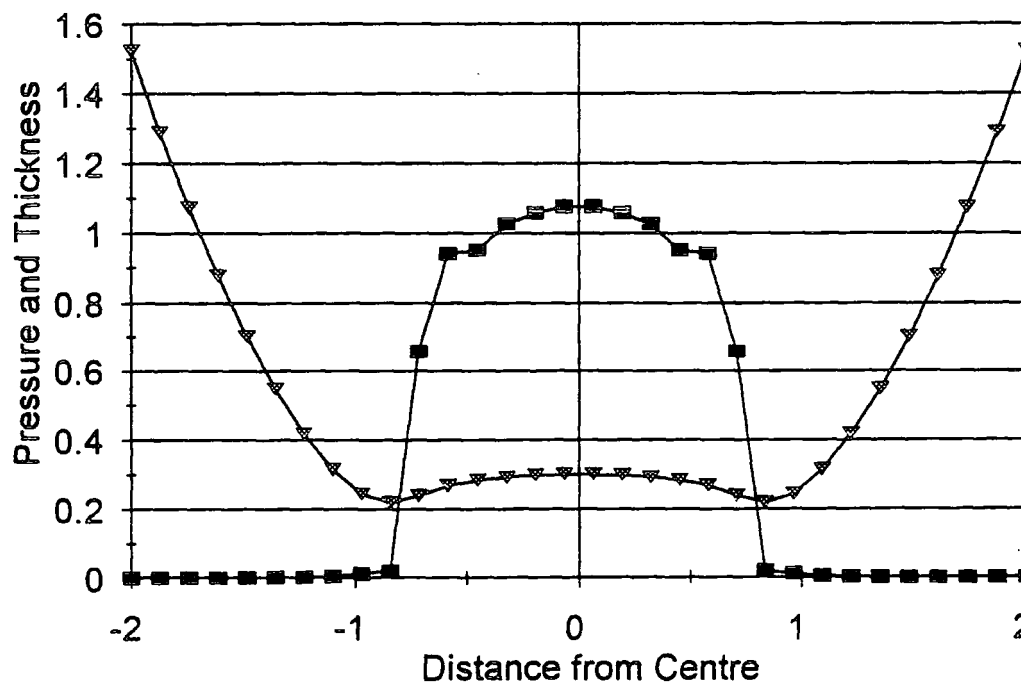

Figure II.12. Pressure and Film Thickness Profile Along Centre Line of Contact Perpendicular to Direction of Flow, 200rpm, 3.8 Newtons.

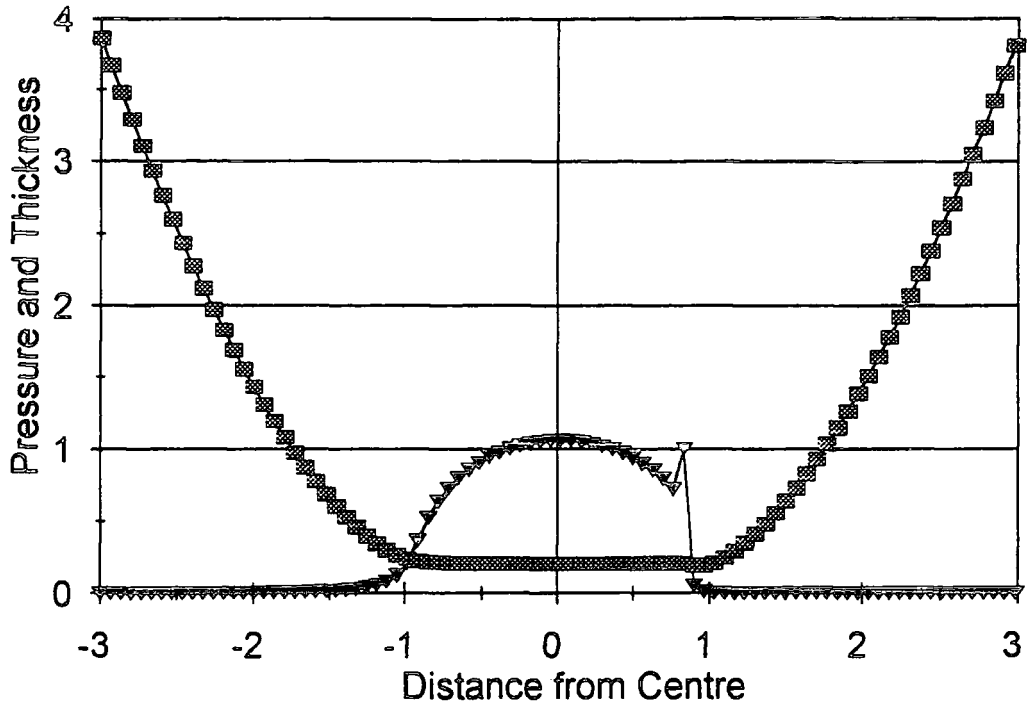

Figure II.13. Pressure and Film Thickness Profile Along Centre Line of Contact in Direction of Flow, 200rpm, 6.5 Newtons.

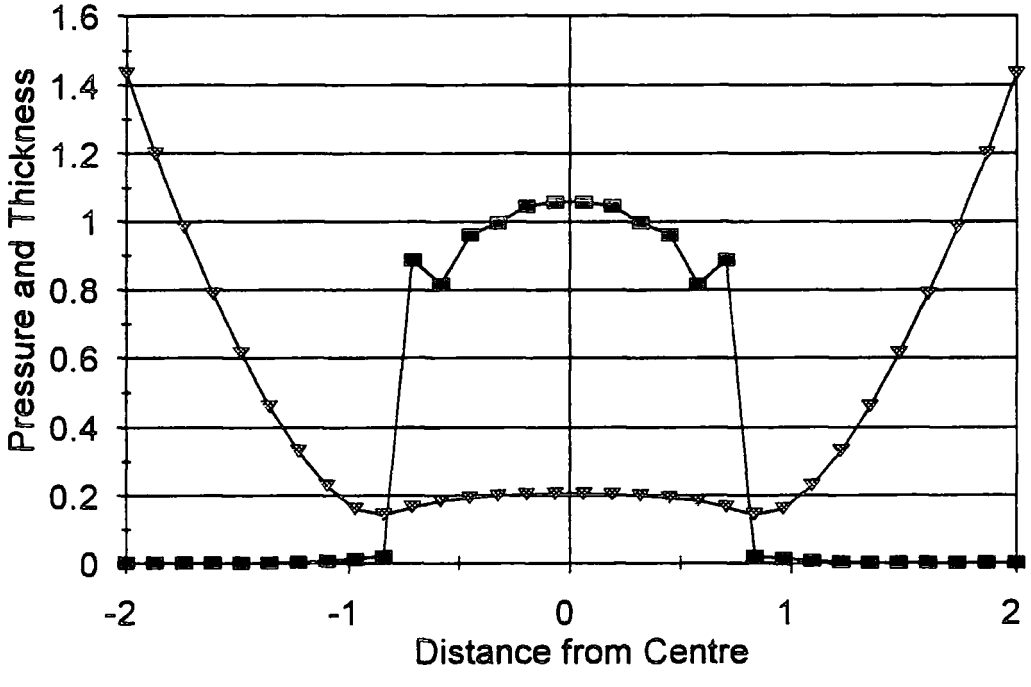

Figure II.14. Pressure and Film Thickness Profile Along Centre Line of Contact Perpendicular to Direction of Flow, 200rpm, 6.5 Newtons.

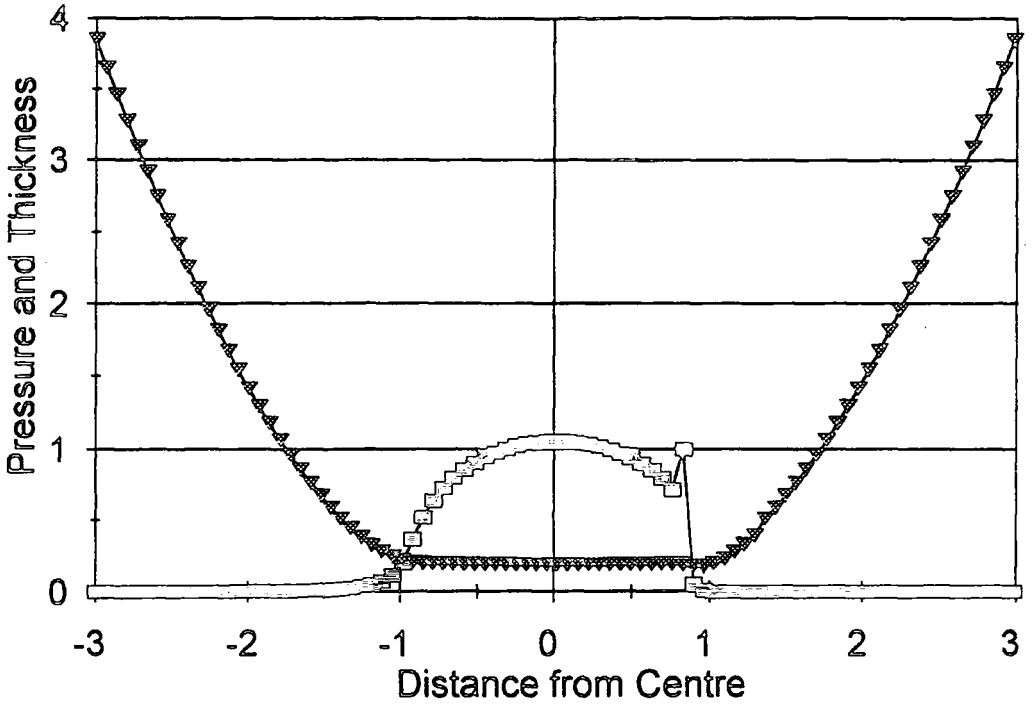

Figure II.15. Pressure and Film Thickness Profile Along Centre Line of Contact in Direction of Flow, 200rpm, 7.3 Newtons.

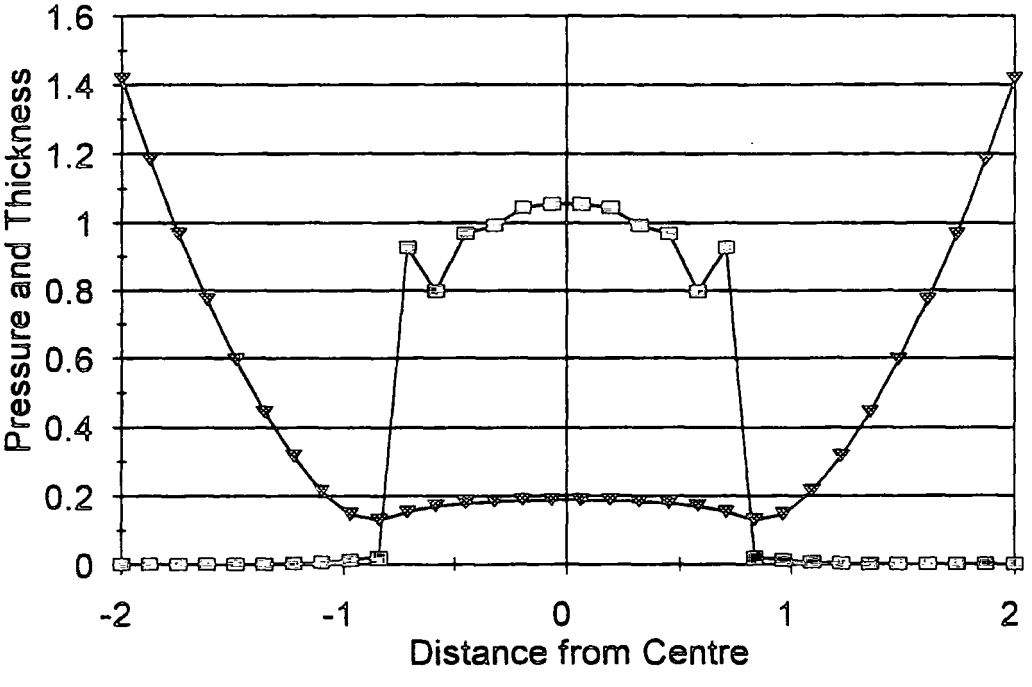

Figure II.16. Pressure and Film Thickness Profile Along Centre Line of Contact Perpendicular to Direction of Flow, 200rpm, 7.3 Newtons.

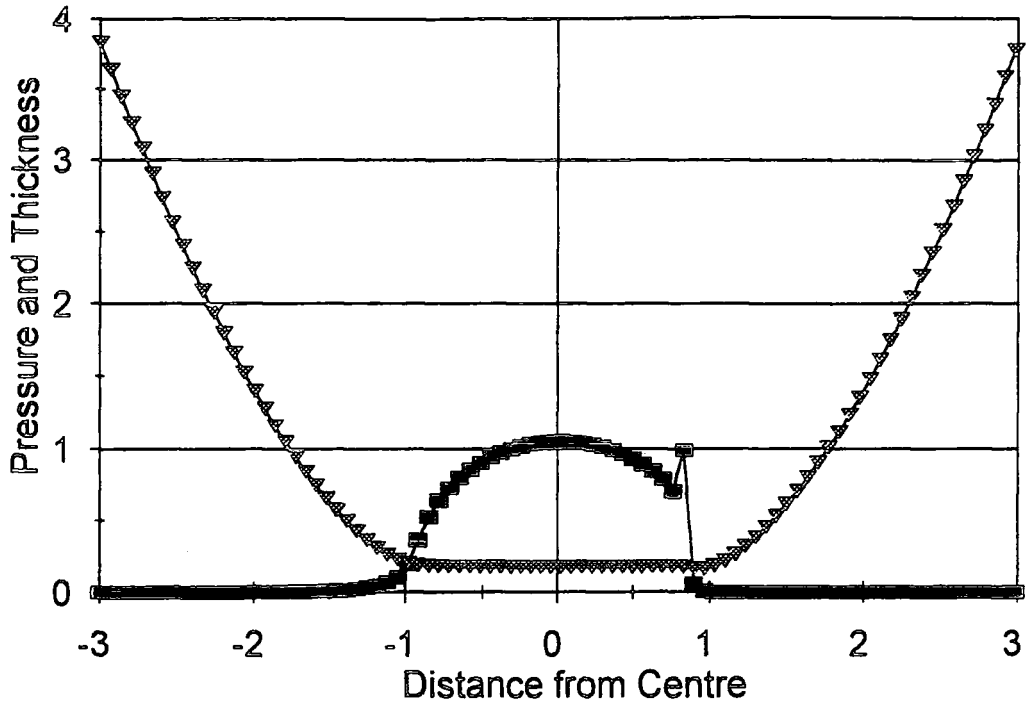

Figure II.17 Pressure and Film Thickness Profile Along Centre Line of Contact in Direction of Flow, 200rpm, 8.1 Newtons.

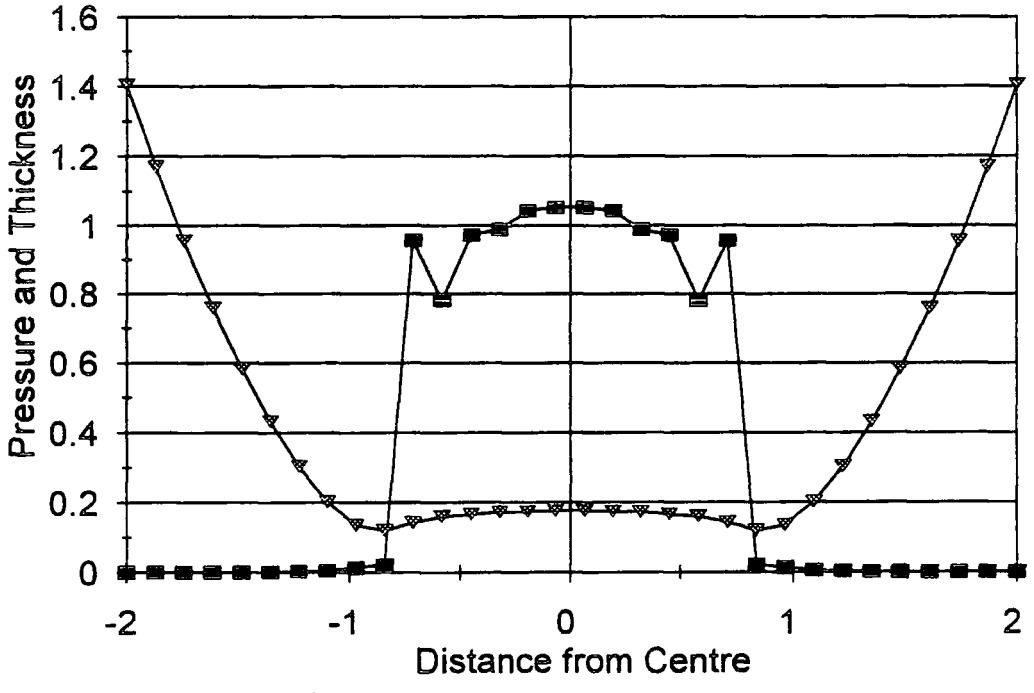

Figure II.18. Pressure and Film Thickness Profile Along Centre Line of Contact Perpendicular to Direction of Flow, 200rpm, 8.1 Newtons.

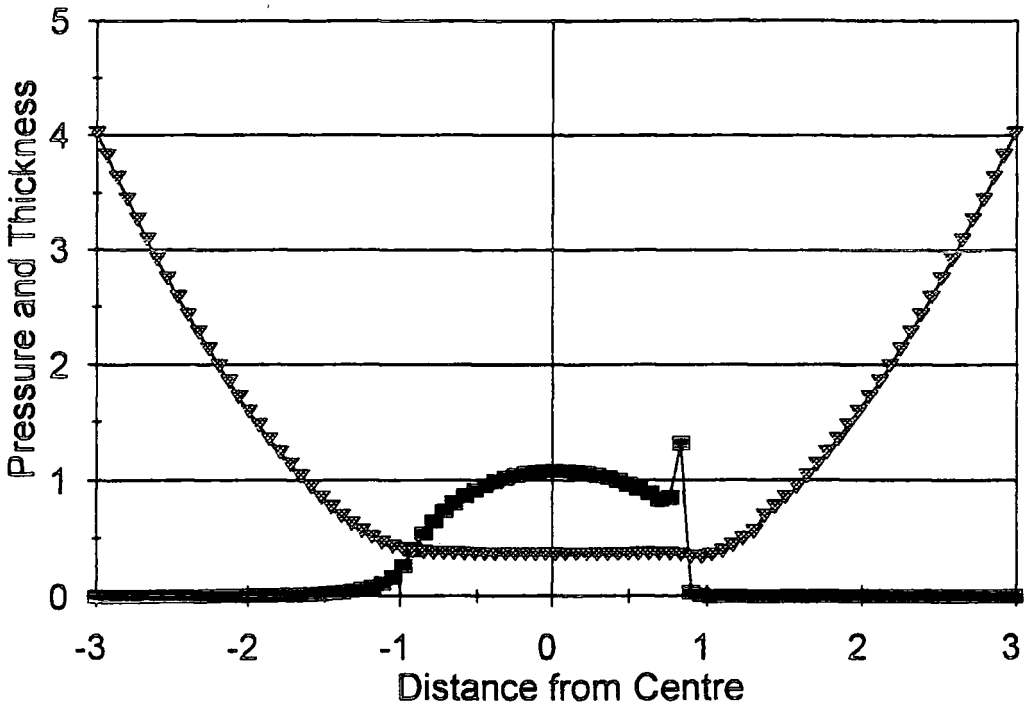

Figure II.19. Pressure and Film Thickness Profile Along Centre Line of Contact in Direction of Flow, 600rpm, 8.1 Newtons.

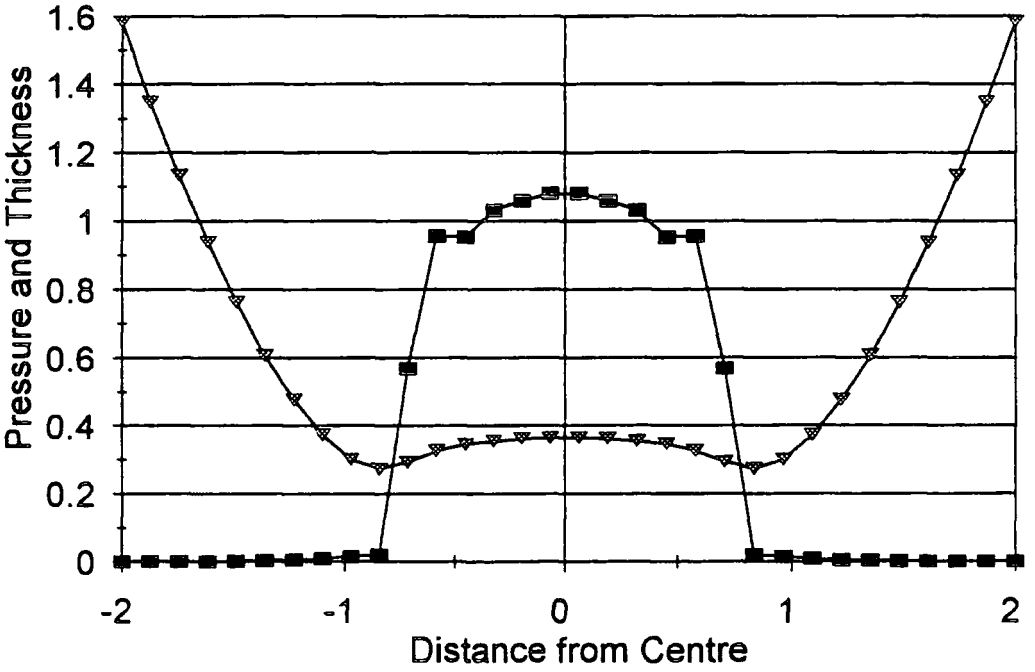

Figure II.20. Pressure and Film Thickness Profile Along Centre Line of Contact Perpendicular to Direction of Flow, 600rpm, 8.1 Newtons.

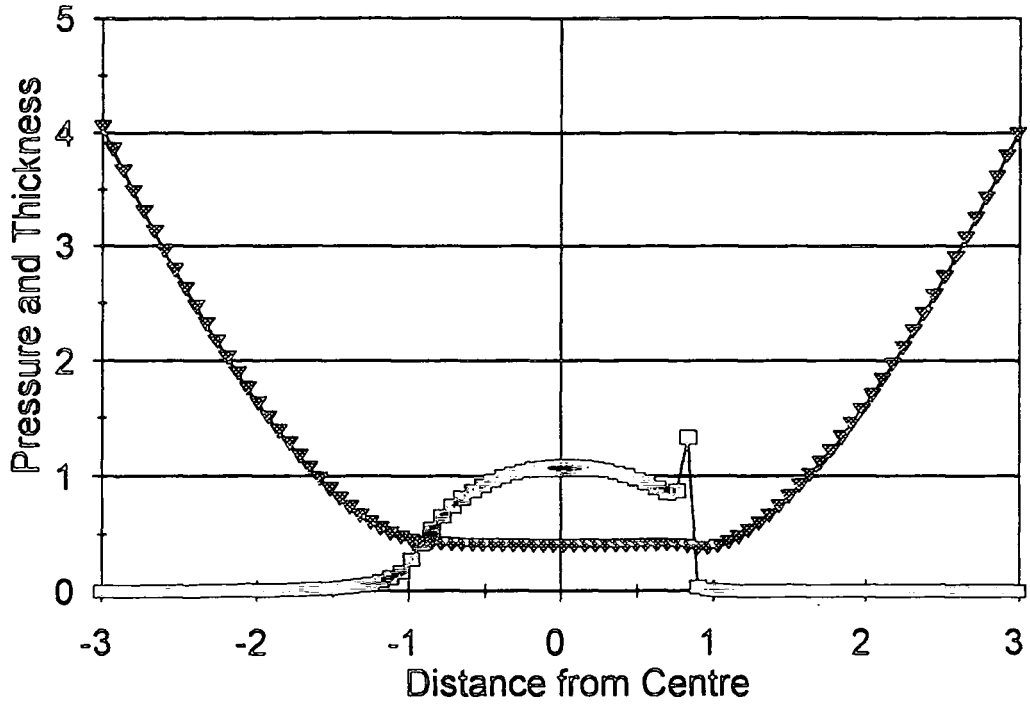

Figure II.21. Pressure and Film Thickness Profile Along Centre Line of Contact in Direction of Flow, 700rpm, 8.1 Newtons.

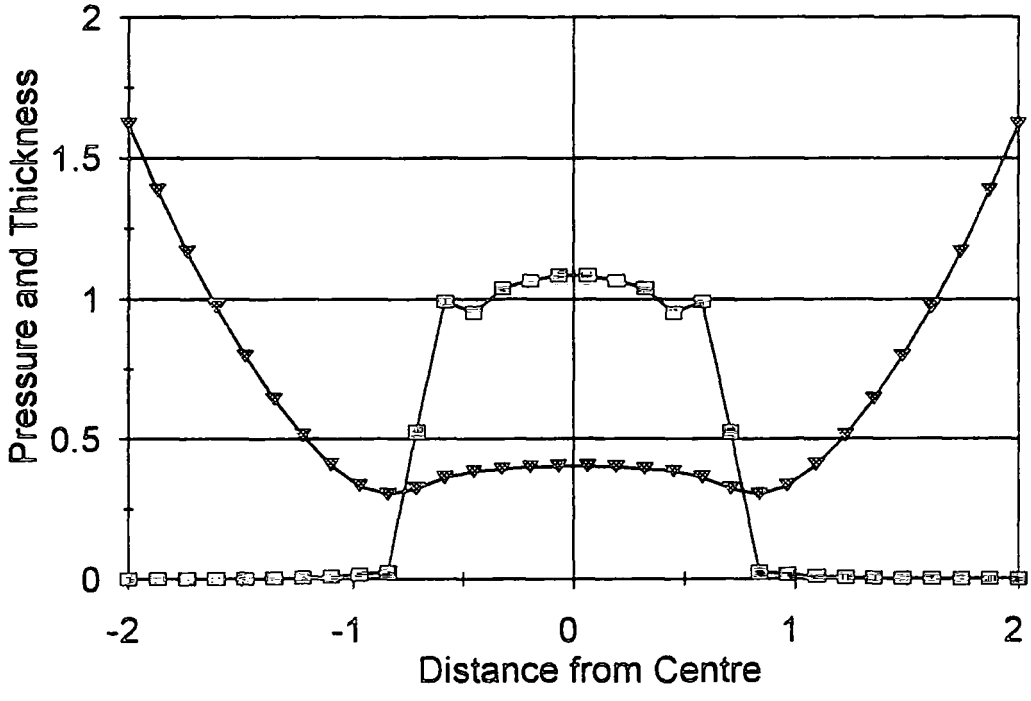

Figure II.22. Pressure and Film Thickness Profile Along Centre Line of Contact Perpendicular to Direction of Flow, 700rpm, 8.1 Newtons.

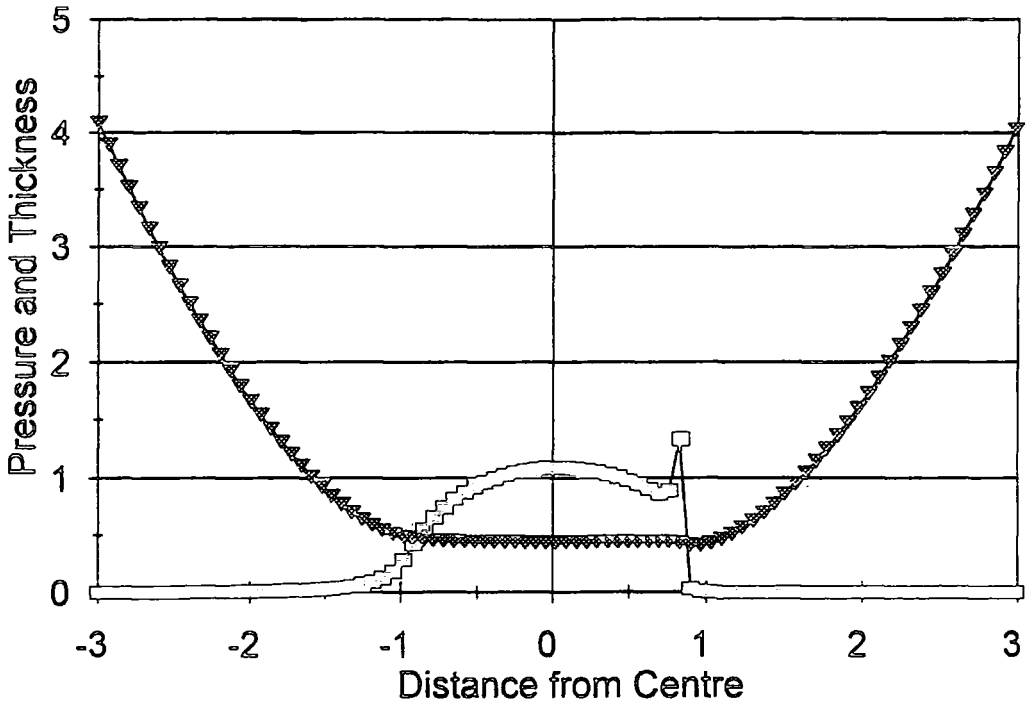

Figure II.23. Pressure and Film Thickness Profile Along Centre Line of Contact in Direction of Flow, 800rpm, 8.1 Newtons.

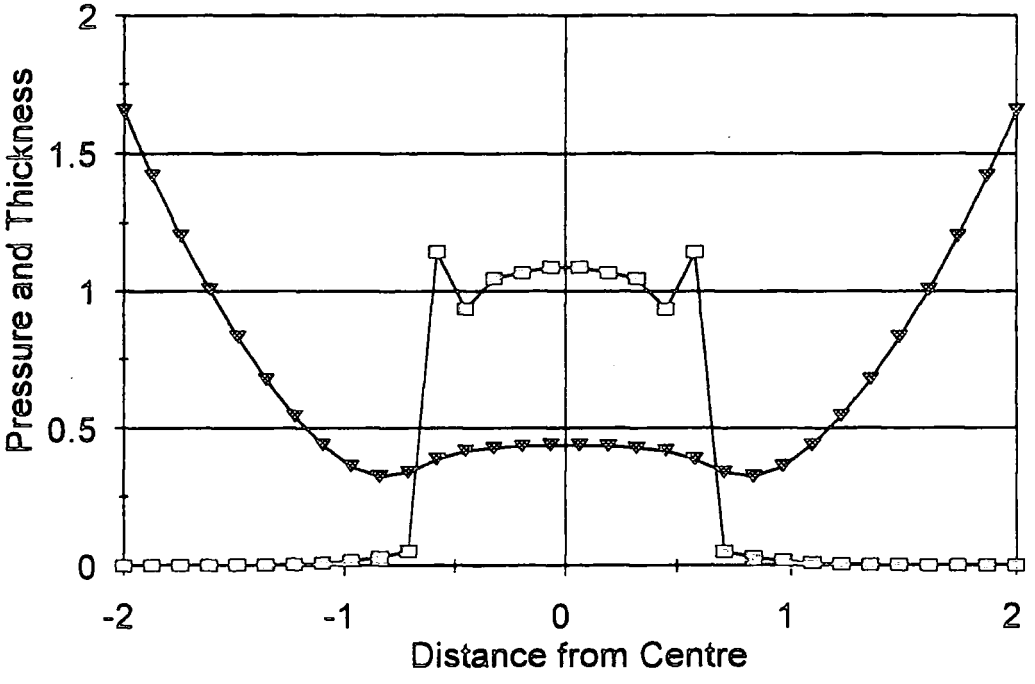

Figure II.24. Pressure and Film Thickness Profile Along Centre Line of Contact Perpendicular to Direction of Flow, 800rpm, 8.1 Newtons.

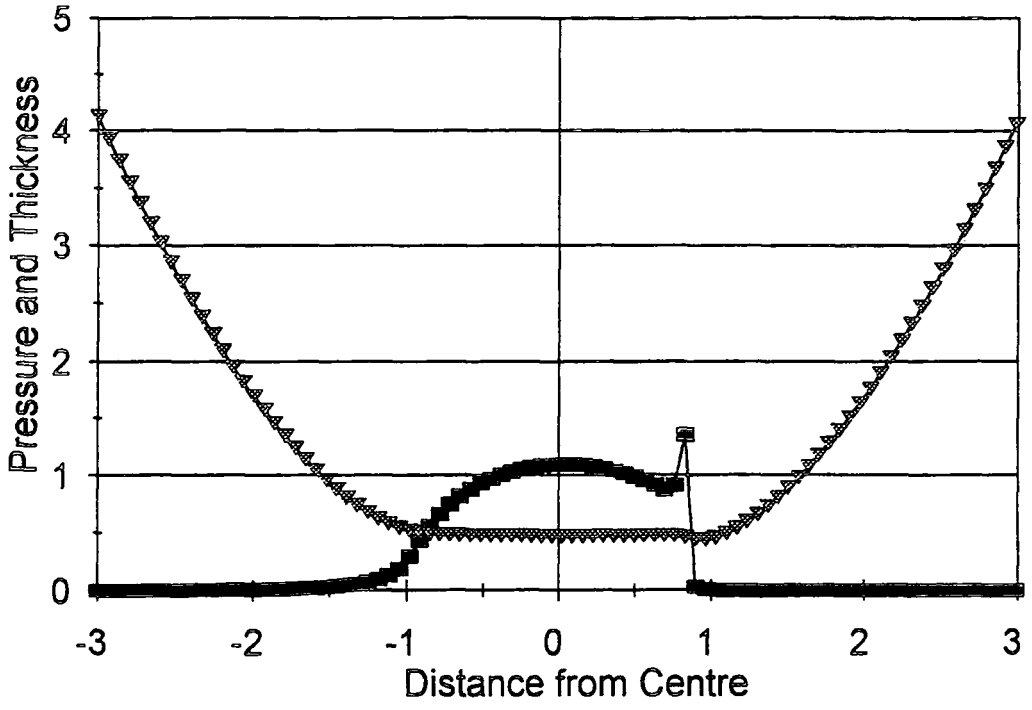

Figure II.25. Pressure and Film Thickness Profile Along Centre Line of Contact in Direction of Flow, 800rpm, 9.1 Newtons.

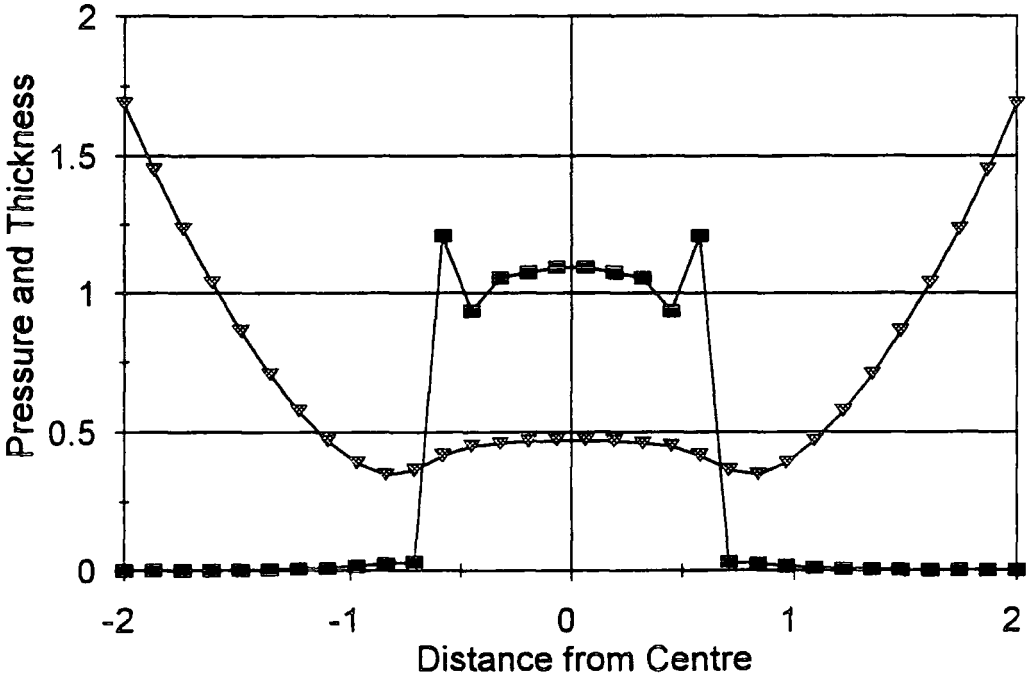

Figure II.26. Pressure and Film Thickness Profile Along Centre Line of Contact Perpendicular to Direction of Flow, 800rpm, 9.1 Newtons.

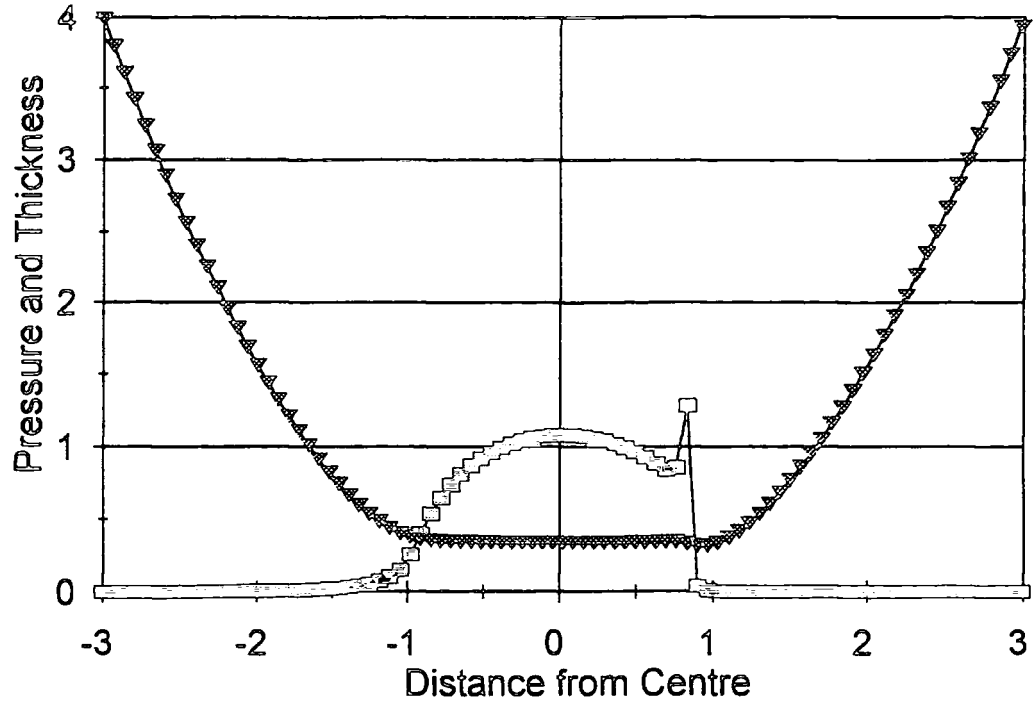

Figure II.27. Pressure and Film Thickness Profile Along Centre Line of Contact in Direction of Flow, 600rpm, 9.1 Newtons.

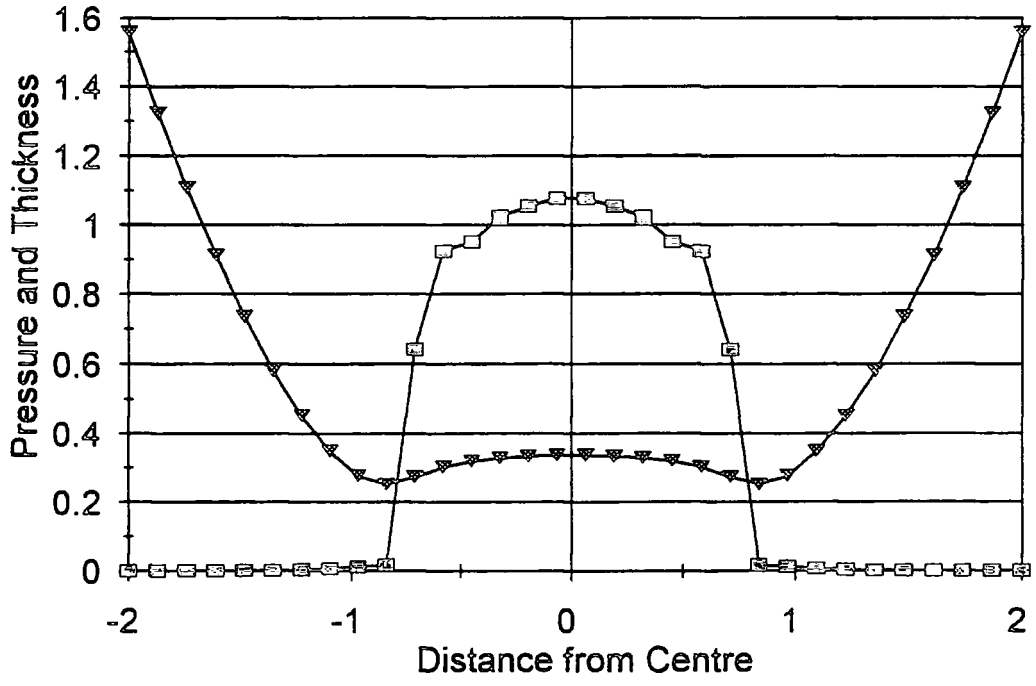

Figure II.28. Pressure and Film Thickness Profile Along Centre Line of Contact Perpendicular to Direction of Flow, 600rpm, 9.1 Newtons.

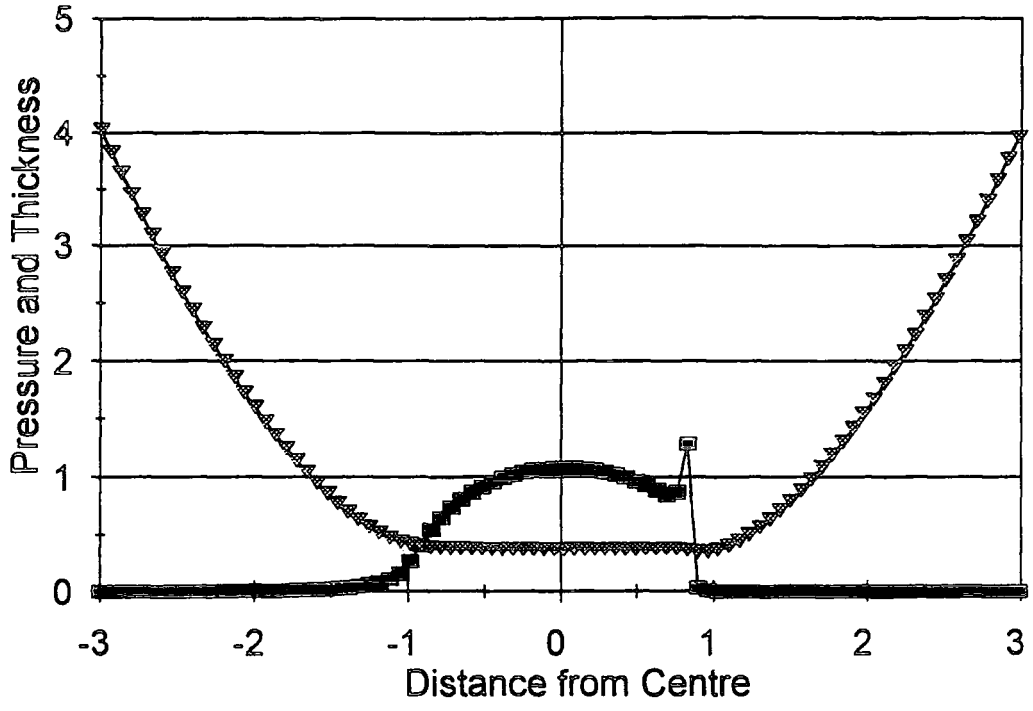

Figure II.29. Pressure and Film Thickness Profile Along Centre Line of Contact in Direction of Flow, 700rpm, 9.1 Newtons.

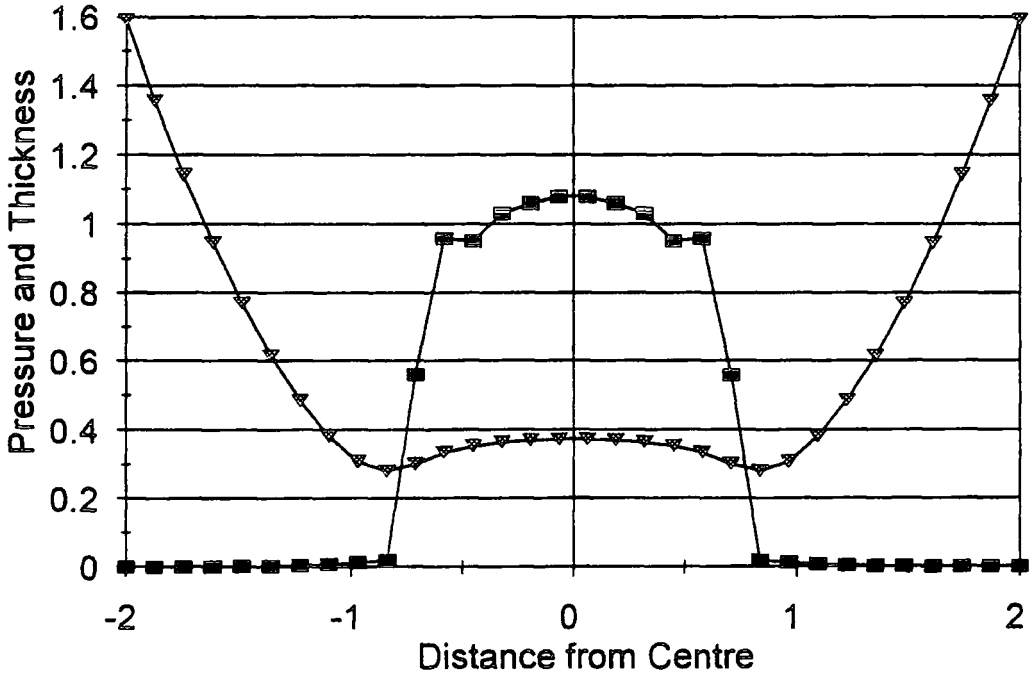

Figure II.30. Pressure and Film Thickness Profile Along Centre Line of Contact Perpendicular to Direction of Flow, 700rpm, 9.1 Newtons.

III. Lectures Attended October 1991 - September 1994.

COURSES ATTENDED

- o Chemistry Department induction courses;
- o Physical Organic Chemistry, 6 lectures;
- o Inoganic Polymers, 6 lectures.

LECTURES (* denotes attendance)

1991

Sept. 17 Prof. R. D. Fischer, University of Hamburg, Germany
Organo-f-element Systems to Organo-Main-Group Polymers

October 17 Dr. J. A. Salthouse, University of Manchester
Son et Lumiere - a Demonstration Lecture*

October 31 Dr. R. Keeley, Metropolitan Police Forensic Science
Modern Forensic Science*

Nov. 6 Prof. B. F. G. Johnson, Edinburgh University
Cluster-Surface Analogies*

Nov. 7 Dr. A. R. Butler, University of St. Andrews
Traditional Chinese Herbal Drugs: a Different Way of Treating Disease*

Nov. 13 Prof. D. Gani, University of St. Andrews
The Chemistry of PLP-dependent Enzymes

Nov. 20 Dr. R. M. O'Ferral, University College, Dublin
Some Acid-catalyzed Rearrangements in Organic Chemistry

Nov. 28 Prof. I. M. Ward, IRC in Polymer Science, University of Leeds
The Science and Technology of Orientated Polymers*

Dec. 4 Prof. R. Grigg, Leeds University
Palladium-catalyzed Cyclization and Ion Capture Processes*

Dec. 5 Dr. W. D. Cooper, Shell Research
Colloid Science, Theory and Practice*

Dec. 5 Prof. A. L. Smith, ex Unilever
Soap, Detergents and Black Puddings*

1992

January 22 Dr. K. D. M Harris, University of St. Andrews
Understanding the Properties of Solid Inclusion Compounds*

January 29 Dr. A. Holmes, Cambridge University

	Cycloaddition Reactions in the Service of the Synthesis of Piperidine and Indolizidine Natural Products
January 30	Dr. M. Anderson, Shell Research Recent Advances in the Safe and Selective Chemical Control of Insect Pests*
February 12	Prof. D. E. Fenton, Sheffield University Polynuclear Complexes of Molecular Clefts as Models for Copper Biosites
February 13	Dr. J. Saunders, Glaxo Group Research Molecular Modelling in Drug Discovery*
February 19	Prof. E. J. Thomas, Manchester University Applications of Organostannanes to Organic Synthesis
February 20	Prof. E. Vogel, University of Cologne Porphyrins, Molecules of Interdisciplinary Interest
February 25	Prof. J. F. Nixon, University of Sussex Phosphalkynes, New Building Blocks in Inorganic and Organometallic Chemistry
March 5	Dr. N. C. Billingham, University of Sussex Degradable Plastic - Myth or Magic*
March 11	Dr. S. E. Thomas, Imperial College Recent Advances in Organoiron Chemistry
March 12	Dr. R. A. Hann, ICI Imagedata Electronic Photography - An Image of the Future*
March 18	Dr. H. Maskill, Newcastle University Concerted or Step-wise Fragmentation in a Deamination-type Reaction
April 7	D. M. Knight, University of Durham Interpreting Experiments: the Beginning of Electrochemistry
May 6	Prof. T. Marder, University of Waterloo Metal-catalyzed Alkene Hydroboration
May 6	Dr. J. C. Gehret, Ciba-Geigy Some Aspects of Industrial Agrochemical Research
October 15	Dr M. Glazer & Dr. S. Tarling, Oxford University & Birbeck College, London It Pays to be British! - The Chemist's Role as an Expert Witness in Patent Litigation*
October 20	Dr. H. E. Bryndza, Du Pont Central Research

Synthesis, Reactions and Thermochemistry of Metal (Alkyl) Cyanide Complexesand Their Impact on Olefin Hydrocyanation Catalysis

October 22 — Prof. A. Davies, University College London
The Behaviour of Hydrogen as a Pseudometal*

October 28 — Dr. J. K . Cockcroft, University of Durham
Recent Developments in Powder Diffraction

October 29 — Dr. J. Emsley, Imperial College, London
The Shocking History of Phosphorus*

Nov. 4 — Dr. T. P. Kee, University of Leeds
Synthesis and Co-ordination Chemistry of Silylated Phosphites

Nov. 5 — Dr. C. J. Ludman, University of Durham
Explosions, A Demonstration Lecture*

Nov. 11 — Prof. D. Robins, Glasgow University
Pyrrolizidine Alkaloids : Biological Activity, Biosynthesis and Benefits

Nov. 12 — Prof. M. R. Truter, University College, London
Luck and Logic in Host - Guest Chemistry*

Nov. 18 — Dr. R. Nix, Queen Mary College, London
Characterisation of Heterogeneous Catalysts*

Nov. 25 — Prof. Y. Vallee. University of Caen
Reactive Thiocarbonyl Compounds

Nov. 25 — Prof. L. D. Quin, University of Massachusetts, Amherst
Fragmentation of Phosphorous Heterocycles as a Route to Phosphoryl Species with Uncommon Bonding

Nov. 26 — Dr. D. Humber, Glaxo, Greenford
AIDS - The Development of a Novel Series of Inhibitors of HIV*

Dec. 2 — Prof. A. F. Hegarty, University College, Dublin
Highly Reactive Enols Stabilised by Steric Protection

Dec. 2 — Dr. R. A. Aitken, University of St. Andrews
The Versatile Cycloaddition Chemistry of $Bu_3P.CS_2$

Dec. 3 — Prof. P. Edwards, Birmingham University
The SCI Lecture - What is Metal?*

Dec. 9 — Dr. A. N. Burgess, ICI Runcorn
The Structure of Perfluorinated Ionomer Membranes*

1993

January 20 Dr. D. C. Clary, University of Cambridge
Energy Flow in Chemical Reactions*

January 21 Prof. L. Hall, Cambridge
NMR - Window to the Human Body*

January 27 Dr. W. Kerr, University of Strathclyde
Development of the Pauson-Khand Annulation Reaction : Organocobalt Mediated Synthesis of Natural and Unnatural Products

January 28 Prof. J. Mann, University of Reading
Murder, Magic and Medicine*

February 3 Prof. S. M. Roberts, University of Exeter
Enzymes in Organic Synthesis

February 10 Dr. D. Gillies, University of Surrey
NMR and Molecular Motion in Solution*

February 11 Prof. S. Knox, Bristol University
The Tilden Lecture Organic Chemistry at Polynuclear Metal Centres

February 17 Dr. R. W. Kemmitt, University of Leicester
Oxatrimethylenemethane Metal Complexes

February 18 Dr. I. Fraser, ICI Wilton
Reactive Processing of Composite Materials*

February 22 Prof. D. M. Grant, University of Utah
Single Crystals, Molecular Structure, and Chemical-Shift Anisotropy

February 24 Prof. C. J. M. Stirling, University of Sheffield
Chemistry on the Flat-Reactivity of Ordered Systems*

March 10 Dr. P. K. Baker, University College of North Wales, Bangor
Chemistry of Highly Versatile 7-Coordinate Complexes

March 11 Dr. R. A. Y. Jones, University of East Anglia
The Chemistry of Wine Making*

March 17 Dr. R. J. K. Taylor, University of East Anglia
Adventures in Natural Product Synthesis

March 24 Prof. I. O. Sutherland, University of Liverpool
Chromogenic Reagents for Cations

May 13 Prof. J. A. Pople, Carnegie-Mellon University, Pittsburgh, USA
Applications of Molecular Orbital Theory*

May 21 Prof. L. Weber, University of Bielefeld

Metallo-phospha Alkenes as Synthons in Organometallic Chemistry

June 1 — Prof. J. P. Konopelski, University of California, Santa Cruz
Synthetic Adventures with Enantiomerically Pure Acetals

June 2 — Prof. F. Ciardelli, University of Pisa
Chiral Discrimination in the Stereospecific Polymerisation of Alpha Olefins

June 7 — Prof. R. S. Stein, University of Massachusetts
Scattering Studies of Crystalline and Liquid Crystalline Polymers

June 16 — Prof. A. K. Covington, University of Newcastle
Use of Ion Selective Electrodes as Detectors in Ion Chromatography

June 17 — Prof. O. F. Nielsen, H. C. _rsted Institute, University of Copenhagen
Low-Frequency IR - and Raman Studies of Hydrogen Bonded Liquids*

Sept. 13 — Prof. Dr. A.D. Schlüter, Freie Universität Berlin, Germany
Synthesis and Characterisation of Molecular Rods and Ribbons

Sept. 13 — Dr. K.J. Wynne, Office of Naval Research, Washington, USA
Polymer Surface Design for Minimal Adhesion*

Sept. 14 — Prof. J.M. DeSimone, University of North Carolina, Chapel Hill, USA
Homogeneous and Heterogeneous Polymerisations in Environmentally Responsible Carbon Dioxide

Sept. 28 — Prof. H. Ila, North Eastern Hill University, India
Synthetic Strategies for Cyclopentanoids via Oxoketene Dithioacetals

October 4 — Prof. F.J. Feher, University of California, Irvine, USA
Bridging the Gap between Surfaces and Solution with Sessilquioxanes

October 14 — Dr. P. Hubberstey, University of Nottingham
Alkali Metals: Alchemist's Nightmare, Biochemist's Puzzle and Technologist's Dream*

October 20 — Dr. P. Quayle, University of Manchester
Aspects of Aqueous ROMP Chemistry

October 21 — Prof. R. Adams, University of South Carolina, USA
Chemistry of Metal Carbonyl Cluster Complexes : Development of Cluster Based Alkyne Hydrogenation Catalysts

October 27 — Dr. R.A.L. Jones, Cavendish Laboratory, Cambridge
Perambulating Polymers*

Nov. 10 — Prof. M.N.R. Ashfold, University of Bristol

	High Resolution Photofragment Translational Spectroscopy : A New Way to Watch Photodissociation*
Nov. 17	Dr. A. Parker, Rutherford Appleton Laboratory, Didcot Applications of Time Resolved Resonance Raman Spectroscopy to Chemical and Biochemical Problems*
Nov. 24	Dr. P.G. Bruce, University of St. Andrews Structure and Properties of Inorganic Solids and Polymers
Nov. 25	Dr. R.P. Wayne, University of Oxford The Origin and Evolution of the Atmosphere*
Dec. 1	Prof. M.A. McKervey, Queen's University, Belfast Synthesis and Applications of Chemically Modified Calixarenes
Dec. 8	Prof. O. Meth-Cohn, University of Sunderland Friedel's Folly Revisited - A Super Way to Fused Pyridines
Dec. 16	Prof. R.F. Hudson, University of Kent Close Encounters of the Second Kind
1994	
January 26	Prof. J. Evans, University of Southampton Shining Light on Catalysts*
February 2	Dr. A. Masters, University of Manchester Modelling Water Without Using Pair Potentials
February 9	Prof. D. Young, University of Sussex Chemical and Biological Studies on the Coenzyme Tetrahydrofolic Acid
February 16	Prof. K.H. Theopold, University of Delaware, USA Paramagnetic Chromium Alkyls : Synthesis and Reactivity
February 23	Prof. P.M. Maitlis, University of Sheffield Across the Border : From Homogeneous to Heterogeneous Catalysis*
March 2	Dr. C. Hunter, University of Sheffield Noncovalent Interactions between Aromatic Molecules
March 9	Prof. F. Wilkinson, Loughborough University of Technology Nanosecond and Picosecond Laser Flash Photolysis*
March 10	Prof. S.V. Ley, University of Cambridge New Methods for Organic Synthesis
March 25	Dr. J. Dilworth, University of Essex Technetium and Rhenium Compounds with Applications as Imaging Agents

April 28 — Prof. R. J. Gillespie, McMaster University, Canada
The Molecular Structure of some Metal Fluorides and Oxofluorides: Apparent Exceptions to the VSEPR Model.

May 12 — Prof. D. A. Humphreys, McMaster University, Canada
Bringing Knowledge to Life